Ultrafast modifications of graphitic carbon nanostructures and nanohybrids for energy storage and catalysis

A Thesis submitted to the Indian Institute of Technology Guwahati for the degree of

Doctor of Philosophy

by

Golam Masud Karim

Under the supervision of

Dr. Uday Narayan Maiti

Department of Physics
Indian Institute of Technology Guwahati
Guwahati-781039, India
January 2025

Acknowledgments

For me, pursuing a Ph.D. has been a transformative journey fuelled by an unrelenting quest for knowledge. As I stand at the threshold of completing this incredible chapter of my life, I am overwhelmed with gratitude for the many individuals who have supported and guided me along the way. Without their unwavering encouragement, this thesis would not have come to fruition.

First and foremost, I extend my heartfelt gratitude to my supervisor, **Dr. Uday Narayan Maiti**, for his invaluable mentorship, unyielding support, and constant encouragement throughout my Ph.D. journey. Being a part of his research group has been a privilege. His profound knowledge, dedication to science, and infectious enthusiasm have continually inspired me to strive for excellence. This thesis would not have been possible without his guidance.

I am deeply grateful to my doctoral committee members, **Prof. Padma K. Padmanabhan**, **Prof. Gagan Kumar**, and **Prof. Chandan Das**, for their insightful suggestions and constructive feedback, which have greatly enriched my research work. I also sincerely thank **Prof. Subhradip Ghosh**, the former Head of the Department of Physics at IIT Guwahati, for his administrative support and encouragement, and the Central Instruments Facility (CIF) at IIT Guwahati for providing access to cutting-edge instrumentation and facilities.

I am immensely thankful for the financial support provided by **IIT Guwahati** through the institute **fellowship**, which enabled me to carry out my research. I also appreciate the support and cooperation of the **faculty members**, **scientific officers**, and **non-teaching staff** in the Department of Physics.

My deepest appreciation goes to **Dr. Youngtak Oh** (Korea Institute of Science and Technology), **Dr. Arup K. Rath** (CSIR-National Chemical Laboratory Pune), **Dr. Ranjit Thapa** (SRM University AP), and **Dr. Uttam Manna** (IIT Guwahati) for their critical contributions, including theoretical studies, access to facilities, and valuable discussions that have greatly enriched my research.

I have been fortunate to share this journey with an incredible group of lab mates. My heartfelt thanks go to **Dr. Anirban Sikdar**, **Dr. Abhisek Majumdar**, **Dr. Pronoy Dutta**, **Sujit Da**, **Amalika**, **Snehasish**, **Priyam**, **Pranab**, **Hemanta**, **Urbismita**, and **Harish** for their companionship, support, and countless shared experiences. I am also grateful to my collaborators, **Neha V. Dambhare**, **Jaysri Das**, **Narad Barman**, and **Waleed Ahmad**, whose expertise has added significant value to this work.

To my dear friends **Sumit**, **Roni**, **Partha**, **Sahabub**, **Mrinal**, **Prantik**, **Suruj**, **Suchit** and **Nikhil**-thank you for your unwavering support and for making my Ph.D. journey filled with cherished memories. I am also grateful to my juniors, **Shantanu**, **Chinmoy**, **Dipankar**, and **Swarup**, for their camaraderie and for fostering a collaborative and balanced environment.

I owe everything to my family, whose unconditional love and belief in me have been my foundation. I am forever indebted to my father, **Golam Mostafa**, whose blessings and values continue to guide me, and to my mother, **Moslima Khatun**, whose strength and sacrifices have been my greatest inspiration. I deeply appreciate the encouragement of my siblings and their families, especially **Boro Di**, **Mej Di**, and **Chhot Di**, whose constant support has been invaluable.

Finally, I extend my deepest love and gratitude to my wife, **Nagma**, for her patience, understanding, and unwavering belief in me. Her support has been my anchor throughout this journey. This thesis is dedicated to my beloved son, **Naveed**, whose presence has brought immense joy and purpose to my life. You inspire me every day to pursue excellence and happiness.

To anyone I may have unintentionally overlooked in these acknowledgments, please know that your contributions have not gone unnoticed and are sincerely appreciated in my heart.

Golam Masud Karim

IIT Guwahati

CONTENTS

Abstract

Utilizing renewable energy sources to transform/store energy in either electrochemical energy in battery/supercapacitors or chemical fuel such as hydrogen via electrocatalytic hydrogen evolution reaction (HER) puts forward a clean and sustainable future. The ever-increasing requirements for a persistent source of environmentally benign clean energy for powering portable, wearable electronic devices and other appliances stipulate the meteoric rise of supercapacitors and electrocatalytic hydrogen evolution reaction (HER) devices. Carbon, one of the most abundant materials, is a natural choice for supercapacitor electrodes and catalyst support for HER due to its robustness, corrosion-free, and conductive properties. Graphene and related carbon nanomaterials derived from organic compounds, especially metal-organic framework (MOF) derived graphitic nanostructures, are frontrunners in developing electrode materials for supercapacitors and electrocatalytic HER catalysts. Specifically, porous graphene and MOF-derived porous graphitic nanostructures, owing to their high surface area to volume ratio, accessible ion transportation channel, and high conductivity, are the leading contenders for supercapacitor electrodes. Due to their excellent anchoring property with electronic and morphological tunability, MOF-derived graphitic nanostructures are also the optimal choice as a robust and conducting support for holding efficient HER catalysts. Noble metal-based (Pt, Ir, Pd, Ru, Rh, etc.) catalysts are the best electrocatalysts due to their high activity, selectivity, and long-term durability towards HER. However, scarcity and sky-high costs hinder their practical adaptability in HER applications. In developing low-cost HER catalysts, the optimal approach should be considered either by minimizing the usage of noble metals or by replacing the noble metals with earth-abundant transition metals. One of the most successful strategies is uniform dispersion of the metal catalysts in tiny nanoclusters (<2 nm) or single-atom over electronic tunable support like the MOF-derived graphitic nanostructures, providing the maximum atomic utilization towards HER catalysis. Whether it is nanoscale drilling of graphene and related carbon nanomaterials for supercapacitors or nano-dispersion of metal catalysts over MOF-derived graphitic nanostructures for HER, high-temperature heating is the common need for both. Consequently, a high thermal budget and significant time consumption are inevitable, which limits their practical applications. Hence, more focus is required to optimize material performance in energy storage/transformation and develop cost-effective, time/energy-efficient material processing techniques. The present thesis meticulously addresses the mentioned challenges in energy storage and catalysis by developing high-performing

supercapacitor electrodes and efficient electrocatalysts for HER using a novel, ultrafast, energy-efficient, and cost-effective strategy, namely transient Joule heating (TJH).

For instance, using millisecond current pulses, the TJH strategy was utilized to realize a multimodal porous network of perforated graphene by on-site reduction and activation of graphene oxide. The multimodal porosity and surface functionalities of graphene were regulated at an ultrafast rate for the optimized fabrication of ready-to-use electrodes with nano-to-micro pores, providing ample ion-transport channels with high accessible surface area. The symmetric supercapacitor device made of the as-developed electrodes exhibited a high areal capacitance of 380.2 mF cm^{-2} with an energy density of 52.8 μWh cm^{-2} at a power density of 950.5 μW cm^{-2}. A flexible solid-state supercapacitor (SSC) for wearable electronic devices was also asymmetrically designed with Mxene, a graphene-like 2D nanomaterial. The wearable asymmetric solid-state supercapacitor (ASC), made of as-developed perforated graphene linked to commercial carbon cloth (CC) as a positive electrode and Mxene-coated CC as a negative electrode, showed excellent electrochemical energy storage performance and mechanical stability. The wearable ASC displayed a specific capacitance of 303.1 mF cm^{-2} with an extended potential window of 1.6 V. Nevertheless, it can deliver a maximum energy density of 107.8 μWh cm^{-2} at a power density of 485.0 μW cm^{-2}, which is more than double the energy density of the as-fabricated symmetric device. After 10000 charge-discharge and 5000 bending cycles, the wearable device still exhibited stable and repeatable performance. High energy density, operational and mechanical stability, together with direct, simple processing of electrodes by the unique TJH strategy and its orders of magnitude lower cost–and–processing–time, signifies the importance of the as-developed device for practical wearable energy storage applications. Furthermore, utilizing the TJH strategy in a two-step ultrafast processing, a Ru-based superefficient catalyst was realized for electrocatalytic HER application. In the first step, a transient electro-graphitization (TEG) process was developed to transform an array of leaf-like nanostructures of Co-MOF having a high surface-to-volume ratio vertically linked to commercial carbon cloth (CC) into an array of vertical carbon nano leaves firmly linked to CC. The TEG process converted the MOFs into Co-nanoparticle-embedded carbon nano leaves with progressively higher graphitization levels by adjusting the current pulse duration from a few hundred milliseconds to one second. In the next step of thermal shock resulting from a 50-millisecond current pulse, ruthenium was uniformly dispersed and arrested in either single-atom, ultrasmall nanoclusters of amorphous, or crystalline state over the surface of graphitic nano leaves depending on the graphitization level.

The resulting ultrafine ($\approx 0.7\ nm$) amorphous ruthenium nanoclusters linked with graphitic nano leaves exhibited state-of-the-art HER performance, requiring very low overpotentials of only 23 and 285 mV to achieve current densities of 10 and 500 mA cm^{-2}, respectively. Further, it demonstrated exceptional operational stability for 200 hours under high 200 and 400 mA cm^{-2} HER currents. Additionally, the synergistic interplay of graphitization-controlled support, the unique electronic structure of supported amorphous Ru nanocatalysts, and efficient bubble release dynamics of super-aerophobic graphitic nano leaves contributed to reduced overpotentials. Density functional theory suggests the unique electronic structure of amorphous Ru-nanocluster and the cooperative effect of cobalt embedded in the graphitic layer, resulting in an accelerated HER process. Thanks to the tunability of the TJH technique in controlling the graphitization level of TEG-processed MOF-derived graphitic nano leaves and its rapid heating-cooling features in dispersing and stabilizing size and crystallinity-controlled ruthenium, especially in the unusual amorphous phase. Thus, in synthesizing superefficient HER catalysts, the TJH, a time and energy-efficient technique, reduces the thermal budget and maximizes the atomic utilization of noble metal (Ru) catalysts by dispersing them in tiny nanoclusters, making it a two-fold cost-reduction strategy.

In a further study, the TEG-processed MOF-derived graphitic nano leaves were used as a scaffold in developing porous graphitic nano leaves for supercapacitor electrode fabrication. A unique electrochemical process was carried out for the perforation. The Co-nanoparticles embedded into the graphitic nano leaves were etched out, leaving behind the nano-to-micro pores. The as-developed porous graphitic nano leaves vertically linked to carbon cloth are directly used as supercapacitor electrodes, which displayed a maximum capacitance of 229.0 mF cm^{-2} with a voltage window of 1V. The voltage window and, thus, the energy density of the supercapacitor were further improved by utilizing the unique water-in-salt electrolyte (WISE). The WISE supercapacitor has an extended voltage window of 2.3 V. It exhibits an energy density (power density) of 127.5 μWh cm^{-2} (11891.0 μW cm^{-2}), which is almost 3.2 times the energy density (40.4 μWh cm^{-2}) of the best-performing sample in aqueous electrolyte. Furthermore, in search of a low-cost earth-abundant HER catalyst, the TEG-processed MOF-derived carbon nano leaves vertically attached to carbon cloth were directly used as an electrode for electrocatalytic HER. The HER activity was improved by simultaneously optimizing the graphitization level of the carbon nano leaves and the size of the Co-nanoparticles by tuning the current pulse duration (milliseconds) of the TJH method. The tiny Co-nanoparticle-embedded carbon nano leaves showed an overpotential of only 91 mV to achieve a current density of 10 mA cm^{-2}, making it a significantly active, earth-abundant transition metal catalyst for HER. With the success of low-cost single transition metal catalyst synthesis, the ultrafast TJH strategy was also extended to develop bimetallic and trimetallic transition metal catalysts with improved HER activity. The as-prepared bimetallic nickel-copper (NiCu) based nanoparticles embedded into carbon nanostructure showed an enhanced HER activity with an overpotential of only 46 mV at a current density of 10 mA cm^{-2}.

We believe the present thesis will provide a guideline for developing carbon nanostructure-based functional materials via large-scale, facile, cost-effective processing and will find widespread applications not only in energy storage but in other fields like oxygen reduction reaction, nitrogen reduction reaction, carbon dioxide reduction reaction, and other electrocatalytic valuable production through electrochemical processes.

List of abbreviation

HER	Hydrogen evolution reaction
OER	Oxygen evolution reaction
GO	Graphene oxide
EDLC	Electrochemical double-layer capacitor
JG	Joule heated graphene
AJG	Activated Joule heated graphene
GNL	Graphitic nano-leave
lGNL	Low-graphitized nano-leave
mGNL	Moderately graphitized nano-leave
CV	Cyclic voltammetry
GCD	Galvanostatic charge-discharge
EIS	Electrochemical impedance spectroscopy
MOF	Metal-organic framework
ECSA	Electrochemical active surface area
FESEM	Field emission scanning electron microscopy
FETEM	Field emission transmission electron microscopy
HRTEM	High-resolution transmission electron microscopy
STEM	Scanning transmission electron microscopy
BET	Brunauere–Emmette–Teller
XRD	X-ray diffraction
XPS	X-ray photoelectron spectroscopy
XANES	X-ray absorption near-edge spectroscopy
EXAFS	Extended X-ray absorption fine structure spectroscopy

List of publications

Journal publications:

1. **G.M. Karim**, A. Patra, S.K. Deb, H. Upadhya, S. Das, P. Mukherjee, W. Ahmad, N. Bar man, R. Thapa, N.V. Dambhare, A.K. Rath, J. Das, U. Manna, R.R. Urkude, Y. Oh, U.N. Maiti, "Transient Electro-Graphitization of MOFs affecting the crystallization of ruthenium nanoclusters for highly efficient hydrogen evolution", **Adv. Funct. Mater.**, 34 (2024), 2315460.
2. **G. M. Karim**, P. Dutta, A. Majumdar, A. Patra, S. K. Deb, S. Das, N. V. Dambhare, A. K. Rath, U. N. Maiti, "Ultra-fast electro-reduction and activation of graphene for high energy density wearable supercapacitor asymmetrically designed with Mxene", **Carbon**, 203, 2023, 191-201,0008-6223.
3. **G.M. Karim**, S. K. Deb, A. Patra, S. Das, P. Bera, U. N. Maiti, " Current-pulse-programmed manipulation of graphitic order impacting the perforation of MOF-derived carbon hierarchy for high areal-energy-density supercapacitors ", **Adv. Funct. Mater.** (communicated).
4. **G.M. Karim**, P. Mukherjee, P. Bera, S. Das, U. N. Maiti, "Rapid cathodic phase evolution of pulsed-thermal-shock tuned Cu/Cu2O/Cu heterostructures towards optimized reaction kinetics during highly boosted hydrogen evolution", (ready to cmmunicate).
5. P. Dutta, S. K. Deb, A. Patra, A. Majumdar, **G. M. Karim**, C. K. Parashar, M. K. Mohanta, M. Qureshi, U. N. Maiti, "Electric Field Guided Fast and Oriented Assembly of MXene into Scalable Pristine Hydrogels for Customized Energy Storage and Water Evaporation Applications" Adv. Funct. Mater. 2022, 2204622, 2204622.
6. P. Dutta, A. Patra, S. K. Deb, A. Sikdar, A. Majumdar, **G. M. Karim**, U. N. Maiti, "Freestanding MXene-hydrogels prepared via critical density-controlled self-assembly: high-performance energy storage with ultrahigh capacitive vs. diffusion-limited contribution", **J. Mater. Chem. A**, 2021, 9, 25013-25023.
7. M. Bora, A. Sikdar, S. Kapse, A. Majumdar, P. Dutta, **G. M. Karim**, S. Deb, R. Thapa, U. N. Maiti, "Stable and boosted oxygen evolution efficiency of mixed metal oxide and borate planner heterostructure over heteroatom (N) doped electrochemically exfoliated graphite foam", **Catalysis Today**, 2021, 370, 83-92.
8. S. Swain, V. Kandathil, **G. M. Karim**, U. N. Maiti, S. A. Patil, A. K. Samal, "Computational and Experimental Design of the Octahedral PdFe Alloy Nanocatalyst for

Hiyama Cross-Coupling and Environmental Pollutant Degradation", **ACS Appl. Nano Mater.** 2023, 6, 3254-3267.

9. A. Majumdar, P. Dutta, Y. Kang, **G. M. Karim**, A. Sikdar, S. K. Deb, S. O. Kim, U. N. Maiti, "Energy-efficient ultrafast microwave crystalline phase evolution for designing highly efficient oxygen evolution catalysts", **Applied Surface Science**, 2023, 617, 156622.
10. P. Dutta, S. K. Deb, A. Patra, **G. M. Karim**, A. Majumdar, P. Kumar, P. K. Iyer, N. Padma, U. N. Maiti, "Activating Ion Channels in Collapsed Hydrogel Derived Densifed MXene Films with Cellulose Nanofbers to Overcome the Areal Versus Volumetric Capacitance Trade-Off", **Small**, 2024, 20, 2400119.
11. A. Patra, P. Dutta, M. Das, **G. M. Karim**, S. K. Deb, S. Das, P. Mukherjee, S. Ghosh, U. N. Maiti, "Harnessing true capacitive activity of nitrogen-doped MXene through hydrogel assembly and theoretical understanding of the role of dopant sites", **Carbon**, 2024, 229, 119485.
12. S. K. Deb, P. Dutta, **G. M. Karim**, A. Patra, P. Bera, S. Das, P. Mukherjee, K. Rengasamy, A. Borbora, U. Manna, V. Subramanian, U. N. Maiti, "Bulk versus surface-limited polymer encapsulation: A current pulse-induced approach for confined polymer coating selectively over quasi-oriented MXene aerogel", **Chemical Engineering Journal**, 2024, 484, 149617.
13. A. Majumdar, **G. M. Karim**, P. Dutta, H. Lee, S. K. Deb, A. Sikdar, Y. Oh, U. N. Maiti, "Microwave induced rapid surface amorphization of metal oxide nanowire into sulfides shell for electronically modulated efficient hydrogen evolution catalyst", **Catalysis Today**, 2023, 423, 113962.

Patents:

1. Ultra-fast on-site perforation of graphene via transient Joule heating and stable wearable energy storage devices thereof. **Inventors: Golam Masud Karim**, Uday Narayan Maiti, Patent Application Number: 202211069760, 2022, Indian Patent Office (Application Pending).

2. Ultrafast development of crystallinity tuneable nanocatalysts over graphitization-controlled carbon nanostructure for highly efficient hydrogen evolution. **Inventors: Golam Masud Karim**, Uday Narayan Maiti, Patent Application Number: 202331062341, 2023, Indian Patent Office (Application Pending).

Conferences attended:

1. IIChE - CHEMCON 2023, Kolkata, India. Rapid synthesis of Ni@NiCo2O4 heterostructure catalyst for HER.
2. IISF-Young Scientist Conclave-2024, IIT Guwahati, Guwahati-781039, Assam, India, The ultrafast development of graphitic nano-leaves supported Ru-nanoclusters with tunable crystallization to boost H2 generation from water.

Chapter 1

Introduction

1. Introduction

The exhaustion of fossil fuel resources and growing environmental concerns over their use call for the adoption of clean and renewable energy sources like solar, wind, and hydropower. However, the intermittent nature of these renewable sources highlights the need for advanced energy storage solutions. Efficient energy storage is therefore crucial, and electrochemical energy storage systems have a pivotal role in addressing this challenge. The leading and fastest-developing electrochemical energy storage technologies are generally classified into two main systems, depending on their energy storage mechanisms. Firstly, batteries and supercapacitors store renewable energy as electrical energy.[1–6] On the other hand, the electrolyzers utilized renewable energy to split water into hydrogen (H_2) and oxygen (O_2) by electrocatalytic hydrogen evolution reaction (HER) and oxygen evolution reaction (OER) at the cathode and anode, respectively.[3,7–11] H_2, being a green fuel, has a very high specific energy density and can be stored as chemical energy for use as green fuel on demand.

Both energy technologies have gained tremendous success over the years. Unlike batteries, supercapacitors, due to their high power density, can deliver a rapid energy supply to appliances depending on demand requirements.[12,13] Supercapacitor technology solely relies on choosing suitable nanomaterials for electrodes, electrolytes, and their development in a facile, environmentally benign, and cost-effective way.[14–18] Significant attention is also paid to the electrocatalytic hydrogen evolution reaction (HER) for environment-friendly green H_2 fuel production. However, the progress in HER exclusively depends on selecting and designing efficient nanomaterials as electrocatalysts, supporting materials to hold the nanocatalysts firmly, and their facile, energy-efficient, and cost-effective synthesis.[7,19,20]

Significant research efforts have been devoted to finding suitable electrode materials for supercapacitors and efficient electrocatalyst materials for HER, of which carbon is a common choice.[21–24] Carbon, one of the most abundant elements on Earth, is ubiquitous in various forms, including organic compounds like polymers and hydrocarbons, inorganic materials like diamonds and graphite, and in all living organisms, where it plays a crucial role in their structure and function. Due to their robustness, corrosion-free properties, and high conductivity, graphite and graphitic carbon (derived from high-temperature pyrolysis of organic compounds) have been extensively used as electrode materials for electrochemical energy harvesting technologies.[1,25–27] Despite the aforementioned crucial properties, bulk carbon lacks a surface-to-volume ratio and cannot provide enough room for ions to be stored for supercapacitor electrodes.[25,28] The lack of easy ion transport makes most of the volume inaccessible. Also, a high surface area is desirable in catalyst support materials for HER electrodes as the catalytic reaction happens on the surface.[29,30] The low specific surface area of bulk carbon cannot hold sufficient HER catalysts, leading to low HER activity.

Carbon nanostructures, e.g., graphene and graphitic carbon nanostructures derived from metal-organic framework (MOF), owing to their easy tunability of morphology and electronic properties, have significantly high surface area to volume ratio and conductivity, deserving the best materials for electrochemical energy applications.[31–35] Further processing of graphene and MOF-derived graphitic carbon nanostructures provides a porous graphene framework and porous MOF-derived graphitic nanostructures having an enormous specific surface area and ion transporting channels ideal for supercapacitor electrodes.[2,15,36–38] On the other hand, the carbon nanostructures alone cannot exhibit efficient activity toward HER; instead, active HER catalysts are loaded over the surface of the carbon nanostructures to fabricate the HER electrodes.[39–43] Currently, state-of-the-art electrocatalysts for HER predominantly rely on precious metals like platinum (Pt), ruthenium (Ru), iridium (Ir), palladium (Pd), and rhodium (Rh) due to their exceptional efficiency and long-term stability in these catalytic processes.[7,33,44–53] Considering the high cost of noble metals, enormous research efforts have been paid to develop low-cost catalysts based on earth-abundant transition metals (Ni, Co, Cu, Fe, and V, etc.).[23,24,49,54–59] However, the performance and durability of the catalysts of earth-abundant transition metals are still far from that of noble metals-based catalysts. Nevertheless, developing highly efficient catalysts while minimizing the usage of noble metals is considered the most feasible approach to lower the cost of catalysts with guaranteed performance. In this direction, ultra-small nanoclusters and single-atom catalysts (SAC) uniformly dispersed over the surface of a conducting support, e.g., MOF-derived graphitic carbon nanostructure, have become a prime research focus due to the most effective atomic utilization in catalysis.[60–64]

The processing of such materials, porous graphene network, porous MOF-derived carbon nanostructure for supercapacitor electrodes, and uniformly dispersed tiny metal nanoclusters or single-atom catalyst-linked MOF-derived graphitic carbon nanostructures involves high-temperature heating for thermal activation of graphene and pyrolysis of MOFs.[11,15,28,65–68] Several hours of furnace heating are traditionally engaged for the said material processing, leading to a high thermal budget and lengthy time consumption.[31,69] Many researchers have recently been employed to develop time/energy-efficient, cost-effective novel thermal processing, including microwave heating, laser heating, and transient Joule heating (TJH).[24,64,70,71] Among all the techniques, TJH is the best method, as it does not involve any sophisticated instrument but rather an electric power supply capable of supplying a current pulse. In the TJH technique, the temperature can reach >10^3 K within a fraction of a second and suddenly drop to ambient temperature after switching it off, making it an economically viable technique. Indeed, the TJH method is one of the most suitable strategies, whether it is porous graphene synthesis by high-temperature thermal activation of graphene for supercapacitor electrodes or pyrolysis of MOFs and uniform dispersion of tiny metal nanoclusters and single-atom over the MOF-derived carbon nanostructures for HER catalyst electrode.

This chapter accentuates a concise prospect of two pivotal facets of renewable energy storage technology: energy storage through electrochemical supercapacitors and energy transformation via the electrocatalytic HER process. Current breakthroughs in graphene and MOF-derived carbon nanostructures as supercapacitors and HER electrode materials have also been included. Then, current impediments to developing the finest supercapacitor electrodes and efficient electrocatalysts for HER have been encompassed. Further, we have emphasized the architectural principles of electrodes for practical applications at the commercial level. The electrochemical characterization techniques for supercapacitors and HER are also included briefly. The motivation and objectives of this thesis are also presented at the end of this chapter.

1.1. Principles of supercapacitor as energy storage device

Electrochemical energy storage (EES) systems like batteries, supercapacitors, and water electrolyzers combined with fuel cells are the popular choices for on-demand controlled energy supply in our everyday lives. Although batteries have dominated the EES systems due to their high energy density, low cycle life, severe safety issues, high cost, and low power density are the few challenges to addressing desired energy storage solutions. In this regard, supercapacitors have gained much attention by introducing carbon nanomaterials such as graphene, carbon nanotube, and other graphitic carbon nanostructures. Although supercapacitors possess relatively low energy density compared to batteries, they offer several compelling advantages. Notably, they boast ultra-high-power densities, enabling rapid charging-discharging, making them ideal for a power boost, such as a power grid, heavy electric vehicles, etc. Furthermore, supercapacitors exhibit an extensive cycle life, ensuring extended durability and reliability. Their simple configuration also enhances safety, making them ideal for use in wearable electronics as a power supplier, while their lower cost of production makes them a more affordable option.

1.1.1. The charge storage mechanism of supercapacitors and performance determining factors

Conventional capacitors consist of two parallel conducting plates and a dielectric medium in between them. They store charges electrostatically. When a voltage is applied between the plates, it creates excess charges at one plate and a deficiency of equal and opposite charges at another plate. The capacitance of a parallel plate capacitor is defined as,

$$C = \frac{\varepsilon A}{d} \tag{1.1}$$

Where ε, A, and d are the dielectric constant, area of the electrode, and distance between the conducting plates, respectively. So, the capacitance of the capacitor solely depends on the geometrical area and distance between the plates. The limited geometrical area and plate separation of the conventional capacitors often result in limited capacitance, as shown in the Regone plot in **Figure 1.1**.

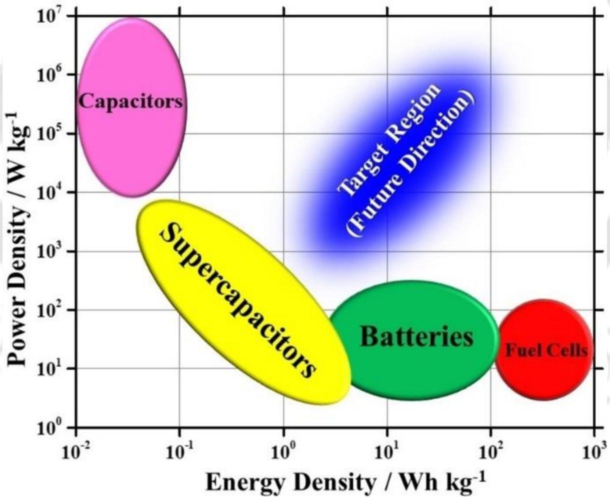

Figure 1.1: Regone plot.[72]

Conversely, an electrochemical supercapacitor consists of two electrodes, an electrolyte, and a separator between the electrodes to avoid short-circuit, as shown in **Figure 1.2**. When a voltage is applied between the electrodes, the electrolyte ions, surrounded by solvent molecules, move toward the electrodes and induce equal and opposite charges on the surfaces of the electrodes, forming two layers at electrode-electrolyte interfaces. Each layer, consisting of induced charges on electrode surfaces and solvated ions separated by solvent molecules, acts as an individual capacitor, where solvent molecules act as a dielectric medium. Thus, the separation, d, is equal to the diameter of the solvent molecule, resulting in several-fold increased capacitance of the layers due to the tiny atomistic separation between the positive and negative charges; thus, the name is supercapacitor. In an electrochemical supercapacitor, two layers at the electrode-electrolyte interfaces act as two capacitors connected in series, and this is why it is also called an electrochemical double-layer capacitor (EDLC). The overall capacitance of an EDLC supercapacitor can be defined as,

$$\frac{1}{C_{dl}} = \frac{1}{C_{l_1}} + \frac{1}{C_{l_2}} \tag{1.2}$$

Where, C_{l_1} and C_{l_2} are the capacitance of the individual capacitors made of the layers of positive and negative charges separated by solvent molecules near positive and negative electrode-electrolyte interfaces, respectively. Notably, these capacitance values (C_{l_1} and C_{l_2}) can be considered as the capacitances of positive and negative electrodes individually.

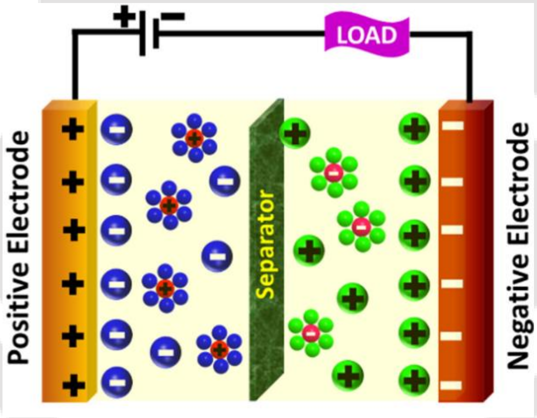

Figure 1.2: Schematic of an electrochemical supercapacitor.[73]

Although the capacitance value of an EDLC supercapacitor is several-fold higher than that of conventional capacitors, thanks to the tiny separation (d) between positive and negative charges separated by a single-molecular layer of the solvent. However, the capacitance is limited by the electrodes' surface area (A). Therefore, electrode materials play a crucial role in determining the performance of a supercapacitor. The electrodes' conductivity and surface area (A) should be very high to achieve optimal supercapacitor performance. In this regard, carbon nanomaterials like graphene, carbon nanotube (CNT), and MOF-derived graphitic nanostructures (GNs) are the frontrunners as supercapacitor electrode materials due to their high conductivity (e.g., ~10^8 S m^{-1}, 10^7 S m^{-1}, and 10^2-10^4 S m^{-1} for graphene, CNT, GNs, respectively), large specific surface area (e.g., 2630 m^2 g^{-1}, 100-1300 m^2 g^{-1}, and 500-3000 m^2 g^{-1} for graphene, CNT, GNs, respectively), robustness, and corrosion resistance. Unlike batteries, supercapacitors require minimal time to accumulate the electrolyte ions throughout the electrodes' surface during charging and disperse the ions into the electrolyte during discharging. This quick charging-discharging capability of supercapacitors results in higher power density than batteries. However, supercapacitors have lower energy density than batteries. The energy density of a supercapacitor is defined by

$$E = \frac{1}{2} CV^2 \tag{1.3}$$

where C and V are the capacitance and voltage window of the device. The energy density (E) can be improved by optimizing the capacitance and extending the potential window of the device.

1.1.2. Supercapacitor Characterization Methods:

The performance of a supercapacitor is assessed using several techniques, including cyclic voltammetry (CV), galvanostatic charge-discharge (GCD) profiling, and electrochemical impedance spectroscopy (EIS). These methods involve measuring parameters such as current, voltage, and time to calculate energy and power densities. A supercapacitor's electrochemical cell can operate in either a three-electrode configuration, which includes a working electrode (WE), reference electrode (RE), and counter electrode (CE), or a two-electrode configuration, where both electrodes are equipped with active materials. However, the two-electrode setup provides a more accurate evaluation of performance since it better reflects the conditions under which the device operates in practical applications. [54]

Cyclic voltammetry (CV):

A CV of a supercapacitor illustrates the current as a response to the applied constant potential changes (mV s^{-1}) within a defined potential window. CV curves offer valuable insights about the charge storage mechanism and the capacitance. A smooth, rectangular CV profile suggests an electric double-layer capacitance (EDLC) charge storage mechanism (**Figure 1.3a** and **b**).

On the other hand, a rectangular profile with overlapping oxidation-reduction peaks indicates a pseudo-capacitive charge storage mechanism (Figure **1.3c**).

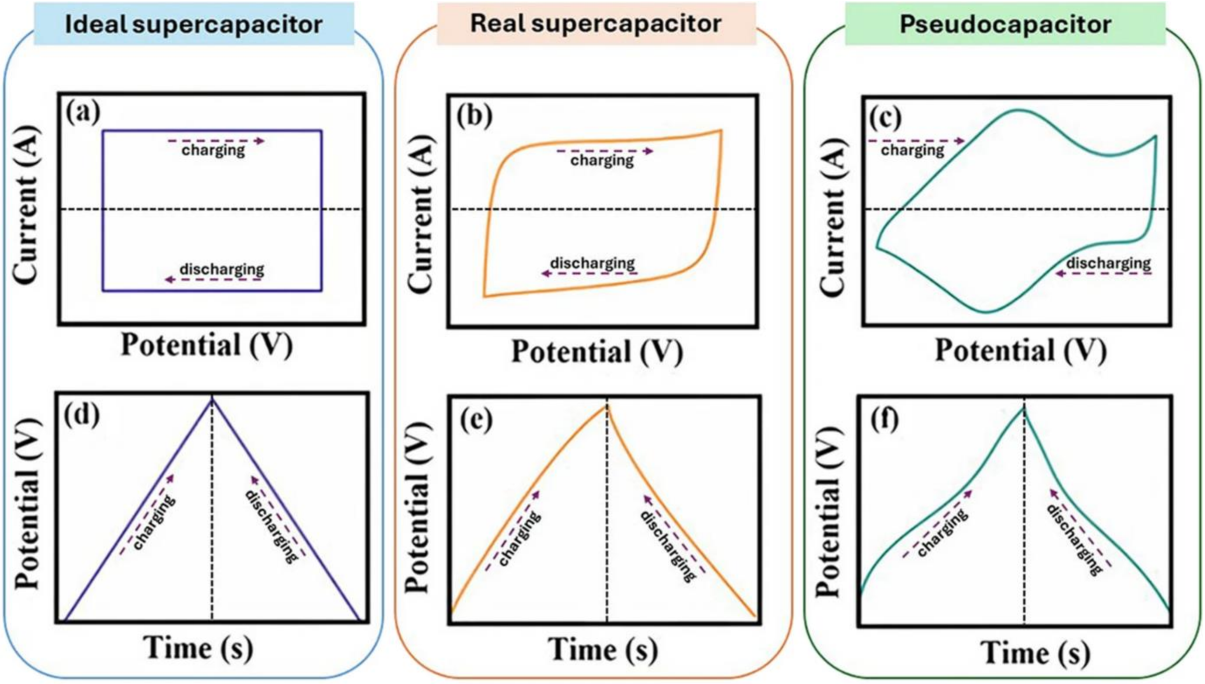

Figure 1.3: Typical CV curves.[74]

In a two-electrode configuration, the storage of charge takes place at the interface between the electrode and electrolyte in both electrodes. Each electrode-electrolyte interface behaves as an individual parallel plate capacitor, with the charges in the electrode forming one plate and the solvated ions accumulated around its surface forming the other (**Figure 1.2**). As a result, a two-electrode supercapacitor is created by combining the capacitive effects at the electrode-electrolyte interfaces of both the positive and negative electrodes. Based on the principle of capacitors in series, the total capacitance of a two-electrode system is given by:

$$\frac{1}{C_{measured}} = \frac{1}{C_{positive}} + \frac{1}{C_{negative}} \tag{1.4}$$

In a symmetric configuration, where both electrodes are of the same type, the capacitance of the positive and negative electrodes is equal, i.e., $C_{positive} = C_{negative} = C_{single}$. In this case, the total capacitance measured is $C_{measured} = C_{single}/2$, leading to $C_{single} = 2C_{measured}$. The capacitance of the electrode material is then determined by normalizing C_{single} with respect to its mass (gravimetric capacitance) or volume (volumetric capacitance). Thus, the gravimetric capacitance of the electrode material is expressed as:

$$C_m = \frac{2C_{measured}}{mass\ of\ a\ single\ eletcrode} = \frac{4C_{measured}}{mass\ of\ both\ eletcrodes} \tag{1.5}$$

In a two-electrode supercapacitor, the gravimetric (C_{m}, F g^{-1}), areal (C_{Area}, F cm^{-2}), and volumetric (C_{Vol}, F cm^{-3}) capacitances of individual electrode are calculated from the integrated area of the CV curve using the following equations:

$$C_m = \frac{4}{mv\Delta V}\int_{V_i}^{V_f} idV \tag{1.6}$$

$$C_{Area} = \frac{4}{Av\Delta V}\int_{V_i}^{V_f} idV \tag{1.7}$$

$$C_{Vol} = \frac{4}{Vol.v\Delta V}\int_{V_i}^{V_f} idV \tag{1.8}$$

where i, V, v, m, A, and Vol represent the current density (A), the potential window (V), the scan rate (mV s^{-1}), total mass (g), the geometric area of the electrode (cm^2), and Vol signifies the volume of the supercapacitor (cm^3), respectively.

CV curves are also utilised to estimate the specific energy (Wh kg^{-1}) and power (W kg^{-1}) densities of the supercapacitor following the equations:

$$E_m = \frac{\Delta V}{3600.mv}\int_{V_i}^{V_f} idV \tag{1.9}$$

$$P_m = \frac{1}{m}\int_{V_i}^{V_f} idV \tag{1.10}$$

Galvanostatic charge-discharge (GCD):

GCD is another key technique for characterizing supercapacitors, where the device is charged to its maximum voltage at a constant current and then discharged at the same current. The charge storage mechanisms of electric double-layer capacitors (EDLCs) and pseudocapacitive materials yield different GCD profiles. A purely linear voltage decrease during discharge indicates EDLC behaviour (**Figure 1.3d** and **e**), while pseudocapacitors exhibit a rapid linear voltage drop followed by a slower, nonlinear decay (**Figure 1.3f**). Additionally, a voltage drops

(V_{drop}) is typically seen at the beginning of the discharge curve, caused by resistive losses during the discharge process **(Figure 1.3d-f**).

In a two-electrode setup, C_m (F g^{-1}), C_{Area} (F cm^{-2}), and C_{Vol} (F cm^{-3}) of an individual electrode in a supercapacitor are determined from the GCD data using the following equations:

$$C_m = \frac{4I}{m(\frac{\Delta V}{\Delta t})} \tag{1.11}$$

$$C_{Area} = \frac{4I}{A(\frac{\Delta V}{\Delta t})} \tag{1.12}$$

$$C_{Vol} = \frac{4I}{Vol.(\frac{\Delta V}{\Delta t})} \tag{1.13}$$

where I corresponds the charging-discharging current (A) and Δt is the discharge time (s).

In a three-electrode configuration, since there is only one working electrode, the four factors in the above equations are reduced to two. In this case, m and Vol correspond to the mass and volume of the working electrode, respectively.

Similarly, GCD profiles are used to evaluate the mass-normalized energy (Wh kg^{-1}) and power (W kg^{-1}) densities of a supercapacitor following the equations:

$$E_m = \frac{1}{m}\int iV dt \tag{1.14}$$

$$P_m = \frac{E_s}{\Delta t} \tag{1.15}$$

Electrochemical impedance spectroscopy (EIS):

EIS is a powerful technique for evaluating supercapacitor materials. EIS measurements are typically conducted by using an AC signal with a 10 mV amplitude at the open-circuit potential, over a frequency range from 100 kHz to 10 mHz. The resulting data are often presented in a Nyquist plot, which illustrates the relationship between the imaginary (Z”) and the real (Z’) impedances. Alternatively, EIS data can be shown in a Bode plot, which displays the phase angle as a function of frequency.

Figure 1.4 illustrates a typical Nyquist plot, with three distinct regions visible. At the low-frequency, the plot is nearly horizontal, indicating capacitive behaviour, while at the high-frequency, a semi-circular arc is observed. This semi-circle represents two key resistances: the solution resistance, which can be determined from the intercept of the semi-circle on the *Z'*-axis, and the charge transfer resistance, inferred from the width of the arc. Additionally, a 45° sloped line connecting the low- and high-frequency regions, known as the Warburg region, represents resistance of the electrode during ion diffusion. A short Warburg region typically indicates superior electrode performance, as it signifies minimal resistance to ion diffusion.

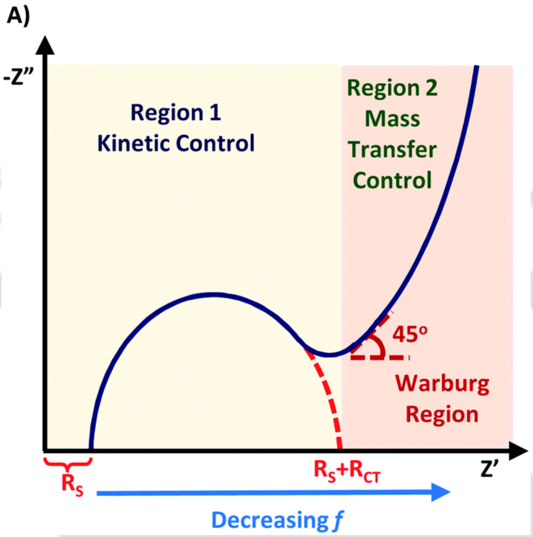

Figure 1.4: A typical EIS spectroscopy (Nyquist plot).[75]

1.2. Graphitic carbon nanostructures for supercapacitor applications:

Due to their exceptional electrical conductivity, chemical stability, and tunable porosity, graphic carbon nanostructures have emerged as versatile materials in energy storage applications, particularly for supercapacitor electrodes. These properties are pivotal for achieving high energy and power densities and extended cycle stability.

This thesis focuses on advancing supercapacitor performance by developing perforated graphene frameworks and MOF-derived porous graphitic nano-leaves (GNLs) using a novel ultrafast strategy (UJH). This method enables the precise control of graphitization and porosity in milliseconds, overcoming the limitations of traditional high-temperature thermal activation. The resulting materials demonstrated multimodal porosity, facilitating efficient ion transport and high charge storage capacity.

Key findings include the fabrication of a symmetric supercapacitor device with an areal capacitance of 380.2 mF cm^{-2} and an energy density of 52.8 μWh cm^{-2}, and the development of wearable asymmetric supercapacitor combining GNLs and MXene, achieving and extended potential window of 1.6 V with excellent durability over 10000 charge-discharge cycles. These advancements underscore the potential of graphitic carbon nanostructures for practical energy storage solutions.

1.3. Principles underlying the electrocatalytic hydrogen evolution reaction (HER):

Water electrolysis is a vital and efficient method for producing hydrogen and oxygen. **Figure 1.5** depicts the overall electrocatalytic reaction, as represented by the equation $2H_2O \rightarrow 2H_2 + O_2$, of the electrolyzer cell. This process requires electrical energy to split water and generate hydrogen, offering a promising electrochemical approach for storing electrical energy directly as fuel.

The overall process can be divided into two reactions, one occurring at the cathode and the other at the anode. The reaction mechanism is strongly influenced by the pH of the electrolyte, which dictates different reaction pathways in various environments. In an acidic medium (pH 0), the corresponding cathodic and anodic reactions are:

$$2H^+ + 2e^- \rightarrow 2H_2 \qquad E_c^0 = 0\,V$$

$$2H_2O \rightarrow O_2 + 4H^+ + 4e^- \qquad E_a^0 = 1.23\,V$$

Where, E_c^0 and E_a^0 refer to the cathodic and anodic potentials at standard conditions (1 atm and 25°C), respectively.

In alkaline medium (pH 14), the reactions are modified to:

$$2H_2O + 2e^- \rightarrow H_2 + 2OH^- \qquad E_c^0 = -0.826\,V$$

$$4OH^- \rightarrow O_2 + 2H_2O + 4e^- \qquad E_a^0 = 0.404\,V$$

In neutral media (pH 7), the reactions are as follows:

$$2H_2O + 2e^- \rightarrow 2H_2 + 2OH^- \qquad E_c^0 = -0.413\,V$$

$$2H_2O \rightarrow O_2 + 4H^+ + 4e^- \qquad E_a^0 = 0.817\,V$$

Thus, regardless of the electrolyte's pH, the overall water splitting process requires a thermodynamic voltage of 1.23 V. However, in practice, an additional potential is needed for the reaction to proceed efficiently, and the operating potential can be expressed as:

$$V_{op} = 1.23\,V + \eta_a + |\eta_c| + \eta_{IR} \qquad (1.16)$$

Here, η_{IR} represents the internal resistance of the cell, which includes both contact and solution resistance, and can be minimized by improving the design of the electrolyzer cell. The η_a and $|\eta_c|$ are the additional potentials needed to overcome the inherent energy barriers at the anode and cathode, respectively. These barriers can be significantly reduced by employing highly efficient electrocatalysts.

An electrolyzer cell has an anode and a cathode, with the voltage difference between the two electrodes being directly measurable, representing the applied voltage required for water splitting. However, to fully understand the mechanisms of HER at the cathode and OER at the anode, it is essential to determine the precise potential for each reaction relative to a standard potential that remains unchanged during the reaction.

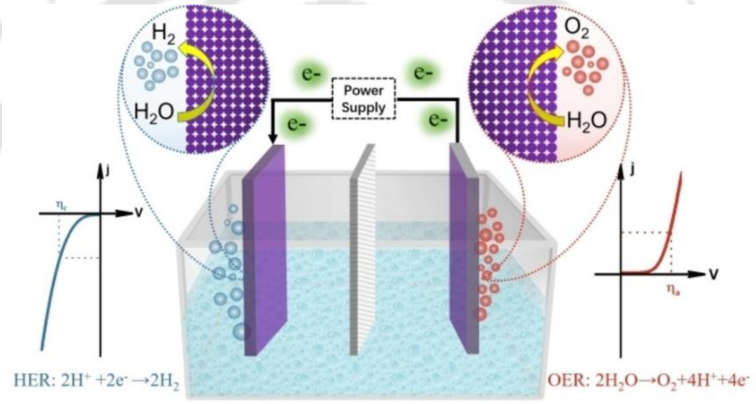

Figure 1.5: Schematic of a typical electrolyzer cell for HER.[76]

Different reference electrodes are used based on the stability of the electrolyte system in the electrocatalytic process. For instance, the Ag/AgCl reference electrode is commonly employed in acidic electrolytes, while the saturated calomel electrode (SCE, Hg/Hg_2Cl_2) is used in alkaline electrolytes. These electrodes do not actively participate in the water-splitting reactions but instead maintain a constant potential through their redox couple. The absolute potential values measured for each half-reaction will differ depending on the reference electrode used. To maintain consistency, usually, the reversible hydrogen electrode (RHE) is considered as the universal reference electrode. Any potential measured relative to Ag/AgCl or SCE is converted to a potential relative to RHE using the following standard equation:

$E^{RHE} = E^{WP} + 0.059pH + E^0$. Where, E^{WP} is the operational potential of Ag/AgCl or SCE, E^0 is the standard potential of the cell, for Ag/AgCl, E^0 = 0.1976 V, for SCE, E^0 = 0.242 V.

1.3.1. Mechanism and performance determining parameters of HER:

HER is a two-electron transfer process that occurs at the cathode surface and involves three primary steps: the Volmer reaction, followed by either the Heyrovsky or the Tafel reaction. In the Volmer step, a proton is adsorbed onto the cathode surface and combines with an electron to form an adsorbed hydrogen intermediate (H_{ads}), as depicted in **Figure 1.6**. Afterward, in the Heyrovsky reaction, the adsorbed hydrogen interacts with another proton and electron, leading to the formation of a hydrogen molecule. Alternatively, in the Tafel reaction, two adjacent adsorbed hydrogen atoms combine to generate a hydrogen molecule.

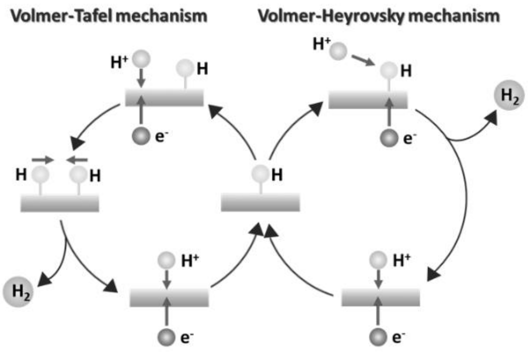

Figure 1.6: Volmer reaction pathways of HER.

All the reaction pathways are as follows: [10]

Volmer reaction (hydrogen adsorption):

$* + H^+ + e^- \rightarrow H^*$ (in acidic electrolyte)

$* + H_2O + e^- \rightarrow H^* + OH^-$ (in alkaline electrolyte)

Heyrovsky reaction (desorption):

$H^* + H^+ + e^- \rightarrow * + H_2$ (in acidic electrolyte)

$H^* + H_2O + e^- \rightarrow * + OH^- + H_2$ (in alkaline electrolyte)

Tafel step (desorption):

$H^* + H^* \rightarrow H_2$

The free energy of hydrogen adsorption (ΔG_{H*}) is often used as a key indicator for materials involved in HER, irrespective of pH. For an ideal material like platinum, ΔG_{H*} should be close to zero. Weak adsorption results in poor proton-electrode interaction, while strong adsorption demands excessive energy to break the bonds between hydrogen and the catalyst surface, which slows down hydrogen desorption. Consequently, the catalytic activity for HER depends on the strength of proton adsorption on the electrode surface. This correlation can be represented through a volcano plot, where the ΔG_{H*} values of different catalysts, derived from density functional theory (DFT), are plotted against the logarithm of their corresponding exchange current densities (log j_0), as shown in **Figure 1.7**. The volcano plot provides a clear comparison of various metals' HER activity, highlighting that platinum exhibits the highest HER activity, which aids in optimizing material design.

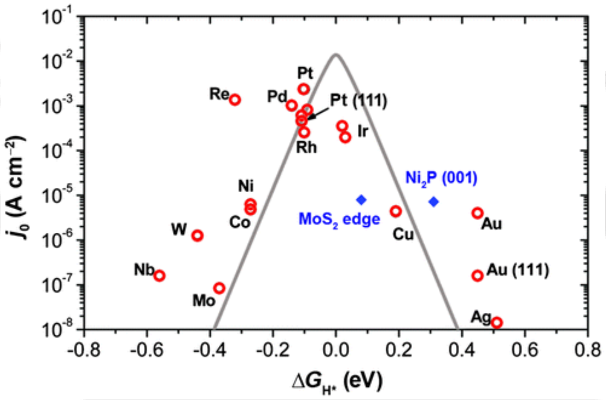

Figure 1.7: HER Volkano plot.[77]

1.3.2. Performance metrics of HER:

Electrocatalysts play a pivotal role in determining the performance and efficiency of HER. To evaluate the effectiveness of an electrocatalyst, it is essential to consider several critical factors or parameters.

Overpotential (η):

The overpotential (η) is a crucial parameter for assessing the performance of the HER catalysts. Ideally, HER would occur when the applied potential becomes equal to the equilibrium potential. However, due to intrinsic energy barriers, HER occurs at a higher voltage than the equilibrium potential. According to the Nernst equation, the applied potential for an electrocatalytic redox reaction is:

$$E = E^0 + \frac{RT}{nF} ln \frac{C_O}{C_R} \tag{1.17}$$

Where, E^0 corresponds to the standard potential of the reaction, T refers to the absolute temperature, R signifies the universal gas constant, n represents the number of electrons transferred, F is the Faraday constant, and C_0, C_R are respectively the concentration of oxidized and reduced reagents.

The overpotential (η) is,

$$\eta = E - E^{eq} \tag{1.18}$$

Where, E^{eq} represents the equilibrium potential. The overpotential to achieve a current density of 10 mA cm^{-2} is generally reported, and a low overpotential signifies a superior electrocatalytic activity.

Tafel slope:

Getting a high current at low overpotential is desired. The current (i) density corresponding to an overpotential is represented by the Butler-Volmer equation:

$$i = i_0 \left[e^{\frac{\alpha_a \eta FE}{RT}} + e^{\frac{\alpha_c \eta FE}{RT}} \right] \tag{1.19}$$

Where, i_0 refers to the exchange current density and α_a and α_c correspond to the coefficients for the anode and cathode, respectively. At high overpotentials, equation 1.19 is approximated to the Tafel equations,

$$i \approx i_0 e^{\frac{\alpha_a \eta FE}{RT}} \tag{1.20}$$

and

$$i \approx i_0 e^{\frac{\alpha_c \eta FE}{RT}} \tag{1.21}$$

So the Tafel slope is estimated by the following equation,

$$\eta = b.\log(i/i_0) \tag{1.22}$$

The lower value of the Tafel slope is expected to get a faster HER kinetics.

Activity:

To evaluate the activity of a particular mass of the electrocatalyst, its specific activity should be measured. Since different catalyst loadings on an electrode lead to different activity levels, the mass-normalized current density, commonly referred to as "mass activity," is an important parameter for assessing catalyst performance. Additionally, the electrochemical surface area

(ECSA) of the catalyst must be determined to better understand its intrinsic activity. ECSA is directly related to the number of exposed active sites available for the HER reaction.

Turn over frequency (TOF):

TOF represents the number of molecules undergoing reaction at each active site per unit of time, providing an indication of the intrinsic activity of each active site. The TOF can be expressed as: [19]

$$TOF = jA/\alpha Fn \tag{1.23}$$

Where j, A, α, F, and n represent the current density at a specific overpotential, surface area of the electrode, electron number of the electrocatalyst (electrons mol^{-1}), the Faraday constant (96485.3 C mol^{-1}), and the molar amount of electrocatalyst, respectively.

Since it is challenging to directly count all the accessible active sites engaged in the reaction, precisely calculating the TOF value is difficult. As a result, a more practical method for determining the TOF involves estimating the number of surface atoms or the quantity of easily accessible electrocatalytic sites within the material.

Stability:

The long-term stability of an electrocatalyst is a critical factor for its practical application. Generally, the stability of a catalyst is evaluated using chrono-amperometry or chrono-potentiometry tests, where either the current or potential is monitored at a fixed value over an extended period, respectively, to observe any changes.

1.4. Nanohybrids of graphitic carbon nanostructures for HER:

HER is a cornerstone of renewable energy technologies, converting water into hydrogen as a clean and sustainable fuel. However, the high cost and scarcity of noble metals catalysts, such as platinum, necessitate the development of cost-effective alternatives with comparable performance.

This thesis introduces a strategy for synthesizing MOF-derived graphitic carbon nanostructures embedded with ultra-small metal nanoclusters, such as Ru, Ni, and Cu. The transient electro-graphitization (TEG) approach facilitates independent control over the carbon support's graphitization levels and the nanoclusters' crystallization states, producing materials with enhanced catalytic activity.

For instance, amorphous ruthenium nanoclusters on graphitized nano-leaves exhibited overpotentials of only 23 mV and 91 mV to achieve 10 and 100 mA cm^{-2} current densities, surpassing state-of-the-art Pt/C catalysts. These results highlight the synergy between graphitic supports' electronic properties and the embedded nanoclusters' catalytic activity, paving the way for high-performance HER catalysts.

1.5. Challenges in graphitic carbon nanostructures and their nanohybrids synthesis for energy applications:

Despite significant progress, several challenges remain in the synthesis and application of graphitic carbon nanostructures and their nanohybrids for energy storage and catalysis:

1. Control over graphitization and porosity:

Achieving precise control over the graphitic order and porosity in nanostructures is crucial for optimizing their performance in supercapacitors and HER, but it remains challenging.

2. Tunability of size and crystallinity of nanoclusters for HER catalysis:

The size and crystallinity of catalyst nanoclusters can significantly impact the HER performance. Adjusting the electronic property that is favorable for HER by precisely tuning the size and crystallinity of the nanocatalysts is highly preferred but faces many challenges.

3. Creating hetero-phase nanocatalyst:

Forming hetero-phase nanocatalysts to tune their intrinsic activity towards HER is another challenge.

4. Comprehensive understanding of catalyst-support interactions:

Understanding and enhancing the electronic interplay between carbon supports and embedded nanoclusters require advanced characterization and computational modeling.

5. Overall performance of the catalysts:

The mass-activity and long-term stability of HER catalysts under high-current conditions need improvement.

6. Scalability and cost-effectiveness:

Traditional methods for activating graphene and other graphitic carbon nanostructures and developing their nanohybrid catalysts are energy-intensive and time-consuming, limiting their practical applicability.

The development of ultrafast synthesis techniques, such as the transient electro-graphitization (TEG) method, offers a promising pathway to address these challenges by enabling precise, energy-efficient, and scalable fabrication of advanced nanostructures.

1.6. Objectives of this thesis work:

The primary objectives of this thesis are:

1. To develop a novel, ultrafast Joule heating technique for fabricating graphitic carbon nanostructures with tunable graphitization and porosity.

2. To design and synthesize MOF-derived carbon nanostructures as high-performance supercapacitor electrodes and catalyst supports for HER.

3 To achieve precise control over the crystallization states and size of metal nanoclusters embedded in graphitic carbon nanostructures for enhanced catalytic activity.

4. To realize tuned hetero-phase nanocatalysts.

4. To investigate the electronic and morphological interplay between nanoclusters and carbon supports using advanced characterization techniques and density functional theory (DFT) calculations.

5. To demonstrate the scalability and practical applicability of the developed materials in energy storage and electrocatalysis.

This thesis successfully addresses its key objectives by developing an ultrafast transient Joule heating (TJH) strategy to synthesize graphitic carbon nanostructures and nanohybrids with precisely tuned graphitization, porosity, and nanocatalyst crystallization states. By achieving millisecond-scale processing, the study overcomes the limitations of conventional high-temperature treatments, demonstrating high-performance supercapacitor electrodes with enhanced capacitance and extended voltage windows. The fabrication of MOF-derived graphitic nano-leaves (GNLs) enabled the development of wearable asymmetric supercapacitors, exhibiting excellent energy density (107.8 µWh cm^{-2}) and mechanical stability. Furthermore, the TJH approach was extended to electrocatalysis, where Ru-based HER catalysts with controlled crystallization states outperformed Pt/C, achieving a low overpotential of 23 mV at 10 mA cm^{-2}. The synthesis of bimetallic Cu/Ni catalysts demonstrated a viable, cost-effective alternative to noble metals, highlighting the potential for scalable hydrogen production. Advanced DFT calculations provided critical insights into electronic interactions between catalysts and supports, guiding rational material design. This thesis successfully meets its objectives by establishing TJH as a highly efficient, scalable, and cost-effective synthesis method for next-generation energy storage and electrocatalysis applications.

1.7. Conclusion:

This chapter has provided a comprehensive overview of the state-of-the-art technologies and challenges in supercapacitive energy storage and electrocatalysis (HER), emphasizing the pivotal role of graphitic carbon nanostructures and their nanohybrids. This discussion highlights the motivation for this work, which seeks to address the limitations of conventional synthesis methods and develop advanced materials with superior performance metrics for supercapacitors and hydrogen evolution reactions.

1.8. Thesis contents and organization:

This thesis is dedicated to developing a unique ultrafast Joule heating technique that offers a temperature rise above 1000 K in a few hundred milliseconds before cooling instantly to produce porous carbon frameworks for wearable supercapacitors and MOF-derived GCNs-supported nanocatalysts for HER. Mainly, the present thesis includes controlled ultrafast synthesis of porous GCNs with variable porosity, GCNs with tunable graphitic order, and GCNs-supported ultra-small nanocatalysts with adjustable size/crystallization. It also consists of the theoretical understanding of the origin of high catalytic activity of the developed catalysts towards HER by density functional theory (DFT) calculations. The thesis is structured into six chapters, beginning with an overview of cutting-edge energy storage technologies and the challenges associated with storing electrical energy in supercapacitors and chemical energy in the form of hydrogen. The subsequent chapters explore various strategies to address these challenges. Finally, the thesis concludes with key findings and future perspectives on energy storage. A summary of each chapter is provided below.

Chapter 1 briefly overviews the cutting edge energy storage technologies, mainly focusing on supercapacitors and electrocatalytic H_2 generation from water. Recent progress in developing and modifying carbon nanostructures with tunable graphitic order (GCNs) as supercapacitor electrodes and as efficient catalyst support for HER has also been presented. Further, the design of electrodes for supercapacitors in commercial-level applications, the development of GCNs-supported efficient nanocatalysts for HER, and their corresponding experimental procedures have also been incorporated. At the end of this chapter, the motivation and objectives to meet the challenges of the present work have been illustrated.

Chapter 2: Precise engineering of graphene nanopores is crucial for overcoming the limitations of pristine graphene in supercapacitors, but traditional methods are energy-intensive and time-consuming. Here, we introduce an ultrafast Joule heating strategy using millisecond current pulses for reduction and activation, creating multimodal porous graphene with nano-to-macro porosity and enhanced surface functionality. This innovative approach transforms graphene oxide into a macroporous framework within 50 ms. At the same time, basal plane nanopores are generated with an additional 100 ms pulses using KOH activation, significantly reducing the thermal budget and processing time compared to conventional methods requiring hours. The process produces a binder-free electrode directly integrated with carbon cloth (AJG@CC), forming a ready-to-use structure for wearable energy storage applications. Optimized perforation yields uniform nanopores (~6 nm) and pseudocapacitive oxidative groups, resulting in exceptional areal capacitance (380.2 mF cm^{-2}) and energy density (52.8 μWh cm^{-2}) in symmetric configurations, 1.6 times higher than non-electro-activated counterparts. Using AJG@CC as the positive electrode and MXene nanosheets as the negative electrode, we fabricated a high-performance wearable asymmetric supercapacitor with an extended operating potential window of 1.6 V. This device delivered a remarkable areal energy density of 107.8 μWh cm^{-2} at 485 μW cm^{-2} and retained 83.9 μWh cm^{-2} at a power density of 4404.5 μW cm^{-2}, demonstrating high energy and power densities. Durability tests showed 94% capacity retention after 10,000 charge-discharge cycles and stable performance under 5,000 bending cycles, making it a reliable candidate for wearable electronics. This method's direct, scalable, and low-cost nature enhances its appeal for practical applications, enabling the integration of high-performance energy storage devices into flexible textiles. The device's resilience was demonstrated by successfully powering small electronics without degradation under repeated bending. This ultrafast activation approach offers a straightforward alternative to conventional methods and enables the creation of high-performance electrodes with reduced processing costs and time. By introducing multimodal porosity and leveraging binder-free integration, this strategy pushes the boundaries of wearable energy storage, presenting a significant advancement for future applications in portable and flexible electronics.

Chapter 3: Precise control of graphitic order in carbon nanostructures is crucial for multifunctional applications like energy storage but remains challenging for scalable implementation. Here, we present an ultrafast pulsed Joule heating (PJH) strategy combined with electrochemical anodic oxidation (EO) to develop tunable graphitic carbon nano-leaves (GNLs) derived from metal-organic frameworks (MOFs) and achieve precise recovery of graphitic order post-oxidation. PJH produces highly graphitized GNLs with embedded cobalt nanoparticles, whose size and graphitization levels depend on the pulse duration. EO further exfoliates graphitic layers and etches cobalt nanoparticles, introducing size-controlled pores (3-10 nm) and surface functionalities but lowering the graphitization level. This reduction in graphitic order is restored by ultra-short 50 ms PJH pulses, yielding porous, graphitization-recovered GNLs (rPGNLs) with optimized conductivity and surface area. These binder-free electrodes deliver excellent performance in supercapacitor applications. For instance, rPGNLs exhibit a 434% capacitance enhancement (290.7 mF cm^{-2}) over pristine GNLs in aqueous electrolytes due to their high conductivity and tailored porosity. The highly porous graphitic framework also facilitates ion transport in water-in-salt (WIS) electrolytes, enabling an extended potential window of 2.3 V and a fourfold increase in energy density (127.5 µWh cm^{-2}) compared to aqueous devices. Furthermore, a wearable asymmetric supercapacitor using rPGNLs as the positive electrode and MXene as the negative electrode has a stable potential window of 1.6 V with exceptional mechanical and operational durability, retaining performance over 5,000 deformation cycles. The sequential process of PJH-tuned graphitization, pore incorporation via EO, and graphitic recovery provides precise control over porosity and conductivity, which is essential for high-performance energy storage and catalytic applications. Notably, rPGNL-based devices demonstrate versatility across aqueous, WIS, and wearable supercapacitors, offering adjustable properties to meet specific energy storage needs. The tunability of graphitic order and functional groups also influences catalytic properties, with linear sweep voltammetry (LSV) suggesting increased hydrogen evolution reaction (HER) onset potential due to defect healing and reduced surface functionalities leading to extended potential window up to 2.3 V. This approach significantly outperforms conventional methods by providing rapid, scalable processing with high flexibility in material properties, making rPGNLs promising candidates for next-generation energy storage devices. The optimized r_2PGNL_{5min} electrodes demonstrate exceptional energy storage performance, durability, and scalability, establishing a new benchmark for MOF-derived carbon nanostructures in advanced applications.

Chapter 4: Fine control over graphitization in carbon nanostructures plays a pivotal role in tuning the crystallization of supported nanocatalysts, significantly influencing catalytic kinetics. This study introduces a current pulse-induced transient electro-graphitization (TEG) strategy to develop MOF-derived graphitic nano-leaves (GNLs) with tunable graphitization and supported ultra-small ruthenium nanoclusters (≈ 0.7 nm) exhibiting tailored crystallization states. By decoupling MOF pyrolysis and nanocluster growth, TEG enables independent control over graphitization and ruthenium crystallinity. Current pulses (200-1000 ms) transform ZIF-67 MOFs into GNLs with progressively higher graphitization levels, while ultrashort pulses (50 ms) facilitate the formation of ruthenium single atoms (Ru-SAs), amorphous nanoclusters (a-Ru-NCs), or crystalline nanoparticles (c-Ru-NPs), depending on graphitization and nitrogen doping. Among the catalysts, amorphous Ru nanoclusters on GNLs graphitized with a 500 ms pulse (a-Ru@GNL$_{500}$) demonstrated state-of-the-art hydrogen evolution reaction (HER) performance, requiring overpotentials of only 23.0 and 91.4 mV to achieve current densities of 10 and 100 mA cm^{-2}, respectively, surpassing benchmark Pt/C catalysts. The catalyst also exhibited exceptional durability, maintaining stability for over 100 hours under high HER currents (200-400 mA cm^{-2}). Density functional theory (DFT) calculations revealed a unique electronic interplay between amorphous Ru and cobalt embedded in the graphitic layers, reducing antibonding orbital occupancy and accelerating HER kinetics. The super-aerophobic nature of a-Ru@GNL$_{500}$ (bubble contact angle of 152.3°) and low bubble adhesion force (0.8 μN) ensured efficient bubble release, minimizing mass transport limitations and destructive tensile forces during high-current operation. The hierarchical GNL structure provided high conductivity, enhanced mass transport, and reduced resistive and mass transport overpotentials. This ultrafast, scalable method offers precise control over graphitization and nanocatalyst crystallization, creating a robust framework for high-performance catalysts. The approach can be extended to other catalytic applications, including oxygen evolution (OER), urea oxidation (UOR), nitrogen reduction (NRR), oxygen reduction (ORR), carbon dioxide reduction (CO$_2$RR), and nitrate reduction (NitRR). The versatility of this strategy arises from its ability to generate materials with high conductivity, large surface areas, and excellent mass transfer properties, paving the way for efficient, scalable, and durable electrocatalysts tailored to energy and environmental applications while addressing challenges in high-current catalytic operations.

Chapter 5: We have developed a hetero-interface of earth-abundant, low-cost, non-noble transition metals, and their oxides using a novel ultrafast Joule heating technique, achieving synthesis in just a few milliseconds, unfeasible with traditional resource- and energy-intensive furnace heating, which requires hours. This innovative method transforms bimetallic MOFs into metal/metal oxide interfaces linked to carbon nanostructures (CNs) derived from MOFs with exceptional controllability, enabling precise structural tuning. As a prime example, the Cu/Cu_2O/Ni catalyst linked to CNs demonstrates excellent hydrogen evolution reaction (HER) catalytic activity, achieving a current density of 10 mA cm^{-2} with an overpotential of only 46 mV, which rivals the performance of state-of-the-art Pt/C HER catalysts (33 mV at 10 mA cm^{-2}). Remarkably, this catalyst undergoes a rapid morphological transformation during the first linear sweep voltammetry (LSV) cycle of HER, leading to significant performance enhancement. Advanced characterizations revealed that this transformation results from the partial phase reduction of Cu_2O to Cu and partial oxidation of Ni to a few thin amorphous Ni $(OH)_2$ layers, which occurs on the catalyst surface during the cathodic reaction. This unique surface phase evolution, inducing morphological transformation, is a critical factor in boosting the catalytic activity of the hetero-interface. This ultrafast Joule heating technique represents a game-changing approach for designing efficient electrocatalysts, addressing essential limitations of traditional methods in achieving a controlled synthesis of transition metal-based hetero-interface materials. Moreover, the methodology and insights gained are broadly applicable to other electrocatalytic reactions, including CO_2 reduction (CO_2RR), nitrogen reduction (NRR), oxygen reduction (ORR), oxygen evolution (OER), and nitrate reduction (NitRR). Combining rapid synthesis, cost efficiency, and structural tunability establishes a new paradigm for advancing sustainable catalysis technologies with significant implications for clean energy and chemical production applications.

Chapter 6 highlights the key findings of this work with concluding remarks. The prospects of the modified graphitic carbon nanostructures and their nanohybrid-based electrodes in energy storage are discussed at the end of this thesis.

References

[1] W. Shi, Z. Li, Z. Gong, Z. Liang, H. Liu, Y. C. Han, H. Niu, B. Song, X. Chi, J. Zhou, H. Wang, B. Y. Xia, Y. Yao, Z. Q. Tian, *Nat. Commun.* **2023**, *14*, DOI 10.1038/s41467-023-38023-5.

[2] J. Ji, J. Liu, L. Lai, X. Zhao, Y. Zhen, J. Lin, Y. Zhu, H. Ji, L. L. Zhang, R. S. Ruoff,

ACS Nano **2015**, *9*, 8609.

[3] X. Wang, X. Zhou, C. Li, H. Yao, C. Zhang, J. Zhou, R. Xu, L. Chu, H. Wang, M. Gu, H. Jiang, M. Huang, *Adv. Mater.* **2022**, *34*, 1.

[4] C. Wan, Y. Jiao, D. Liang, Y. Wu, J. Li, *Adv. Energy Mater.* **2018**, *8*, 1.

[5] R. You, Y. Q. Liu, Y. L. Hao, D. D. Han, Y. L. Zhang, Z. You, *Adv. Mater.* **2020**, *32*, 1.

[6] P. Pachfule, D. Shinde, M. Majumder, Q. Xu, *Nat. Chem.* **2016**, *8*, 718.

[7] D. Wang, Q. Li, C. Han, Q. Lu, Z. Xing, X. Yang, *Nat. Commun.* **2019**, *10*, 1.

[8] J. T. Ren, L. Chen, H. Y. Wang, W. W. Tian, X. L. Song, Q. H. Kong, Z. Y. Yuan, *ACS Catal.* **2023**, 9792.

[9] J. Feng, X. Wang, H. Pan, *Adv. Mater.* **2024**, *2411688*, 1.

[10] G. Wu, X. Zheng, P. Cui, H. Jiang, X. Wang, Y. Qu, W. Chen, Y. Lin, H. Li, X. Han, Y. Hu, P. Liu, Q. Zhang, J. Ge, Y. Yao, R. Sun, Y. Wu, L. Gu, X. Hong, Y. Li, *Nat. Commun.* **2019**, *10*, 1.

[11] Q. Wang, C. Q. Xu, W. Liu, S. F. Hung, H. Bin Yang, J. Gao, W. Cai, H. M. Chen, J. Li, B. Liu, *Nat. Commun.* **2020**, *11*, 1.

[12] Y. Deng, T. Shang, Z. Wu, Y. Tao, C. Luo, J. Liang, D. Han, R. Lyu, C. Qi, W. Lv, F. Kang, Q.-H. Yang, Y. Deng, C. Luo, R. Lyu, W. Lv, F. Kang, T. Shang, Z. Wu, Y. Tao, J. Liang, D. Han, C. Qi, Q. Yang, *Adv. Mater.* **2019**, *31*, 1902432.

[13] Z. Wang, S. Qin, S. Seyedin, J. Zhang, J. Wang, A. Levitt, N. Li, C. Haines, R. Ovalle-Robles, W. Lei, Y. Gogotsi, R. H. Baughman, J. M. Razal, *Small* **2018**, *14*, 1.

[14] X. Pu, L. Li, M. Liu, C. Jiang, C. Du, Z. Zhao, W. Hu, Z. L. Wang, *Adv. Mater.* **2016**, *28*, 98.

[15] J. Wang, S. Kaskel, *J. Mater. Chem.* **2012**, *22*, 23710.

[16] H. Fang, H. Bian, H. Zhang, M. Wang, S. Zhang, L. He, *Appl. Surf. Sci.* **2023**, *614*, 156154.

[17] Q. Dou, S. Lei, D. W. Wang, Q. Zhang, D. Xiao, H. Guo, A. Wang, H. Yang, Y. Li, S. Shi, X. Yan, *Energy Environ. Sci.* **2018**, *11*, 3212.

[18] L. Suo, O. Borodin, Y. Wang, X. Rong, W. Sun, X. Fan, S. Xu, M. A. Schroeder, A. V. Cresce, F. Wang, C. Yang, Y. S. Hu, K. Xu, C. Wang, *Adv. Energy Mater.* **2017**, *7*, 1.

[19] J. Ren, Q. Wang, Q. Xiang, C. Yang, Y. Liang, J. Li, J. Liu, D. Qian, *Chem. Eng. Sci.* **2023**, *280*, 119026.

[20] D. H. Kweon, M. S. Okyay, S. J. Kim, J. P. Jeon, H. J. Noh, N. Park, J. Mahmood, J. B. Baek, *Nat. Commun.* **2020**, *11*, 1.

[21] C. Wang, X. Yuan, L. Luo, Z. Ma, P. Li, Y. Miao, *J. Alloys Compd.* **2022**, *900*, 163330.

[22] P. C. Chen, C. Chen, Y. Yang, A. L. Maulana, J. Jin, J. Feijoo, P. Yang, *J. Am. Chem. Soc.* **2023**, *145*, 10116.

[23] W. Jiang, L. Xia, B. Ferreira Gomes, M. Haumann, H. Dau, C. Roth, W. Lehnert, M. Shviro, *Small* **2024**, *20*, 1.

[24] G. M. Karim, A. Patra, S. K. Deb, H. Upadhya, S. Das, P. Mukherjee, W. Ahmad, N. Barman, R. Thapa, N. V. Dambhare, A. K. Rath, J. Das, U. Manna, R. R. Urkude, Y. Oh, U. N. Maiti, *Adv. Funct. Mater.* **2024**, *34*, 1.

[25] K. Shen, X. Chen, J. Chen, Y. Li, *ACS Catal.* **2016**, *6*, 5887.

[26] Y. Wu, L. Wang, L. Chen, Y. Li, K. Shen, *Small* **2023**, *19*, DOI 10.1002/smll.202207689.

[27] T. Luo, J. Huang, Y. Hu, C. Yuan, J. Chen, L. Cao, K. Kajiyoshi, Y. Liu, Y. Zhao, Z. Li, Y. Feng, *Adv. Funct. Mater.* **2023**, *33*, 1.

[28] S. H. Kang, G. Y. Lee, J. Lim, S. O. Kim, *ACS Omega* **2021**, *6*, 19578.

[29] J. Ying, G. Jiang, Z. Paul Cano, L. Han, X. Y. Yang, Z. Chen, *Nano Energy* **2017**, *40*, 88.

[30] J. Zhu, R. Lu, W. Shi, L. Gong, D. Chen, P. Wang, L. Chen, J. Wu, S. Mu, Y. Zhao, *Energy Environ. Mater.* **2023**, *6*, 1.

[31] G. Li, H. Zhang, X. Yu, Z. Lei, F. Yin, X. He, *Int. J. Hydrogen Energy* **2022**, *47*, 12882.

[32] L. Chai, P. Wang, X. Liu, Y. Sun, X. Li, J. Pan, *J. Power Sources* **2022**, *532*, 231324.

[33] H. Liu, C. Liu, X. Zong, Y. Wang, Z. Hu, Z. Zhang, *Int. J. Hydrogen Energy* **2023**, DOI 10.1016/j.ijhydene.2023.04.150.

[34] X. Han, L. Zhou, S. Cao, L. Zhang, G. Xiang, J. F. Chen, *Energy and Fuels* **2021**, *35*, 4447.

[35] B. Geng, F. Yan, X. Zhang, Y. He, C. Zhu, S. L. Chou, X. Zhang, Y. Chen, *Adv. Mater.* **2021**, *33*, 1.

[36] Z. Pan, H. Zhi, Y. Qiu, J. Yang, L. Xing, Q. Zhang, X. Ding, X. Wang, G. Xu, H. Yuan, M. Chen, W. Li, Y. Yao, N. Motta, M. Liu, Y. Zhang, *Nano Energy* **2018**, *46*, 266.

[37] X. Ning, W. Zhong, S. Li, Y. Wang, W. Yang, *J. Mater. Chem. A* **2014**, *2*, 8859.

[38] R. R. Salunkhe, Y. V. Kaneti, J. Kim, J. H. Kim, Y. Yamauchi, *Acc. Chem. Res.* **2016**, *49*, 2796.

[39] H. Zhang, H. Su, M. A. Soldatov, Y. Li, X. Zhao, M. Liu, W. Zhou, X. Zhang, X. Sun, Y. Xu, P. Yao, S. Wei, Q. Liu, *Small* **2021**, *17,* DOI 10.1002/smll.202105231.

[40] Y. C. Han, M. L. Liu, L. Sun, X. C. Li, Y. Yao, C. Zhang, S. Y. Ding, H. G. Liao, L. Zhang, F. R. Fan, M. Moskovits, Z. Q. Tian, *Nano Energy* **2022**, *97*, 107125.

[41] Y. Liu, S. Liu, Y. Wang, Q. Zhang, L. Gu, S. Zhao, D. Xu, Y. Li, J. Bao, Z. Dai, *J. Am. Chem. Soc.* **2018**, *140*, 2731.

[42] Y. Zhao, X. Hu, G. D. Stucky, S. W. Boettcher, *J. Am. Chem. Soc.* **2024**, *146*, 3438.

[43] J. Guan, W. Chen, Y. Zhu, L. Wang, Y. Fu, B. Guo, M. Zhang, *J. Alloys Compd.* **2023**, *942*, 168941.

[44] C. Zhang, J. Sha, H. Fei, M. Liu, S. Yazdi, J. Zhang, Q. Zhong, X. Zou, N. Zhao, H. Yu, Z. Jiang, E. Ringe, B. I. Yakobson, J. Dong, D. Chen, J. M. Tour, *ACS Nano* **2017**, *11*, 6930.

[45] T. Jiang, Y. Yuan, S. Liu, A. J. Hunt, G. Tan, *ACS Omega* **2020**, *5*, 16021.

[46] Z. Zhao, Z. Liu, A. Zhang, X. Yan, W. Xue, B. Peng, H. L. Xin, X. Pan, X. Duan, Y. Huang, *Nat. Nanotechnol.* **2022**, *17*, 968.

[47] S. Mondal, S. Sarkar, D. Bagchi, T. Das, R. Das, A. K. Singh, P. K. Prasanna, C. P. Vinod, S. Chakraborty, S. C. Peter, *Adv. Mater.* **2022**, *34*, DOI 10.1002/adma.202202294.

[48] Z. Li, J. Zou, X. Xi, P. Fan, Y. Zhang, Y. Peng, D. Banham, D. Yang, A. Dong, *Adv. Mater.* **2022**, *34*, 1.

[49] A. Majumdar, P. Dutta, A. Sikdar, H. Lee, D. Ghosh, S. N. Jha, S. Tripathi, Y. Oh, U. N. Maiti, *Small* **2022**, *18*, 1.

[50] Y. Weng, K. Wang, S. Li, Y. Wang, L. Lei, L. Zhuang, Z. Xu, *Adv. Sci.* **2023**, *10*, 1.

[51] Y. Li, T. Xu, Q. Huang, L. Zhu, Y. Yan, P. Peng, F. F. Li, *ACS Catal.* **2023**, *13*, 7597.

[52] L. Lin, C. Pei, R. Ding, Y. Li, H. S. Park, X. Yu, *Int. J. Hydrogen Energy* **2023**, *48*, 20350.

[53] M. Ghidiu, M. R. Lukatskaya, M. Q. Zhao, Y. Gogotsi, M. W. Barsoum, *Nat. 2014 5167529* **2014**, *516*, 78.

[54] M. H. Tsai, Y. Juang, C. C. Hu, L. C. Hua, C. Huang, *J. Environ. Chem. Eng.* **2024**, *12*, 112339.

[55] X. Gao, W. Zang, X. Li, Z. Wang, L. Zheng, Z. Kou, *Chem. Eng. J.* **2022**, *451*, 138698.

[56] X. Shan, J. Zhu, Z. Qiu, P. Liu, Y. Zhong, X. Xu, X. He, Y. Zhang, J. Tu, Y. Xia, C. Wang, W. Wan, M. Chen, X. Liang, X. Xia, W. Zhang, *Small* **2024**, *20*, 1.

[57] Y. Jiang, J. Liang, L. Yue, Y. Luo, Q. Liu, Q. Kong, X. Kong, A. M. Asiri, K. Zhou, X. Sun, *J. Colloid Interface Sci.* **2021**, *604*, 319.

[58] H. Huang, H. Jung, C. Y. Park, S. Kim, A. Lee, H. Jun, J. Choi, J. W. Han, J. Lee, *Appl. Catal. B Environ.* **2022**, *315*, 121554.

[59] K. H. Kim, Y. H. Choi, *Mater. Res. Express* **2022**, *9*, DOI 10.1088/2053-1591/ac5f89.

[60] X. Li, S. Han, Z. Qiao, X. Zeng, D. Cao, J. Chen, *Chem. Eng. J.* **2023**, *453*, 139803.

[61] Y. Wang, H. Su, Y. He, L. Li, S. Zhu, H. Shen, P. Xie, X. Fu, G. Zhou, C. Feng, D. Zhao, F. Xiao, X. Zhu, Y. Zeng, M. Shao, S. Chen, G. Wu, J. Zeng, C. Wang, *Chem. Rev.* **2020**, *120*, 12217.

[62] B. Yan, D. Liu, X. Feng, M. Shao, Y. Zhang, *Adv. Funct. Mater.* **2020**, *30*, 1.

[63] J. Zhang, Y. Gu, Y. Lu, C. Zhu, G. Liu, C. Wang, D. Sun, Y. Tang, H. Sun, *Appl. Catal. B Environ.* **2023**, *325*, 122316.

[64] H. Huang, S. Zhou, C. Yu, H. Huang, J. Zhao, L. Dai, J. Qiu, *Energy Environ. Sci.* **2020**, *13*, 545.

[65] Y. Zhang, P. Wang, J. Yang, S. Lu, K. Li, G. Liu, Y. Duan, J. Qiu, *Carbon N. Y.* **2021**, *177*, 344.

[66] C. Zheng, X. Zhou, H. Cao, G. Wang, Z. Liu, *J. Power Sources* **2014**, *258*, 290.

[67] Y. Wang, X. Zheng, D. Wang, *Nano Res.* **2022**, *15*, 1730.

[68] P. Li, W. Wei, J. Li, Y. Liu, K. Fan, L. Zong, L. Wang, *J. Alloys Compd.* **2023**, *947*, 169630.

[69] J. Yang, J. Peng, Y. Tang, P. Liu, Y. Lei, J. Zeng, C. Yi, Y. Shen, L. Zheng, X. Wang, *J. Energy Storage* **2024**, *101*, 113914.

[70] Y. Jiang, Y. Wang, H. Wu, Y. Wang, R. Zhang, H. Olin, Y. Yang, *Nano-Micro Lett.* **2019**, *11*, 1.

[71] H. Liu, Y. Xie, J. Liu, K. sik Moon, L. Lu, Z. Lin, W. Yuan, C. Shen, X. Zang, L. Lin, Y. Tang, C. P. Wong, *Chem. Eng. J.* **2020**, *393*, 124672.

[72] P. Naskar, P. Chakraborty, D. Kundu, A. Maiti, B. Biswas, A. Banerjee, *ChemistrySelect* **2021**, *6*, 1127.

[73] A. Dutta, S. Mitra, M. Basak, T. Banerjee, *Energy Storage* **2023**, *5*, 1.

[74] E. Muslu, E. Eren, A. U. Oksuz, *Emergent Mater.* **2024**, *7*, 2205.

[75] N. O. Laschuk, E. B. Easton, O. V Zenkina, *RSC Adv.* **2021**, *11*, 27925.

[76] X. Chen, J. Yang, Y. Cao, L. Kong, J. Huang, *ChemElectroChem* **2021**, *8*, 4427.

[77] E. Pomerantseva, C. Resini, K. Kovnir, Y. V. Kolen’ko, *Adv. Phys. X* **2017**, *2*, 211.

Chapter 2

Ultra-fast electro-reduction and activation of graphene for supercapacitor asymmetrically designed with MXene

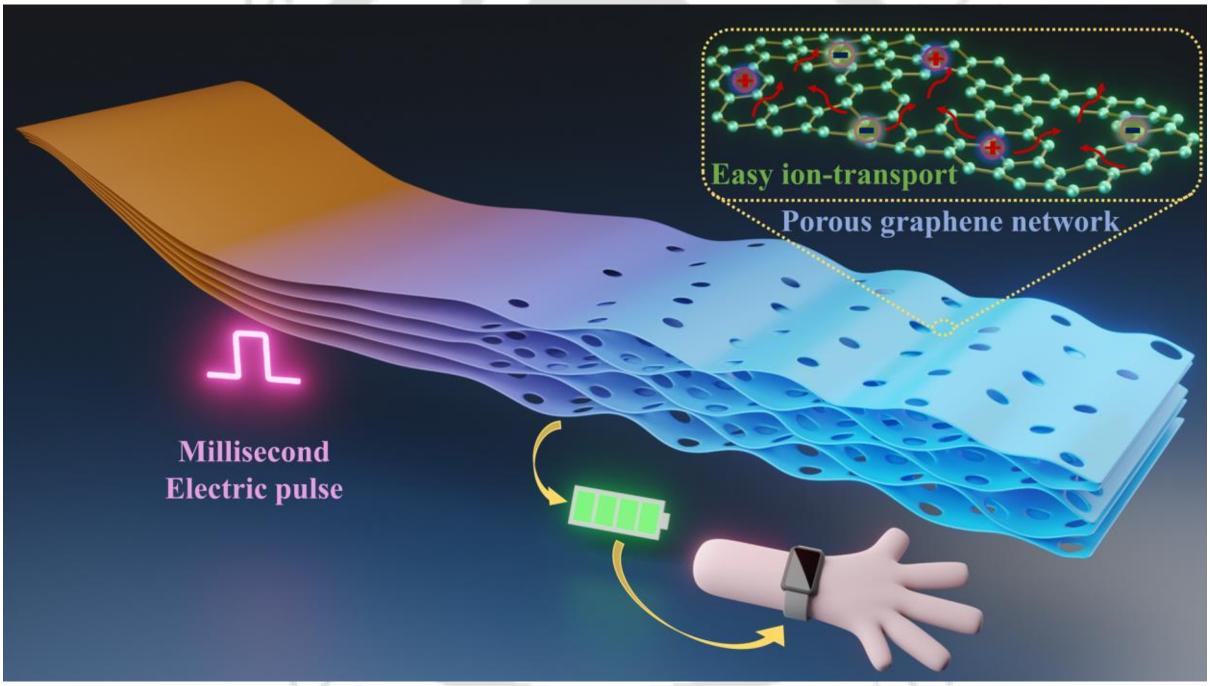

Ultra-fast electro-reduction and activation of graphene for supercapacitor asymmetrically designed with MXene

Controlled perforation of graphene is vital to surpass the performance of supercapacitors that rely on their pristine form. However, their practical utilization has been halted by energy-inefficient and lengthy processing. Here, we report a pulse Joule heating strategy for on-site reduction and activation to realize a multimodal porous framework made of perforated graphene using millisecond current pulses. The multimodal porosity and surface functionalities of graphene were regulated at an ultrafast rate by passing a transient current. As-developed ready-to-use electrode composed of nano-to-macro multimodal porosity displays a high areal capacitance of 380.2 mF cm^{-2} in symmetric two-electrode configuration, nearly 1.6 times higher than the non-electro activated counterpart. Furthermore, a high-performance wearable asymmetric supercapacitor with an areal energy density of 107.77 μWh cm^{-2} was realized using this multimodal porous graphene combined with suitable negative MXene electrodes. High energy density, together with stable and repeatable performance of the wearable device for 10000 cycles of charge-discharge and 5000 cycles of bending, signifies the importance of the as-developed device for practical wearable applications. Direct, simple processing of electrodes and orders of magnitude lower cost–and–processing–time can make the process appealing for practical wearable and other energy storage applications.

2.1. Introduction

With the tremendous success of graphene in energy storage and catalysis, it has been realized that extensive surface modification is inevitable to push the performance further. Controlled perforation of the basal plane of graphene to incorporate nanoscale holes has been regarded as a suitable strategy in this regard.[1,2] The energy storage electrodes of perforated graphene can offer easy ion transportation paths and a large electrochemically accessible surface area, thus exhibiting high energy and power densities.[3,4] However, the search for a facile and low-cost strategy for such nanoscale drilling of graphene is still ongoing.[5–7]

To date, the perforation of graphene has been done mainly via thermal activation and selective chemical etching.[2,8–10] Although chemical etching can be done at low temperatures with different oxidative etchants, the tedious purification and post-treatments lower the effectiveness of this process. In addition, these chemical processes are associated with safety and environmental concerns. On the other hand, thermal activation, which the Ruoff group initially invented [11], is a facile, safe, and environmentally benign technique for creating pores over graphene basal planes.[1,2,12–15] In this thermal activation strategy, graphene oxide (GO) is first partially reduced, and its programmed thermal treatment is done with potassium hydroxide (KOH), which acts to etch the graphene surface by reacting at elevated temperatures.[6,9,16,17] The requirement of a high thermal budget and the long processing time of tens of minutes to several hours are practical concerns associated with this thermal activation process. However, specific non-conventional techniques like laser etching and microwave plasma processing are costly, and sophisticated equipment is required for the processing, which can hinder their widespread application.[18,19]

Apart from the abovementioned concerns, nearly all these protocols produce bulk powder-like products that can get restacked during electrode preparation with a polymeric binder, reducing the overall conductivity and, thereby, sacrificing the advantage introduced by the perforation.[6,12,13,17,20,21] Besides the restacking issue, perforated graphene powder usage is limited in certain critical areas of energy storage, like wearable systems. [22–24] Wearable energy storage is a highly demanding system to power next-generation innovative, portable, and wearable electronics, which must possess high energy density and excellent mechanical stability.[25–31] The powder form of perforated graphene is unsuitable for wearable use as the polymeric binder required to make the electrodes can not ensure mechanical stability, and material detachment can happen during repeated mechanical deformations. [32]

We report facile and low-cost processing for developing multimodal porous graphene with intersheet macropores and in-plane nanopores using an ultrafast Joule heating strategy involving short current pulses.[33–35] We have shown here that a brief current pulse of 50 ms duration is enough to get a non-restacked macroporous graphene framework, and controlled perforation of graphene can be done by application of only several current pulses of 100 milliseconds duration. In contrast, conventional graphene activation requires hours of programmed heating. Importantly, this on-site activation produces a binder-free electrode with perforated graphene directly linked with fibers of carbon cloth (AJG@CC), thus making it a standalone binder-free electrode for wearable energy storage devices. This unique protocol causes ultra-fast reduction and nano-to-macro pore development over a wearable carbon cloth textile current collector at the local site. It reduces the thermal budget by orders of magnitude. Optimized perforation greatly enhances the capacitance of the as-developed graphene-based textile supercapacitor device, and an areal value as high as 380.2 mF cm^{-2} was obtained, which is among the top values with graphene-based textile supercapacitor devices. [36–43] This wearable asymmetric supercapacitor device with high energy and power density was realized by utilizing this high-performance metric via ultra-fast perforation. The AJG@CC works as a positive electrode in this solid-state asymmetric supercapacitor, whereas the negative electrode was prepared from nanosheets of titanium carbides, known as MXene.[44,45] The asymmetric device displays an extended potential window of 1.6V compared to symmetric devices (~1V), with a high areal energy density of 107.8 µWh cm^{-2} and exceptional capacity retention of 94% after 10000 cycles. Together with high energy storage, the solid-state device displays highly stable performance (90% capacity retention) under repeated bending and folding for more than 5000 cycles, making it a viable candidate for powering future wearable electronics.

2.2. Materials and methods

2.2.1. Materials

Natural graphite flakes and LiF powder (≤100 µm) were purchased from Sigma Aldrich. KOH (Emsure), H_2SO_4 (95-97 wt%, Emsure), HCl (32 wt%, Emsure), $KMnO_4$, and H_2O_2 (30 wt%) were purchased from Merck. Ti_3AlC_2 was purchased from Carbon Ukraine. Commercial carbon cloth (CC) (Plain Carbon Cloth - 1071 HCB) was purchased from AvCarb Material Solutions.

2.2.2. Preparation of Graphene Oxide Coated Carbon Cloth (GO@CC) and MXene Coated Carbon Cloth (MXene@CC)

At first, Carbon Cloth (CC) (13.2 mg/cm^2) was washed in ethanol and DI water in a bath sonicator for 10 minutes each. The clean CC was then dipped into Graphene Oxide (GO) aqueous suspension (7.2 mg/mL) (synthesized by modified Hummer's method, [46,47] for 1 minute and dried in air. This dip & dry process was repeated six times until the mass loading of GO over CC became 5.5 mg/cm^2. After drying at room temperature, the obtained GO@CC will be ready for further processing. Similarly, MXene Coated CC (MXene@CC) was prepared by immersing the clean CC into $Ti_3C_2T_x$ aqueous solution (15 mg/mL) and was dried in air. The MXene@CC was directly used as the flexible electrode for electrochemical measurement. $Ti_3C_2T_x$ aqueous dispersion was synthesized by etching of MAX phase (Ti_3AlC_2) powder as reported in one of our previous reports,[45,48,49] where the minimally intensive layer delamination (MILD) method as introduced by Gogotsi group was used.[44] The GO and MXene mass loading over CC can be easily adjusted by varying the coating times.

2.2.3. Preparation of reduced GO Sheets over Carbon Cloth (JG@CC)

The as-prepared GO@CC was cut into pieces (2.8×1 cm^2), and a 50-millisecond voltage pulse of 30 Volt was applied through the length of the GO@CC fabric in the open air using a constant voltage power supply capable of supplying pulse voltage. The short current pulse, flowing through the fabric, produced ultrafast Joule heating. As a result, GO over the CC is reduced and exfoliated simultaneously due to the quick release of volatile gas from various functional groups' gasification. This fast Joule heating resulted in highly porous reduced GO (rGO, simply graphene) sheets over CC (JG@CC), having intersheet macroporosity. The level of reduction can be controlled by varying the applied voltage and the pulse width. The JG@CC was directly used as the flexible electrode for electrochemical measurement.

2.2.4. Development of activated rGO Sheets over Carbon Cloth (AJG@CC)

The JG@CC fabrics, produced in the reduction and exfoliation process, were immersed in a 6M KOH solution and kept for 2 hours. After that, the fabrics were collected and dried entirely in the open air. The KOH-embedded JG@CC fabric was then subjected to ultrafast Joule heating with 20 numbers of 30 V pulses (TJH cycles), 100 ms each, and the time gaps between two consecutive pulses were 1s. This process was done in a nitrogen gas environment. The JG@CC fabric, loaded with KOH and subsequently treated with ultrafast Joule heating, was then immersed in 10% acetic acid for 12 hours to remove the unreacted KOH and other byproducts altogether. The KOH-treated JG@CC fabric was then collected and washed thoroughly in DI water until the pH became neutral. Then, it was dried in the open air to get the final product, AJG@CC. The AJG@CC was directly used as a flexible electrode for electrochemical measurement. The number of pulses and concentration of KOH were varied to optimize the process.

2.2.5. Fabrication of Solid-State Asymmetric Device

The PVA gel was first prepared by adding 0.5 g of PVA into 5 mL 1M H_2SO_4 with continuous stirring at 85 °C until the PVA solution was completely dissolved. The AJG@CC fabric and MXene@CC fabric with a working area of 1 cm^2 were soaked in the hot gel electrolyte (50–60 °C) for 1 min to allow the electrolyte to diffuse into the nanoporous structure of the two electrodes; they were then removed and allowed them to dry under ambient conditions for 10 min. This gel-coating process was repeated three times. The asymmetric SSC device was fabricated by sandwiching the two pieces of porous graphene-coated CC (AJG@CC) and MXene-coated CC (MXene@CC) (serving as the positive and negative electrodes, respectively).

2.2.6. Material Characterization

The morphology and microscopic features of the prepared samples were investigated by using field emission scanning electron microscopy (FESEM, Zeiss, Sigma-300), field emission transmission electron microscopy (FETEM, JEM 2100F, JEOL), and atomic force microscopy (AFM, Oxford Instruments, Cypher S). Samples' crystal properties and interlayer spacing were analyzed using an X-ray diffractometer (Rigaku, SmartLab, 5 kW) with Cu Kα radiation. The Raman spectroscopic measurements were performed on a Raman Spectrometer Horiba, LabRam HR, laser wavelength 514 nm. The surface chemical compositions and Oxidation states were detected by X-ray photoelectron spectroscopy (ESCALAB Xi+, Thermo Fisher).

2.2.7. Surface area measurement and pore size analysis

The well-established methylene blue (MB) adsorption method measured the as-prepared samples' specific surface area measurements. [50,51] A specific surface area was compared for non-activated electro-reduced graphene (JG) and the electro-activated graphene samples (AJGs) with different TJH activation conditions to understand the variation of the specific surface area of activated graphene. Alternatively, the Brunauer-Emmett-Teller N_2 adsorption experiment (Quantachrome Instruments, Autosorb, IQ MP) was also performed for the optimized sample (AJG@CC-6M-20p) to determine the BET surface area and pore size distribution.

2.2.7.1. MB adsorption analysis

The as-prepared electrodes (JG@CC and AJG@CCs) with an area of 1 cm^{-2} were immersed in an MB aqueous solution (0.2 mg mL^{-1}, 5 mL) for 48 hours. After that, the solution was diluted 50 times, and the concentrations of the MB solutions were analyzed by UV-visible spectroscopy. The surface area ($S_{electrodes}$) of the electrodes was calculated using the equation given below,

$$S_{electrode} = 2.54 \times 10^3 \times \Delta M_{MB} \qquad (2.1)$$

where, ΔM_{MB} is the mass (g) change of MB due to adsorption. Detailed surface area calculation from the UV-vis analysis using the MB absorption method is given in the supporting information.

2.2.7.2. BET analysis

THE BET N_2 adsorption experiment was carried out separately for AJG@CC electrode and bare CC. From the results of the two, the specific surface area and pore size distribution of the active material (AJG) were determined. The surface area of the porous graphene sample attached to the carbon cloth was measured by subtracting the result of the bare carbon cloth. The detailed calculation for surface area estimation is given in the supporting information.

2.2.8. Electrochemical Measurements

The electrochemical measurements of single electrodes were carried out in a traditional three-electrode test configuration with 1M H_2SO_4 as an aqueous electrolyte, in which flexible electrodes served as working electrodes, a platinum wire was the counter electrode, and Ag/AgCl in saturated KCl was used as a reference electrode. The optimization of current pulse processing to get the highest capacitive performance of the electrode was done by taking feedback from these three electrode measurements. All electrochemical measurements of the symmetric device were carried out in a two-electrode configuration in 1M H_2SO_4 as an aqueous electrolyte. All electrochemical measurements, including those flexible electrodes and the solid-state asymmetric device, were taken on the Biologic SP-150e electrochemical workstation at room temperature. The galvanostatic charge/discharge test for 10000 cycles at 50 mA cm^{-2} was carried out for cycling stability. The electrochemical impedance spectroscopy (EIS) was obtained in a frequency range from 100 kHz to 0.01 Hz.

2.3. Result and Discussion

Ultrafast reduction, inter-sheet pore formation among graphenes, and their controlled perforation were done through a transient Joule heating (TJH) approach using successive short current pulses, as presented schematically in **Figure 2.1**. In brief, commercial conducting carbon cloth substrates (CC) were coated with graphene oxide (GO), derived from natural graphite through modified Hummer's method [47] via the successive dip-and-dry method. The GO-coated carbon cloth (GO@CC) was used as a current filament, and a transient current of only 50 milliseconds duration was passed through it by connecting it to a 30V voltage source. The current passage through the GO-coated carbon cloth momentarily induces large resistive heating (Joule heating). Due to this fast heating, GO reduces to reduced graphene oxide (rGO, simply graphene) instantaneously. Importantly, this ultrafast Joule heating not only reduces GO into graphene at its local site over CC but also turns it into a non-restacked macroporous structure (JG@CC) due to the rapid release of gases between the graphene sheets during this reduction process(**Figure 2.1**). This simultaneous reduction and exfoliation directly improves the conductivity of graphene sheets and increases the effective surface area of JG@CC. Perforation of the graphene basal plane in the JG@CC electrode was done via a fast alkali activation strategy employing very short current pulses. For this unique activation process, JG@CC electrodes were first impregnated with potassium hydroxide (KOH), and activation was performed by passing a few current pulses of 100 ms duration (**Figure 2.1**). The chemical processes that occur during the KOH activation are

$$4KOH + C \rightarrow 4K + CO_2 + 2H_2O, \tag{2.2}$$

$$6KOH + 2C \rightarrow 2K + 3H_2 + 2K_2CO_3.^{[11]} \tag{2.3}$$

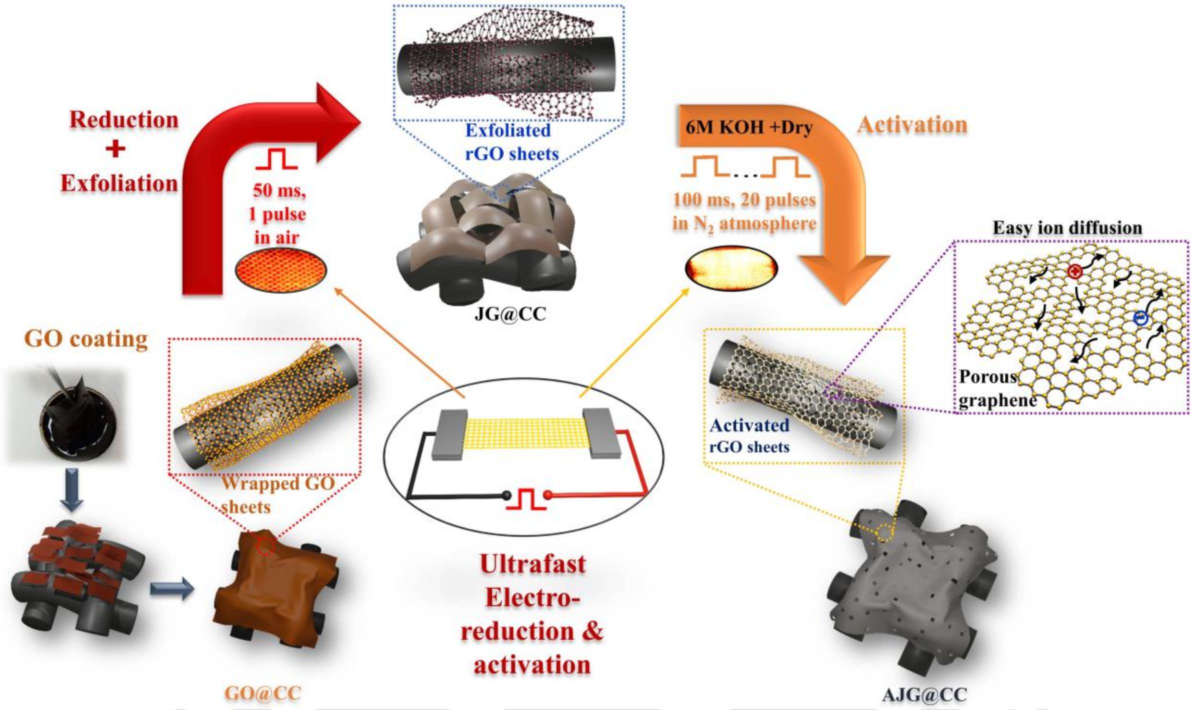

Figure 2.1: (a) Schematic description of ultrafast reduction, exfoliation, and activation of GO coated over carbon cloth (GO@CC) using a unique transient Joule heating (TJH) method.

During the pulse current-induced annealing, the chemical reactions between C-atoms in the basal plane of rGO and KOH result in the gasification of C-atoms (CO_2, CO, etc.), thus creating numerous nanopores within the rGO basal plane [9,52] which leads to the generation of activated JG@CC (AJG@CC). Since graphene tends to restack face-to-face at elevated temperatures [35,53], the duration of each current pulse is very important to avoid excessive heating and resultant restacking. The first pulse of 50 ms was enough to reduce GO into reduced graphene oxide (graphene) and create numerous intersheet pores. Further, it was observed that 20 pulses of 100 ms duration with a cooling period of 1s between the pulses are the optimum condition to accomplish the activation-induced perforation. The optimization of activation was done by taking feedback from the cyclic voltammograms of the samples; the higher the area under the CV curve, the better the energy storage performance, which will be discussed in the energy storage section. Controlled experiments were also done to optimize the activation process by varying the KOH amounts. The current protocol not only gives ready-to-use supercapacitor electrodes through ultrafast processing, but the energy cost is orders of magnitude lower (~0.613 kJ) as compared to the conventional activation process done in a furnace (~10^4 kJ), which makes it a commercially viable technology (**Table 2.1**). The approximate estimation of the energy cost of activation is as follows:

The total energy required to prepare AJG@CC by the TJH method is,

$$I^2Rt = \frac{V^2}{R}t \tag{2.4}$$

$$= \frac{V^2}{R_{GO}} t_{reduction} + \frac{V^2}{R_{JG/KOH}} t_{activation}$$

$$\approx \frac{30^2}{3.4} * 0.05 + \frac{30^2}{3} (20 * 0.1)$$

$$\approx 0.613\ kJ$$

Where,

V is the applied pulse voltage in Volt (V) for Joule heating, $R_{GO,}$ and $R_{JG/KOH}$ are the resistances in ohm of GO-coated carbon cloth (GO@CC), and KOH-impregnated Joule heating treated reduced graphene oxide (JG@CC/KOH), $t_{reduction}$ and $t_{activation}$ are the time in second (s) required for reduction and activation using the TJH method.

Table 2.1: Time and energy cost comparison of traditional furnace heating and TJH method for graphene activation.

	Traditional	**Electric pulse**
Time	**215 min**	**20s**
Energy	**12900 kJ**	**0.613 kJ**

	Ref. [1]	**This work**

The morphological evolution of the electrodes and the basal plane perforation after successive Joule heating were monitored through a field emission scanning electron microscope (FESEM) and transmission electron microscope (TEM), respectively. FESEM image of the GO@CC (**Figure 2.2a**) shows a smooth GO film over CC. After 1st current pulse of 50 ms duration (reduction stage), the film's color immediately changes to dark black, indicating the thermal reduction of GO into graphene. The sample's lower magnification FESEM image (Fig. S1b) after this current pulse (JG@CC) shows cracks and protrusion of sheets. However, a higher magnification image (**Figure 2.2b**) reveals a highly open porous structure having inter-sheet micro/macro pores. The obtained highly porous framework can be related to the rapid gas evolution from the interlayers of GO during their electrothermal reduction. The morphology of the activated electrode (AJG@CC) maintained the open macroporous morphology similar to JG@CC (**Figure 2.2c**).

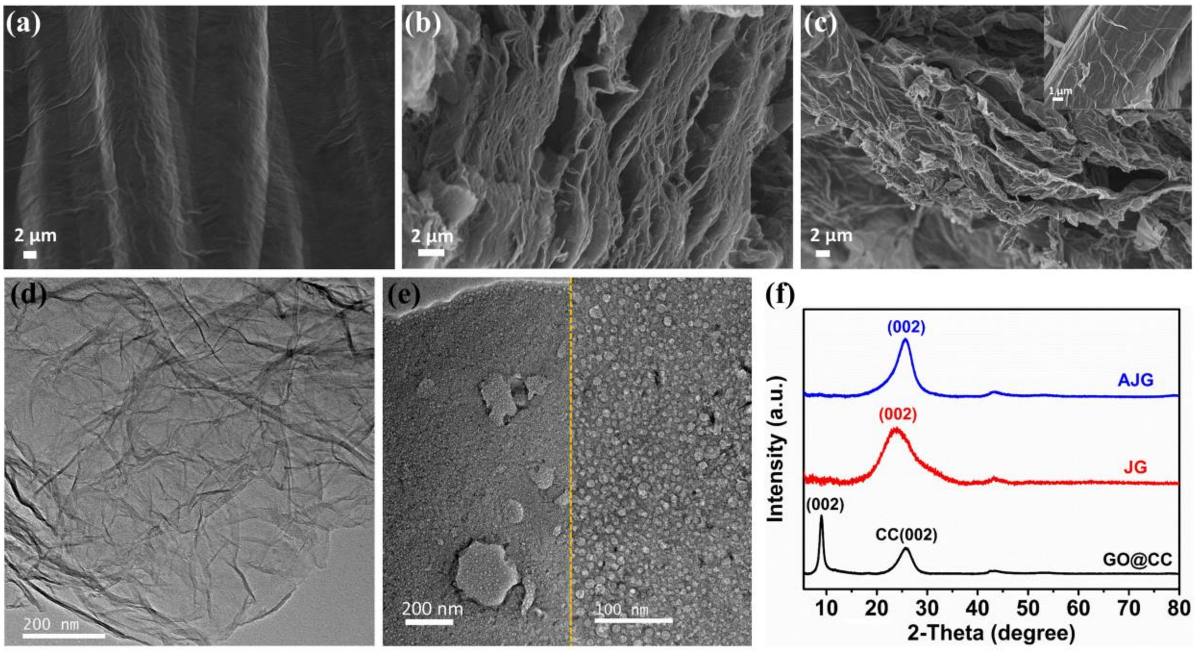

Figure 2.2: FESEM images of (a) GO@CC, (b) exfoliated JG@CC, and (c) activated AJG@CC; inset: magnified FESEM image showing crumpled activated graphene sheets tightly wrapped over carbon microfiber. FETEM images of (d) JG, (e) AJG (left: low magnified; right: high magnified), and (f) XRD patterns of GO@CC and as-prepared electrode materials (JG and AJG).

Inspection through TEM reveals that the graphene of the JG@CC sample shows a wrinkled sheetlike structure without pores in the basal plane (**Figure 2.2d**). Highly nanoporous sheets can be detected on ultrafast activation from the TEM images (**Figure 2.2e**). There are occasional bigger nanopores in the 100-200 nm range; however, the porous structure is dominated by uniform nanopores of much smaller sizes and narrow size distribution. The average pore size of those nanopores was estimated to be around 6 nm only (**Figure 2.3**).

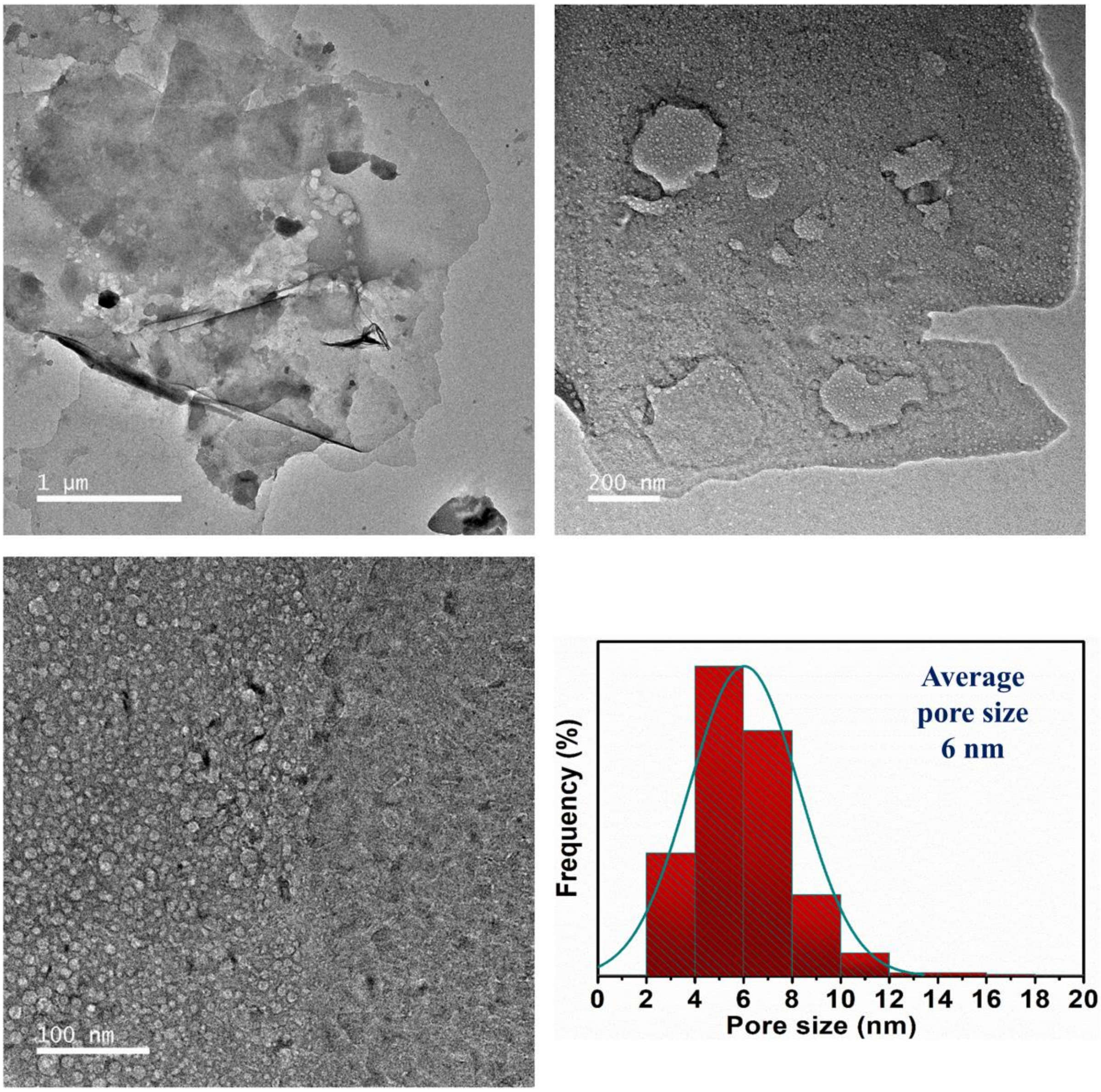

Figure 2.3: Low and High magnified FETEM images of AJG, activated with 6M KOH and 20 TJH cycles (20p), and the pore size distribution, estimated from FETEM images.

The reduction process and crystalline modification via this TJH process were investigated through X-ray diffraction analysis. Since the underlying carbon cloth exhibits graphitic crystallinity, its XRD peak will overlap with the peaks of graphene. XRD was performed to avoid overlapping peaks by scratching the samples (JG and AJG) from the CC substrate after electrothermal modifications. The XRD peak at $2\theta = 9°$ for the GO@CC sample is associated with (002) planes of graphene oxide (GO) (**Figure 2.2f**). The disappearance of this peak in JG, AJG and the appearance of peaks at 23.94° and 25.62° indicates a successful reduction of GO in millisecond Joule heating and restoration of the crystalline graphitic structure in the samples (**Figure 2.2f**).

The Nature of surface functional groups and the modification of graphitic structure at different stages of processing of electrodes were analyzed through Raman and X-ray photoelectron spectroscopy (XPS). The high-resolution C 1s spectra of GO, JG, and AJG are shown in **Figure 2.4a**, **b**, and **c**, respectively. For all the cases, the C 1s spectra exhibited three prominent peaks located at 284.5 eV, 286.3 eV, and 288.3 eV corresponding to sp^2 carbons (C=C), hydroxyl groups/epoxides (C-O/C-O-C) and carboxyl groups (C=O/O-C=O), respectively. The dominance of hydroxyl/epoxide and carboxyl peaks over the sp^2 carbon peak depicted in the C 1s spectra of GO (**Figure 2.4a**) indicates the presence of large amounts of oxygen-containing groups. For the case of JG, the intensity of the peaks associated with the functional groups reduces significantly compared to the peak due to C=C, which confirms the reduction of GO to reduced graphene oxide (rGO, simply graphene) during this ultrafast Joule heating (**Figure 2.4b**). After activation, the area and the intensity of the hydroxyl/epoxide peak of AJG decreases (**Figure 2.4c**) compared to JG's corresponding peak, confirming the further removal of hydroxyl/epoxide groups from the basal plane of graphene. However, the intensity and area of the carboxyl peak increased slightly after activation compared to the carboxyl peak of JG due to the introduction of a few additional COOH groups to the edge carbon of the nanopores during electrothermal KOH activation. This is because edge carbons are prone to be functionalized with carboxylic (-COOH) groups, according to the Lerf-Klinowski model. [53–55] Raman spectra of GO and its derivatives obtained from pulsed Joule heating treatment are presented in **Figure 2.4d**. All the spectra display D and G peaks, characteristic peaks of carbonaceous materials. The G peak is attributed to the graphitic in-plane vibration, while the D peak is directly related to the lattice defects and disorder of the graphitic structure. The position of the G peak for GO is 1594 cm^{-1}, which shifts to 1574.5 cm^{-1} for JG, which indicates a successful reduction of GO by 50 ms of current pulse only. The peaks' relative intensities

(I_D/I_G) are generally used to measure graphene's degree of structural disorder and its derivative materials. The ratio $I_D/I_G = 1.26$ is the maximum for GO, indicating the presence of large amounts of disorder and defects originating from its surface structure consisting of –OH, -COOH, and -C-O-C- groups.

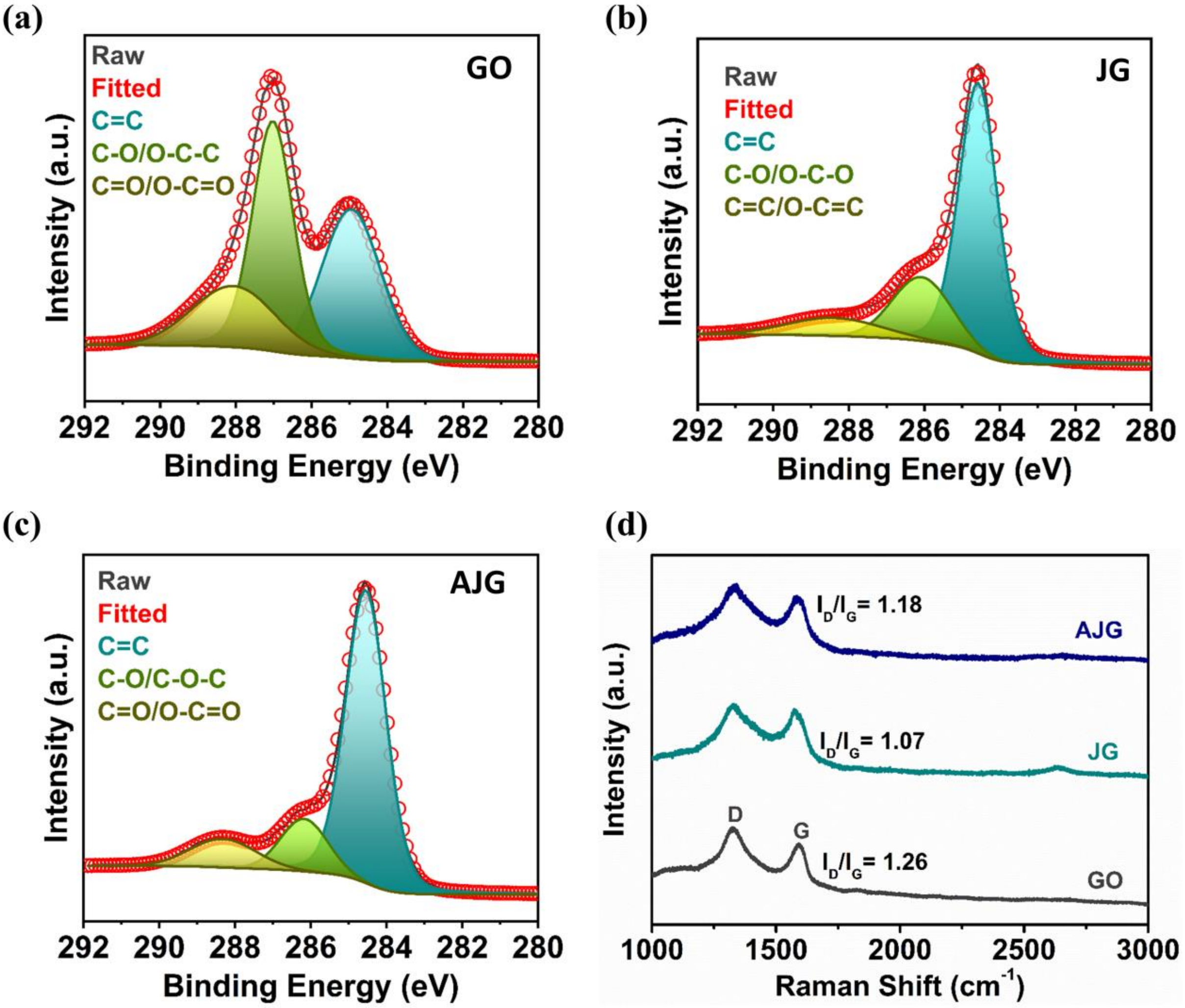

Figure 2.4: Spectroscopic characterization of as-prepared GO, JG, and AJG. High-resolution XPS spectra of C 1s for (a) GO, (b) JG, (c) AJG; (d) Raman spectra of GO, JG, and AJG.

The value I_D/I_G reduces to a value of 1.07 for graphene in the JG@CC sample, which indicates the removal of oxygen-containing groups at the time of electro-reduction, confirming the restoration of the graphitic structure. After electro-activation with KOH, the I_D/I_G ratio again increases from 1.07 for JG to 1.18 for AJG. This increase in intensity ratio can be associated with surface modification via nanopore incorporation, equivalent to intentionally incorporating structural defects within the graphene plane. Moreover, additional defects and disorders could also be generated due to incorporating the carboxyl (-COOH) group at the edge carbons of the nanopores during the KOH activation. To confirm the role of KOH in pore creation and introduction of functional groups during pulse heating, a sample (FJG) was prepared using the same Joule heating condition as AJG but without using any KOH. This sample shows only G and 2D peaks, and the D-peak nearly vanishes, which indicates complete restoration of the graphite structure (**Figure 2.5**). This parallel experiment highlights that using KOH in pulsed electrothermal heating can significantly modify the basal plane of graphene to incorporate nanopores.

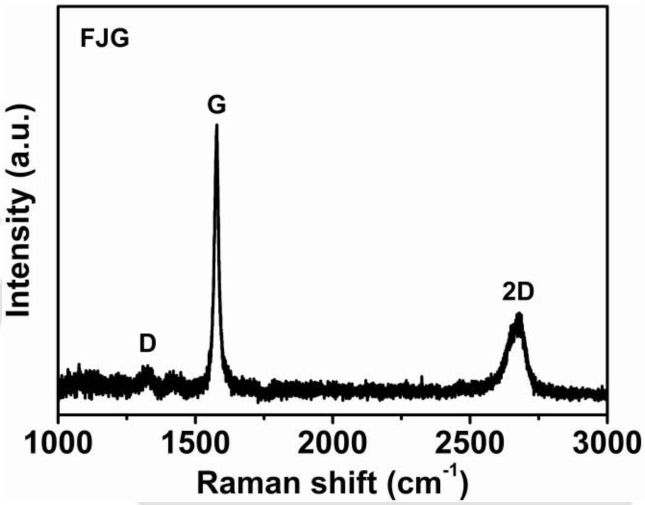

Figure 2.5: Raman spectrum of FJG.

Due to inter-sheet and basal plane porosity, the as-developed multimodal porous electrode can be an attractive candidate for supercapacitor energy storage applications. To optimize the electro-reduction and electro-activation process, the electrochemical performances were measured in the three-electrode configuration in 1M H_2SO_4 electrolyte (Materials and methods). Cyclic voltammograms (CVs) of JG@CC and AJG@CC electrodes with different TJH cycles (number of current pulses during activation) (**Figure 2.6a**) show that with an increase in the number of TJH cycles (p) from 10 to 20, the area under the curves and hence geometric area normalized capacitance increases from 393.7 mF cm^{-2} for JG@CC electrode to 576.1 mF cm^{-2} and 667.5 mF cm^{-2} at 10 mV s^{-1} for AJG@CC electrode (activated with 6M KOH). The further increment of the number of TJH cycles (e.g., 30 cycles (p)) led to the decrement of area normalized capacitance (from 667.5 to 203.0 mF cm^{-2}) by 69.6 % (at 10 mV s^{-1}), estimated from the voltammograms (**Figure 2.6a**). Instead of a pulsed Joule heating cycle, continuous electrothermal activation (for 2s) was also employed, resulting in a capacitance decrement of 77.2% (152 mF cm^{2}) estimated from the CV curves in **Figure 2.6a**. The EIS spectra of JG@CC and AJG@CC electrodes prepared by different Joule heating configurations are also provided for comparison (**Figure 2.6b**). The decrement in capacitance in a higher number of TJH cycles and continuous electrothermal activation mode can be associated with higher restacking at a much higher elevated temperature, as is evident from EIS curves. The less steep rise of EIS curves in AJG@CC-6M-30p and AJG@CC-6M-2s compared to AJG@CC-6M-20p indicates higher diffusion resistance in the former two samples, leading to less capacitance. This observation highlights the importance of cyclic fast Joule heating and cooling, where activation proceeds without allowing the temperature to reach too high to avoid restacking.

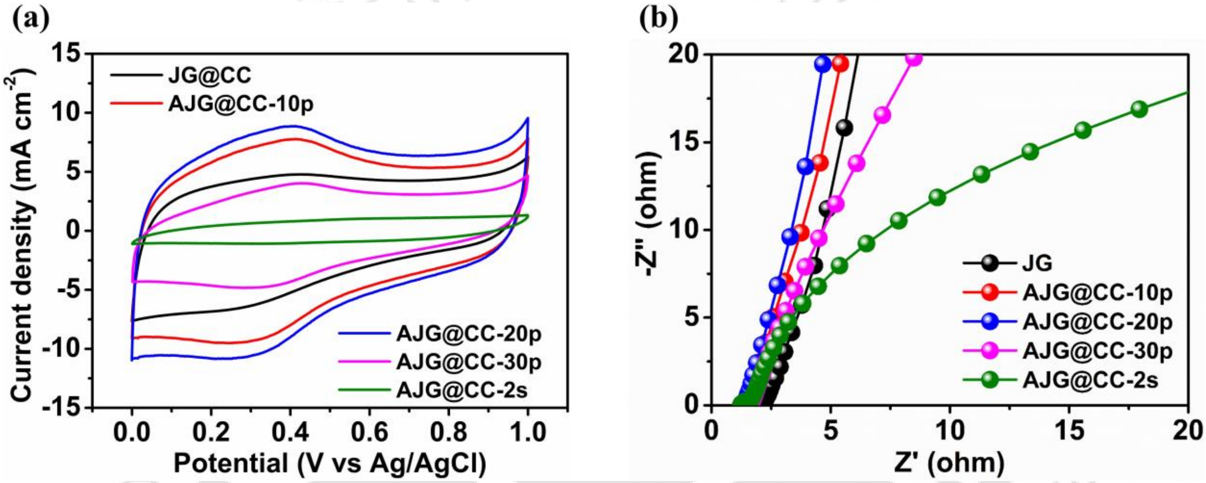

Figure 2.6: (a) Variation of CV curves with an increase in number of TJH cycles (p), and (b) the corresponding EIS spectra.

This observation indicates that the extent of perforation increases with the increase of TJH cycles from zero (non-activated, JG) to 10 and 20, which increases specific surface area and capacitance. However, further increments of TJH cycles (e.g., 30) led to the restacking of graphene sheets at elevated temperatures, resulting in less specific surface area and, hence, the capacitance. To understand the effect of TJH cycles on the specific surface area of graphene during the activation, a methylene blue (MB) adsorption experiment was performed for non-activated JG and AJGs activated with different TJH cycles (e.g., 10, 20, 30) (**Figure 2.7**). The specific surface area of as-prepared JG, AJG-6M-10p, AJG-6M-20p, and AJG-6M-30p estimated from the MB adsorption analysis are 166.54 m^2 g^{-1}, 755.91 m^2 g^{-1}, 974.63 m^2 g^{-1}, and 224.17 m^2 g^{-1}, respectively (**Table 2.2**). This analysis suggests that the surface areas increased with increased TJH activation cycles from JG to AJG-6M-10p (10 TJH cycles) and then AJG-

6M-20p (20 TJH cycles) due to the increased porosity. It also suggests that further increments of TJH cycles to 30 eventually decrease specific surface area due to the restacking of graphene sheets at elevated temperatures. The variation in surface area due to TJH cycles is also consistent with the trends of the electrodes’ electrochemical performance (**Figure 2.6**), in which capacitance follows the following series JG<AJG-6M-30p<AJG-6M-10p<AJG-6M-20p.

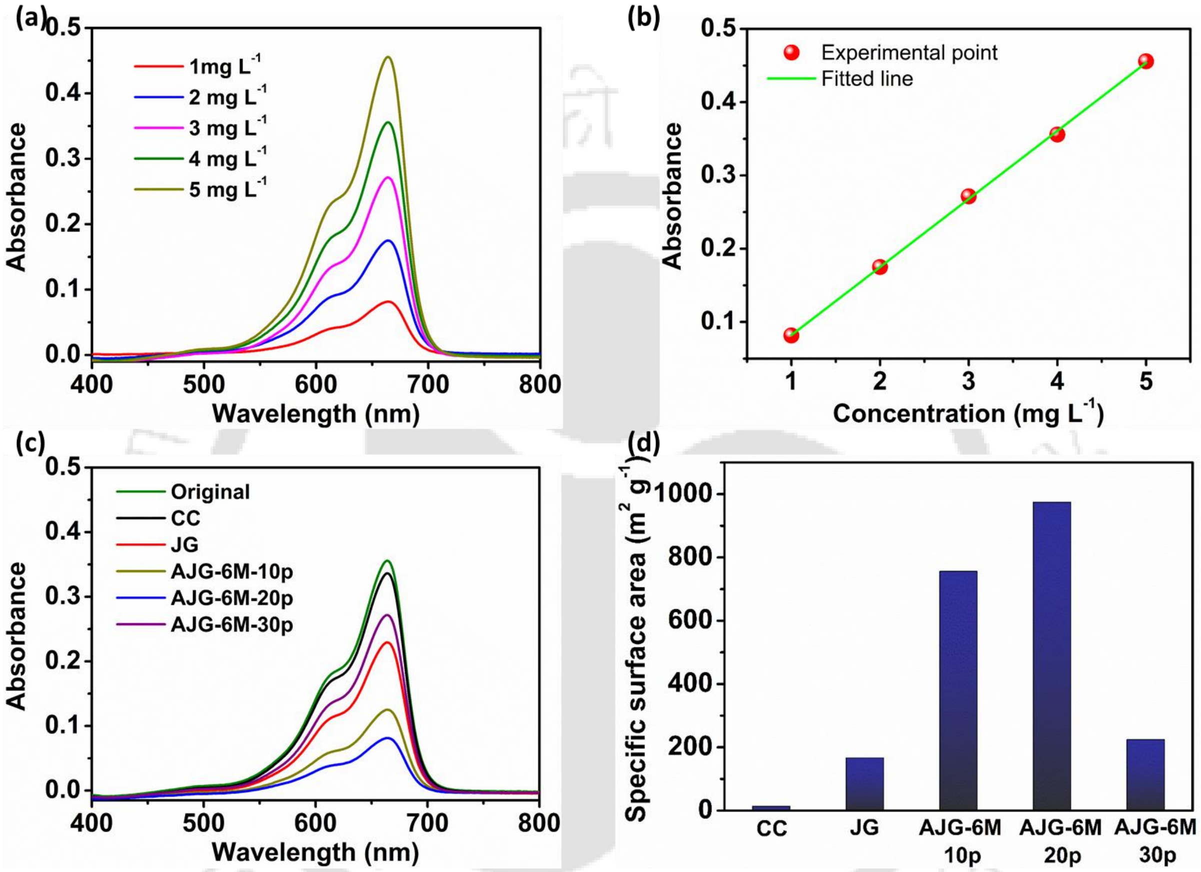

Figure 2.7: (a) UV-visible spectra of MB aqueous solutions for different concentrations of MB (mg L^{-1}). (b) calibration curve of MB concentration vs absorbance obtained from UV-visible spectra. (c) UV-visible spectra of MB aqueous solutions after adsorption in different electrodes compared to the original solution (4 mg L^{-1}). (d) bar diagram of specific surface areas of as-prepared TJH-activated graphene (AJGs) compared to non-activated graphene (JG) and bare CC.

Calculation of surface area by MB adsorption experiment

The slope of the concentration calibration curve (**Figure 2.7a**, **b**), $b = 0.0929$, and intercept, $a = -0.0107$. The actual concentration of MB aqueous solution, $C = 0.2\, mg\, mL^{-1}$, the volume of MB solution used during adsorption for each sample, $V = 5\,mL$, absorbance of original solution after diluting 50 times (concentration, $c = 4\,mg\,L^{-1}$) $A = 0.35575$. Masses per cm^2 of CC, JG, AJG-6M-10p, AJG-6M-20p, and AJG-6M-30p are 13.20, 4.39, 1.90, 1.79, and 1.97 mg cm^{-2}, respectively. The calculated specific surface areas (**Equation 2.1**) (subtracting the surface area contribution of CC) of the samples from the UV-vis spectra (**Figure 2.7c**) are given in the bar diagram (**Figure 2.7d**) and the table below (**Table 2.2**).

Table 2.2: Specific surface area of JG and AJGs from MB adsorption analysis.

Sample	Absorbance (A)	Concentration (c) (mg L^{-1})	Change (Δc) (mg mL^{-1})	Actual change (ΔC) (mg mL^{-1})	Mass change (ΔM_{MB})	Surface area per unit area (cm^2) of the electrode (m^2)	Specific surface area of CC, JG, and AJGs (m^2 g^{-1})
Bare CC	0.33637	3.73649	0.26351	0.01318	0.06588	167.33	12.68
JG@CC	0.22934	2.58439	1.41561	0.07078	0.3539	898.91	166.54
AJG@CC-6M-10p	0.12529	1.46437	2.53563	0.12678	0.63391	1610.12	755.91
AJG@CC-6M-20p	0.08131	0.99096	3.00904	0.15045	0.75226	1910.74	974.63
AJG@CC-6M-30p	0.27169	3.04026	0.95974	0.04799	0.23994	609.44	224.17

Alternatively, the N_2 adsorption analysis by the BET method was also carried out for the best-performing electrode (AJG@CC-6M-20p) to determine the pore size and BET surface area (**Figure 2.8**). The BET-specific surface area of the active material (AJG) was estimated (**Equation 2.5**) to be 499.20 m^2 g^{-1}, and the average pore size is 7.30 nm, with the most frequent pore size of 4.20 nm (**Table 2.3**). This lower surface area value obtained with BET than the MB absorption method is commonly observed. [51,56]

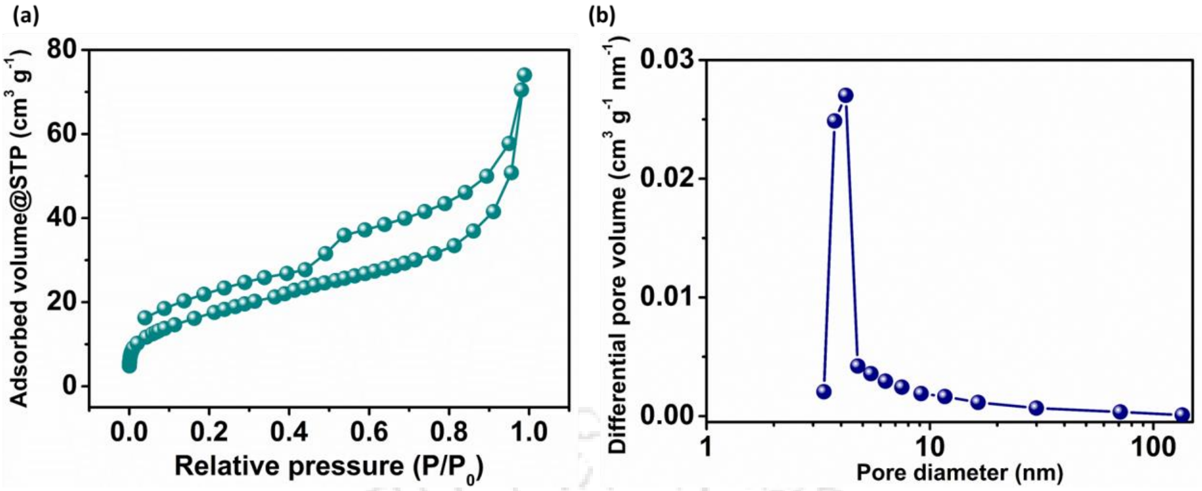

Figure 2.8: (a) Nitrogen adsorption isotherms at 77 K. (b) BJH adsorption pore-size distribution profile of AJG@CC-6M-20p.

Calculation of BET surface area

The BET surface area (S_{AJG}, $m^2\ g^{-1}$) of the activated porous graphene (AJG) was estimated using the equation given below,

$$x_1 \times S_{AJG} + x_2 \times S_{CC}^{BET} = S_{Total}^{BET} \tag{2.5}$$

where, x_1 and x_2 are the fraction of mass of activated porous graphene (AJG) and bare CC, respectively, in 1 gram of AJG@CC-6M-20p electrode. S_{CC}^{BET} and S_{Total}^{BET} are the specific surface area ($m^2\ g^{-1}$) of bare CC and the AJG@CC-6M-20p electrode, respectively, obtained from the BET N_2 adsorption experiment.

The mass loading of AJG-6M-20p is 1.79 mg cm^{-2}, and the mass of bare CC is 13.20 mg cm^{-2}. Thus, the mass contribution of AJG-6M-20p is 11.90 %, and bare CC is 88.10 %.

Table 2.3: Specific surface area of AJG-6M-20p from BET.

Experimental value of S_{CC}^{BET} (m^2 g^{-1})	Experimental value of S_{Total}^{BET} (m^2 g^{-1})	Mass fraction (x_1) of AJG in 1g AJG@CC electrode (g)	Mass fraction of (x_2) CC in 1g AJG@CC electrode (g)	Specific surface area of AJG S_{AJG} (m^2 g^{-1})	Average pore diameter (nm)	The most frequent pore diameter (nm)
3.82	62.77	0.1190	0.8810	499.20	7.30	4.20

To demonstrate the practical adaptability of the as-developed electrodes, symmetric supercapacitor devices in aqueous electrolytes were made using AJG@CC as both electrodes. The CV and constant current charge-discharge (CD) curves of the symmetric devices show noticeable variation with the concentration of KOH solution used to coat KOH particles over JG@CC (**Figure 2.9a**, **b**, and **Figure 2.10a**). The areal capacitance of the device made of AJG@CC electrode activated with 6M KOH was estimated to be 380.2 mF cm^{-2} at 5 mV s^{-1}, which is much higher as compared to the devices made of AJG@CC activated with 1M (298.3 mF cm^{-2} at 5 mV s^{-1}), 3M (309.9 mF cm^{-2} at 5 mV s^{-1}) concentrations.

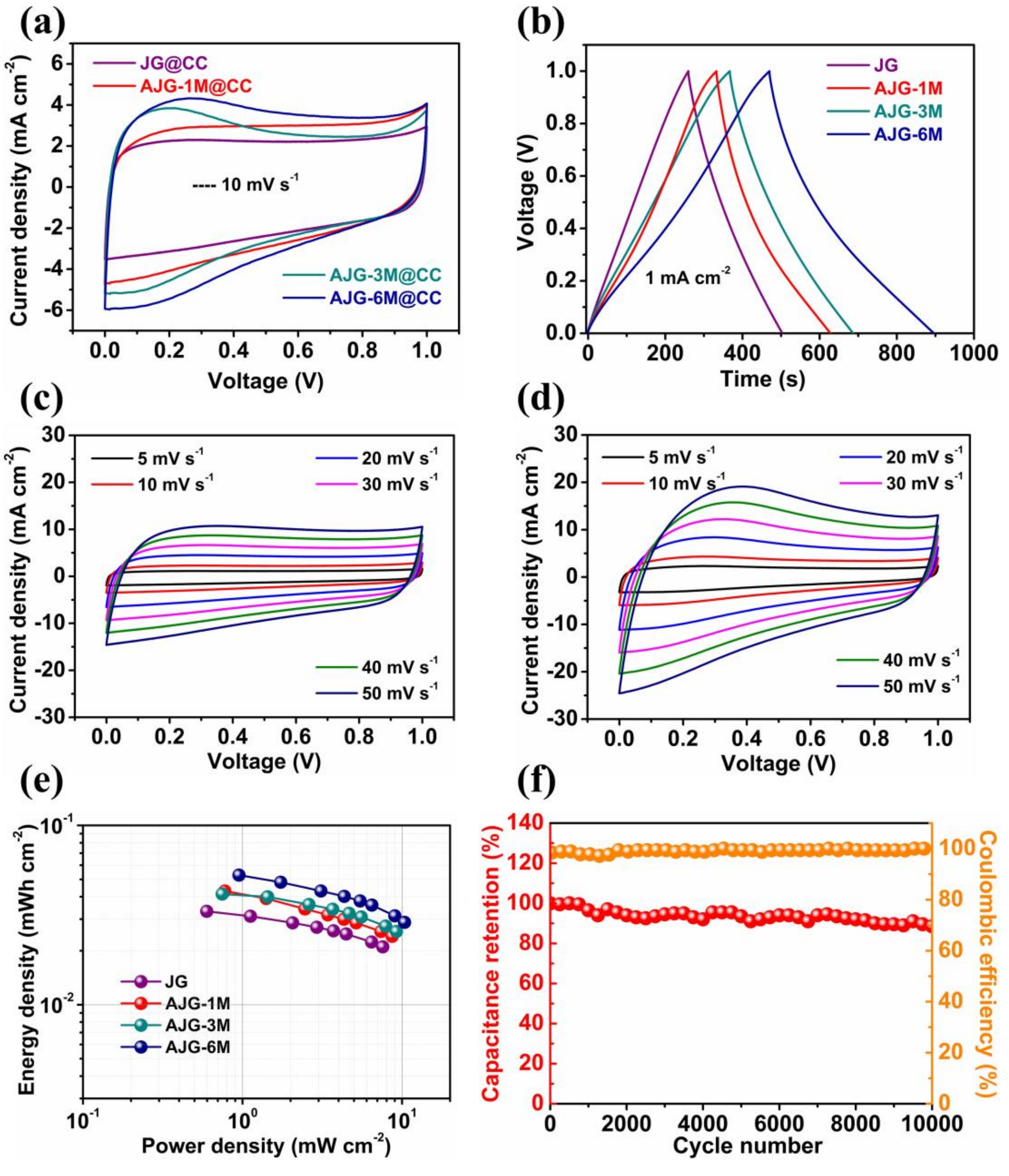

Figure 2.9: Electrochemical performances of symmetric supercapacitor devices made of JG@CC, AJG@CC electrodes. (a) CV curves at 10 mV s^{-1} of symmetric supercapacitor devices

made of JG@CC and AJG@CC (activated by KOH of different concentrations) electrodes. (b) Corresponding GCD profiles. (c) and (d) CV curves of symmetric supercapacitors made of JG@CC and AJG@CC electrodes, respectively, at scan rates varying from 5 to 100 mV s^{-1}. (e) Ragone plots of the devices. (f) Cycling stability of the symmetric device of AJG@CC as both positive and negative electrodes at 20 mA cm^{-2}.

The KOH concentration higher than 6M was not used for the activation process as it was almost impossible to dry the samples coated with KOH having more than 6M KOH concentrations. Even after completely drying in a vacuum oven, it got wet after exposure to air before activation, as KOH is very moisture-sensitive. Electrochemical impedance spectroscopy (EIS) analysis can provide a deeper understanding of the observed variation in capacitance with the variation in KOH amount used in activation. EIS spectra become more and more parallel to the imaginary axis with an increase in activating-KOH concentration, which signifies progressively lower ion diffusion resistances (**Figure 2.10b**). The charge transfer resistance (R_{ct}) values are estimated to be 1.80 ohms, 0.30 ohms, 0.24 ohms, and 0.20 ohms for JG@CC, AJG@CC-1M, AJG@CC-3M, and AJG@CC-6M, respectively. The lower R_{ct} and diffusion resistance mean the sample activated with 6M KOH has the highest porosity, as evident from the FETEM images (**Figure 2.3**, **2.11**, and **2.12**). The inter-sheet macro-porosity and in-plane nano-porosity help the electrolyte ions access more surface area to display high capacitance. From the analysis, the sample synthesized with 20 cycles (of 100 ms duration) of pulsed Joule heating and 6M KOH concentration was the best-performing one and was used for further device fabrications.

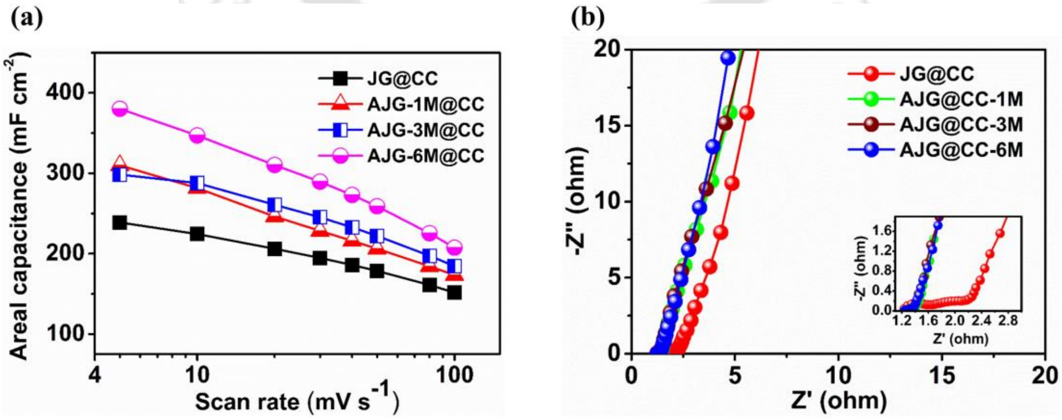

Figure 2.10: (a) variation of areal capacitance of as-prepared symmetric supercapacitors with a variation of activating KOH concentration. (b) corresponding EIS spectra.

The non-activated Joule heated sample JG@CC shows no contribution of functional groups, as is evident from the nearly rectangular CV shape and CD's triangular profile (Fig. 4b and c). On the other hand, the CV profiles of AJG@CC at different scan rates maintain a nearly rectangular shape with an initial hump (Fig. 4d). The quasi-rectangular Nature of the curves signifies that the charge storage mechanism is mainly an electrical double layer (EDLC) type, and the initial hump is associated with the faradic process coming from carboxylic functional groups of AJG@CC.[57–59] In constant current charge-discharge (CD) curves (Fig. 4b), the EDLC mechanism results in its triangular shape, a deviation from the perfect triangular behavior of CD curves of AJG@CC signifies the faradic contribution coming from its functional groups. The areal capacitance of the device (AJG@CC-6M) estimated in a two-electrode configuration (symmetric supercapacitor device (SC)) is 380.2 mF cm^{-2} at 5 mV s^{-1}, which is very high compared to the JG@CC SC device (238.8 mF cm^{-2} at 5 mV s^{-1}).

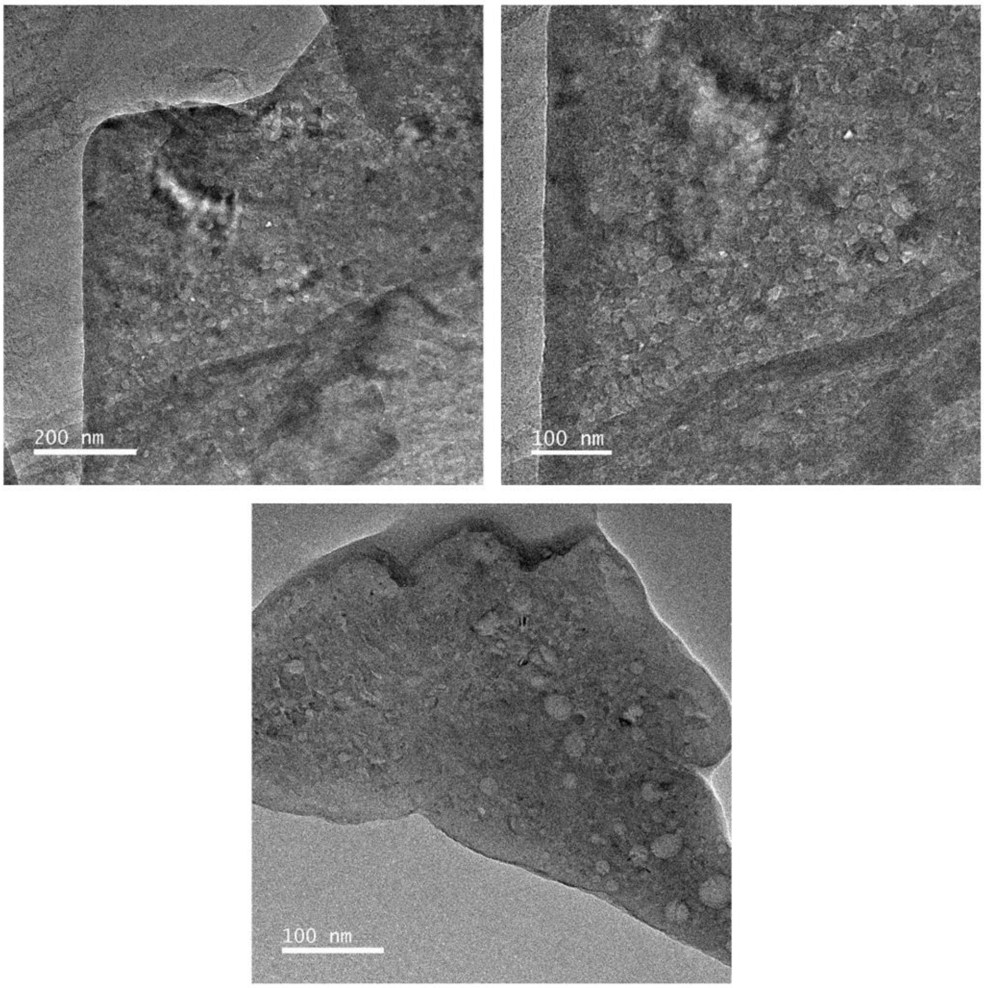

Figure 2.11: FETEM images of AJG, activated with 1M KOH and 20 TJH cycles (20p) at different magnifications.

The areal energy and power densities estimated from the CV curves have been presented through the Ragone plots (**Figure 2.9e**). The plots show that the maximum energy density of the AJG@CC SC device is 52.8 µWh cm^{-2} at a power density of 950.5 µW cm^{-2}, nearly 1.6 times higher than that of the non-activated sample (JG@CC) (33.2 µWh cm^{-2} at 597.1 µW cm^{-2}). Even at a high power density of 10368 µW cm^{-2}, AJG@CC maintains a very high energy density value of 28.8 µWh cm^{-2}. These energy density values are much higher than most of the purely graphene-based supercapacitor devices reported to date (**Table 2.4**). These results suggest that ultrafast electro-activation effectively improves energy and power density, which is critical for a supercapacitor device. The cycling stability test of the symmetric supercapacitor device was carried out for the 10000 charge-discharge cycles at a constant current density of 20 mA cm^{-2} (**Figure 2.9f**). After 10000 cycles, the device showed excellent capacity retention of 92%, which suggests that the AJG@CC has a very long life span while being used as an electrode of a supercapacitor device.

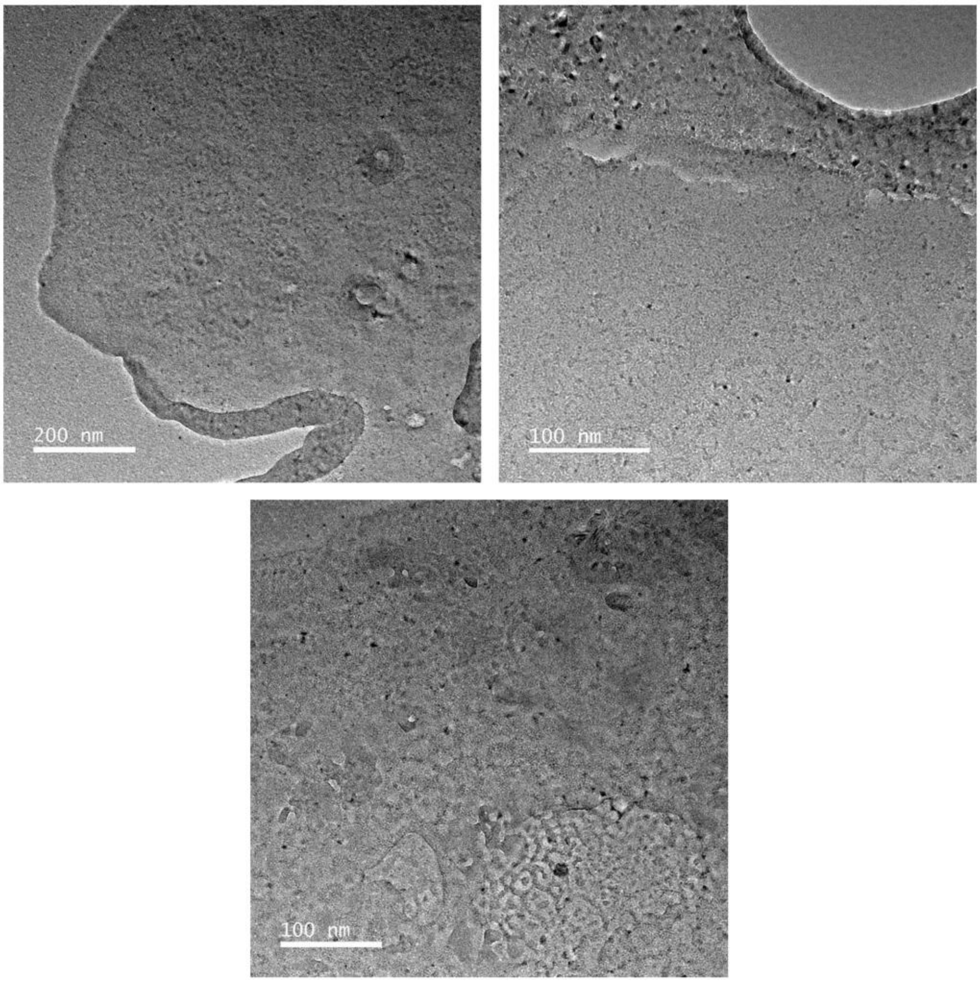

Figure 2.12: Low and High magnified FETEM images of AJG, activated with 3M KOH and 20 TJH cycles (20p).

The final goal of this work is to design high-energy density wearable supercapacitors using the ready-to-use high-performance electrodes obtained through the Joule heating modification approach. We have already received the symmetric device's high specific capacitance and energy density using the unique electro-activation method. A suitable asymmetric supercapacitor design strategy has been adopted to increase the energy density and the operational potential window. An asymmetric supercapacitor (ASC) device consists of two different types of electrodes. One operates in the negative potential window, and the other operates in the positive. Here, AJG@CC was chosen as the positive electrode for the fabrication of ASC. As a potential negative electrode, we have introduced Ti_3C_2-MXene, another 2D material like graphene, which can operate in a negative potential window from -0.7 V to +0.3 V, possesses metallic conductivity and high pseudocapacitance and is stable in the aqueous H_2SO_4 electrolyte.[45,60] Hence, CC coated with MXene (MXene@CC) was used as the negative electrode of the ASC.

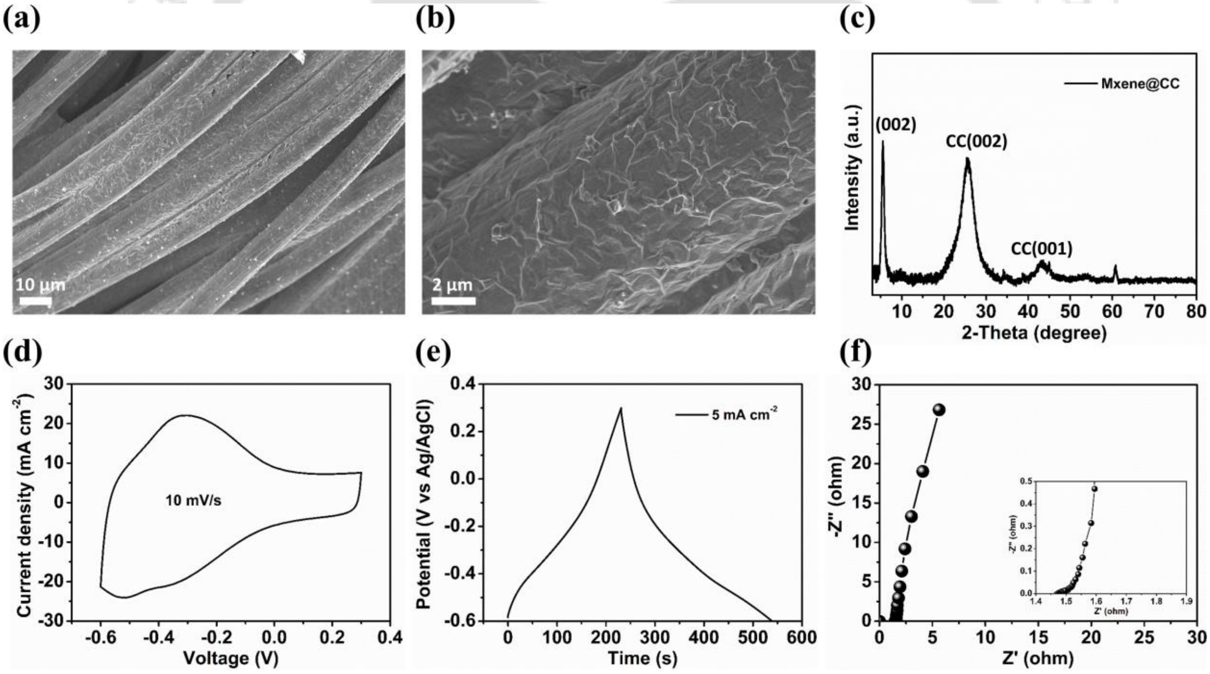

Figure 2.13: Characterization of the negative electrode MXene@CC in 1M H_2SO_4 electrolyte with 3-electrode configuration. (a) low, and (b) high magnified FESEM images of MXene@CC. (c) XRD pattern of MXene@CC, (d) cyclic voltammogram (CV) at 10 mV s^{-1}, (e) GCD profile for constant current 5 mA cm^{-2}, and (f) EIS of MXene@CC electrode.

Before constructing the solid-state wearable asymmetric device, the performance of the MXene-based negative electrode was measured in an aqueous electrolyte, and processing was optimized. The MXene-based flexible negative electrode (MXene@CC) was obtained by coating a carbon cloth with MXene through a simple dip-and-dry technique (Materials and methods). FESEM images and XRD pattern of the as-prepared MXene@CC electrode have been shown in **Figure 2.13a**, **b**, and **c**. The XRD peak at around 5.8° represents the (002) plane of the Mxene sheets. The CV, GCD profiles, and EIS spectra of MXene@CC in a three-electrode configuration have been presented in **Figure 2.13d**, **e**, and **f**, respectively. In its CV profile, prominent pseudocapacitance peaks are superimposed over the rectangular CV profile. The area-normalized capacitance of the MXene@CC electrode was estimated to be 1100.1 mF cm^{-2} at 10 mV s^{-1}.

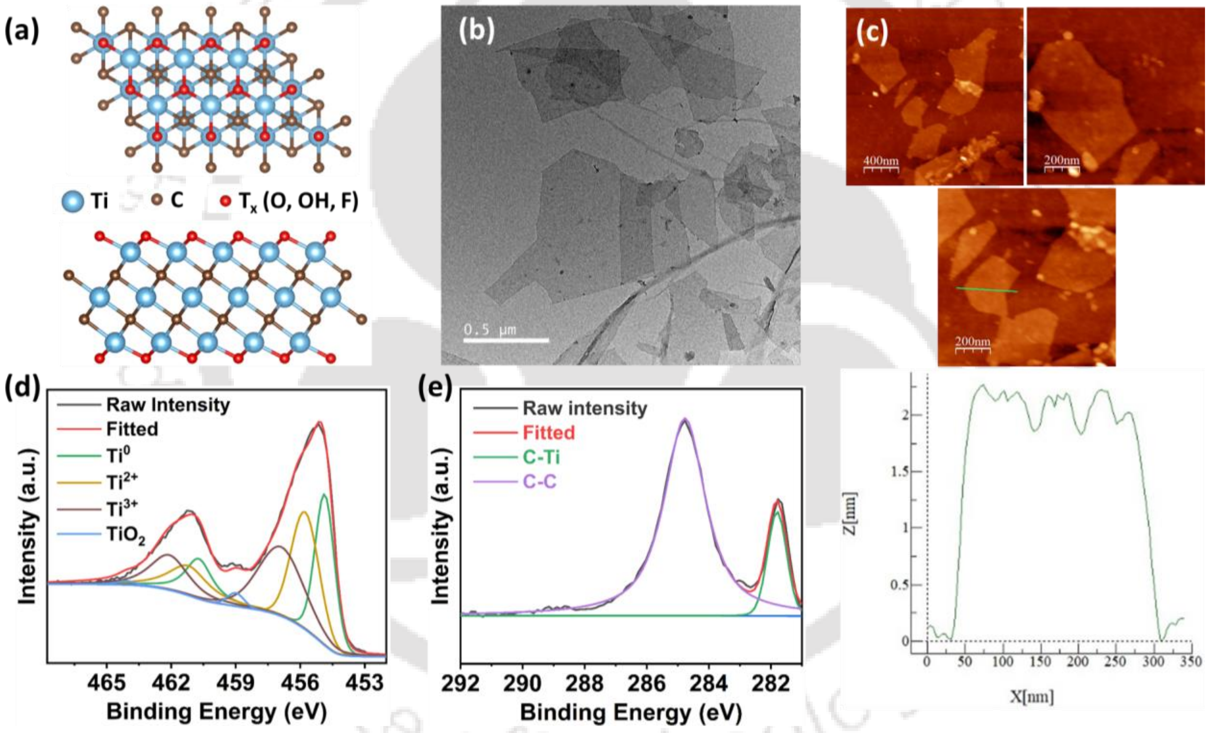

Figure 2.14: (a) Schematic illustration of MXene ($Ti_3C_2T_x$) 2D sheets. (b) FETEM image and (c) AFM image and height profile of MXene 2D sheets used to construct the MXene@CC negative electrode. High-resolution XPS spectra of (d) Ti 2p, (e) C 1s.

Figure 2.14a shows the schematic of top and side views of MXene ($Ti_3C_2T_x$) nanosheets. Further structural and morphological investigations of the MXene 2D nanosheets used to construct negative electrodes (MXene@CC) were carried out by FETEM and AFM analysis. From the FETEM image, the MXene nanosheets' size was estimated to range from 200 nm to

800 nm (**Figure 2.14b**). The AFM images and the corresponding height profile are shown in **Figure 2.14c**. From the height profile, the thickness of the MXene nanosheet was estimated to be around 2 nm, which signifies that the sheets are exfoliated to monolayers.[61] An XPS analysis was performed to investigate the chemical compositions and the nature of the functional group present in Mxene used to construct the MXene@CC electrode. The high-resolution XPS spectra of Ti 2p (**Figure 2.14d**) consist of prominent peaks of $2p_{3/2}(2p_{1/2})$ at around 455.0 eV(461.0 eV), 455.8 eV(461.3 eV) and 457.1 eV(462.4 eV) corresponding to Ti^0, Ti^{2+}, Ti^{3+}, respectively and faint peaks at around 458.9 eV(464.1 eV) corresponding to TiO_2.[62] This result suggests that most species are Ti0, Ti2+, and Ti^{3+} (Ti atoms), and almost negligible oxidation of Ti happened during MXene synthesis. The C 1s spectra (**Figure 2.14e**) consist of two prominent peaks at around 281.8 eV and 284.8 eV, corresponding to C-Ti and C-C, respectively.

The asymmetric supercapacitor device exhibits an extended operation potential window of 1.6 V, which takes advantage of stability windows of positive AJG@CC and negative MXene@CC electrodes, as is shown in **Figure 2.15a**. A Solid-state wearable asymmetric supercapacitor device was developed using PVA/H_2SO_4 as gel electrolytes, which was expected to be a promising flexible energy storage device for wearable electronics.

To test the operationality of ASC at any potential window from 0 to 1.6 V, CV curves at 10 mV s^{-1} and GCD profiles at a constant current density of 5 mA cm^{-2} were obtained for different voltage windows, as shown in **Figure 2.15b** and **c**. It is worth noting that the ASC could operate at any voltage window ranging from 1 V to 1.6 V. Similar CV and GCD shapes were observed in the voltage range of 1 to 1.6 V.

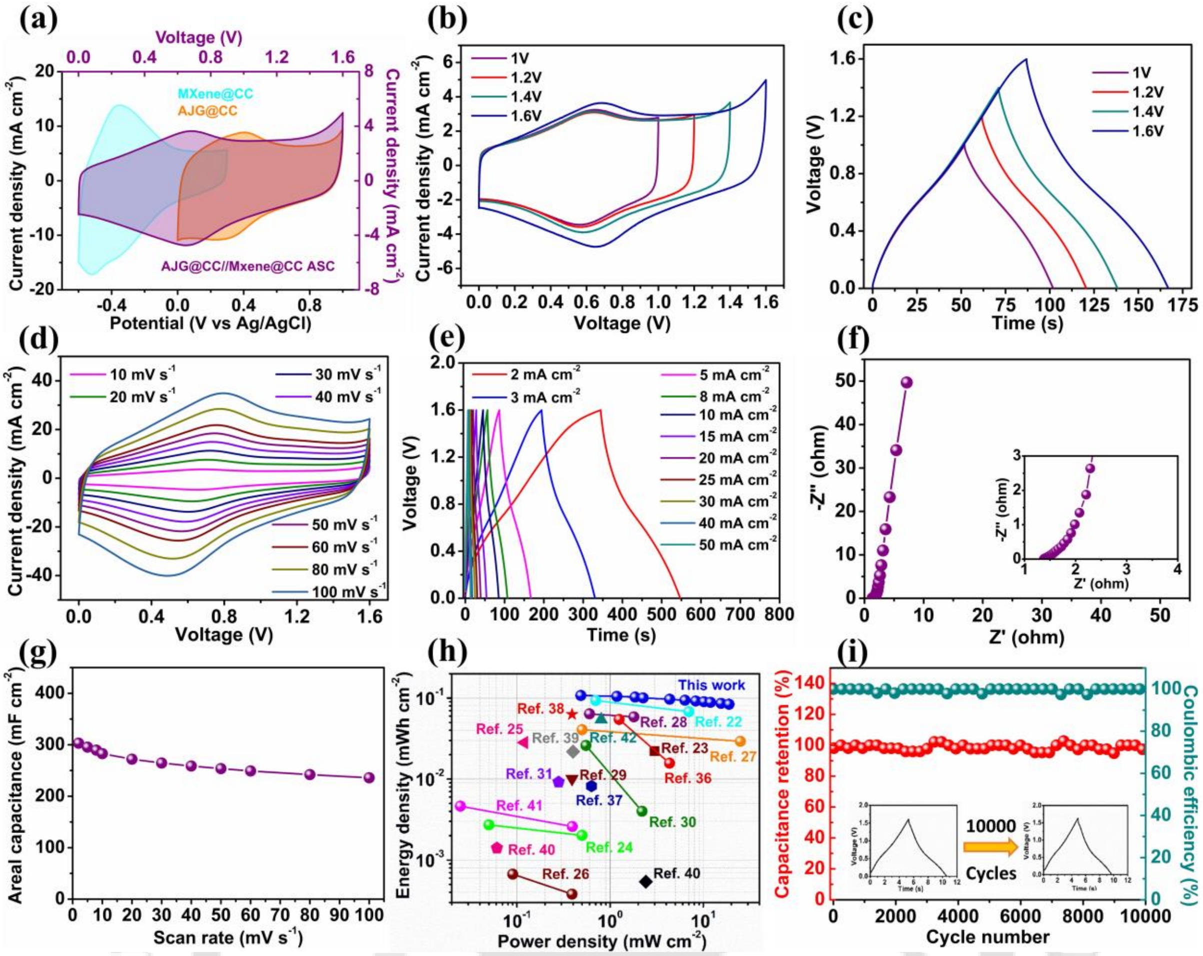

Figure 2.15: Electrochemical performances of AJG@CC//MXene@CC asymmetric supercapacitor device. (a) CV curves of MXene@CC, AJG@CC electrodes, and assembled asymmetric solid-state Supercapacitor (ASC) at 10 mV s^{-1}. (b) CV curves of ASC measured over operating voltage windows from 1 to 1.6 V at 10 mV s^{-1}. (c) GCD curves for different voltage windows at a current density of 5 mA cm^{-2}. (d) CV curves at different scan rates with a voltage window of 1.6 V. (e) GCD curves for various current densities. (f) Nyquist plot of ASC. The inset shows a magnified version of the high-frequency region. (g) The areal capacitance of ASC at scan rates varying from 2 to 100 mV s^{-1}. (h) Ragone plot of ASC compared to other state-of-the-art asymmetric supercapacitors. (i) Cycling stability of the asymmetric device at 50 mA cm^{-2}; inset: GCD curves for first and last cycles of cycling stability test.

The CV shapes of the ASC from scan rate 10 to 100 mV s^{-1} maintain their original shape even at the higher scan rates (**Figure 2.15d**), suggesting rapid charge transfer kinetics and easy ion transport between positive and negative electrodes. The GCD profiles obtained for constant current densities ranging from 2 to 50 mA cm^{-2} also showed almost symmetric shapes with a slight deviation from the ideal triangular shape due to pseudocapacitive nature, indicating good reversibility (**Figure 2.15e**). **Figure 2.15f** depicts the EIS spectra of the ASC has a small semicircle (R_{ct}) in the high-frequency region and an almost vertical slope in the low-frequency region, suggesting fast charge transfer and ion diffusion between the electrodes. The ASC has a maximum areal capacitance of 303.1 mF cm^{-2} at a scan rate of 2 mV s^{-1}. The rate performance of ASC was obtained for scan rates ranging from 2 to 100 mV s^{-1}. It exhibited a maximum areal capacitance of 235.92 mF cm^{-2} at a high scan rate of 100 mV s^{-1} with an excellent capacity retention of 77% (**Figure 2.15g**), which is superior to most state-of-the-art asymmetric supercapacitors (**Table 2.4**).

Furthermore, the ASC can deliver a maximum energy density of 107.77 µWh cm^{-2} at a power density of 485 µW cm^{-2}. The value of the areal energy density of ASC was more than two times the areal energy density of the symmetric device. Even at a high power density of 4404.54 µW cm^{-2}, it maintains an energy density of 83.88 µWh cm^{-2}. Moreover, the ASC exhibited superior energy and power density compared to the other state-of-the-art graphene//MXene flexible solid-state textile ASC, as shown in **Figure 2.15h** and **Table 2.2**. The as-prepared ASC exhibited excellent electrochemical stability; after 10000 cycles of charge-discharge at a constant current density of 50 mA cm^{-2}, it was able to retain 94% of its initial capacitance with 100 % coulombic efficiency retention (**Figure 2.15i**). Thus, the ASC we have designed has a long life span.

Table 2.4: Comparison table for the electrochemical performance of textile-based flexible and wearable solid-state symmetric/asymmetric devices.

Devices	Voltage window (V)	Test condition	Areal capacitance (mF cm^{-2})	Maximum Energy density (areal) (µWh cm^{-2})	Maximum Power density (areal) (µW cm^{-2})	Ref
$NiCo_2S_4$@CC // Fe_2O_3@CC	1.4	1 mA cm^{-2}	343.2	93.43	700.7	[2]

		5 mA cm^{-2}	250.1	68	7000	
$Ti_3C_2T_x$@NiCoAl-LDH-Ag // AC	1.5	0.25 mA cm^{-2} 1 mA cm^{-2} 4 mA cm^{-2}	71 55 17	22.18	3000	[3]
$Ti_3C_2T_x$-PANI@CNTs	1	0.1 mA cm^{-2} 1 mA cm^{-2}	78.2 58.08	2.72 2.02	50 500	[4]
CWF/PANI/rGO	1	1 mA cm^{-2} 20 mA cm^{-2}	197.6 119.2	28.21	120	[5]
PET@MXene	0.6	5 mV s^{-1} 100 mV s^{-1}	18.39 6.85	0.38 0.67	390 90	[6]
Graphene/nanotube/PANI	0.8	0.1 mA cm^{-2} 0.7 mA cm^{-2}	164 122	9.196	280	[7]
PPy-rGO//PPy-rGO	1.2	1 mA cm^{-2} 20 mA cm^{-2}	320 264	63.9 58.58	600 1800	[8]
		1 mA cm^{-2}	118			

CWM//CWM		20 mA cm^{-2}	92.28	10.1	389.9	[9]
CNF@Fe$_2$O$_3$ // CNF@MnO$_2$	2	0.55 mA cm^{-2}	46.97	26	550	[10]
				4	2200	
PPy/MXene/PMFF	0.8	1 mA cm^{-2}	458	40.7	500	[11]
		50 mA cm^{-2}	328	29.2	25000	
MXene-graphene YSC	0.8	5 mV s^{-1}	367.3	54.5	1251.5	[12]
		100 mV s^{-1}	137.46	15.7	4335.9	
rGO/MXene LBL@CC	1.2	0.02 mA cm^{-2}	40.8			[13]
		0.7 mA cm^{-2}		8.2	630.1	
			10.5			
G/PANI@HF	0.8	1 mA cm^{-2}	707.9	62.92	390	[14]
G/PHSC		1 mA cm^{-2}	245.5	21.82	400	[15]
		5 mV s^{-1}	335.4			

		200 mV s^{-1}	92.4			
CNT-rGO@F	0.8	0.1 mA cm^{-2}	10.13	1.41	61	[16]
MWCNT/rGO @PEDOT-PSS@textile	1	0.025 mA cm^{-2} 2 mA cm^{-2}	30.4 20.2	4.63 2.6	24.7 393.5	[17]
V_2O_5 NWs@MWCNT // VN@MWCNT	1.6	1 mA cm^{-2} 16 mA cm^{-2}	152.7 116	54.3	801.4	[18]
rGO-Ni-Yarn	0.8	10 mV s^{-1} 1000 mV s^{-1} 1 mA cm^{-2} 10 mA cm^{-2}	72.1 24.4 49.4 27.7	1.60 0.54	2420	[19]
AJG@CC // AJG@CC	1	5 mV s^{-1} 50 mV s^{-1}	380.2 258.87	52.8 28.8	950.5 10368	This Work

SC						
AJG@CC // MXene@CC ASC	1.6	2 mV s^{-1} 100 mV s^{-1}	303.1 235.92	107.77 83.88	485 18873	This Work

To bring the ASC into the practical application of power supply for wearable electronics, the ASC should deliver excellent and stable energy storage performance during extreme bending conditions. **Figure 2.16a** shows the digital photographs of MXene@CC//AJG@CC ASC at different bending angles of 45°, 90°, and 180°, confirming the device's robustness and great flexibility.

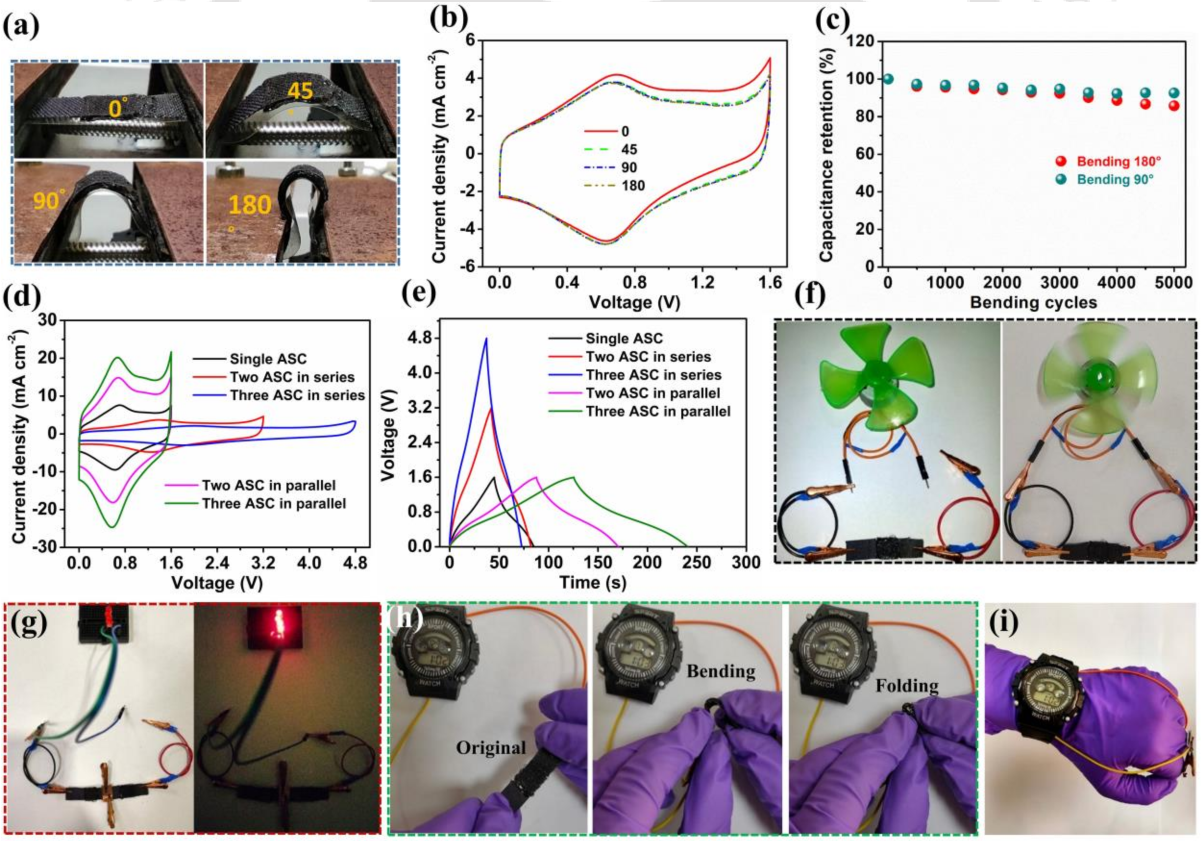

Figure 2.16: (a) Digital photographs of flexible solid-state ASC bent at different angles. (b) CV curves of ASC under various bending conditions at 10 mV s^{-1}. (c) Bending stability test for 5000 continuously repeated bending cycles at 90° and 180 ° angles. (d) CV, (e) GCD curves

of single ASC and two and three ASC connected in series and parallel, respectively. Digital photographs of (f) a single ASC (1 × 1 cm^2) driving a fan, (g) two ASCs connected in series powering four red LED lights, and (h) one ASC operating a digital watch at different deformed states. (i) wearable exhibition of ASC as a flexible energy storage device.

The CV curves recorded for different bending angles are shown in **Figure 2.16b**, which depict almost no change in shapes and areas after extreme bending, indicating no influence on supercapacitor performance. After 5000 cycles of bending at the angles of 90° and 180°, the ASC retained almost 90 % capacity, suggesting the outstanding durability of the device (**Figure 2.16c**). Furthermore, two and three devices can be connected in series or parallel combinations to achieve desirable voltage windows (e.g., 3.2 V and 4.8 V) and currents, as depicted in CV and GCD profiles in **Figure 2.16d**, **e**, respectively. Owing to the low resistance of ASCs, the shapes of the CV curves of series-connected devices are well maintained. **Figure 2.16f** and **g** are the digital photographs of an ASC powering an electronic fan to its full speed and two ASCs in series powering four red LEDs to glow with maximum brightness, respectively. As a practical application, the ASC can supply power to an electronic wristwatch even in repeated bending conditions (**Figure 2.16h**). **Figure 2.16i** shows the wearable exhibition of our ASC powering the wristwatch. With all the valuable features in mind, MXene@CC//AJG@CC ASC can be a reliable power supply for ever-growing wearable electronics.

2.4. Conclusion

In summary, we have, for the first time, demonstrated on-site electro-reduction and electro-activation of graphene through milli-second scale current pulses. Compact graphene oxide film over carbon cloth (CC) turns into a macroporous graphene structure after a single current pulse of 50 ms duration. In contrast, basal plane nanopores were incorporated through KOH activation by passing successive ultra-short (100 ms) current pulses. The optimized activation incorporates uniform nanopores of an average diameter of 6 nm while introducing some additional pseudocapacitive oxidative functional groups during the activation. Compared to the conventional thermal and chemical strategy to engineer graphene surfaces, this electro-activation process is straightforward, requires a very low thermal budget, and gives rise to ready-to-use electrodes. On behalf of a binder-free multimodal porous structure together with contributions of pseudocapacitive groups, such electro-activated graphene-based symmetric device showed high areal capacitance and energy density of 380.2 mF/cm^2 and 52.8 µWh $cm^{-2,}$ respectively, which are much higher as compared to non-electro-activated counterpart (33.2 µWh cm^{-2}). Wearable solid-state asymmetric supercapacitors were realized using as-developed electro-activated graphene as the positive electrode and a suitable MXene-based negative electrode, which displays excellent performance metrics with high durability. The CC textile integrated wearable asymmetric device exhibits an operation potential window of 1.6V and a high areal energy density of 107.77 μWh cm^{-2} at a power density of 485 μW cm^{-2}, and it still maintains a high value of 83.88 μWh cm^{-2} at a very high areal power density of 4404.54 μW cm^{-2}. The wearable device exhibits excellent operational durability under repeated folding and bending over 5000 cycles and superb stability over 10000 charge-discharge cycles. The performance of the wearable devices was demonstrated in practical applications by operating small electronics, in which their performance remained unaltered by repeated bending of the as-developed wearable asymmetric energy storage device.

References

[1] S. Murali, J. R. Potts, S. Stoller, J. Park, M. D. Stoller, L. L. Zhang, Y. Zhu, R. S. Ruoff, *Carbon N. Y.* **2012**, *50*, 3482.

[2] L. L. Zhang, X. Zhao, M. D. Stoller, Y. Zhu, H. Ji, S. Murali, Y. Wu, S. Perales, B. Clevenger, R. S. Ruoff, *Nano Lett.* **2012**, *12*, 1806.

[3] Z. Fan, Q. Zhao, T. Li, J. Yan, Y. Ren, J. Feng, T. Wei, *Carbon N. Y.* **2012**, *50*, 1699.

[4] Y. Li, Z. Li, P. K. Shen, *Adv. Mater.* **2013**, *25*, 2474.

[5] H. G. Kang, J. M. Jeong, S. B. Hong, G. Y. Lee, D. H. Kim, J. W. Kim, B. G. Choi, *J. Alloys Compd.* **2019**, *770*, 458.

[6] H. Li, Y. Tao, X. Zheng, Z. Li, D. Liu, Z. Xu, C. Luo, J. Luo, F. Kang, Q. H. Yang, *Nanoscale* **2015**, *7*, 18459.

[7] H. Park, R. B. Ambade, S. H. Noh, W. Eom, K. H. Koh, S. B. Ambade, W. J. Lee, S. H. Kim, T. H. Han, *ACS Appl. Mater. Interfaces* **2019**, *11*, 9011.

[8] X. Yu, Y. Kang, H. S. Park, *Carbon N. Y.* **2016**, *101*, 49.

[9] J. Wang, S. Kaskel, *J. Mater. Chem.* **2012**, *22*, 23710.

[10] Z. Pan, H. Zhi, Y. Qiu, J. Yang, L. Xing, Q. Zhang, X. Ding, X. Wang, G. Xu, H. Yuan, M. Chen, W. Li, Y. Yao, N. Motta, M. Liu, Y. Zhang, *Nano Energy* **2018**, *46*, 266.

[11] Y. Zhu, S. Murali, M. D. Stoller, K. J. Ganesh, W. Cai, P. J. Ferreira, A. Pirkle, R. M. Wallace, K. A. Cychosz, M. Thommes, D. Su, E. A. Stach, R. S. Ruoff, *Science (80-.).* **2011**, *332*, 1537.

[12] W. Y. Tsai, R. Lin, S. Murali, L. Li Zhang, J. K. McDonough, R. S. Ruoff, P. L. Taberna, Y. Gogotsi, P. Simon, *Nano Energy* **2013**, *2*, 403.

[13] T. Kim, G. Jung, S. Yoo, K. S. Suh, R. S. Ruoff, *ACS Nano* **2013**, *7*, 6899.

[14] J. Ji, J. Liu, L. Lai, X. Zhao, Y. Zhen, J. Lin, Y. Zhu, H. Ji, L. L. Zhang, R. S. Ruoff,

ACS Nano **2015**, *9*, 8609.

[15] M. D. Stoller, S. Murali, N. Quarles, Y. Zhu, J. R. Potts, X. Zhu, H. W. Ha, R. S. Ruoff, *Phys. Chem. Chem. Phys.* **2012**, *14*, 3388.

[16] J. Huang, J. Wang, C. Wang, H. Zhang, C. Lu, J. Wang, *Chem. Mater.* **2015**, *27*, 2107.

[17] X. Ning, W. Zhong, S. Li, Y. Wang, W. Yang, *J. Mater. Chem. A* **2014**, *2*, 8859.

[18] H. Liu, Y. Xie, J. Liu, K. sik Moon, L. Lu, Z. Lin, W. Yuan, C. Shen, X. Zang, L. Lin, Y. Tang, C. P. Wong, *Chem. Eng. J.* **2020**, *393*, 124672.

[19] T. Odedairo, J. Ma, Y. Gu, W. Zhou, J. Jin, X. S. Zhao, Z. Zhu, *Nanotechnology* **2014**, *25*, DOI 10.1088/0957-4484/25/49/495604.

[20] L. Sun, C. Tian, M. Li, X. Meng, L. Wang, R. Wang, J. Yin, H. Fu, *J. Mater. Chem. A* **2013**, *1*, 6462.

[21] K. Xia, Q. Li, L. Zheng, K. You, X. Tian, B. Han, Q. Gao, Z. Huang, G. Chen, C. Zhou, *Microporous Mesoporous Mater.* **2017**, *237*, 228.

[22] X. Liang, H. He, X. Yang, W. Lü, L. Wang, X. Li, *J. Energy Storage* **2021**, *42*, 103105.

[23] C. Zhang, R. Guo, H. Wang, X. Xie, C. Du, *Appl. Surf. Sci.* **2022**, *598*, 153796.

[24] Q. Wang, Y. Fang, M. Cao, *Ceram. Int.* **2022**, *48*, 21976.

[25] Y. Lin, H. Zhang, W. Deng, D. Zhang, N. Li, Q. Wu, C. He, *J. Power Sources* **2018**, *384*, 278.

[26] W. Shao, M. Tebyetekerwa, I. Marriam, W. Li, Y. Wu, S. Peng, S. Ramakrishna, S. Yang, M. Zhu, *J. Power Sources* **2018**, *396*, 683.

[27] K. Liu, Y. Yao, T. Lv, H. Li, N. Li, Z. Chen, G. Qian, T. Chen, *J. Power Sources* **2020**, *446*, 227355.

[28] X. Zhang, Y. Chen, J. Yan, K. Zhu, M. Zhang, K. Ye, G. Wang, L. Zhou, K. Cheng, D. Cao, *Chem. Eng. J.* **2020**, *388*, DOI 10.1016/j.cej.2020.124197.

[29] W. Chen, M. Luo, K. Yang, C. Liu, D. Zhang, X. Zhou, *Chem. Eng. J.* **2021**, *423*, 130242.

[30] Y. Yan, J. Yan, X. Gong, X. Tang, X. Xu, T. Meng, F. Bu, D. Cai, Z. Zhang, G. Nie, H. Zhang, *Chem. Eng. J.* **2022**, *433*, 133580.

[31] X. Li, J. Hao, R. Liu, H. He, Y. Wang, G. Liang, Y. Liu, G. Yuan, Z. Guo, *Energy Storage Mater.* **2020**, *33*, 62.

[32] Y. Wang, X. Wang, X. Li, X. Li, Y. Liu, Y. Bai, H. Xiao, G. Yuan, *Adv. Funct. Mater.* **2021**, *31*, 1.

[33] D. X. Luong, K. V. Bets, W. A. Algozeeb, M. G. Stanford, C. Kittrell, W. Chen, R. V. Salvatierra, M. Ren, E. A. McHugh, P. A. Advincula, Z. Wang, M. Bhatt, H. Guo, V. Mancevski, R. Shahsavari, B. I. Yakobson, J. M. Tour, *Nature* **2020**, *577*, 647.

[34] Y. Liu, P. Li, F. Wang, W. Fang, Z. Xu, W. Gao, C. Gao, *Carbon N. Y.* **2019**, *155*, 462.

[35] C. Li, X. Zhang, K. Wang, X. Sun, G. Liu, J. Li, H. Tian, J. Li, Y. Ma, *Adv. Mater.* **2017**, *29*, 1.

[36] N. He, J. Liao, F. Zhao, W. Gao, *ACS Appl. Mater. Interfaces* **2020**, *12*, 15211.

[37] J. Yun, I. Echols, P. Flouda, Y. Chen, S. Wang, X. Zhao, D. Holta, M. Radovic, M. J. Green, M. Naraghi, J. L. Lutkenhaus, *ACS Appl. Mater. Interfaces* **2021**, *13*, 14068.

[38] Z. Li, M. Li, Q. Fan, X. Qi, L. Qu, M. Tian, *ACS Appl. Mater. Interfaces* **2021**, *13*, 14778.

[39] Z. Li, Y. Ma, L. Wang, X. Du, S. Zhu, X. Zhang, L. Qu, M. Tian, *ACS Appl. Mater. Interfaces* **2019**, *11*, 46278.

[40] S. H. Kang, G. Y. Lee, J. Lim, S. O. Kim, *ACS Omega* **2021**, *6*, 19578.

[41] H. Lee, G. Jung, K. Keum, J. W. Kim, H. Jeong, Y. H. Lee, D. S. Kim, J. S. Ha, *Adv. Funct. Mater.* **2021**, *31*, 1.

[42] J. Zhao, H. Lu, Y. Zhang, S. Yu, O. I. Malyi, X. Zhao, L. Wang, H. Wang, J. Peng, X. Li, Y. Zhang, S. Chen, H. Pan, G. Xing, C. Lu, Y. Tang, X. Chen, *Sci. Adv.* **2021**, *7*, 1.

[43] X. Pu, L. Li, M. Liu, C. Jiang, C. Du, Z. Zhao, W. Hu, Z. L. Wang, *Adv. Mater.* **2016**, *28*, 98.

[44] M. Alhabeb, K. Maleski, B. Anasori, P. Lelyukh, L. Clark, S. Sin, Y. Gogotsi, *Chem. Mater.* **2017**, *29*, 7633.

[45] P. Dutta, A. Patra, S. K. Deb, A. Sikdar, A. Majumdar, G. M. Karim, U. N. Maiti, *J. Mater. Chem. A* **2021**, *9*, 25013.

[46] A. Sikdar, A. Majumdar, P. Dutta, M. Borah, S. O. Kim, U. N. Maiti, *Electrochim. Acta* **2020**, *332*, 135492.

[47] U. N. Maiti, J. Lim, K. E. Lee, W. J. Lee, S. O. Kim, *Adv. Mater.* **2014**, *26*, 615.

[48] P. Dutta, A. Sikdar, A. Majumdar, M. Borah, N. Padma, S. Ghosh, U. N. Maiti, *Carbon N. Y.* **2020**, *169*, 225.

[49] A. Sikdar, P. Dutta, S. K. Deb, A. Majumdar, N. Padma, S. Ghosh, U. N. Maiti, *Electrochim. Acta* **2021**, *391*, 138959.

[50] Y. Wen, H. Chen, M. Wu, C. Li, *Adv. Funct. Mater.* **2022**, *32*, DOI 10.1002/adfm.202111613.

[51] L. Chen, C. Batchelor-McAuley, B. Rasche, C. Johnston, N. Hindle, R. G. Compton, *Appl. Mater. Today* **2020**, *18*, 100506.

[52] Y. Zhu, S. Murali, M. D. Stoller, K. J. Ganesh, W. Cai, P. J. Ferreira, A. Pirkle, R. M. Wallace, K. A. Cychosz, M. Thommes, D. Su, E. A. Stach, R. S. Ruoff, **2011**, *332*, 1537.

[53] A. Lerf, H. He, M. Forster, J. Klinowski, *J. Phys. Chem. B* **1998**, *102*, 4477.

[54] D. R. Dreyer, S. Park, C. W. Bielawski, R. S. Ruoff, *Chem. Soc. Rev.* **2009**, *39*, 228.

[55] K. Krishnamoorthy, M. Veerapandian, K. Yun, S. J. Kim, *Carbon N. Y.* **2013**, *53*, 38.

[56] M. J. McAllister, J. L. Li, D. H. Adamson, H. C. Schniepp, A. A. Abdala, J. Liu, M.

Herrera-Alonso, D. L. Milius, R. Car, R. K. Prud'homme, I. A. Aksay, *Chem. Mater.* **2007**, *19*, 4396.

[57] Q. Wang, H. Gao, C. Zhao, H. X. Yue, G. Gao, J. Yu, Y. U. Kwon, Y. Zhao, *Electrochim. Acta* **2021**, *369*, DOI 10.1016/j.electacta.2020.137700.

[58] A. Bagri, C. Mattevi, M. Acik, Y. J. Chabal, M. Chhowalla, V. B. Shenoy, *Nat. Chem.* **2010**, *2*, 581.

[59] S. Kerisit, B. Schwenzer, M. Vijayakumar, *J. Phys. Chem. Lett.* **2014**, *5*, 2330.

[60] P. Dutta, S. K. Deb, A. Patra, A. Majumdar, G. M. Karim, C. K. Parashar, M. K. Mohanta, M. Qureshi, U. N. Maiti, *Adv. Funct. Mater.* **2022**, DOI 10.1002/adfm.202204622.

[61] A. VahidMohammadi, M. Mojtabavi, N. Mai Caffrey, M. Wanunu, M. Beidaghi, A. VahidMohammadi, M. Beidaghi, M. Mojtabavi, M. Wanunu, N. M. Caffrey, *Adv. Mater.* **2019**, *31*, 1806931.

[62] J. Halim, K. M. Cook, M. Naguib, P. Eklund, Y. Gogotsi, J. Rosen, M. W. Barsoum, *Appl. Surf. Sci.* **2016**, *362*, 406.

Chapter 3

Current-pulse-programmed manipulation and perforation of MOF-derived graphitic carbon hierarchy for high areal-energy-density supercapacitors

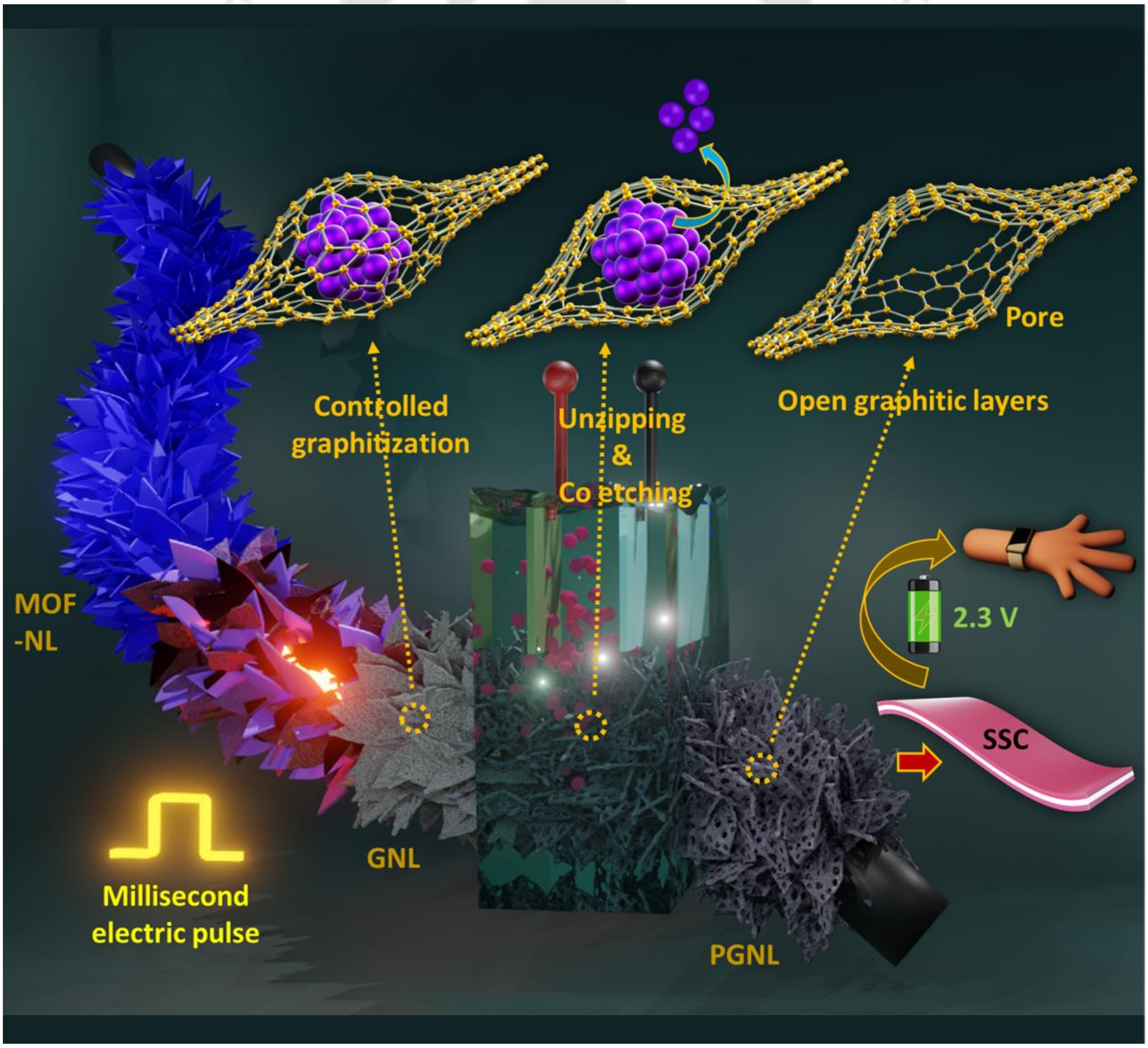

Current-pulse-programmed manipulation and perforation of MOF-derived graphitic carbon hierarchy for high areal-energy-density supercapacitors

Precise manipulation of graphitic order in carbon nanostructures and derived materials can be a key strategy to avail their full potential in multifunctional applications; however, it is incredibly challenging to implement on a practical scale. Here, we report a unique ultrafast pulsed Joule heating (PJH) strategy for the development of graphitization tunable carbon nanoleaves (GNL) from the metal-organic framework (MOF) and PJH-programmed precise recovery of graphitic order of GNL after it undergoes pore-forming surface oxidation. A unique electrochemical perforation (ECP) strategy is employed to unlock and remove the PJH-generated size-controlled metal nanoparticles from graphitization tunable GNL. The intrinsic high conductivity of GNL, its increment of surface area through ECP, and conductivity recovery by programmed PJH are highly effective in getting optimized energy storage performance in supercapacitor devices. As-modified GNLs exhibit an areal capacitance as high as 290.7 mF cm^{-2} in aqueous electrolytes, which is 434% higher than that of pristine GNLs. The high conductivity and open porosity greatly benefitted the performance of water-in-salt electrolyte supercapacitors to deliver very high energy density (127.5 µWh cm^{-2}), much higher than GNLs. These ready-to-use binder-free electrodes also show very stable and excellent performance in wearable asymmetric supercapacitor devices.

3.1. Introduction

Electronic and surface modifications of carbon-based nanomaterials (CN) have been the key to their success in various practical applications, namely energy storage, catalysis, gas absorption, sensing, etc.[1–5] In particular, tuning electronic conductivity and controlled incorporation of porosity in CN are well-known strategies for designing electrodes for energy storage in electrochemical supercapacitor devices.[6–8] To impart high electronic conductivity in CN, its graphitization level must be increased, enhancing its conductivity by increasing the concentration of highly mobile delocalized pi-electrons.[9,10] On the other hand, surface functionalization and controlled incorporation of porosity in carbon can increase the intrinsic electrochemical charge storage capacity; however, such surface modifications decrease the conductivity and sacrifice energy storage performance.[3] A suitable balance of graphitization and surface modification can ensure high overall energy storage performance in supercapacitor devices that rely on CN electrodes; however, such a processing scheme with precise controllability is rare.

Graphitic nanomaterials like graphene and carbon nanotubes (CNT) become the primary choices for energy storage in supercapacitors due to their intrinsic high conductivity and high surface area. Further, surface modifications of graphene/CNT can significantly increase their energy storage performance.[11] However, the complex and expensive processing of CNT/graphene, intrinsic restacking tendency, and their tedious surface modification guide the researcher to focus on alternative sources of carbon nanomaterials. Carbon nanomaterials directly obtained from pyrolysis of metal-organic frameworks (MOFs), polymers, and bio-mass have shown great promise in energy storage applications due to cost-effectiveness and easy processing.[12–14] Particularly, MOF-based nanostructures have the unique advantage of being synthesized on a large scale in various morphologies through elementary methods, even at room temperature. Its straightforward pyrolysis can produce morphology-preserved nanostructures with high surface area.[15] MOF-derived CNs thus quickly emerge as suitable materials for supercapacitor energy storage.[13,16–19]

Modifications regarding chemical activation with KOH are frequently adopted to increase the accessibility of the surface of MOF-derived carbons.[20,21] For example, Xu's group reported the development of 1D carbon nanorods (CN-rods) through pyrolysis of MOF-74 rods and then sonicated and subsequently activated at high temperature to get porous graphene nanoribbon that exhibits suitable capacitance of 193 F g^{-1} which is higher than CN-rods (164 F g^{-1}).[13] Pan et al. have shown that the thermal transformation of magnesium-based MOF and its subsequent activation with KOH is an effective route for good supercapacitor activity in the derived carbon. [22] Yamaguchi group manipulated the electronic conductivity and porosity by varying the graphitization degree of zinc-based MOF-derived carbon through annealing at different temperatures for several hours. However, the degree of graphitic order is not as high as is evident from broad peaks in XRD and Raman spectra.[17] Nevertheless, all these methods to get MOF-derived materials for supercapacitors rely on prolonged pyrolysis at high temperatures and require hours of thermal activation, which makes all these processing tedious, energy-consuming, and complex. In addition, the customized tunability of the graphitic level is very hard to realize. Thus, there is an urgent need to develop a very new process for customized tuning of graphitization and porosity in MOF-derived carbon-based nanostructures that can be very fast, simple, and low energy-consuming.

Here, we report a unique current-pulse-involved ultrafast processing for the precise tunability of graphitic order in cobalt-based MOF-derived carbon nano-leaves (GNLs) and programmed retrieval of the graphitic order in electrochemically perforated-GNL(PGNLs) counterpart for high-performance supercapacitor applications. We have shown that low to very high graphitic carbon nanostructures can be generated by controlling the duration of current pulses used for very rapid Joule heating. Importantly, cobalt atoms of MOF turned into cobalt nanoparticles embedded within graphitic layers of GNLs, and the size of the nanoparticles also depends on the pulse duration. We have employed a simple electrochemical anodic oxidation process to exfoliate the graphitic layers and etch the Co nanoparticles. Removing Co nanoparticles and anodic oxidation generates size-tunable pores within GNL and lowers the graphitization level due to surface functionalization. We have shown that the graphitic order can be suitably restored by passing programmed current pulses of a very short duration (50 ms), which greatly affected the energy storage property of the porous graphitization recovered GNLs (rPGNLs). These rPGNLs can be essential for versatile energy storage applications due to their high surface area, tunable conductivity, and binder-free, ready-to-use electrode structure. As proof of concept, we have employed rPGNLs as electrodes in a variety of supercapacitor technologies like aqueous electrolyte-based, water-in-salt (WIS) electrolyte-based and wearable solid-state gel-electrolyte supercapacitors. In all these applications, rPGNLs show outstanding performance, and a considerable capacitance enhancement was observed depending on the porosity and graphitic order tunability. The symmetric supercapacitor of optimized rPGNLs exhibited more than 400% capacitance increment in aqueous electrolyte (1M H_2SO_4) compared to its pristine GNLs counterpart. The highly porous graphitic nano-leaves with numerous mesopores provide numerous ion transport channels, ideal for application in water-in-salt (WIS) electrolytes of extremely high ion concentrations. The symmetric supercapacitor device of rPGNLs linked to CC and WIS electrolyte (17m $NaClO_4$) displayed an extended potential window of 2.3 V, leading to a nearly four-fold increment in energy density compared to the aqueous electrolyte. A wearable solid-state supercapacitor consisting of rPGNLs linked to CC as the positive electrode was asymmetrically designed with MXene ($Ti_3C_2T_x$) as the negative electrode also showed an impressive potential window of 1.6 V with excellent operational and mechanical stability.

3.2. Materials and methods

3.2.1. Materials

Cobalt nitrate hexahydrate ($Co(NO_3)_2 \cdot 6H_2O$), 2-methylimidazole ($C_4H_6N_2$), and absolute ethanol were purchased from Sigma-Aldrich. H_2SO_4 (95-97wt%, Emsure) and HNO_3 (65%, Emsure) were purchased from Merck. Commercial carbon cloth (CC) (Plain Carbon Cloth – 1071 HCB) was purchased from AvCarb Material Solutions. Ti_3AlC_2 was purchased from Carbon Ukraine. Millipore type III deionized water was used throughout all the experiments while needed.

3.2.2. Preparation of ZIF-67 nano leaves over CC

Firstly, the commercial carbon cloth (CC) (3×4.5 cm^2) was washed with ethanol and DI water in a bath sonicator successively for 10 minutes each. Then, ZIF-67 nano leaves were grown vertically over each microfibre of cleaned CC using a facile method at room temperature.[1] Briefly, 1.314 g of 2-methyl imidazole and 0.582 g of $Co(NO_3)_2 . 6H_2O$ were dissolved in 40 mL of DI water each, respectively. Then, the two solutions were mixed in a 100 mL beaker, and the cleaned CC was placed vertically in the mixed solution. After 4 hours of reaction, the CC was collected, washed with DI water several times, and dried to obtain ZIF-67 nano leaves vertically grown over CC.

3.2.3. Preparation of GNLs

The as-prepared ZIF-67 linked to CC was cut into pieces (3×1 cm^2), and a milliseconds voltage pulse of 30 V was applied through the length of the CC in an N_2-saturated airbag (Sigma-Aldrich) using a constant power supply capable of supplying voltage pulse. The transient current passing through CC produced ultrafast Joule heat, resulting in ZIF-67-derived graphitized nano leaves (lGNL, mGNL, and GNL obtained by 0.2 s, 0.5 s, and 1 s (four pulses) current pulses, respectively) vertically linked to CC. The graphitization level can be precisely controlled by the voltage amplitude or pulse duration (as the higher voltage and pulse duration could result in higher Joule heating).

3.2.4. Preparation of porous graphitic nano leaves, namely $PGNL_{2min}$, $PGNL_{5min}$, $PGNL_{10min}$

The as-developed GNLs (lGNL, mGNL, and GNL) linked to CC (3×1 cm^2) and a platinum foil with the same geometrical area were immersed into concentrated HNO_3 (65%, Emsure) to use as anode and cathode, respectively. A voltage of 2.2 V was applied between the GNL anode and the platinum foil cathode for x minutes to obtain $PGNL_{xmin}$ (x=2, 5, and 10 minutes).

Finally, the $PGNL_{xmin}$ samples were collected and washed in DI water several times until the pH became neutral. Then, they were dried in a vacuum oven overnight.

3.2.5. Preparation of electro-reduced porous graphitic nano leaves, namely r_1PGNL_{5min}, r_2PGNL_{5min}, r_4PGNL_{5min}

A sequence of ultrashort millisecond voltage pulses of 50 milliseconds duration, 30 V, was applied through the length of the $PGNL_{xmin}$ linked to CC to reduce $PGNL_{xmin}$ and obtain r_yPGNL_{xmin} (y=1 for a single electro-reduction pulse, y=2 for two successive electro-reduction pulses, and so on).

3.2.6. Fabrication of symmetric aqueous supercapacitor and water-in-salt (WIS) electrolyte supercapacitor

The as-developed GNLs, $PGNL_{xmin}$, and r_yPGNL_{xmin} were used as ready-to-use electrodes for aqueous and WIS supercapacitor devices. In the aqueous supercapacitor, 1M H_2SO_4 was used as an electrolyte. In the WIS supercapacitor, 17m $NaClO_4$ was used as the electrolyte.

3.2.7. Fabrication of asymmetric solid-state-supercapacitor (ASSC) for wearable application

The PVA gel was first prepared by adding 0.5 g of PVA into 5 mL 1 M H_2SO_4 with continuous stirring at 90°C until the PVA solution was completely dissolved. The r_2PGNL_{5min} linked to CC and Mxene ($Ti_3C_2T_x$) connected to CC, both having a working area of 1 cm^2, were soaked in the hot gel electrolyte (50–60 °C) for 1 min to allow the electrolyte to diffuse into the nanoporous structure of the two electrodes; they were then collected and allowed them to dry under ambient conditions for 10 min. This gel-coating process was repeated three times. The asymmetric SSC device was fabricated by sandwiching the two pieces of r_2PGNL_{5min}-coated CC and MXene-coated CC (the positive and negative electrodes, respectively) to develop the r_2PGNL_{5min}@CC//MXene@CC asymmetric device.

3.2.8. Flexibility test of the wearable ASSC device

The flexibility test of the ASSC device was carried out using our lab-made programmable instrument designed to achieve the desired device bending with a precise angle.

3.2.9. Materials characterization

The as-developed samples' morphology and microscopic features were investigated using field emission scanning electron microscopy (FESEM, Zeiss, Sigma-300) and field emission transmission electron microscopy (FETEM, JEOL, 2100F). The crystalline structure of samples was analyzed using an X-ray diffractometer (Rigaku Technologies, Smartlab) with Cu Kα radiation. Raman spectroscopic measurements were performed on a Raman Spectrometer (Horiba Jobin Vyon, LabRam HR, laser wavelength 514 nm). The chemical compositions and oxidation states were detected by X-ray photoelectron spectroscopy (ESCALAB Xi+, Thermo Fisher). Surface area and pore size distribution were estimated using BET (Quantachrome Instruments, Autosorb, IQ MP) and UV-vis spectroscopy (Perkin Elmer, Lambda 950)-assisted MB adsorption experiment.

3.2.9.1. BET analysis

A BET N2 adsorption experiment was performed on the best-performing sample (r_2PGNL_{5min} linked to CC) and a moderately-performing sample ($PmGNL_{5min}$ linked to CC). From the results and the known specific surface area of CC, the samples' specific surface area and pore size distribution were estimated. The calculation details are given in the Supporting Information.

3.2.9.2. MB adsorption experiment

The as-developed electrode samples (GNL, PGNLs, rPGNLs) with an area of 1 cm^2 were immersed in a methylene blue (MB) aqueous solution (0.2 mg/ml, 5 ml) for 48 h. Then, the electrode samples were removed, the solutions were diluted 50 times, and the final concentrations of the MB solutions were evaluated by UV-vis spectroscopy. The calculation details of the electrode surface area are provided in the Supporting Information.

3.2.10. Electrochemical measurements

All electrochemical measurements, including symmetric cells and the asymmetric solid-state device, were taken on the Biologic SP-150e electrochemical workstation at room temperature. The cyclic voltammetry (CV) test and galvanostatic charge-discharge (CD) test were carried out to evaluate the performance of the supercapacitors. The GCD test for 50000 cycles at 50 mA cm^{-2} was carried out for cycling stability. The electrochemical impedance spectroscopy (EIS) was obtained in a frequency range from 100 kHz to 0.01 Hz.

3.3. Results and Discussion

3.3.1. Synthesis, graphitization control, tunable pore formation, and graphitic order recovery of carbon nanostructures

Hierarchically oriented carbon nanostructures with tunable porosity were obtained through sequential three-stage processing involving unique programmed current-pulse-induced methodology. This three-stage processing involved the transformation of metal-organic frameworks (MOFs) into graphitic carbon nanostructures, controlled electrochemical perforation, and current pulse-induced graphitization recovery. **Figure 3.1** presents a schematic representation of the processing. In the first step, vertically oriented cobalt-based imidazole metal-organic framework (ZIF-67) nano-leaves on carbon cloth (CC) were converted into cobalt nanoparticle-embedded graphitic nano-leaves (Co/GNL) via ultrafast Joule heating by passing current pulses through it using a pulsed voltage source. This ultrafast Joule heating can attain a very high temperature within the pulse duration (details in Materials and methods) during the passage of pulses. This high temperature can pyrolyze the MOFs into Co/GNL with a highly adjustable graphitization level. Notably, the magnitude and duration of electric pulses determine the degree of graphitization of GNLs [lGNL (200 ms), mGNL (500 ms), and GNL (1000 ms, 4 pulses). A high level of graphitization controllability makes the processing unique and offers a massive opportunity for multifunctional use. In the second step, the as-developed Co/GNL was used as an anode and electrochemically oxidized in concentrated HNO_3 for only a few minutes, transforming it into porous GNL (PGNL). As a result, the surface of GNL gets oxidized, leading to loosening up the graphitic layers, which in turn etch out the Co nanoparticles, leaving behind partially exposed numerous nanopores uniformly distributed all over the PGNL surface. Notably, the degree of graphitization of GNL assesses the level of porosity of the surface of PGNLs ($PGNL_{2min}$, $PGNL_{5min}$, $PGNL_{10min}$), depending on the duration of electrochemical perforation (ECP). Generally, surface functionalization during ECP, due to oxidation and the introduction of defects, reduces the level of graphitization and consequently negatively affects the conductivity of GNL.[23] Ultrafast programmed current pulses (50 ms duration) were passed through GNL-containing CC in the last stage to recover the graphatization. These ultrafast pulses act to electro-reduce the PGNL, resulting in porous GNL with restored conductivity (rPGNL). Significantly, the number of short current pulses (r1-r4, 50 ms each) determines the degree of conductivity recovery of the electro-reduced porous rPGNLs (r_1PGNL_{5min}, r_2PGNL_{5min}, and r_4PGNL_{5min}).

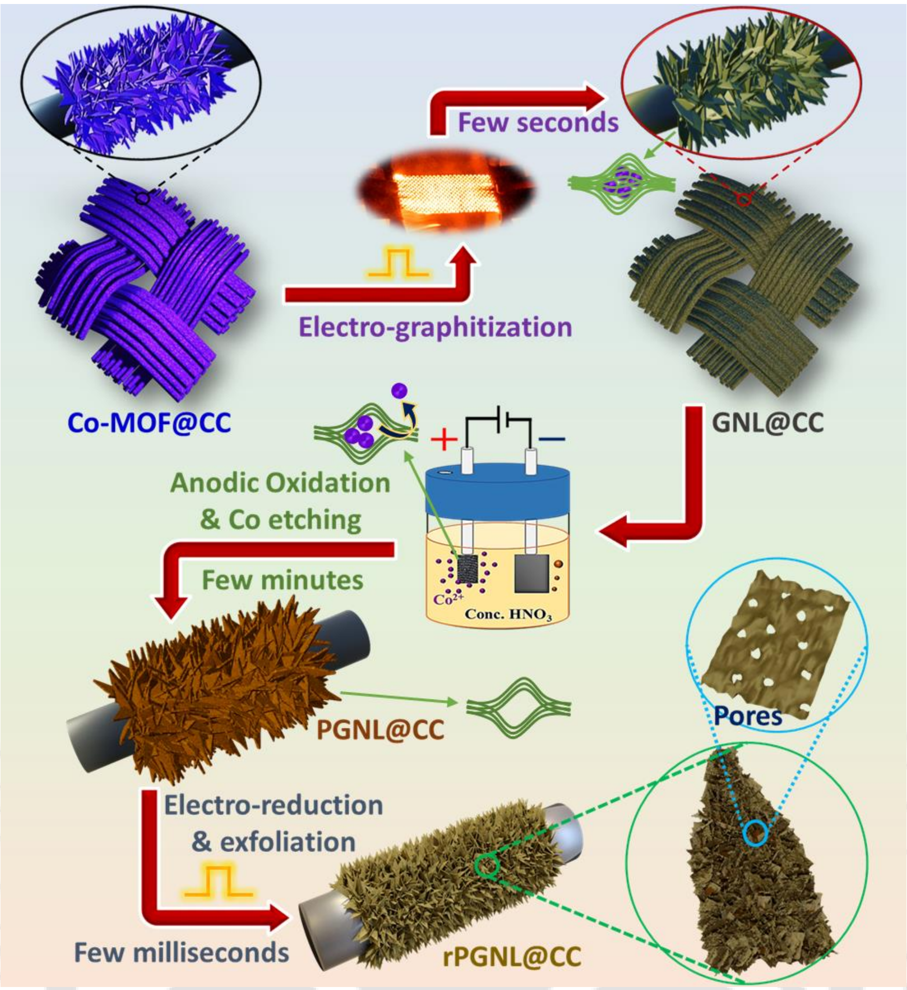

Figure 3.1: Schematic depiction of the synthesis process of the electro-reduced porous graphitic nano-leaves (rPGNLs).

Raman spectroscopy was employed to investigate the graphitization degree of the GNLs (**Figure 3.2a**), the level of the defect (deviation from the graphitic structure, $sp^2 \rightarrow sp^3$) incorporated during ECP in PGNLs (**Figure 3.2b**), and the recovery of the graphitization level ($sp^3 \rightarrow sp^2$) after e-reduction in rPGNLs (**Figure 3.2c**). Raman spectra were acquired for individual nano leaves of GNLs (**Figure 3.3a**) to exclude the effect of the CC substrate. The Raman spectrum of graphitic structures exhibits three characteristic peaks (a D-peak at 1350 cm^{-1}, a G-peak at 1578 cm^{-1}, and a 2D-peak at 2700 cm^{-1}).[24] The G-peak represents the in-plane C=C stretching vibration (E_{2g} modes) and is characteristic of the graphitic structures. The D-peak is related to the defects present in the graphitic structure, and the 2D peak is the overtone of the D peak. The degree of graphitization is generally estimated by the intensity ratio of D and G-peak (I_D/I_G) or the FWHM of G-peak. The lower the value of I_D/I_G and Γ_G, the higher the level of graphitization. The Raman spectra in **Figure 3.2a** suggest that I_D/I_G ratios and FWHM of G-peak follow the order: lGNL < mGNL < GNL, indicating a gradual increase in graphitization with the rise in pulse duration and, hence, adequate Joule heating time.

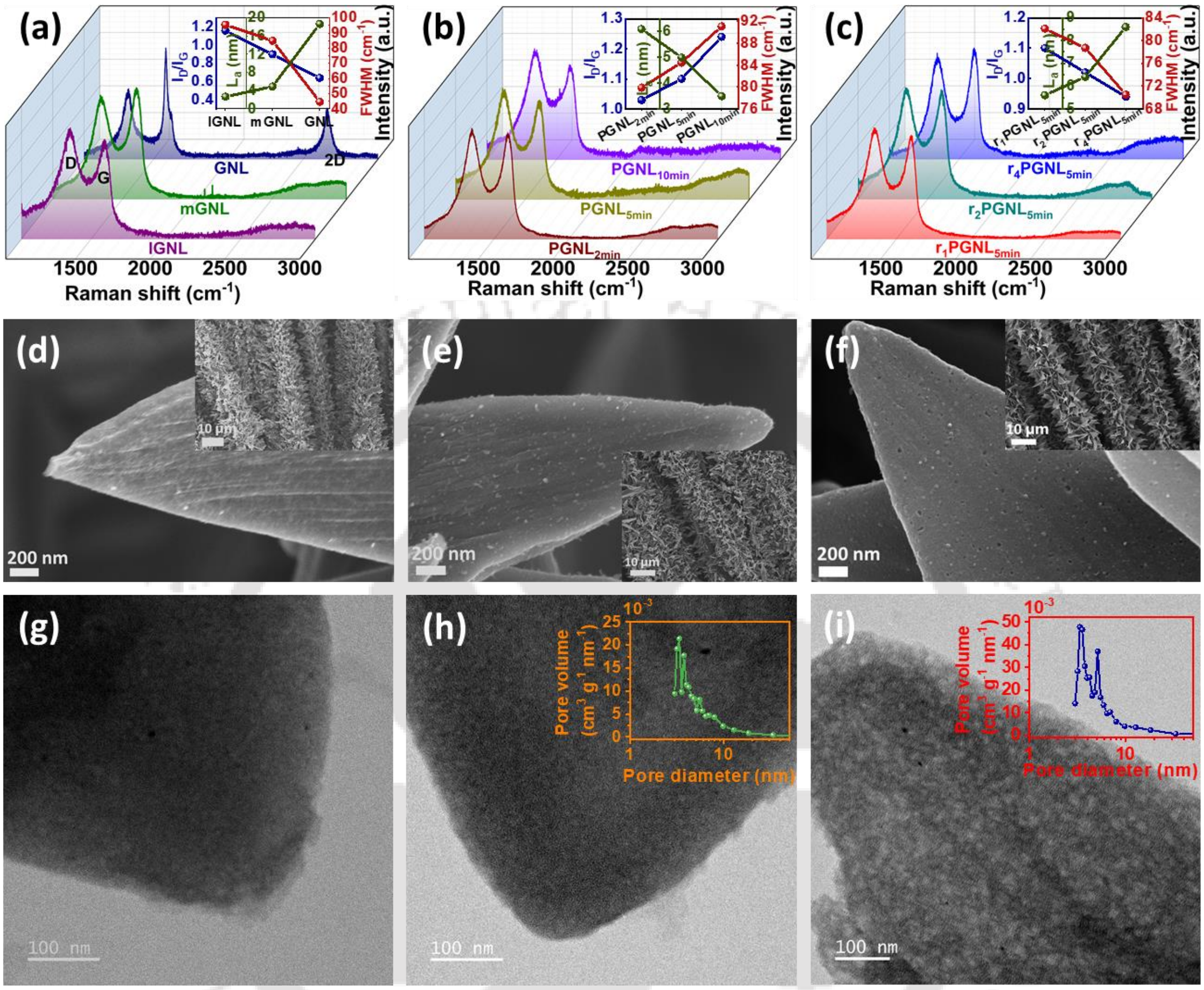

Figure 3.2: Characterization of MOF-derived GNLs, their electrochemically perforated (GNL_{xmin}), and subsequent electro-reduced ($r_yGNL_{x\ min}$) counterparts. Raman spectra of (a) lGNL, mGNL, and GNL, (b) $PGNL_{2min}$, $PGNL_{5min}$, and $PGNL_{10min}$, and (c) r_1PGNL_{5min}, r_2PGNL_{5min}, and r_4PGNL_{5min} with estimated I_D/I_G, FWHM (G), and sp^2 domain size L_a plotted in the insets, (d-f) high magnified FESEM images of electrochemically perforated and subsequently electro-reduced GNLs (r_2PlGNL_{5min}, r_2PmGNL_{5min}, and r_2PGNL_{5min} respectively) (insets: low magnified FESEM images of the corresponding samples), (g-i) corresponding FETEM images of those samples, respectively (in the insets of h and i: BET pore size distribution of the respective samples).

The level of graphitization was judged and quantitatively analyzed using Raman spectroscopy. Notably, I_D/I_G ratios and FWHM of G-peak were assessed by fitting three characteristic peaks of the Raman spectra (**Figure 3.3**). The calculated I_D/I_G ratio and FWHM of the G-peak are plotted and tabulated in the **insets** of **Figure 3.2a** and **Figure 3.3**, respectively. Additionally, the graphitization level can be directly quantified from the average domain size (L_a) of the ordered graphitic region (sp^2 domain) (insets of **Figure 3.2a** and **Figure 3.3**). [24,25] An increase in L_a implies an increase in graphitic order. The value L_a (nm) was estimated from the FWHM of the G-peak (**Equation 3.1**) using the following equation,

$$\boldsymbol{\Gamma_G(L_a) = \Gamma_G(\infty) + Ce^{-L_a/(l_c/2)}} \qquad \textbf{3.1}$$

where, $\Gamma_G(L_a)$ is the full-width half maxima (FWHM) of G-peak, $\Gamma_G(\infty) = 15\ cm^{-1}$, FWHM of G-peak of pristine graphene, $C = 95\ cm^{-1}$, $l_c = 32\ nm$, known as phonon coherence length.[6] Considerably, the FWHM of G-peak decreases from 95.5 cm^{-1} to 44.6 cm^{-1}, and I_D/I_G decreases from 1.16 to 0.64 as pulse duration increases from 0.2s in lGNL to four successive pulses of 1s in GNL. The gradual increase in L_a from 2.65 nm to 18.66 nm proposes a progressive rise in the graphitization degree with increasing pulse duration. Thus, it is evident from Raman analysis that the graphitization level of the obtained GNL derived from MOF can be easily tuned by controlling the pulse width of the applied current. This tunability offers a new platform for further manipulating the graphitic structure via subsequent processing.

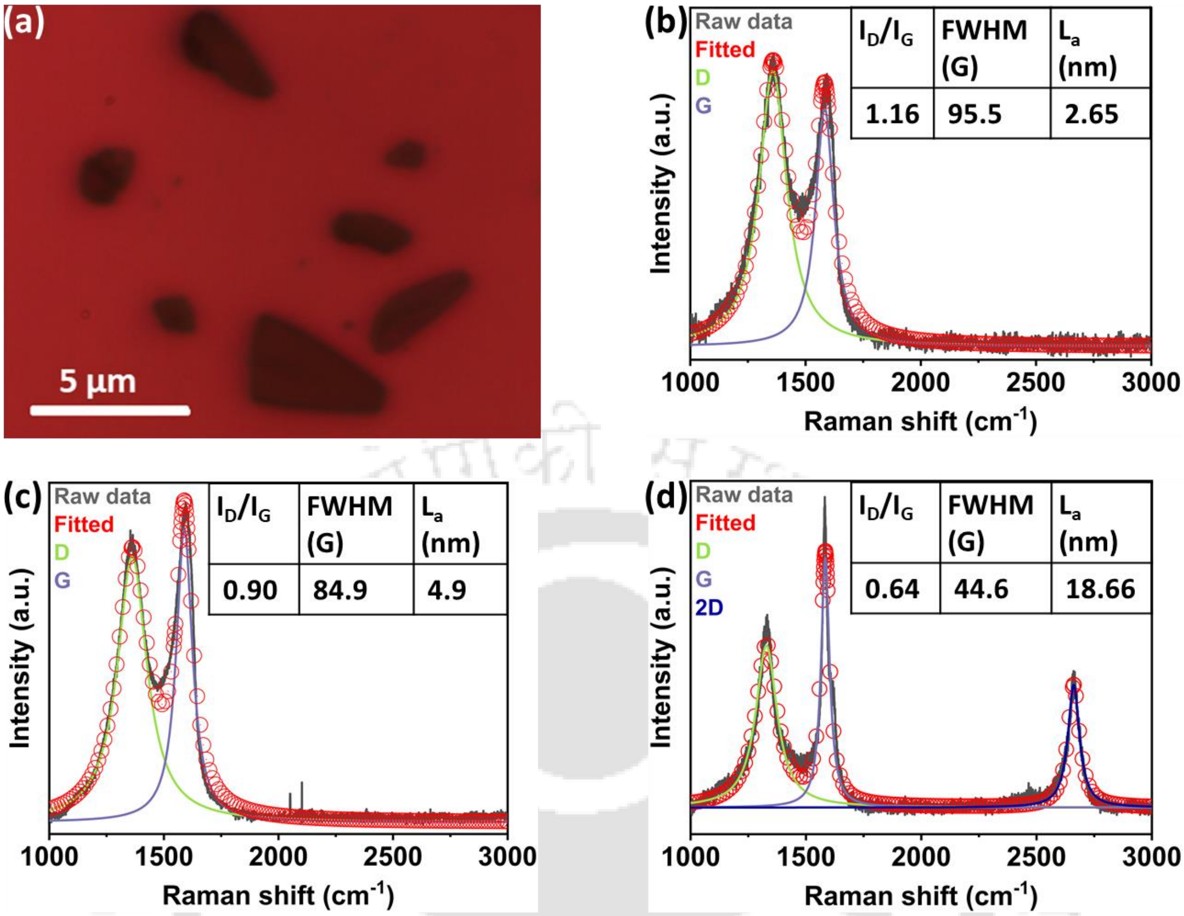

Figure 3.3: (a) Optical images of graphitic nano-leaves (GNLs) captured during Raman Spectroscopy, (b-d) fitted Raman spectra of lGNL, mGNL, and GNL, respectively (insets: table of estimated I_D/I_G, FWHM of G-peak, and sp^2 domain size).

Carbonaceous materials are generally graphitized at high temperatures (3000^{o}C) due to the reorganization of carbon bonds or catalytic growth from carbonaceous precursors at the transition metal surface. Both these mechanisms come into play in our process to control the graphitization; however, compared to hours (4-12 h) of complex conventional processing, our controlled processing is completed within several hundred milliseconds to seconds. The ultrafast current pulse leads to rapid Joule heating, which can even reach magma temperature within milliseconds. In our case, the rapid Joule heating pyrolyzes the MOF into a graphitic structure within a few seconds by the current pulse-induced high temperature, where in-situ generated cobalt nanoparticles act as the catalysts to graphitize the MOF-pyrolyzed carbon. Highly graphitized GNLs were considered for further processing as efficient electrode material due to their desired conductivity, a crucial parameter for supercapacitor application that benefits performance by reducing resistive energy loss during charge-discharge. It was subjected to ECP to increase the surface area of GNLs to increase the capacitance of this electrode. Controlled ECP (details are in Materials and methods) removed the in-situ generated cobalt nanoparticles from the graphitic pockets of GNLs and thereby generated uniform nanopores. The removal of cobalt is also helpful in removing the possibility of leaching in acidic electrolytes and negating the catalytic activity in water-in-salt electrolytes.

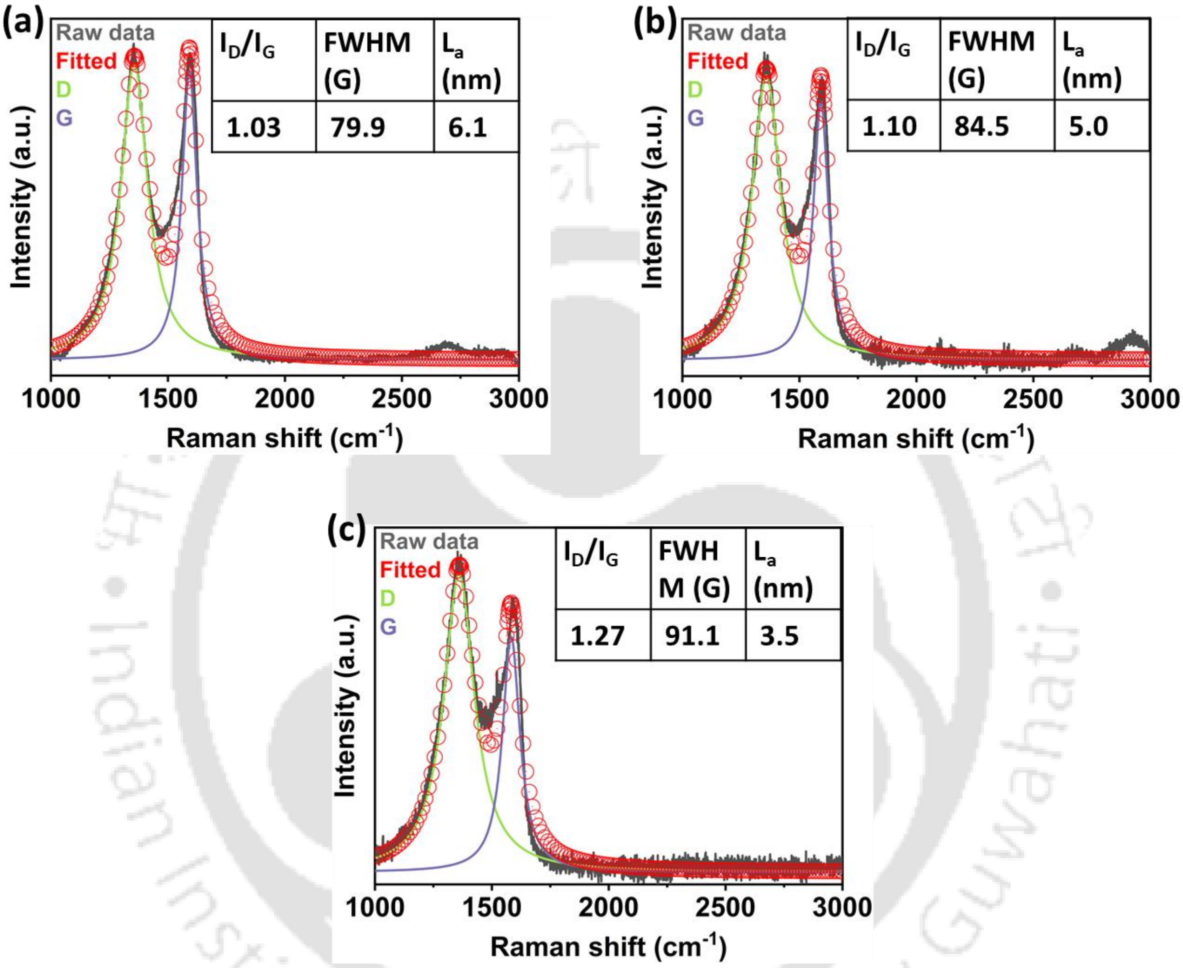

Figure 3.4: (a-c) Fitted Raman spectra of EC perforated (varying ECP duration) $PGNL_{2min}$, $PGNL_{5min}$, and $PGNL_{10min}$, respectively.

A detailed analysis of the Raman spectra was conducted to check the modification of the graphitic structure due to ECP. The Raman spectra (fitted Raman spectra) of porous GNLs ($PGNL_{2min}$, $PGNL_{5min}$, and $PGNL_{10min}$) (**Figure 3.2b**, insets of **Figure 3.2b**, **Figure 3.4**) reveal a gradual rise of I_D/I_G ratios and FWHM (G) values. As a result, a gradual drop in sp^2 domain size (L_a) is noticed if the ECP duration increases from 2 minutes to 5 minutes to 10 minutes, implying a continual decay of the graphitic structure. The I_D/I_G increases from 0.64 for pristine GNL to 1.07 for $PGNL_{2min}$, 1.10 for $PGNL_{5min}$, and a drastic surge of 1.27 in $PGNL_{10min}$.

Likewise, the value of FWHM (G) also increases from 44.6 cm^{-1} for pristine GNL to 79.9 cm^{-1} in $PGNL_{2min}$, a moderate value of 84.5 cm^{-1} in $PGNL_{5min}$, and an extreme rise of 91.1 cm^{-1} in $PGNL_{10min}$. Consequently, the value of L_a falls from 18.66 nm pristine value to 6.1 nm and 5.0 nm after 2 minutes and 5 minutes of anodic oxidation, respectively, signifying relative deviation from the graphitic nature. The value of L_a further falls to only 3.5 nm after 10 minutes of anodic oxidation, hinting at severe damage in the graphitic structure of GNL. Due to the intentional defect incorporation during nanopore formation using ECP, the continuous deviation from the graphitic nature of GNL with the increase in oxidation time can compromise the conductivity and, hence, the supercapacitor performance.

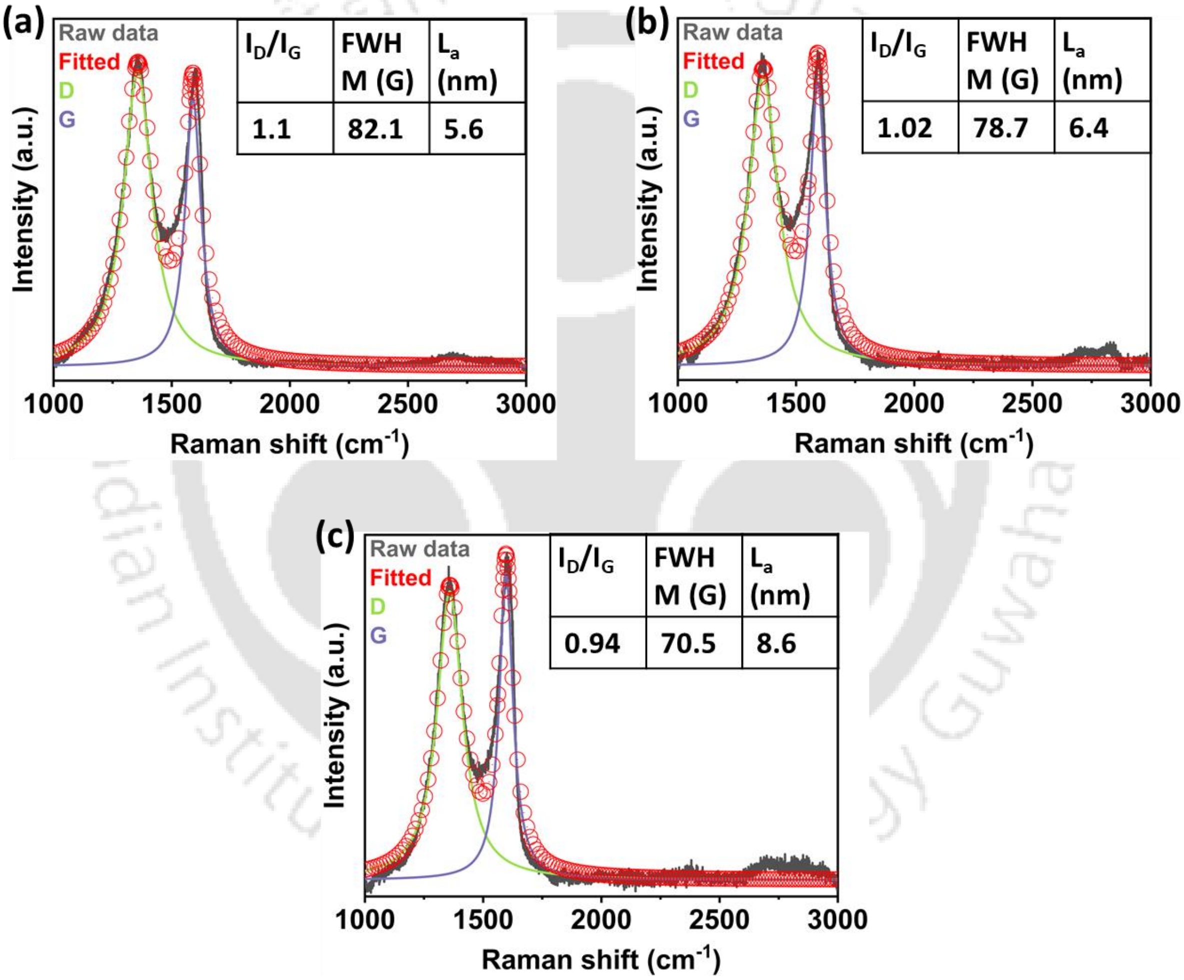

Figure 3.5: (a-c) Fitted Raman spectra of electro-reduced (varying number of reduction pulses) r_1PGNL_{5min}, r_2PGNL_{5min}, and r_4PGNL_{5min}, respectively.

Therefore, the oxidation duration was optimized by taking feedback from electrochemical cyclic voltammetry (CV) measurements, which will be discussed in the energy storage section later. The CV measurements for the supercapacitor suggested that the 5-minute ECP is sufficient for streamlined performance. Therefore, 5 minutes as the optimized ECP time was considered for further processing toward enhanced supercapacitor output. To further improve the performance of $PGNL_{5min}$, it went through the graphitization restore stage by passing a programmed pulse of 50 ms ON and 1s OFF time, avoiding the overlaying of the nanopores due to over-reduction. Interestingly, depending on the number of pulses, the extent of graphitic restoration can be precisely tuned. The graphitization recovery level in the samples obtained with 1-4 number of 50 ms pulses (r_1PGNL_{5min}, r_2PGNL_{5min}, and r_4PGNL_{5min}) was monitored again through Raman spectroscopy. The Raman spectra (fitted Raman spectra) of r_1PGNL_{5min}, r_2PGNL_{5min}, and r_4PGNL_{5min} electro-reduced by single, two, and four successive 50 ms-current pulses, respectively, exhibited a gradual decrease in I_D/I_G and FWHM (G) with the increase in the number of electro-reduction pulses (**Figure 3.2c**, inset of **Figure 3.2c**, **Figure 3.5**). After one electro-reduction pulse, although I_D/I_G remains unaltered in r_1PGNL_{5min} (1.10) compared to $PGNL_{5min}$, FWHM (G) decreases slightly from 84.5 cm^{-1} to 82.1 cm^{-1}, implying a slight healing of graphitic nature (L_a increases from 5 nm to 5.6 nm) maintaining the analogous defective porous configuration. Applying two electro-reduction pulses, I_D/I_G and FWHM (G) drop to 1.02 and 78.7 cm^{-1}, respectively, inferring moderate reconstruction of graphitic structure (L_a increases to 6.4 nm) in r_2PGNL_{5min}. On the other hand, four electro-reduction pulses further contracted I_D/I_G and FWHM (G) to 0.94 and 70.5 cm^{-1}, suggesting significant restoration of graphitization level (L_a rises to 8.6 nm).

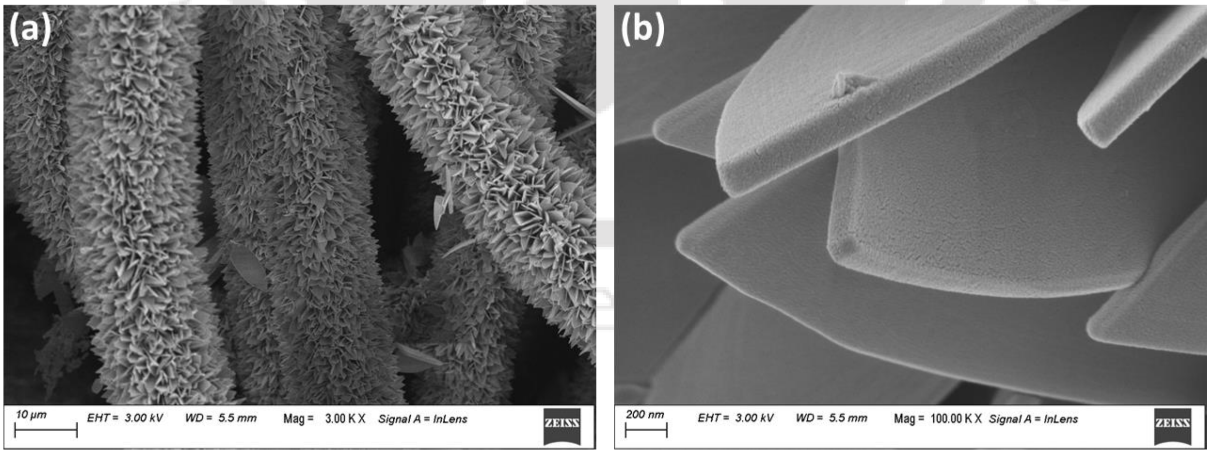

Figure 3.6: (a) Low and (b) high magnified FESEM images of Co-MOF-NL, respectively.

The morphology and the nanoscopic variation in the surface of the synthesized materials were investigated with Field emission scanning electron microscopy (FESEM) and Transmission electron microscopy (TEM). The FESEM images in **Figure 3.6** depict leaf-like MOF arrays that were hierarchically grown over CC. The electro-graphitization of the MOF nano-leaves led to Co embedded GNLs when the pulse duration was varied from 0.2 s (lGNL), 0.5 s (mGNL), to 1 s (GNL), preserving the hierarchical nano-leaf morphology (**Figure 3.7**). Closer inspection with TEM revealed that the sizes of the in-situ generated Co-nanoparticles gradually increase with the increase of electro-graphitization pulse duration, as is evident from the corresponding TEM images of lGNL (**Figure 3.8 a-c**), mGNL (**Figure 3.8 d-f**), and GNL (**Figure 3.8 g-i**). The average Co-nanoparticle size increased from 3.5 nm in lGNL (inset of **Figure 3.8 a**) to 15 nm (inset of **Figure 3.8 g**) in the case of GNL. The particle size enlargement is linked with higher temperatures due to extended Joule heating and a longer time for migration with more extensive pulse durations, which allows the cobalt to aggregate in bigger sizes.

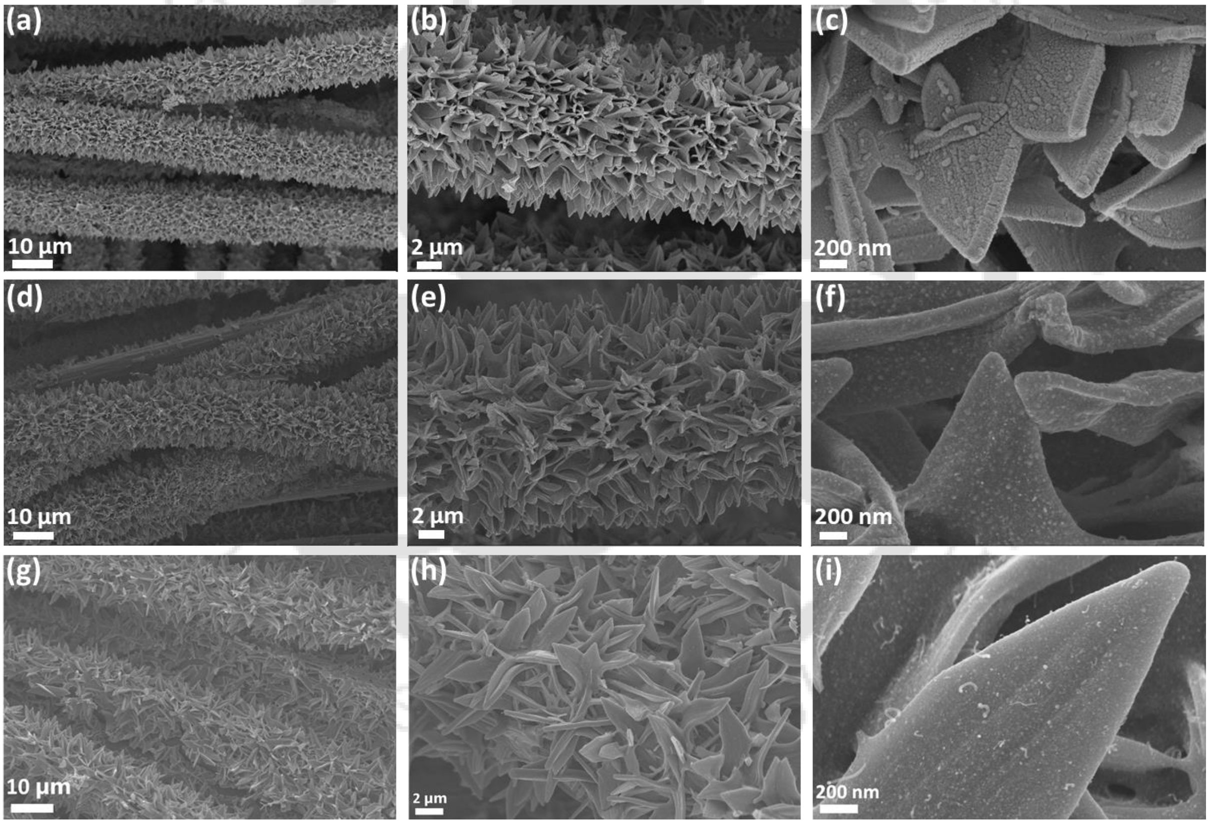

Figure 3.7: FESEM images of (a-c) lGNL, (d-f) mGNL, and (g-i) GNL.

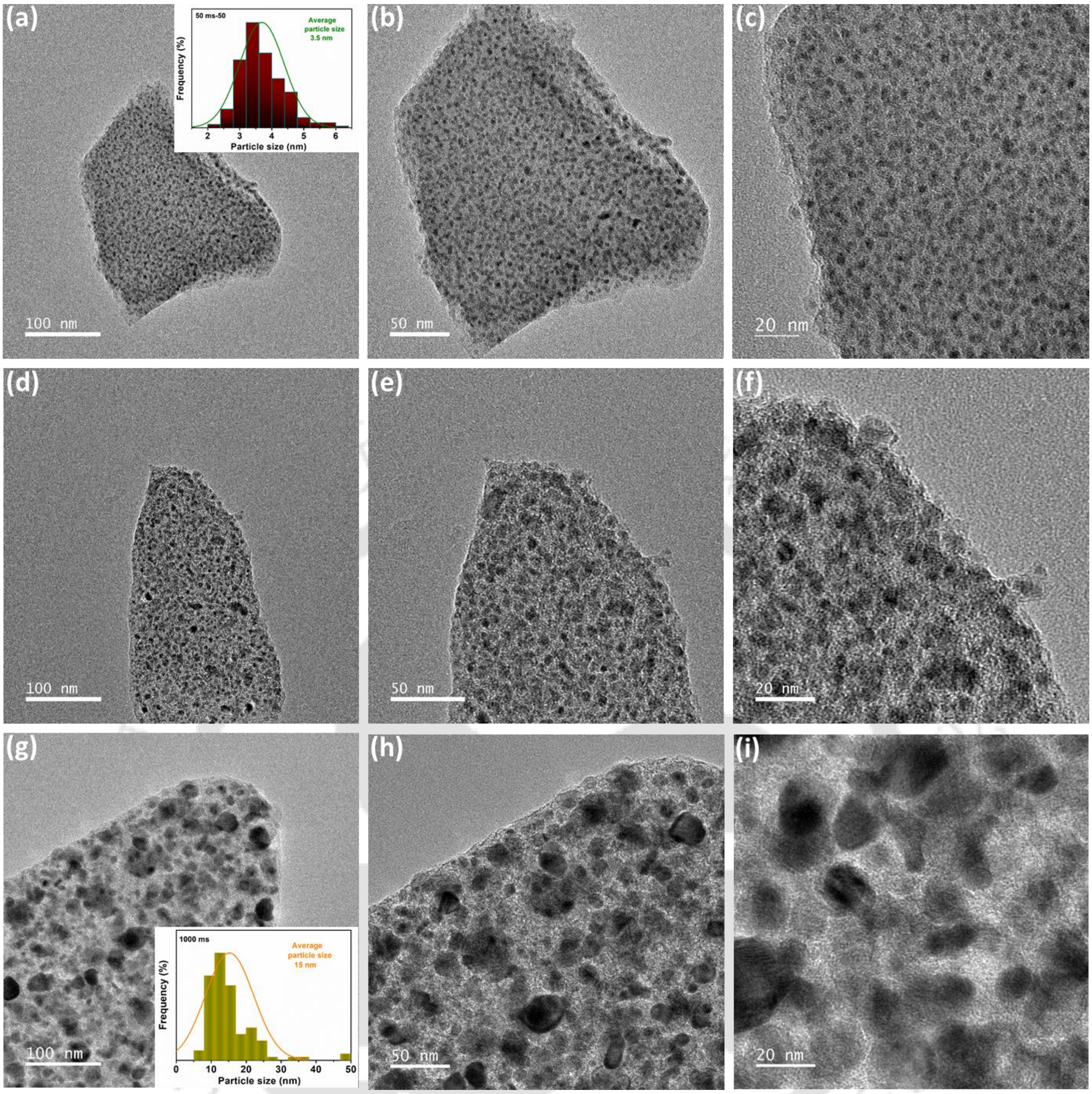

Figure 3.8: FETEM images of (a-c) lGNL, (d-f) mGNL, and (g-i) GNL (insets: size distributions of in-situ generated Co nanoparticles).

Now, if these in-situ generated particles are removed from the carbon matrix in a controlled way, pores can be generated at the sites of removed cobalt. However, removing the cobalt from its locked state in the carbon matrix is hard. We employed a simple electrochemical perforation (ECP) technique to unzip the graphitic layers of GNL and remove the Co, resulting in numerous pores at the sites of cobalt particles. The SEM images (**Figure 3.2d**, **e**) of the low and moderate graphitized samples after ECP and graphitization recovery stages (r_2PlGNL_{5min} and r_2PmGNL_{5min}) show smooth surfaces, which indicate that the removal of Co-particles may have introduced tiny pores not resolved with SEM. On the other hand, the nanopores created on the surface of $PGNL_{5min}$ (**Figure 3.9**) during ECP of highly graphitized GNLs are visible and distinguishable in r_2PGNL_{5min} (**Figure 3.2f**, **Figure 3.10**).

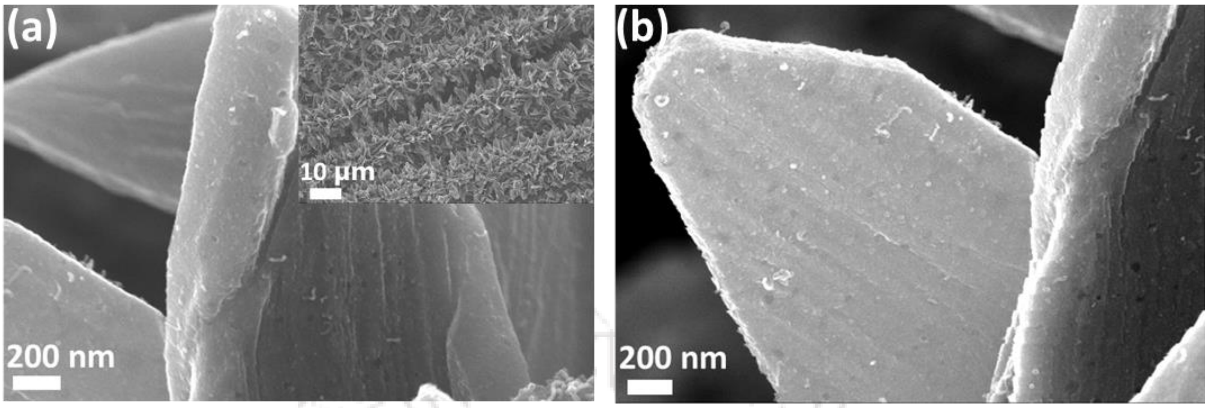

Figure 3.9: (a) and (b) FESEM images of $PGNL_{5min}$ (inset: corresponding low magnified FESEM image).

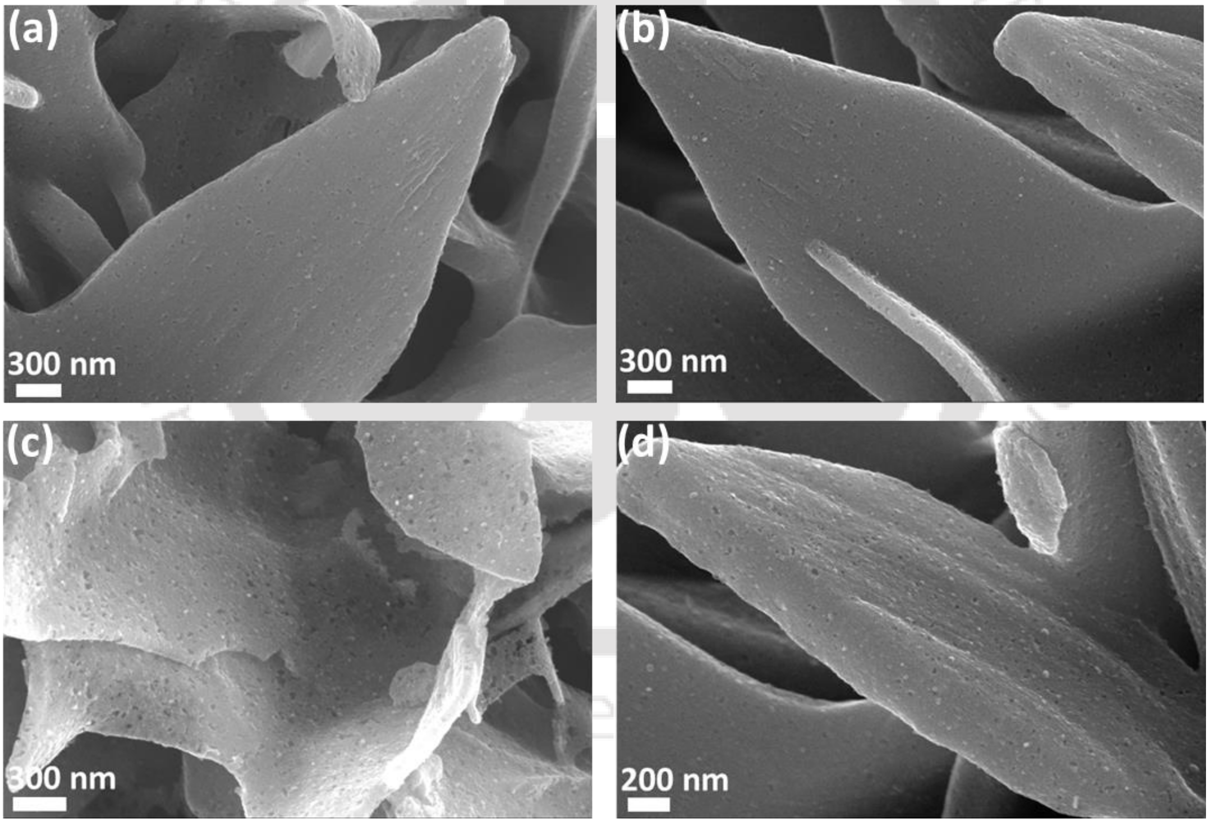

Figure 3.10: (a-d) FESEM images of r_2PGNL_{5min}.

TEM investigations were further performed to inspect the removal of cobalt particles and pore formation. **Figure 3.2g-i** and **Figure 3.11-3.13** clearly show that Co-particles are nearly entirely removed through this electrochemical perforation strategy, leaving pores behind the system. The size of the pores in r_2PlGNL_{5min} and r_2PmGNL_{5min} are much smaller than those of

r_2PGNL_{5min}, which clarifies why the pores were not detectable with SEM in the former two samples. The observations from TEM indicate that the co-nanoparticle size increases as the graphitization level of GNL increases with the help of increased electro-graphitization duration. Depending on the progressively increased Co-nanoparticle size and the graphitization level of the host GNL, the size and density of pores increase, proving the earlier observations of FESEM analysis.

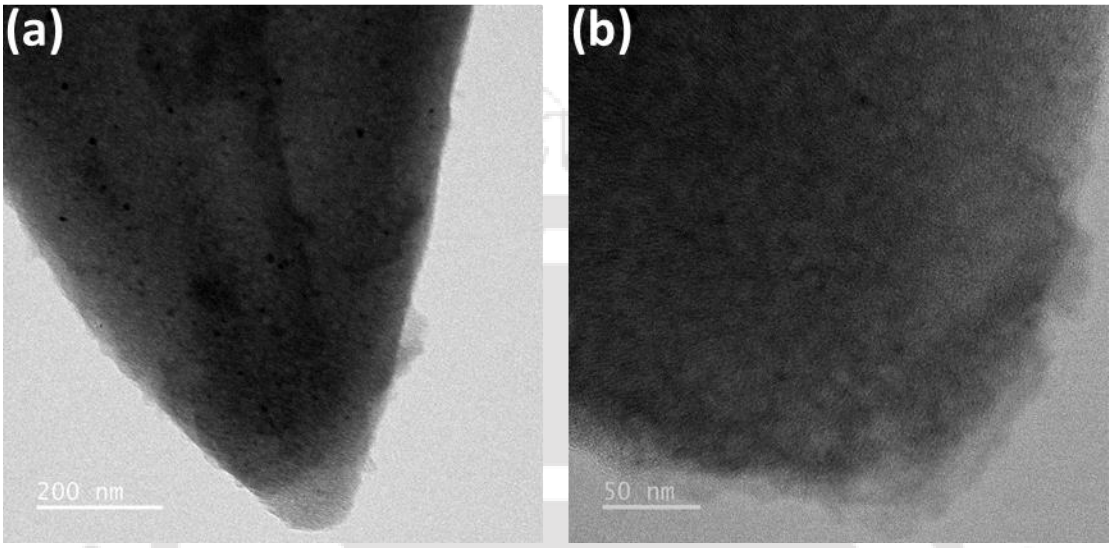

Figure 3.11: FETEM images of r_2PlGNL_{5min}.

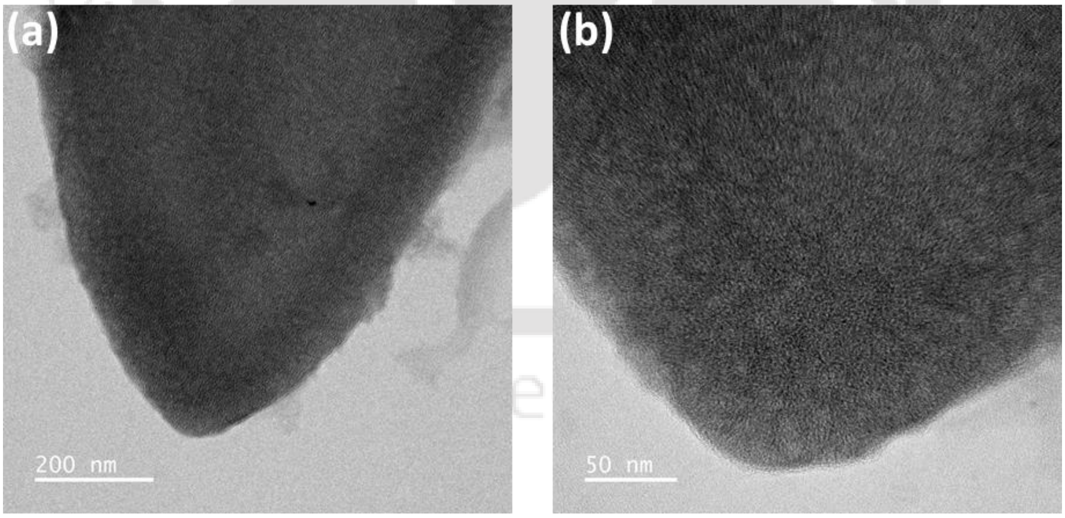

Figure 3.12: FETEM images of r_2PmGNL_{5min}.

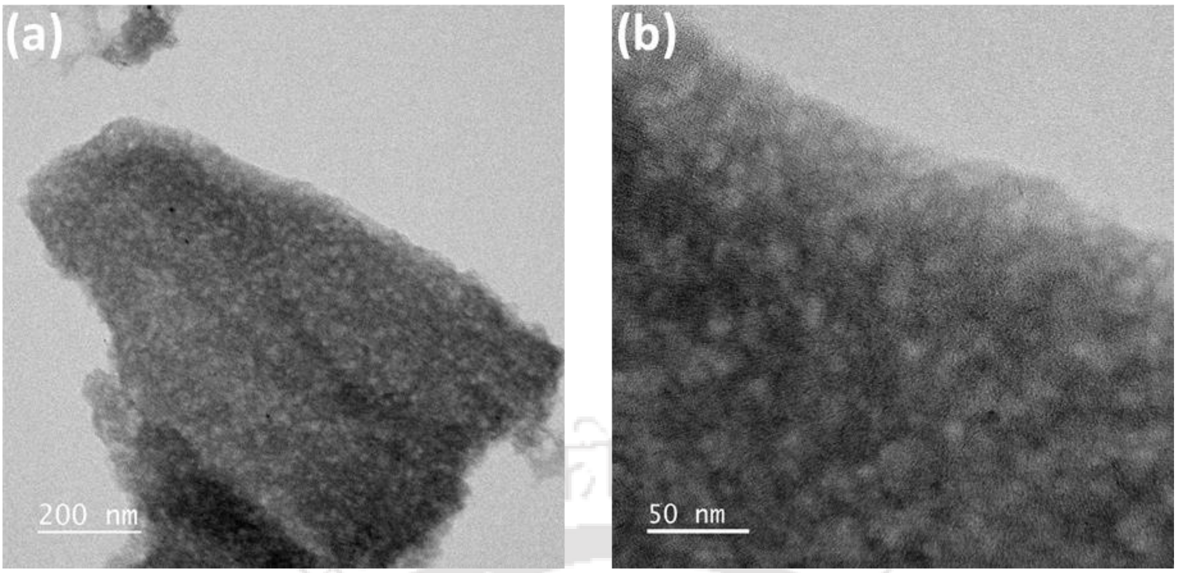

Figure 3.13: FETEM images of r_2PGNL_{5min}.

The surface area of the developed porous nano leaves was estimated using Brunauer-Emmett-Teller (BET) analysis (**Figure 3.14**) and UV-vis spectroscopy-assisted methylene blue (MB) adsorption experiment (**Figure 3.15**). The following equation estimates the BET surface area,

$$x_1 S_{sample} + x_2 S_{CC} = S_{total} \quad 3.2$$

where, x_1, x_2 are the mass fraction of the sample and carbon cloth, respectively. S_{CC}, S_{sample} are the BET surface area of the carbon cloth and the sample, respectively. S_{total} is the total experimental BET surface area.

The values of BET surface area are tabulated in **Table 3.1**. The following equations were used to calculate the surface area from the MB adsorption experiment.

$$S_{electrode} = 2.54 \times 10^3 \times \Delta M_{MB} \quad 3.3$$

Where ΔM_{MB} is the mass (g) change of MB due to adsorption.

ΔM_{MB} is estimated from the concentration calibration curve,

$$y = mx + c \quad 3.4$$

Where y is the absorbance, x is the concentration (mg L^{-1}), **m = 0.2037** is the slope, and **c = -0.0223** is the intercept of the fitted calibration line. The values of the MB adsorption experiment-estimated surface area are tabulated in **Table 3.2**.

As expected, the highest BET surface area and MB adsorption-derived surface area are estimated to be 533.56 m2 g^{-1} and 639.54 m2 g^{-1}, respectively, for the optimized porous r_2PGNL_{5min}. The estimated specific surface areas of the other developed samples (**Table 3.2**) follow the trend GNL < mGNL < $PmGNL_{5min}$ < $PGNL_{2min}$ < r_4PGNL_{5min} < $PGNL_{5min}$ <

PGNL$_{10min}$ < r$_1$PGNL$_{5min}$ < r$_2$PGNL$_{5min}$, which aligns with the earlier observations from Raman, FESEM, and TEM analysis. Notably, a relatively higher anodic oxidation duration, e.g., 10 minutes, resulted in high-density pores with larger sizes over the surface of PGNL$_{10min}$ (**Figure 3.16**), which could significantly damage the nano-leaves and affect the conductivity. These FESEM and TEM observations revealed that a precise tunability of particle size in our fast-pulsed Joule heating strategy could offer an excellent platform to introduce tunable porosity through subsequent oxidative cobalt etching.

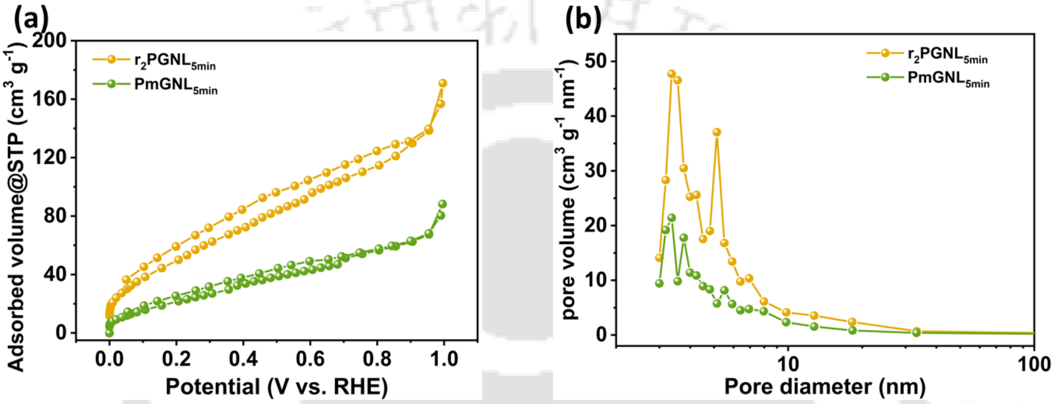

Figure 3.14: (a) BET isotherms, (b) BET pore size distributions.

Table 3.1: Estimated BET surface area.

Sample	x_1	x_2	S_{CC}	S_{total}	S_{sample}
PmGNL$_{5min}$	0.1094	0.8906	3.82	27.17	217.29
r$_2$PGNL$_{5min}$	0.1086	0.8914		61.35	533.56

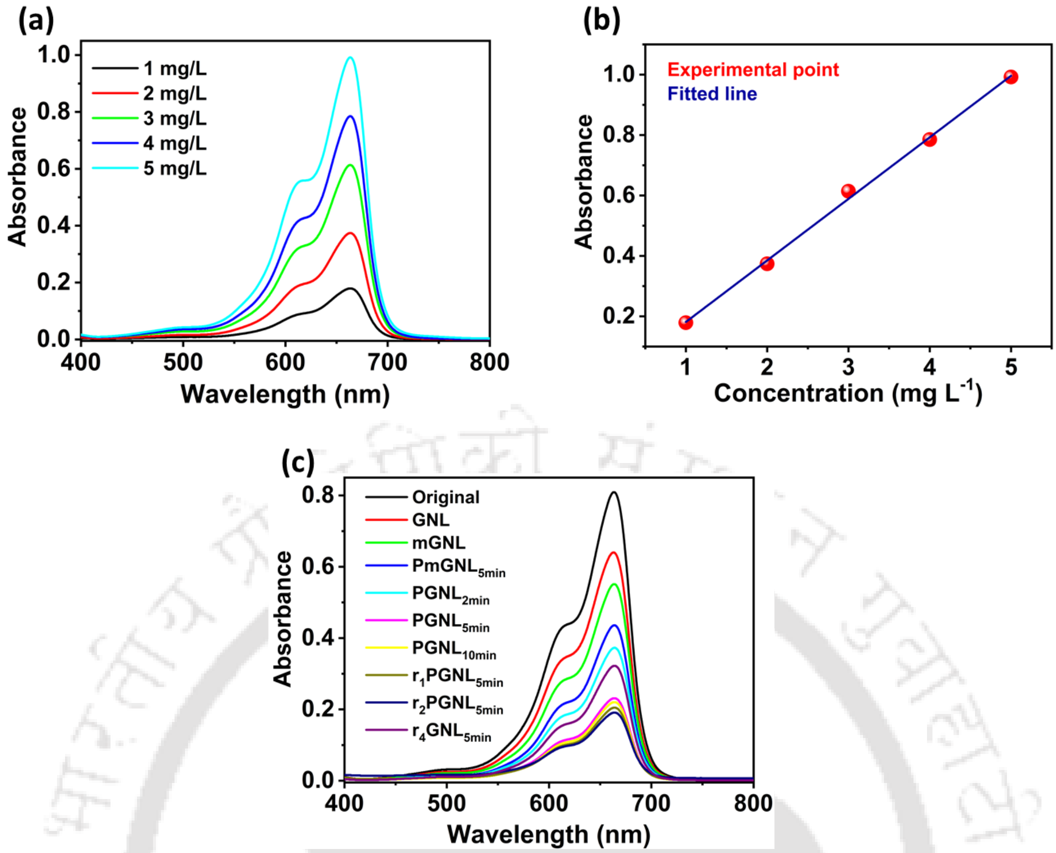

Figure 3.15: (a) UV-vis spectra of the methylene blue (MB) reference solutions for concentration calibration, (b) concentration calibration curve, and (c) UV-vis spectra of the MB solutions after adsorption in different samples.

Table 3.2: Estimated surface area by MB adsorption experiment.

Sample	y	x	Concentration (C) of MB ($50 \times x$) (mg L^{-1})	Change in C (mg L^{-1})	ΔM_{MB} (10^{-6}) (g)	$S_{electrode}$ (m^2 per geometrical area (cm^2) of the electrode)	Mass loading of active electrode materials (mg cm^{-2})	**S** (m^2 g^{-1})
Stock solution	0.809	4.081	204.05					
GNL	0.640	3.251	162.55	41.5	207.5	0.52705	3.64	144.79
mGNL	0.551	2.814	140.7	63.35	316.75	0.80455		
PmGNL	0.436	2.250	112.5	91.55	457.75	1.16269	3.03837	382.67
PGNL$_{2min}$	0.373	1.941	97.05	107	535	1.3589		
PGNL$_{5min}$	0.231	1.243	62.15	141.9	709.5	1.80213		
PGNL$_{10min}$	0.220	1.190	59.5	144.55	722.75	1.83579		

r_1PGNL_{5min}	0.205	1.116	55.8	148.25	741.25	1.88278		
r_2PGNL_{5min}	0.191	1.047	52.35	151.7	758.5	1.92659	3.01245	639.54
r_4PGNL_{5min}	0.322	1.690	84.5	119.55	597.75	1.51829		

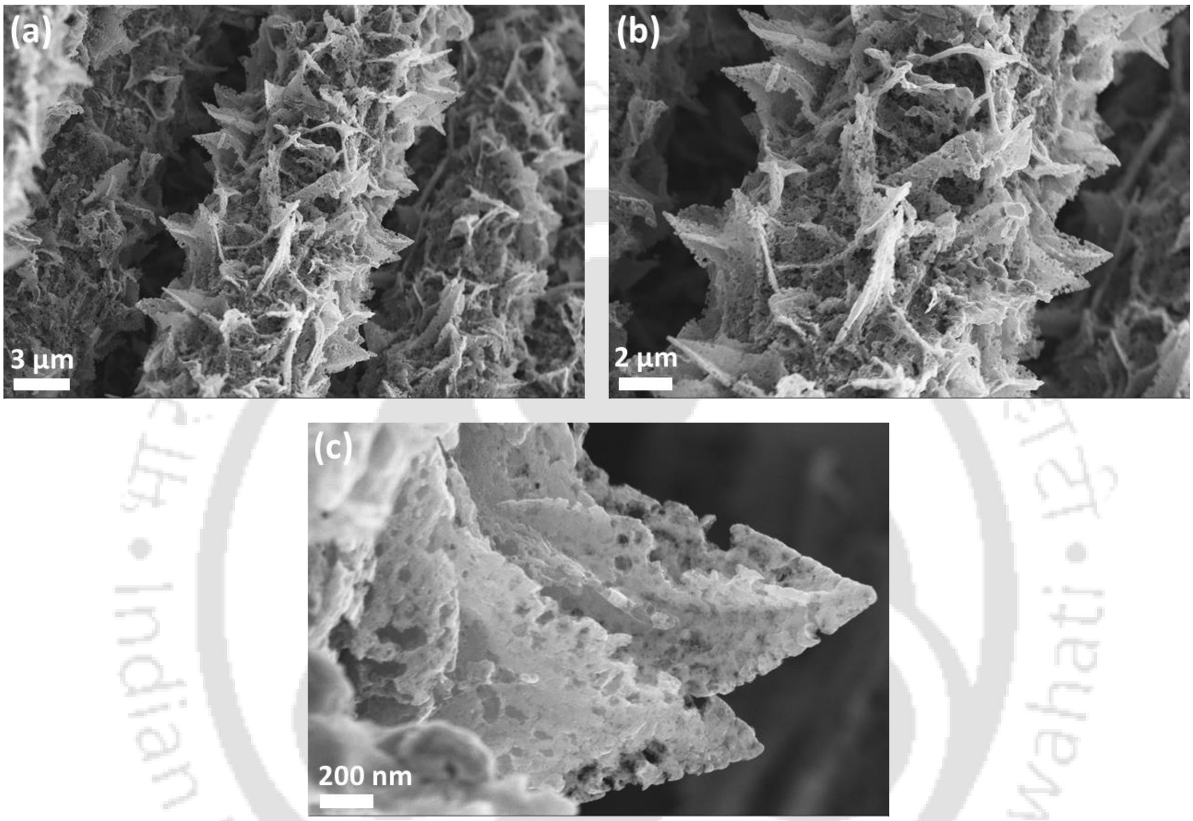

Figure 3.16: (a-c) FESEM images of $PGNL_{10min}$.

X-ray photoelectron spectroscopy (XPS) analysis was performed to understand the mechanism of pore creation during anodic oxidation and then electro-reduction by decoding the chemical compositions and the emerged surface functional groups (-OH, -COOH, -O-, etc.) in GNLs. The high-resolution C1s XPS spectra of graphitic structures generally consist of three deconvoluted peaks. The first peak at around 284.8 eV corresponds to the C=C sp^2 hybridized pristine graphitic region. The second peak at around 286.2 eV related to sp^3 hybridized carbons arises from C-O/C-O-C surface functional groups. Finally, the third peak at 288.3 eV is responsible for sp^3 carbons related to C=O/O-C=O functional groups linked to the edge carbons of graphitic structure, according to the Lerf-Klinowski model.[26,27] The FWHM of C1s spectra peaks of lGNL, mGNL, and GNL follow a trend: lGNL (1.63 eV) > mGNL (1.46 eV) > GNL

(1.07 eV) (**Figure 3.17a**), meaning a gradual growth of C=C sp^2 carbons, respectively. The continuous rise of C=C sp^2 contribution suggested a gradual decrease in sp^3 carbons coming out of the defect and surface functional groups, evident from the fitted deconvoluted peaks of C1s spectra of lGNL, mGNL, and GNL (**Figure 3.18a**, **b**, and **Figure 3d**). This trend indicates progressively increased graphitization levels in lGNL, mGNL, and GNL with increased pulse duration, as confirmed by the earlier Raman analysis. However, the FWHM of C1s peaks and the contribution of functional groups gradually increase from 1.40 eV to 1.45 eV (**Figure 3.17b**, **Figure 3e**, and **Figure 3.19**) and 33.7% to 44.3% (inset of **Figure 3.17b**), respectively, with the increased ECP duration from 2 minutes to 10 minutes.

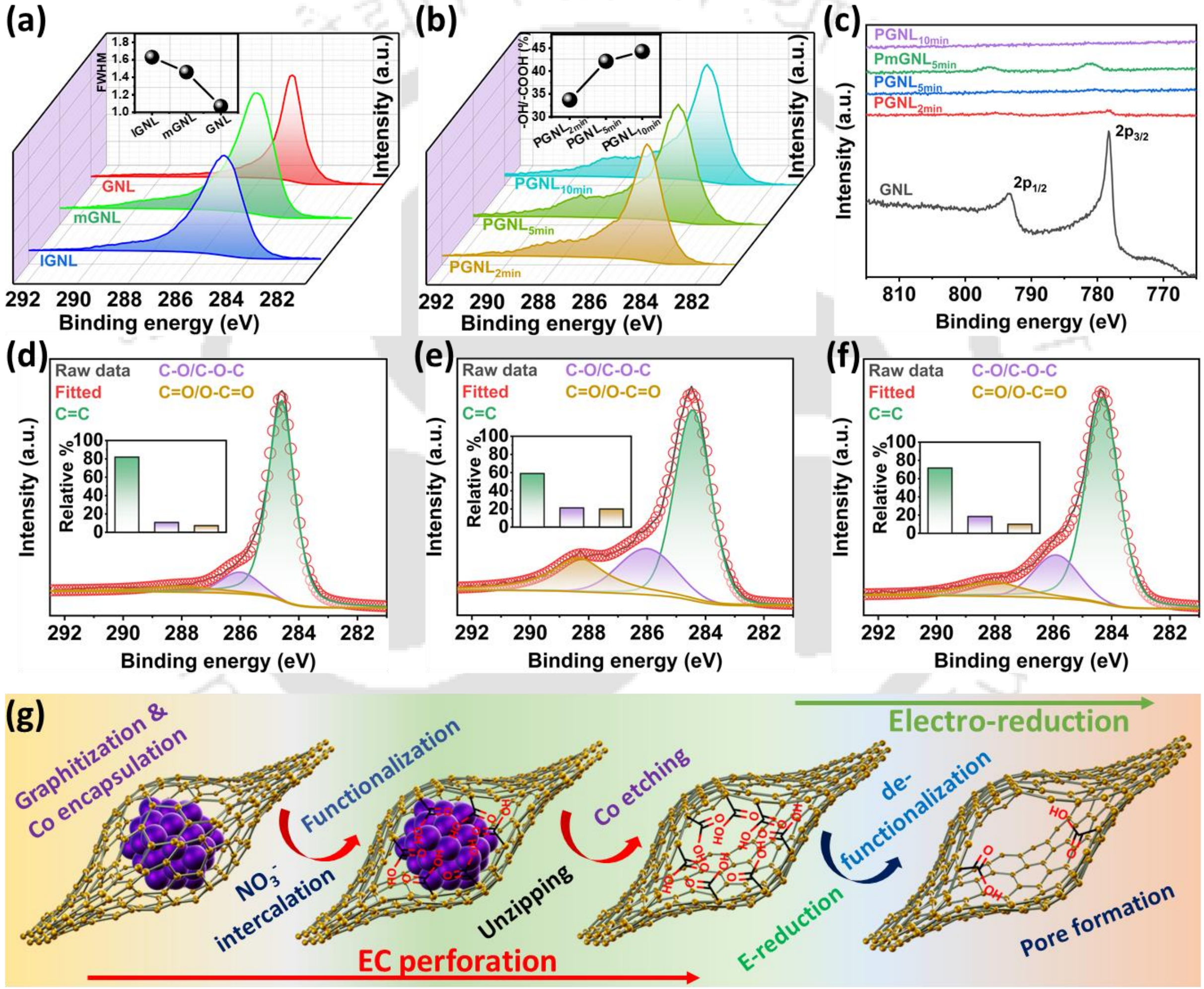

Figure 3.17: XPS analysis to understand the pore formation process in GNL. C1s spectra of (a) lGNL, mGNL, and GNL (inset: variation of FWHM of C1s peak) and (b) $PGNL_{2min}$, $PGNL_{5min}$, and $PGNL_{10min}$ (inset: variation of relative percentile of functional group contribution after ECP at varying duration), (c) Co 2p spectra of porous PGNLs compared to GNL, deconvoluted C1s spectra of (d) GNL, (e) $PGNL_{5min}$, and (f) electro-reduced r_2PGNL_{5min},

(g) schematic illustration of the pore formation mechanism by ECP and ultrafast electro-reduction.

This signifies a deviation from the graphitic structure with increased ECP duration, consistent with Raman analysis. Further, the absence of Co 2p-related peaks indicates that the in-situ generated Co-nanoparticles were successfully removed by the acid-assisted (65% HNO_3) ECP process (**Figure 3.17c**). The deconvoluted C1s spectra of pristine GNL (**Figure 3.17d**) and ECP-derived $PGNL_{5min}$ (**Figure 3.17e**) were compared to understand the pore formation phenomena during our ECP process. The results signify that the relative percentile of C=C sp^2 carbons reduces from 83% in GNL (inset of **Figure 3.17d**) to 59% in $PGNL_{5min}$ (inset of **Figure 3.17e**) after 5 minutes of ECP. Consequently, the percentile of C-O/C-O-C and C=O/O-C=O type groups rises from 11% and 6% to 21% and 19%, respectively, recommending significant deviation from the pristine graphitic nature of GNL in $PGNL_{5min}$ due to intentional defect incorporation by pore formation and surface functionalization. The decay of graphitic nature always results in a decrease of conductivity; hence, the graphitization level needs to be revived by thermal reduction-induced de-functionalization of $PGNL_{5min}$.

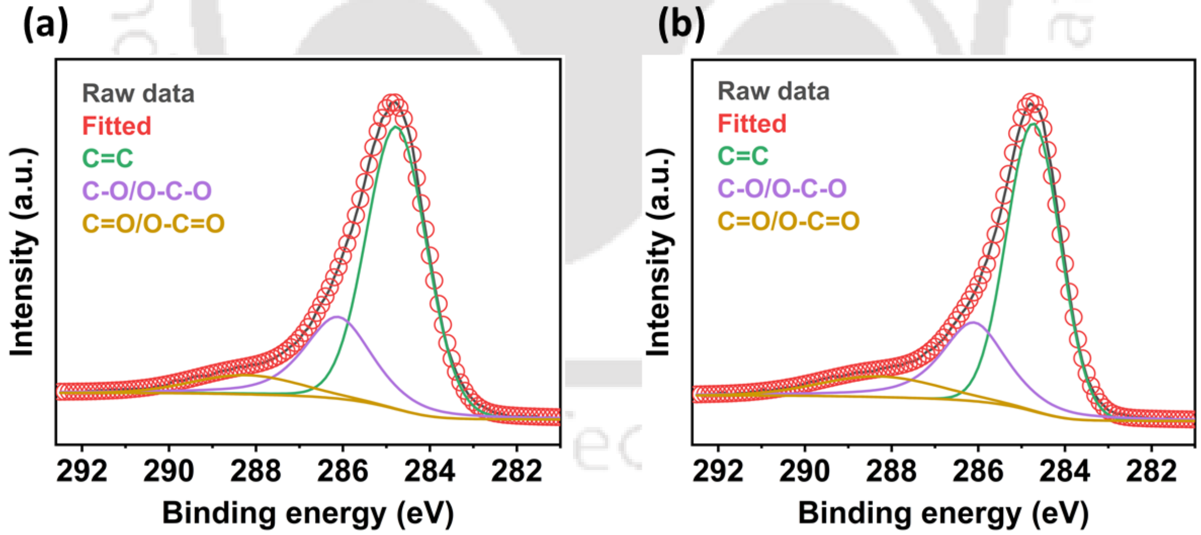

Figure 3.18: C1s XPS spectra of (a) lGNL and (b) mGNL.

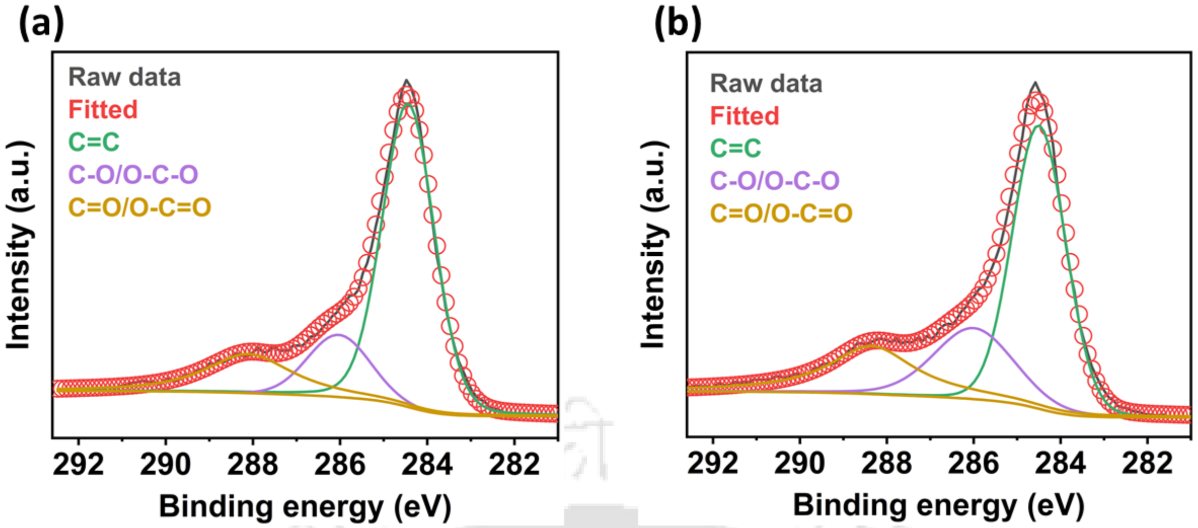

Figure 3.19: C1s XPS spectra of (a) PGNL$_{2min}$ and (b) PGNL$_{10min}$.

Ultrafast current pulse-induced electro-reduction strategy was employed to recover the graphitization level of PGNL$_{5min}$. The C1s spectra, after two consecutive 50 ms current pulse-assisted electro-reduction derived r$_2$PGNL$_{5min}$, exhibited a significant reduction of relative percentile of C-O/C-O-C and C=O/O-C=O type functional groups (**Figure 3.17f**) compared to PGNL$_{5min}$. The contribution of C-O/C-O-C and C=O/O-C=O groups drop to 15% from 21% and 8% from 19%, respectively. Conversely, the C=C sp^2 carbon contribution jumps to 77% from 59%, establishing the electro-reduction process as a graphitization recovery process. Remarkably, the graphitization recovery increases with the increase in the number of electro-reduction current pulses, which may vary from a single pulse (r$_1$PGNL$_{5min}$) to two (r$_2$PGNL$_{5min}$) to four (r$_4$PGNL$_{5min}$) successive pulses. While r$_1$PGNL$_{5min}$ witnessed a minimal recovery, as indicated by C1s spectra (**Figure 3.20a**), r$_2$PGNL$_{5min}$ showed a significant recovery (**Figure 3.17f**), as discussed. Interestingly, r$_4$PGNL$_{5min}$ exhibited a higher graphitization recovery than r$_2$PGNL$_{5min}$, indicated by its C1s spectra (**Figure 3.20b**), implying an almost complete recovery by four consecutive 50 ms electro-reduction pulses.

In brief, the current three-step strategy consisting of electro-graphitization of MOF, electrochemical perforation of MOF-derived GNL, and electro-reduction for graphitization recovery gives a unique platform to generate a highly pore-tunable carbon framework with customized graphitization level. The as-developed ultrafast tunable nanostructures can be used as ready-to-use electrodes for various supercapacitors, e.g., aqueous supercapacitors, water-in-salt (WIS) electrolyte supercapacitors, and a flexible wearable solid-state supercapacitor (SSC).

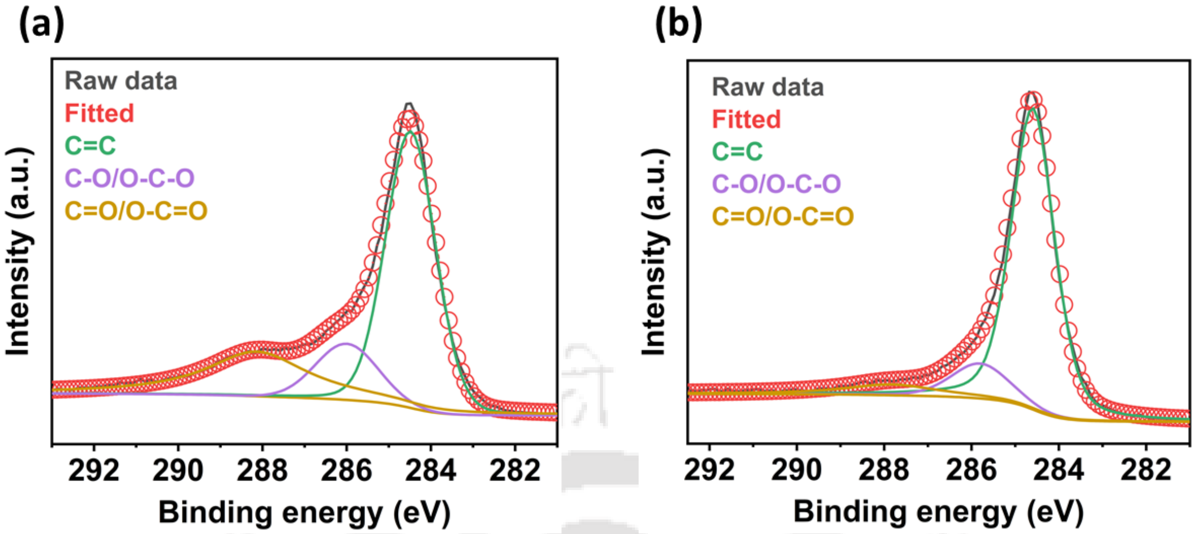

Figure 3.20: C1s XPS spectra of (a) r_1PGNL_{5min} and (b) r_4PGNL_{5min}.

Based on the observations from Raman, FESEM, TEM, BET, MB adsorption experiment, and XPS analyses, the mechanism of pore formation is revealed by the schematic representation in **Figure 3.17g**. In brief, during the electro-graphitization of MOF to develop GNL, in-situ generated Co-nanoparticles are encapsulated by the graphitic layers of the GNL, as shown in the schematic. Applying a positive potential (+2.2V) through GNL during electrochemical perforation (ECP) in 65% HNO_3, the NO_3^- ions are intercalated into the graphitic layers and decoupled. The graphitic layers then become exposed for functionalization with various oxygen-containing groups (-OH, -COOH) due to anodic oxidation during ECP, as presented in the schematic. The breaking of the C-C bond and surface functionalization unzipped the graphitic layers, unveiling the Co-nanoparticles to the strongly acidic environment, which in turn etched out the Co-nanoparticles, as depicted in the schematic. The successful unzipping of the graphitic layers and removing those Co-nanoparticles yielded many voids, creating numerous partially exposed nanopores covered with the functional groups (as shown schematically). Finally, the ultrafast pulsed electro-reduction technique significantly omitted the functional groups, resulting in substantial conductivity restoration and complete exposure of the nanopores.

3.3.2. Electrochemical performance evaluation of the developed supercapacitor devices

Due to the highly conducting GNL's vertical orientation and uniformly distributed dense nanopores all over its surface, the as-developed nanostructures can serve as potential electrodes for various energy storage applications. We have demonstrated their very high performance in aqueous, water-in-salt, and wearable asymmetric supercapacitor applications as proof-of-concepts.

3.3.2.1. performance in aqueous electrolyte

The electrochemical supercapacitor performance of the as-developed electrodes was measured in an aqueous electrolyte (1M H_2SO_4) in symmetric full-cell configurations. The performance was analyzed through cyclic voltammetry (CV), galvanostatic charge-discharge (GCD), and electrochemical impedance spectroscopy (EIS) investigations, and sharp improvement of their performance as compared to pristine GNL was registered. The cyclic voltammograms (**Figure 3.21a**) show that the area under the CV curves of GNL drastically increased after ECP for 2 minutes ($PGNL_{2min}$) and became maximum for 5 minutes ($PGNL_{5min}$). In contrast, after 10 minutes of ECP ($PGNL_{10min}$), the area under the CV curve decreased to even less than that of $PGNL_{2min}$. The higher area of the CV profile of $PGNL_{5min}$ indicates that it has a higher specific capacitance than $PGNL_{2min}$ and $PGNL_{10min}$. The GCD profiles (**Figure 3.21b**) indicate that the $PGNL_{5min}$ sample has the most prolonged discharge duration, suggesting again the highest area-specific capacitance. Estimation of specific capacitances (**Figure 3.22a**) revealed that 2 minutes of ECP increases the capacitance by ~260% (196.2 mF cm^{-2}) as compared to pristine GNL (54.4 mF cm^{-2}), which further increases to ~321% (229.0 mF cm^{-2}) when the ECP time was increased to 5 minutes. A further increase of ECP time to 10 minutes leads to a decline in performance, and the specific capacitance reduces to 190.0 mF cm^{-2}. The observations from CV and GCD profiles signify that the electrochemical perforation of GNL could be an excellent strategy to harness high specific capacitance, and the duration of ECP is critical to achieving optimal energy storage performance. The exhibited high performance can be attributed to an increase in the surface area of GNL due to nanopore formation during the ECP, as discussed earlier. Further, the ECP introduces oxygen functional groups like -OH/-COOH, as revealed by XPS, which can also contribute to pseudocapacitance in the system. A contribution of pseudocapacitance is also evident from the profile of GCD, in which a partial departure from perfect triangular shape, characteristics of purely electrical double-layer type capacitance, was observed. Although the unintentional oxidative functional groups incorporated during ECP via cobalt removal from GNL can positively contribute to the capacitance, its excessive presence can lower the conductivity of graphitic structure and decrease the overall performance, as was observed in the case of $PGNL_{10min}$.

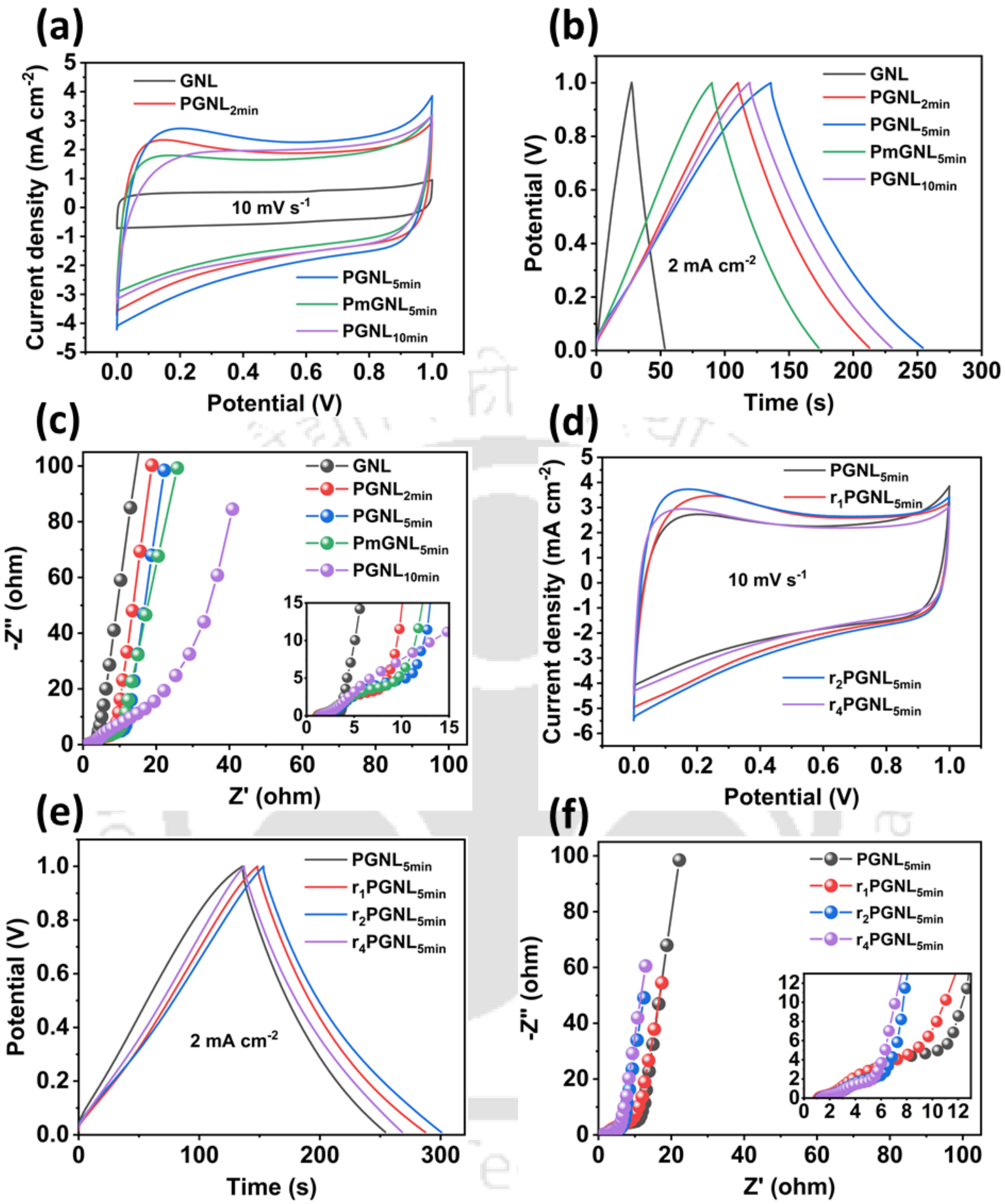

Figure 3.8: Electrochemical supercapacitor performance evaluation of the symmetric cell in aqueous electrolyte (1M H_2SO_4). (a) Cyclic voltammetry (CV) curves of ECP-derived porous GNLs (PGNLs) in comparison to pristine GNL, (b) corresponding galvanostatic charge-discharge (GCD) profiles, and (c) electrochemical impedance spectroscopy (EIS) plots, (d) CV curves of electro-reduced PGNLs (rPGNL$_{5min}$) in comparison with the parent PGNL$_{5min}$, (e) corresponding GCD profiles, and (f) EIS plots.

Electrochemical impedance spectroscopy (EIS) was used to analyze the impedance offered by the as-developed samples and gain insight into the charge storage behavior. The EIS Nyquist plots of GNL, $PGNL_{2min}$, and $PGNL_{5min}$ exhibit nearly vertical characteristics at low frequencies from 0.01 Hz to 10 Hz, which indicates almost ideal capacitive behavior (**Figure 3.21c**). However, the Nyquist plot of $PGNL_{10min}$ deviates significantly from the vertical behavior at lower frequencies, indicating its poor capacitive performance. The presence of slopes at 45^o for all the ECP-activated samples in the mid-frequency region (from 10 Hz to 100 Hz) results from the distributed resistance of porous carbon electrodes.[28] The electrochemical series resistances (ESR) are obtained from higher frequency regions, and it shows the following sequence: GNL< $PGNL_{2min}$< $PGNL_{5min}$<$PGNL_{10min}$. The ESR includes the electrolyte resistance, electrode-electrolyte interface resistance, and collector-electrode contact resistance.[28,29] Since the same electrolytes were used without any additional current collectors for the cases, the increase in ESR values indicates an increase in electrode resistance with increased electrochemical activation times. This monotonic increase in electrode resistance with electrochemical activation duration resulted from incorporating a higher content of functional groups and pores, which reduces the graphitic sp^2 nature of carbon.[23] The lowering of performance in $PGNL_{10min}$ can be attributed to a significant decrease in conductivity due to excessive activation, as evident from its highest ESR value. Comparative electrochemical studies were conducted on low and moderate graphitized samples, keeping the optimal activation time of 5 min ($PlGNL_{5min}$ and $PmGNL_{5min}$) to validate the role of the graphitization level of MOFs. The moderately graphitized GNL (mGNL) after 5 minutes of oxidation ($PmGNL_{5min}$) exhibited a significantly smaller area under the CV curve and a shorter discharge duration (**Figure 3.21a**, **b**) as compared to its higher graphitized counterpart ($PGNL_{5min}$). The maximum specific capacitance of the $PmGNL_{5min}$ was estimated to be 169.2 mF cm^{-2}, much smaller than the fully graphitized GNL counterpart (229.0 mF cm^{-2}). The origin of the lower performance of $PmGNL_{5min}$ is evident in its EIS spectra. The EIS of $PmGNL_{5min}$ is leaning towards the Z' axis more, indicating its lower supercapacitor performance than $PGNL_{5min}$. The lower performance of $PmGNL_{5min}$ as compared to $PGNL_{5min}$ can be attributed to a lower degree of perforation, as suggested by FESEM, TEM images, and BET surface area, and low conductivity, as indicated by higher ESR (9.18 Ω) obtained from Nyquist plot. Thus, the above studies reveal that the novel electrochemical oxidation cum perforation of ultrafast electro-graphitized GNL is a significantly effective way to improve the capacitance, and $PGNL_{5min}$ obtained from the highest graphitized structure with 5 min of electro-activation can exhibit the best performance with a capacitance increase as high as ~321% (from 54.4 to 229.0 mF cm^{-2})

as compared to GNL. The oxidation of GNL leads to perforation of the surface and incorporation of oxygen-containing functional groups, as discussed earlier. The heavy incorporation of functional groups and defects into the GNL resulted in lower conductivity, affecting supercapacitor device performance. We have shown here that the performance of the supercapacitor can be significantly enhanced by the de-functionalization of PGNL$_{5min}$ and graphitic structure restoration through its programmed ultrafast Joule heating.

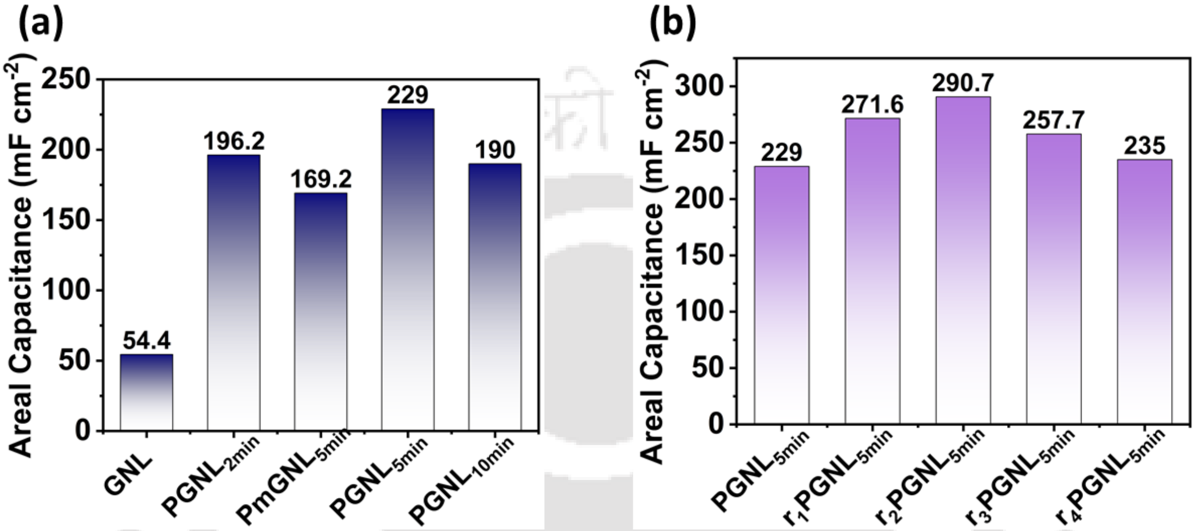

Figure 3.22: Bar diagrams of the areal capacitance of the symmetric cell made of (a) PGNLs with varying ECP durations compared to pristine GNL and (b) rPGNL$_{5min}$s with a varying number of electro-reduction pulses compared to the parent PGNL$_{5min}$.

An ultrafast electro-reduction of 50 ms pulse duration was conducted to restore the conductivity. The supercapacitor performance was optimized by varying the number of electro-reduction pulses (r$_1$: single reduction pulse, r$_2$: two successive reduction pulses, and r$_4$: four such pulses). The CV curves (**Figure 3.21d**) and GCD profiles (**Figure 3.21e**) of the electro-reduced samples suggest that the specific capacitance significantly increases after electro-reduction (**Figure 3.22b**). The capacitance became maximum for the sample electro-reduced by just two successive 50 ms current pulses (r$_2$PGNL$_{5min}$) due to increased conductivity, as suggested by lowering of ESR (from 10.41 Ω to 5.97 Ω) in EIS spectra (**Figure 3.21f**). Despite the increasing conductivity suggested by EIS (**Figure 3.21f**), applying further reduction pulses reduces specific capacitance in r$_4$PGNL$_{5min}$ due to over-healing of the defects incorporated by the generated nanopores, leading to loss of surface area and hence the lower capacitance. The capacitance increases from 229.0 mF cm^{-2} for the PGNL$_{5min}$, 271.6 mF cm^{-2} for r$_1$PGNL$_{5min}$ to 290.7 mF cm^{-2} for r$_2$PGNL$_{5min}$ and decreases to 257.7 mF cm^{-2} for r$_3$PGNL$_{5min}$, 235.0 mF cm^{-2} for r$_4$PGNL$_{5min}$. Likewise, the PGNL$_{2min}$ (**Figure 3.23**) and PGNL$_{10min}$ (**Figure 3.24**) samples and their reduced counterparts exhibited a similar trend in capacitance and conductivity, as CV curves, GCD profiles, and EIS spectra suggested. The maximum specific capacitances of r_2PGNL_{2min} and r_2PGNL_{10min} are 228.0 mF cm^{-2} and 271.9 mF cm^{-2}, respectively, significantly less than the r_2PGNL_{5min}.

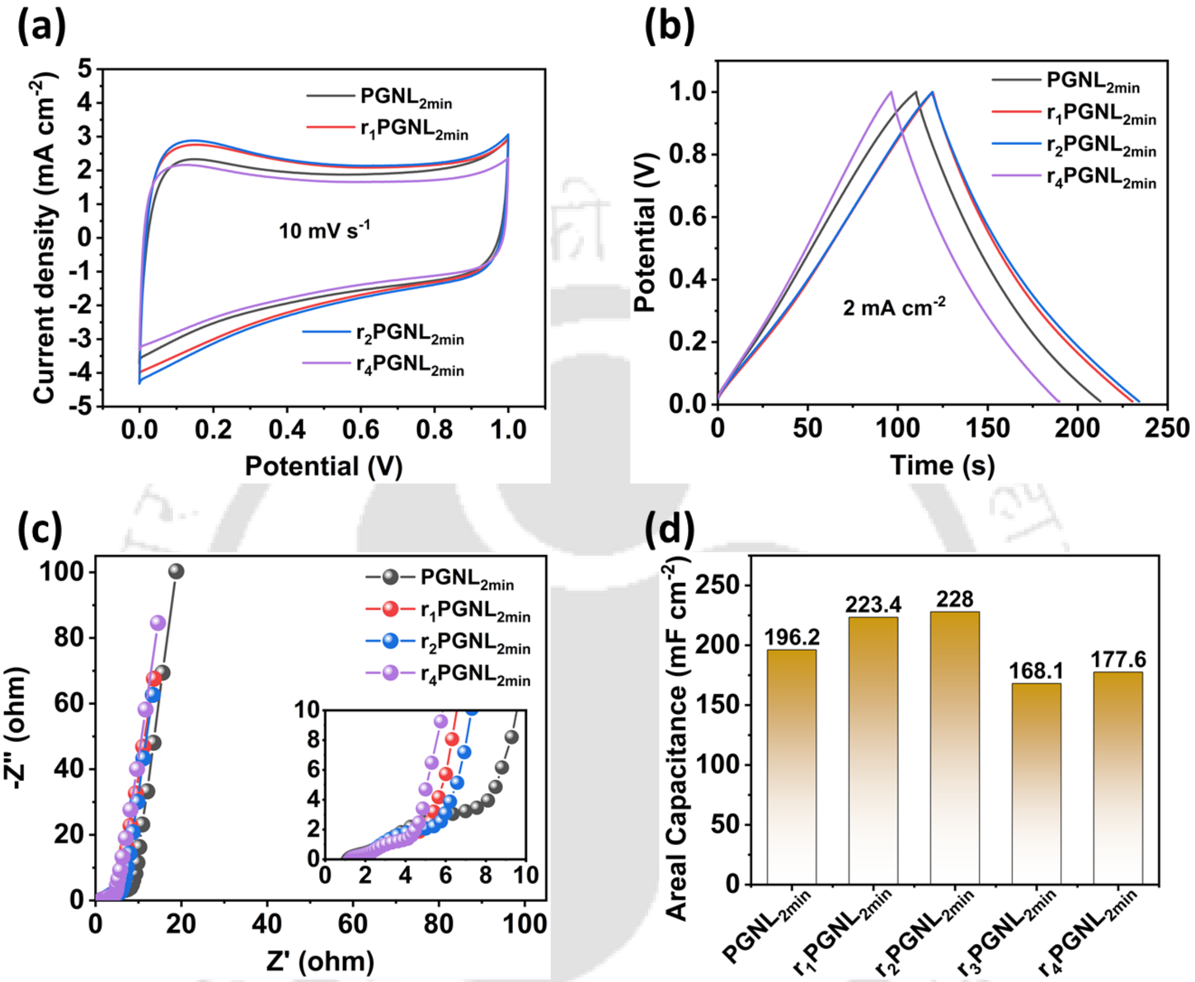

Figure 3.23: Electrochemical performance of the symmetric cell made of $PGNL_{2min}$ and variation of its performance with increased electro-reduction pulses. (a) Cyclic voltammetry (CV) curves, (d) galvanostatic charge-discharge (GCD) profiles, (c) electrochemical impedance spectroscopy (EIS), (d) corresponding bar diagram of areal capacitances.

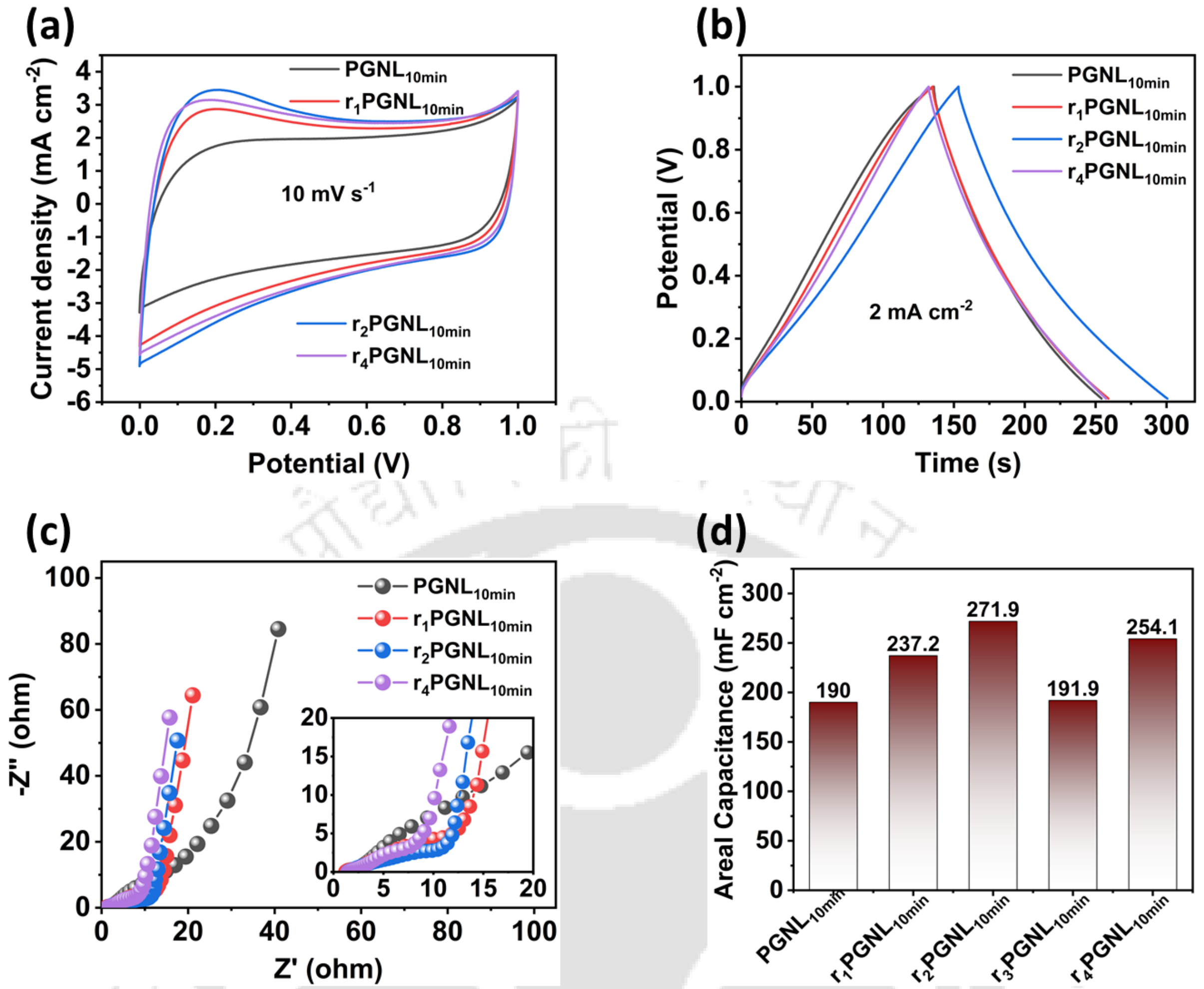

Figure 3.24: Electrochemical performance of the symmetric cell made of PGNL$_{10min}$ and variation of its performance with increased electro-reduction pulses. (a) Cyclic voltammetry (CV) curves, (d) galvanostatic charge-discharge (GCD) profiles, (c) electrochemical impedance spectroscopy (EIS), (d) corresponding bar diagram of areal capacitances.

CV curves were recorded at different scan rates, and then the values of capacitances were estimated from those CV curves. Finally, the capacitance values were plotted against the scan rates to obtain the device's rate performance curve and evaluate the supercapacitor devices' fast charge-discharge capability. The CV curves of GNL (**Figure 3.25a**) suggest that the area under the curves linearly increases with the gradual increase in scan rates. The CV curves maintain the initial rectangular shape due to the superior conductivity of GNL, meaning high capacity retention even at a high scan rate. On the other hand, the CV curves of PGNLs derived by ECP durations of 2 minutes and 5 minutes (**Figure 3.25b-d**) could not maintain the proper linear increase in the area under the curve with the gradual increase in scan rate. The CV curves could not preserve their original rectangular shape and slightly deviated from the initial shape due to less conductivity of oxidized GNL than pristine GNL.

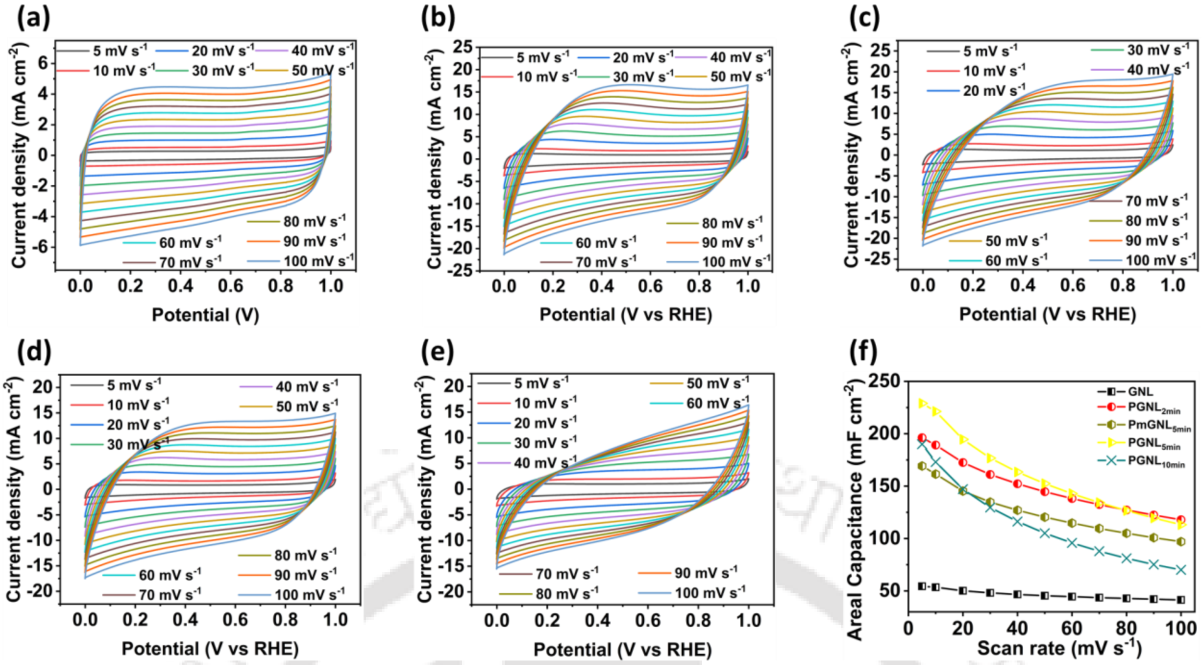

Figure 3.25: CV curves at different scan rates of the symmetric cell for (a) GNL, (b) PGNL$_{2min}$, (c) PmGNL$_{5min}$, (d) PGNL$_{5min}$, and (e) PGNL$_{10min}$, (f) corresponding rate performance curves.

The CV curves of the 10-minute ECP-derived PGNL$_{10min}$ (**Figure 3.25e**) indicate that the higher scan rates curves deviate significantly from their lower scan rates shape, meaning a significant loss of capacitance at high scan rates as 100 mV s^{-1}. The rate performance curves (**Figure 3.25f**) indicate that GNL has the highest rate performance with a capacity retention of as high as 77.4 % at 100 mV s^{-1} of its initial capacitance. Still, the capacitance value of GNL is much lower than the perforated GNLs (PGNLs). However, depending on their conductivity, the capacity retention at 100 mV s^{-1} is the worst (only 40.5 %) for PGNL$_{10min}$ and worse for PGNL$_{5min}$ (51.2 %), and for PGNL$_{2min}$ is 62.3 % which is reasonable. As we have discussed earlier, the conductivity of the sample increases with the gradual increase in the number of electro-reduction pulses. As indicated by the CV curves of rPGNL$_{2min}$s and the rate performance curves (**Figure 3.26**), the capacity retention is significantly improved to a maximum of (73.3 %) due to restoration of conductivity while applying four successive current pulses (50 ms) for reduction.

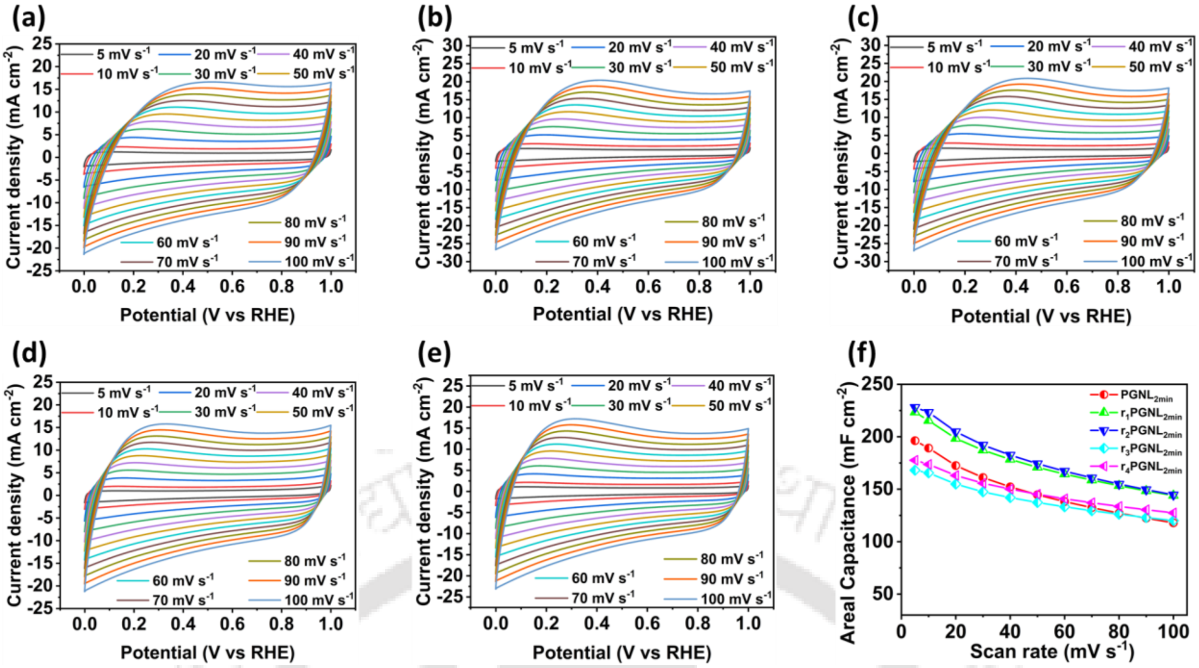

Figure 3.26: Electrochemical performance of the symmetric cell made of $PGNL_{2min}$ and variation of its performance with increased electro-reduction pulses. CV curves at different scan rates of (a) $PGNL_{2min}$, (b) r_1PGNL_{2min}, (c) r_2PGNL_{2min}, (d) r_3PGNL_{2min}, and (e) r_4PGNL_{2min}, (f) corresponding rate performance curves.

However, capacitance's absolute value increases with a single pulse to two consecutive pulses. Despite the conductivity improvement, it decreases to a lower value after multiple (three/four) pulses because with an increase in the number of current pulses, the Joule heating will be higher, and the exfoliated graphitic layers can be restacked during the reduction at this elevated temperature, which in turn results in significantly lesser surface area. Therefore, there is a competition between the conductivity and the surface area, affecting the specific capacitance of the devices. Interestingly, the oxidized GNL, electro-reduced by two successive current pulses of 50 ms (r_2PGNL_{2min}), exhibited the optimized capacitance value (228.0 mF cm^{-2}) with a reasonable rate performance (66.8 % at 100 mV s^{-1}).

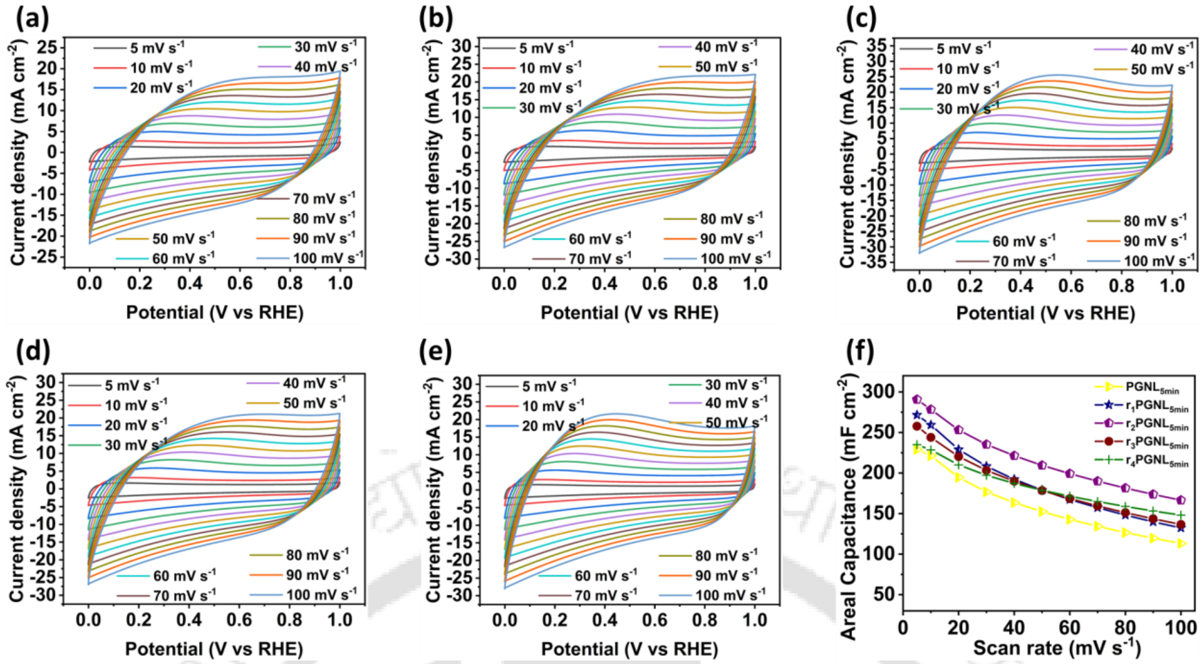

Figure 3.27: Electrochemical performance of the symmetric cell made of $PGNL_{5min}$ and variation of its performance with increased electro-reduction pulses. CV curves at different scan rates of (a) $PGNL_{5min}$, (b) r_1PGNL_{5min}, (c) r_2PGNL_{5min}, (d) r_3PGNL_{5min}, and (e) r_4PGNL_{5min}, (f) corresponding rate performance curves.

Similarly, for $PGNL_{5min}$, the rate performances also improved with the increase in the reduction step, as suggested by the CV and rate performance curves (**Figure 3.27**). The optimized sample (r_2PGNL_{5min}) has the highest specific capacitance (290.7 mF cm^{-2}) among all the samples developed with a reasonable rate performance, having capacity retention of 60 % at a high scan rate of 100 mV s^{-1}. The highest reduced sample (r_4PGNL_{5min}) has a comparably smaller capacitance of 235.0 mF cm^{-2} and has the highest rate performance with a capacity retention of 64.8 %. Likewise, in $PGNL_{10min}$, the rate performance showed a similar trend, as indicated by the CV and rate performance curves (**Figure 3.28**). The sample reduced by two successive pulses (r_2) has a higher capacitance (271.9 mF cm^{-2}) compared to the other samples ($PGNL_{10min}$, r_1PGNL_{10min}, and r_4PGNL_{10min}) with a capacity retention of 49.7 %, whereas, the rate performance is more significant for r_4PGNL_{10min} with a capacity retention of 55.8 % and a capacitance value of 254.1 mF cm^{-2}. Notably, the performance of the aqueous symmetric cell is better than most of the reported aqueous symmetric supercapacitor devices made of MOF-derived porous carbon.

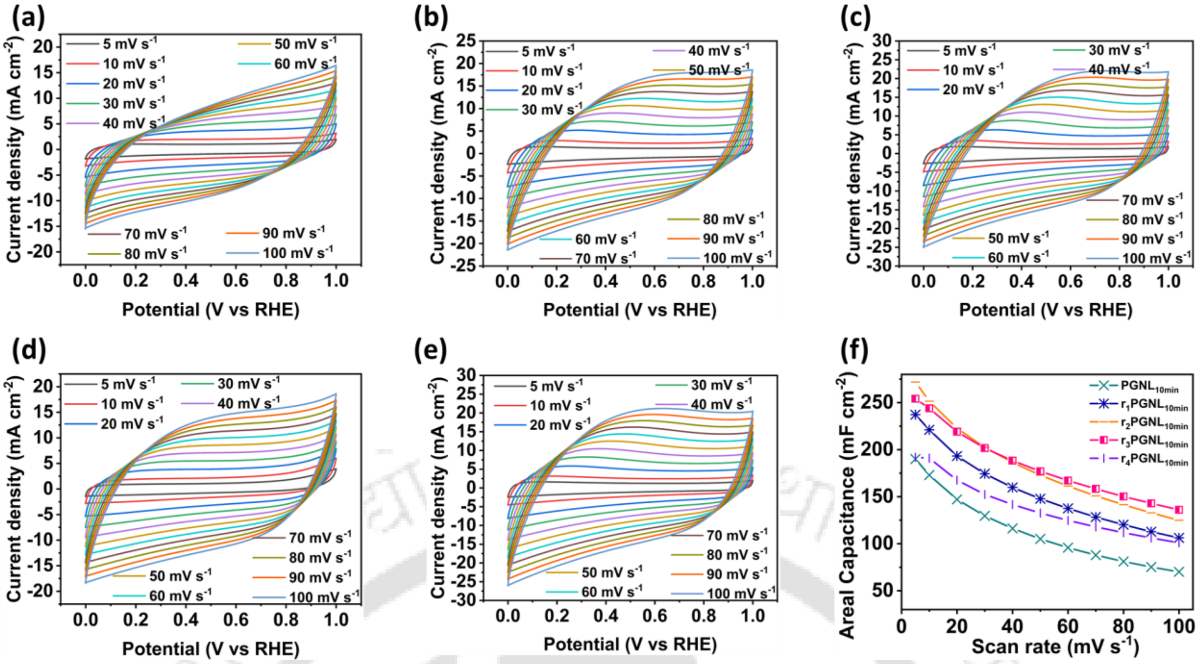

Figure 3.28: Electrochemical performance of the symmetric cell made of PGNL$_{10min}$ and variation of its performance with increased electro-reduction pulses. CV curves at different scan rates of (a) PGNL$_{10min}$, (b) r$_1$PGNL$_{10min}$, (c) r$_2$PGNL$_{10min}$, (d) r$_3$PGNL$_{10min}$, and (e) r$_4$PGNL$_{10min}$, (f) corresponding rate performance curves.

3.3.2.2. Performance in water-in-salt (WIS) electrolyte: a high-energy-density supercapacitor device with an extended voltage window up to 2.3 V

Until now, we have discussed supercapacitor device applications in aqueous electrolytes, where a supercapacitor only has a standard voltage window of 1 V, which limits the energy density. This limitation of the voltage window is to avoid hydrogen and oxygen evolution reactions (HER and OER) in aqueous electrolytes during the operation of the supercapacitor, which sets a thermodynamic potential window of 1.23V. Recently, extensive research has been done to break this intrinsic limit to widen the potential window and significantly increase the energy density. The discovery of water-in-salt (WIS) electrolytes is among them, in which the supercapacitor device's voltage window can be extended beyond 1.23 V. In the WIS electrolyte, the mass of the solute (in this case, $NaClO_4$) is significantly higher than the solvent's (water) mass. Fewer water molecules are available to make the solvation shell of Na^+ and ClO^{4-} ions in the WIS electrolyte. This intrinsic change in the solvation structure leads to very little activity of water around the electrode, which retarded the HER and OER by shifting their onset potentials beyond thermodynamic limits. The potential window of different samples in WIS was checked by LSV curves (**Figure 3.29a**) by considering the permissible voltage range in which there is no water dissociation. The LSV curves suggest that the potential window is the lowest for pristine GNL (1.52 V). In this sample, the presence of Co-nanoparticles starts HER activity at lower potentials by serving as catalysts, which is evident from the lower onset of HER. After removing the Co nanoparticles by ECP, the voltage window was successfully broadened, although narrowed with the increasing oxidation time due to the formation of defects, which could also act as catalysts for water dissociation.[30] However, after two successive electro-reduction steps, the voltage window of r_2PGNL_{5min} becomes reasonably high (2.3 V). The best-performing sample in aqueous electrolyte r_2PGNL_{5min} was chosen for electrochemical supercapacitor device application in WIS electrolyte for extended voltage-window and high energy density.

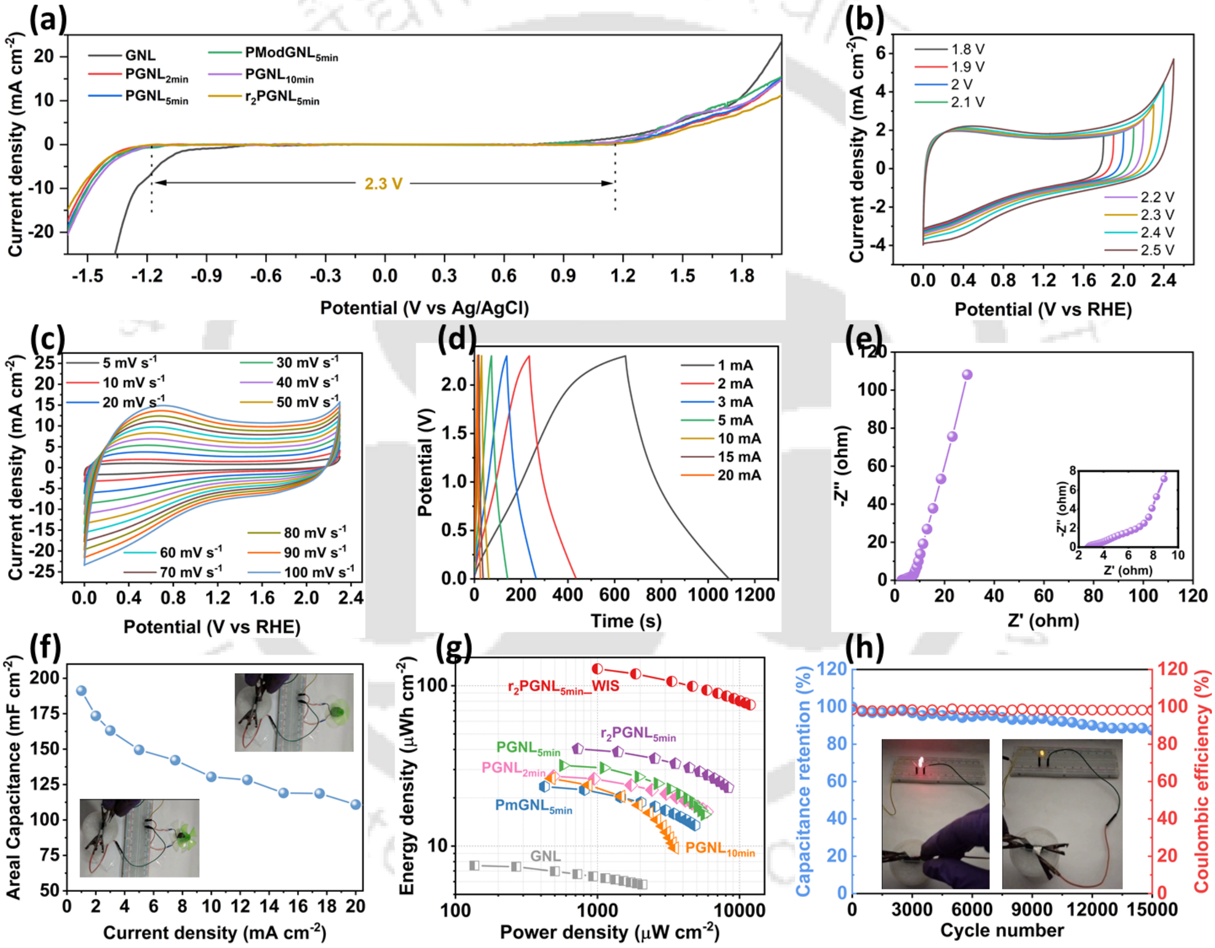

Figure 3.9: Electrochemical supercapacitor performance evaluation of the symmetric cell in water-in-salt (WIS) electrolyte (17m $NaClO_4$). (a) Linear sweep voltammetry (LSV) curves showing potential window variation for different as-developed electrodes, (b) CV curves of the best-performing r_2PGNL_{5min} with varying potential windows (from 1.8 to 2.5 V), (c) CV curves at different scan rates of the best-performing r_2PGNL_{5min} with an impressive potential window of 2.3 V, (d) corresponding GCD profiles, and (e) EIS plot, (f) supercapacitor rate performance of the best-performing r_2PGNL_{5min} with varying GCD current densities, (g) Ragone plot for

comparison of energy and power density of symmetric devices for different electrodes in aqueous (1M H_2SO_4) and WIS (17m $NaClO_4$) electrolytes, (h) Charge-discharge stability of the best-performing r_2PGNL_{5min} based cell at a constant current density of 20 mA cm^{-2} (inset: exhibition of the WIS device powering a fan and LEDs).

The cyclic voltammetry with the varying potential window (1.8-2.5 V) (**Figure 3.29b**) was recorded for the best-performing sample. Up to 2.3 V, the polarization current is not much higher than 2.4 V and beyond, so 2.3 V was chosen as the voltage window for further supercapacitor applications. The CV curves of the WIS device with varying scan rates (**Figure 3.29c**) suggested a linear increment of the area under the curve with increasing scan rates up to 100 mV s^{-1}. The CV profiles maintain their shape even at a scan rate as high as 100 mV s^{-1}, suggesting good rate performance. The GCD profiles with varying currents (**Figure 3.29d**) also indicate the device's good charge-discharge capability. The steeper rise of the EIS spectrum (**Figure 3.29e**) suggests minimal ion transport resistance of the device. The WIS device has a maximum specific capacitance of 173.5 mF cm^{-2} at 5 mV $s^{-1,}$ and the capacity retention was as high as 64.1 % at a reasonably high scan rate of 100 mV s^{-1}, as suggested by the rate performance curve (**Figure 3.29f**). The Ragone plot (**Figure 3.29g**) indicated that the maximum energy density (power density) of GNL as an aqueous supercapacitor device can be improved from 7.56 μWh cm^{-2} (2070.0 μW cm^{-2}) to 40.4 μWh cm^{-2} (8325.0 μW cm^{-2}), which is almost 5.3 times increment after our novel three-step protocol. Implementing the WIS technique further improved energy density (power density) up to as huge as 127.5 μWh cm^{-2} (11891.0 μW cm^{-2}), almost 3.2 times the energy density of the best-performing sample in aqueous electrolyte. Notably, after 15000 charge-discharge operations, the WIS device preserved nearly 89% of its initial capacitance value (**Figure 3.29h**). The performance of the WIS device is superior to most of the WIS devices reported. It is essential to mention that the high viscosity of WIS electrolytes generally reduces the power density, which is the case here. The open porosity of the as-developed structure with sufficient graphitization resulted in low ion diffusion and electronic resistances, which ensures both high energy and power density in our WIS system. As a practical demonstration of the merit of the as-developed materials, supercapacitors based on r_2PGNL_{5min} were developed in WIS electrolyte, which can run an electronic fan and LEDs (inset of **Figure 3.29f**, **h**).

3.3.2.3. performance of asymmetric solid-state supercapacitor (ASSC) device in PVA-gel electrolyte for wearable application

Robust connection of GNL with carbon cloth (CC) substrate through graphitic-graphitic, pulsed Joule heating induced tunable conductivity and open porous structure qualify them as suitable ready-to-use electrode materials for wearable supercapacitor applications. We have developed a high-energy density wearable supercapacitor in an asymmetric device structure using r_2PGNL_{5min} as an anode and a well-known cathode material, MXene ($Ti_3C_2T_x$). The motivation behind designing an asymmetric supercapacitor (ASC) device is to extend the operational potential window, giving rise to higher energy density. The cathode materials (MXene) used here can operate in the potential range (-0.7V to 0.3V), whereas the r_2PGNL_{5min}-based anode can operate in the voltage window 0-1V. These two electrodes' complementary nature helps the ASC operate reliably in the extended potential window of 1.6V. Before the development of the wearable asymmetric solid-state supercapacitor (ASSC), the performance of the MXene-based negative electrode was measured and optimized in an aqueous electrolyte. FESEM images of the as-prepared $Ti_3C_2T_x$@CC electrode have been shown in **Figure 3.30a**. The CV and EIS spectra of $Ti_3C_2T_x$@CC in a three-electrode configuration have been presented in **Figure 3.30b** and **3.30c**, respectively. The areal capacitance of the $Ti_3C_2T_x$@CC electrode is 817.13 mF cm^{-2} at 10 mV s^{-1}.

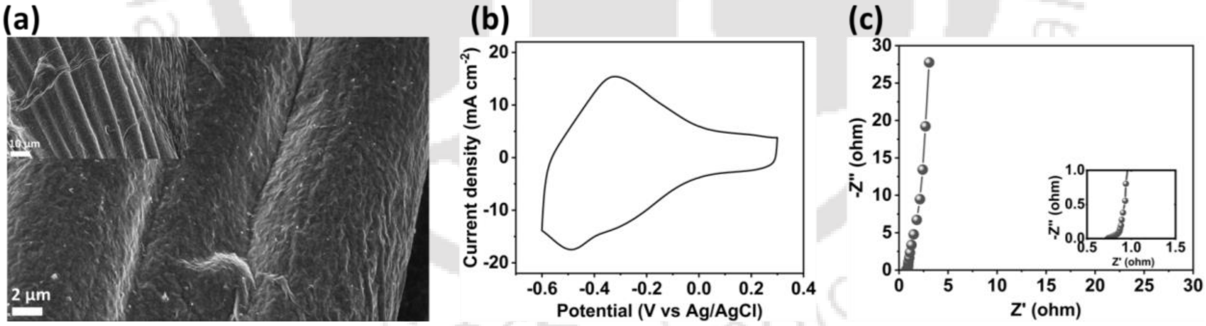

Figure 3.30: Characterization of $Ti_3C_2T_x$@CC negative electrode. (a) FESEM image of $Ti_3C_2T_x$@CC (inset: low magnified FESEM image), (b) CV curve of $Ti_3C_2T_x$@CC in three-electrode configuration at 10 mV s^{-1}, (c) EIS spectra of $Ti_3C_2T_x$@CC electrode.

Finally, a flexible wearable ASSC was developed using PVA/H_2SO_4 as gel electrolytes, which was expected to be a promising flexible energy storage device for wearable electronics. The ASSC device exhibits an extended voltage window of 1.6 V with the advantage of positive r_2PGNL_{5min} and negative $Ti_3C_2T_x$ @CC electrodes (**Figure 3.31a**). GCD curves at 5 mA cm^{-2} were recorded for different voltage windows to test the operationality of ASSC at any potential window from 1 to 1.8 V (**Figure 3.31b**). Notably, the ASSC could operate at a maximum voltage window of 1.6 V, as the GCD profiles maintained their original shapes (coulombic efficiency is almost 100%) up to 1.6 V without polarization due to water dissociation. After 1.6 V, the charging time became slower than the discharging time, making the coulombic efficiency less than 100% due to water dissociation. The CV curves and the GCD profiles of the ASSC retain their original shape even at the higher scan rate of 100 mV s^{-1} and high current density of 20 mA cm^{-2}, respectively (**Figure 3.31c**, **d**), suggesting a quick charge-discharge capability. The EIS spectra of the ASSC have a small semicircle (R_{ct}) in the high-frequency region and an almost vertical slope in the low-frequency region (**Figure 3.31e**), suggesting fast charge transfer and ion diffusion of the porous r_2PGNL_{5min} and $Ti_3C_2T_x$ @CC electrodes.

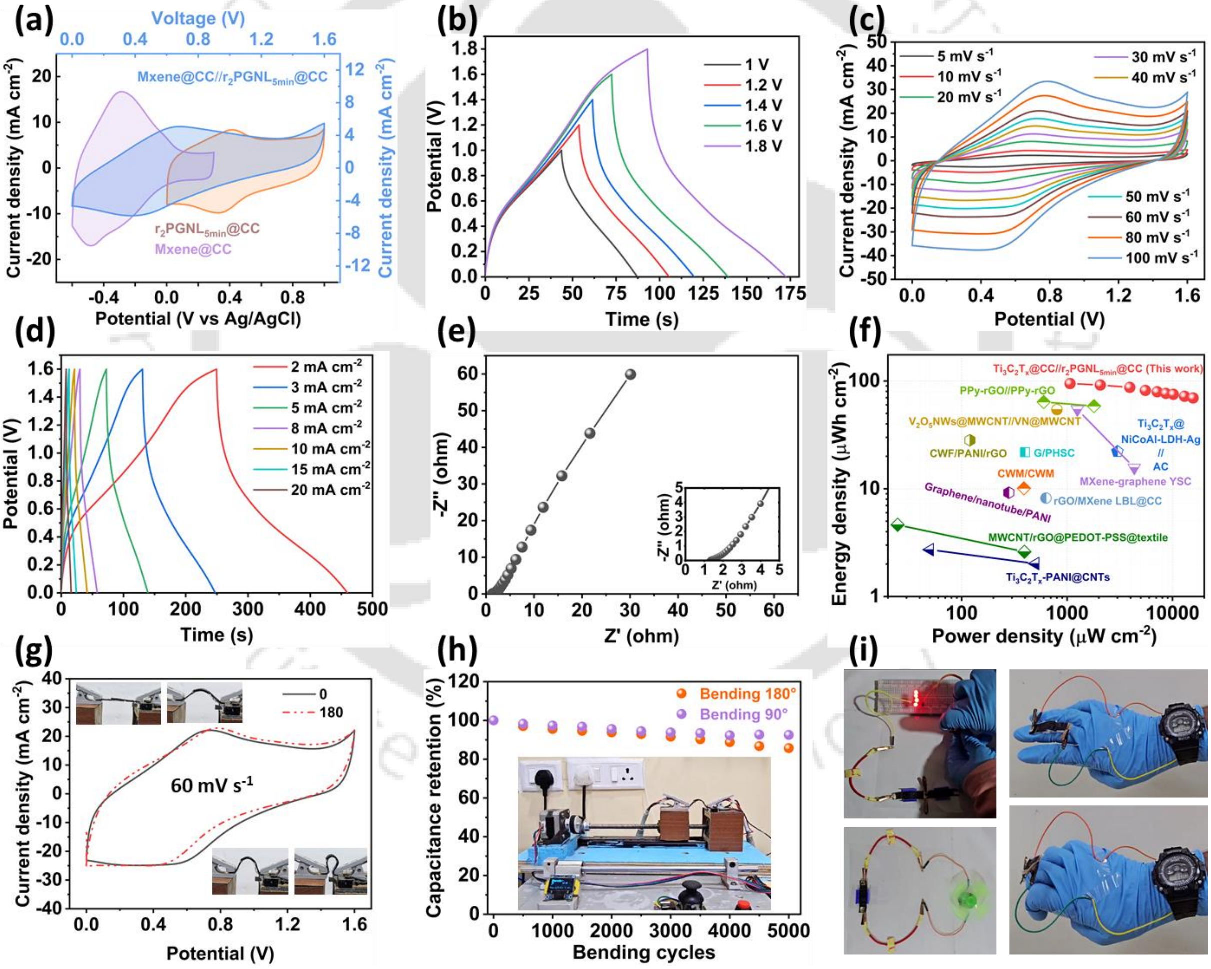

Figure 3.31: Electrochemical Performance of the asymmetric solid-state supercapacitor device in H_2SO_4-PVA gel electrolyte. (a) CV curves of $Ti_3C_2T_x$@CC, r_2PGNL_{5min}@CC in three-electrode configuration, and assembled asymmetric solid-state supercapacitor (ASSC) at 10 mV s^{-1}, (b) GCD profiles of the ASSC measured over the operating voltage windows ranging from 1 to 1.8 V at 5 mA cm^{-2}, (c) CV curves of the ASSC at varying scan rates with a voltage

window of 1.6 V, (d) GCD profiles for various current densities, (e) EIS Nyquist plot of ASSC (inset: magnified version of high-frequency region), (f) Ragone plot of the ASSC compared to the other state-of-the-art ASSC, (g) CV curves of ASSC under different bending conditions at 10 mV s^{-1}, (h) bending stability test for 5000 continuous repeated bending cycles, (i) digital photograph of the ASSC driving a fan, powering four LED lights, operating a digital watch at different deformed state.

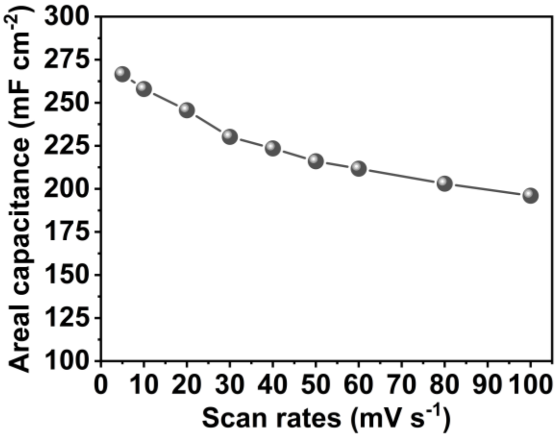

Figure 3.32: Rate performance of the SSC.

The ASSC showed a maximum areal capacitance of 266.6 mF cm^{-2} at a scan rate of 5 mV s^{-1}. It exhibited excellent capacity retention of 73.5% (**Figure 3.32**) at a high scan rate of 100 mV s^{-1}. Moreover, the ASSC can deliver a maximum energy density of 94.8 µWh cm^{-2} at a power density of 1066.4 µW cm^{-2}, which is more than two times the areal energy density of the symmetric device and superior to most of the state-of-the-art solid-state GNs/MXene asymmetric supercapacitors (**Figure 3.31f**, **Table 3.3**). Even at the maximum power density of 15680.0 µW cm^{-2}, it retains an energy density of 69.7 µWh cm^{-2}. To bring the ASC into practical applications in powering wearable electronics, it should be capable of delivering stable energy storage performance during extreme mechanical conditions (0° to 180° bending) (inset of **Figure 3.31g**). The CV curves (at 60 mV s^{-1}) recorded for different bending angles (**Figure 3.31g**) depicted almost no change in shapes and areas, confirming the robustness and great flexibility of the device. The ASC retained nearly 92.5% and 85.7% capacity after 5000 times bending at 90° and 180°, respectively, suggesting the outstanding durability of the device (**Figure 3.31h**). To demonstrate the device's practical applicability, the ASSC was utilized to power an electronic fan, LEDs, and a wristwatch under repeated bending (**Figure 3.31i**). The performance chart of all the as-developed energy storage supercapacitor devices is included in **Table 3.4**.

Table 3.3: Comparison table for the electrochemical performance of the flexible and wearable solid-state symmetric/asymmetric (carbon nanostructure/MXene-based) devices.

Devices	V (V)	Test condition	Areal capacitance (mF cm^{-2})	Maximum Energy density (µWh cm^{-2})	Maximum Power density (µW cm^{-2})	Ref
$Ti_3C_2T_x$@NiCoAl-LDH-Ag // AC	1.5	0.25 mA cm^{-2} 1 mA cm^{-2}	71 55	22.18	3000	[1]
$Ti_3C_2T_x$-PANI@CNTs	1	0.1 mA cm^{-2} 1 mA cm^{-2}	78.2 58.08	2.72 2.02	50 500	[2]
CWF/PANI/rGO	1	1 mA cm^{-2} 20 mA cm^{-2}	197.6 119.2	28.21	120	[3]
Graphene/nanotube/PANI	0.8	0.1 mA cm^{-2} 0.7 mA cm^{-2}	164 122	9.196	280	[4]
PPy-rGO//PPy-rGO	1.2	1 mA cm^{-2} 20 mA cm^{-2}	320 264	63.9 58.58	600 1800	[5]
CWM//CWM		1 mA cm^{-2} 20 mA cm^{-2}	118 92.28	10.1	389.9	[6]
MXene-graphene YSC	0.8	5 mV s^{-1} 100 mV s^{-1}	367.3 137.46	54.5 15.7	1251.5 4335.9	[7]
rGO/MXene LBL@CC	1.2	0.02 mA cm^{-2} 0.7 mA cm^{-2}	40.8 10.5	8.2	630.1	[8]
G/PHSC		1 mA cm^{-2} 5 mV s^{-1}	245.5 335.4	21.82	400	[9]
MWCNT/rGO@PEDOT-PSS@textile	1	0.025 mA cm^{-2} 2 mA cm^{-2}	30.4 20.2	4.63 2.60	24.7 393.5	[10]
V_2O_5NWs@MWCNT // VN@MWCNT	1.6	1 mA cm^{-2} 16 mA cm^{-2}	152.7 116	54.30	801.4	[11]
r_2PGNL_{5min}@CC // $Ti_3C_2T_x$@CC	1.6	5 mV s^{-1} 100 mV s^{-1}	266.6 196.0	94.80 69.70	1066.4 15680.0	This Work

Table 3.4: Electrochemical performance chart of the as-developed supercapacitor devices.

Devices	C@5 mV s^{-1} (mF cm^{-2})	C@100 mV s^{-1} (mF cm^{-2})	C-retention @100 mV s^{-1} w.r.t 10 mV s^{-1}	E@5 mV s^{-1} (μWh cm^{-2})	E@100 mV s^{-1} (μWh cm^{-2})	P@5 mV s^{-1} (μW cm^{-2})	P@100 mV s^{-1} (μWh cm^{-2})
GNL	54.4	41.4	77.4%	7.56	5.8	136.0	2070.0
$PGNL_{2min}$	196.2	117.9	62.3%	27.3	16.4	490.5	5895.0
r_1PGNL_{2min}	223.4	144.0	66.8%	31.0	20.0	558.5	7200.0
r_2PGNL_{2min}	228.0	144.6	64.8%	31.7	20.1	570.0	7230.0
r_4PGNL_{2min}	177.6	127.4	73.3%	24.7	17.7	444.0	6370.0
$PGNL_{5min}$	229.0	113.2	51.2%	31.8	15.7	572.5	5660.0
$PmGNL_{5min}$	169.2	97.0	60.1%	23.5	13.5	423.0	4850.0
r_1PGNL_{5min}	271.6	132.3	51.0%	37.7	18.4	679	6615.0
r_2PGNL_{5min}	290.7	166.5	60.0%	40.4	23.1	726.8	8325.0
r_4PGNL_{5min}	235.0	148.1	64.8%	32.6	20.6	587.5	7405.0
$PGNL_{10min}$	190.0	70.1	40.5%	26.4	9.7	475.0	3505.0
r_1PGNL_{10min}	237.2	106.2	48.0%	32.9	14.8	593.0	5310.0
r_2PGNL_{10min}	271.9	124.9	49.7%	37.8	17.3	679.8	6245.0
r_4PGNL_{10min}	254.1	136.0	55.8%	35.3	18.9	635.3	6800.0
r_2PGNL_{5min} _WIS	173.5	103.4	64.1%	127.5	76.0	997.6	11891.0
ASSC	266.6	196.0	73.5%	94.8	69.7	1066.4	15680.0

3.4. Conclusion

Here, we demonstrated an ultrafast current pulse-programmed processing (PJH) scheme in combination with electrochemical perforation (ECP) to develop conducting graphitic nanoleaves from metal-organic frameworks (MOFs) with precisely tunable graphitization levels and porosity. Compared to conventional processing that generates low graphitic carbon, this unique scheme generates the continuously tunable low to the highest level of graphitic order in MOF-derived carbon (GNLs), as evidenced by a sharp decrease in I_D/I_G ratio from

1.16 to 0.64. The removal of in-situ generated cobalt nanoparticles from the system using the ECP strategy leads to the incorporation of size-controlled pores (3-10 nm) within GNLs ($PGNL_{x\ min}$, x=2, 5,10 min) depending on PJH-tunable Co particle sizes (3.5-15 nm). The decrement in graphitic order during ECP-induced pore incorporation was again retrieved in a controlled way by passing a number (r_y, y=1-4) of ultra-short pulses of 50 ms duration (r_yPGNL_{xmin}). Such unique sequential processing of graphitization tuning, pore incorporation, and again graphitization retrieval can ensure adjustable conductivity and porosity in MOF-derived carbon nanostructures, which can have a wide range of applications in energy storage and catalysis. As a proof of concept, such r_yPGNL_{xmin} have shown to be ready-to-use materials for high-performance energy storage in all different categories of supercapacitors, namely aqueous, water-in-salt, and wearable devices, demonstrating their high potential. The r_2PGNL_{5min} enhances capacitance (290.7 mF cm^{-2}) by 434% compared to pristine GNLs (54.4 mF cm^{-2}), originating from the high surface area and tunable conductivity. The LSV analysis suggests that the HER onset potential can be pushed to higher voltages depending on the graphitization recovery level due to the reduction in functional groups and healing of defects, which can initiate catalysis. The higher onset HER potential allows WIS-based supercapacitors to operate in a wider potential window up to 2.3 V, thereby displaying a high energy density of 127.5 μWh cm^{-2}, which is much higher as compared to 40.4 μWh cm^{-2} for aqueous supercapacitor device. A wearable asymmetric supercapacitor is designed by taking optimized r_2PGNL_{5min} as anode and a well-known cathode material, MXene, which shows stable and high performance under repeated deformations for 5000 cycles.

References

[1] Y. Sun, X. L. Shi, Y. L. Yang, G. Suo, L. Zhang, S. Lu, Z. G. Chen, *Adv. Funct. Mater.* **2022**, *32*, DOI 10.1002/adfm.202201584.

[2] Y. Wang, M. Zhang, X. Shen, H. Wang, H. Wang, K. Xia, Z. Yin, Y. Zhang, *Small* **2021**, *17*, 1.

[3] L. Lai, H. Yang, L. Wang, B. K. Teh, J. Zhong, H. Chou, L. Chen, W. Chen, Z. Shen, R. S. Ruoff, J. Lin, *ACS Nano* **2012**, *6*, 5941.

[4] Y. Feng, J. Jiang, Y. Xu, S. Wang, W. An, Q. Chai, U. H. Prova, C. Wang, G. Huang, *Carbon N. Y.* **2023**, *211*, 118105.

[5] T. Prasankumar, D. Salpekar, S. Bhattacharyya, K. Manoharan, R. M. Yadav, M. A.

Campos Mata, K. A. Miller, R. Vajtai, S. Jose, S. Roy, P. M. Ajayan, *Carbon N. Y.* **2022**, *199*, 249.

[6] Y. Zhu, M. Chen, Y. zhang, W. Zhao, C. Wang, *Carbon N. Y.* **2018**, *140*, 404.

[7] Z. Li, D. Guo, Y. Liu, H. Wang, L. Wang, *Chem. Eng. J.* **2020**, *397*, 125418.

[8] A. R. Selvaraj, A. Muthusamy, Inho-Cho, H. J. Kim, K. Senthil, K. Prabakar, *Carbon N. Y.* **2021**, *174*, 463.

[9] S. Latil, L. Henrard, *Phys. Rev. Lett.* **2006**, *97*, 1.

[10] S. V. Morozov, K. S. Novoselov, M. I. Katsnelson, F. Schedin, D. C. Elias, J. A. Jaszczak, A. K. Geim, *Phys. Rev. Lett.* **2008**, *100*, 11.

[11] H. Park, R. B. Ambade, S. H. Noh, W. Eom, K. H. Koh, S. B. Ambade, W. J. Lee, S. H. Kim, T. H. Han, *ACS Appl. Mater. Interfaces* **2019**, *11*, 9011.

[12] M. Asaduzzaman, O. Faruk, A. A. Samad, H. S. Kim, M. S. Reza, Y. Y. Lee, J. Y. Park, *Adv. Funct. Mater.* **2024**, *2405651*, 1.

[13] P. Pachfule, D. Shinde, M. Majumder, Q. Xu, *Nat. Chem.* **2016**, *8*, 718.

[14] F. Lai, Y. E. Miao, L. Zuo, H. Lu, Y. Huang, T. Liu, *Small* **2016**, *12*, 3235.

[15] H. Huang, S. Zhou, C. Yu, H. Huang, J. Zhao, L. Dai, J. Qiu, *Energy Environ. Sci.* **2020**, *13*, 545.

[16] R. R. Salunkhe, Y. Kamachi, N. L. Torad, S. M. Hwang, Z. Sun, S. X. Dou, J. H. Kim, Y. Yamauchi, *J. Mater. Chem. A* **2014**, *2*, 19848.

[17] C. Young, R. R. Salunkhe, J. Tang, C. C. Hu, M. Shahabuddin, E. Yanmaz, M. S. A. Hossain, J. H. Kim, Y. Yamauchi, *Phys. Chem. Chem. Phys.* **2016**, *18*, 29308.

[18] C. Guan, W. Zhao, Y. Hu, Z. Lai, X. Li, S. Sun, H. Zhang, A. K. Cheetham, J. Wang, *Nanoscale Horizons* **2017**, *2*, 99.

[19] P. Zhang, F. Sun, Z. Shen, D. Cao, *J. Mater. Chem. A* **2014**, *2*, 12873.

[20] M. Kim, X. Xu, R. Xin, J. Earnshaw, A. Ashok, J. Kim, T. Park, A. K. Nanjundan, W. A. El-Said, J. W. Yi, J. Na, Y. Yamauchi, *ACS Appl. Mater. Interfaces* **2021**, *13*, 52034.

[21] S. Liu, L. Kang, J. Zhang, E. Jung, S. Lee, S. C. Jun, *Energy Storage Mater.* **2020**, *32*, 167.

[22] G. Jiang, S. Osman, R. A. Senthil, Y. Sun, X. Tan, J. Pan, *J. Energy Storage* **2022**, *49*, 104071.

[23] J. A. Yan, M. Y. Chou, *Phys. Rev. B - Condens. Matter Mater. Phys.* **2010**, *82*, 21.

[24] J. Bin Wu, M. L. Lin, X. Cong, H. N. Liu, P. H. Tan, *Chem. Soc. Rev.* **2018**, *47*, 1822.

[25] J. Ribeiro-Soares, M. E. Oliveros, C. Garin, M. V. David, L. G. P. Martins, C. A.

Almeida, E. H. Martins-Ferreira, K. Takai, T. Enoki, R. Magalhães-Paniago, A. Malachias, A. Jorio, B. S. Archanjo, C. A. Achete, L. G. Cançado, *Carbon N. Y.* **2015**, *95*, 646.

[26] A. Lerf, H. He, M. Forster, J. Klinowski, *J. Phys. Chem. B* **1998**, *102*, 4477.

[27] D. R. Dreyer, S. Park, C. W. Bielawski, R. S. Ruoff, *Chem. Soc. Rev.* **2009**, *39*, 228.

[28] F. Lufrano, P. Staiti, *Int. J. Electrochem. Sci.* **2010**, *5*, 903.

[29] H. Zhou, S. Zhu, M. Hibino, I. Honma, *J. Power Sources* **2003**, *122*, 219.

[30] J. Zhu, S. Mu, *Adv. Funct. Mater.* **2020**, *30*, 1.

Chapter 4

Transient electro-graphitization of MOFs affecting the crystallization of Ru nanoclusters for highly efficient hydrogen evolution

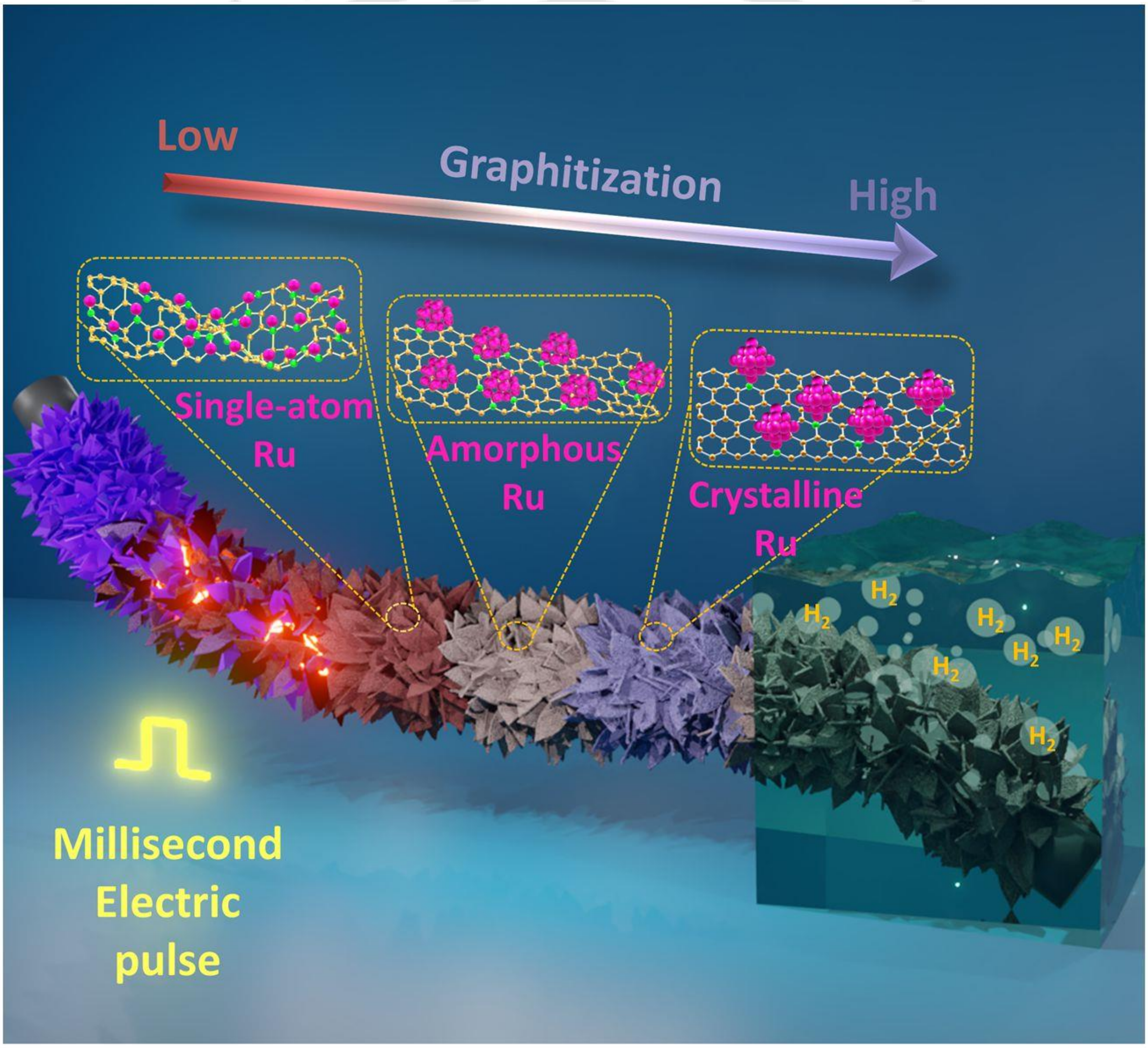

Transient electro-graphitization of MOFs affecting the crystallization of Ru nanoclusters for highly efficient hydrogen evolution

Fine control over the graphitization level of carbonized nanostructures can play a strategic role in tuning the crystallization of supported nanocatalysts, thereby modulating the kinetics of catalysis. However, realizing the synergistic interplay of graphitization-tunable support and supported catalysts poses a significant challenge. This study proposes a current pulse-induced ultrafast strategy for developing MOF-derived graphitic nano-leaves (GNL) and supported ultrafine ruthenium nanoclusters exhibiting selective crystallization states depending on the tunable graphitization level of GNL. The resulting ultrafine (~ 0.7 nm) amorphous-ruthenium nanoclusters linked with GNL (a-Ru@GNL$_{500}$) exhibit state-of-the-art performance in the hydrogen evolution reaction (HER), requiring very low overpotentials of only 23.0 mV and 285.0 mV to achieve current densities of 10 mA cm^{-2} and 500 mA cm^{-2}, respectively. Furthermore, a-Ru@GNL$_{500}$ demonstrates exceptional operational stability for 100 hours under high HER currents of 200 mA cm^{-2} and 400 mA cm^{-2}. Density functional theory reveals that the unique electronic structure of a-Ru and the cooperative effect of cobalt embedded in the graphitic layer lower the occupancy of the antibonding orbital, resulting in an accelerated HER process. Additionally, the unique electronic structure, highly conducting GNL, and efficient bubble release dynamics of super-aerophobic a-Ru@GNL$_{500}$ contribute to reduced overpotentials, particularly at high HER current densities.

4.1. Introduction

Developing durable and highly efficient catalysts is vital for establishing a clean and sustainable hydrogen fuel-based economy reliant on electrochemical hydrogen evolution via water splitting. However, the scarcity, soaring cost, and poor electrochemical stability of benchmark Pt catalysts hamper their large-scale practical usage.[1–5] Ruthenium has quickly emerged as a suitable alternative to platinum due to its much lower price (~4% of Pt),[2,6–14] wide availability,[15–24] and excellent HER kinetics with high stability.[25–32] Ru-nanoclusters' activity is directly correlated to their size, with smaller sizes offering higher uncoordinated surface atoms and active sites, ensuring high HER performance and effective atom utilization-induced cost reduction.[33] Besides the size, the crystallization state can also play a significant role in regulating the catalytic activity.[4,34,35] Recently, it was shown that amorphous Ru clusters are better HER catalysts than their crystalline counterparts owing to the more significant number of active sites in the former.[4] Despite their importance, synthesizing ultrasmall Ru nanoclusters (Ru-NCs) with precise control over the crystallization state poses a significant challenge. In addition to the size and crystalline state of Ru-NCs, their HER activity depends on the morphology and electronic properties of their catalytic support, with carbon nanostructures being a common choice.[36,37] The high electrical conductivity and bubble-releasing aerophobicity of the supporting carbon nanostructure are highly desirable to ensure high performance and stability in practical high-current-density environments.[38–41]

Loading metal precursors over metal-organic frameworks (MOFs) and their controlled pyrolysis have become popular techniques for synthesizing carbon-linked metal nanoclusters, including ruthenium.[18,42–46] Conventional pyrolysis methods are tedious, time-consuming, and associated with a significant thermal budget. The pulse-induced thermal shock method has recently emerged as a favorable technique for rapid pyrolysis of MOFs and concurrent metallic nanocluster loading over carbon supports.[47–49] This process is fast, generally on the millisecond scale, and requires a thermal budget that is an order of magnitude lower than conventional pyrolysis. However, the rapid dynamic transformations of MOF crystals into carbon structures and their simultaneous linkage to metals during pyrolysis make it challenging to control the size, crystallinity, and dispersion of nanoclusters loaded over the carbon support. From the perspective of catalytic support, a conducting graphitic structure is favorable compared to amorphous or poorly crystalline carbon. Thus, tuning the graphitization level of MOF-pyrolyzed carbon is expected to benefit the HER activity by offering highly conductive support and low overpotential due to optimal resistive losses. However, to date, no serious attention has been paid to tuning the graphitization level of MOF-derived nanostructures to enhance HER activity. Furthermore, whether such graphitization level control can be effectively utilized for the precisely tunable linking of nanoclusters remains an unresolved question.

Herein, we report a current pulse-induced transient electro-graphitization (TEG) process for developing MOF-derived hierarchical carbon nano-leaves with adjustable graphitization levels. This TEG method successfully yielded ultra-small Ru-NCs linking with a controllable size and crystalline structure, displaying state-of-the-art HER performance. We decoupled the MOF pyrolysis and the growth stages of loaded nanoclusters, providing tremendous flexibility and independent control over the graphitization level of the MOF-derived carbon support and the crystalline state of ruthenium. This TEG process can convert MOFs into carbon nano-leaves with progressively higher graphitization levels by adjusting the current pulse duration from a few hundred milliseconds to one second. Significantly, the growth of ruthenium in the next stage of millisecond thermal shock can be arrested in either the single-atom, amorphous, or crystalline state, depending on the graphitization level and intrinsic nitrogen doping. All the developed catalysts displayed excellent HER activity; in particular, the amorphous Ru nanoclusters linked with nano-leaves graphitized through a 500 ms pulse (a-Ru@GNL$_{500}$) showed the best performance. Density functional theory calculations revealed an electronic interplay between amorphous Ru and graphitic-layer embedded cobalt, leading to high catalytic activity. In contrast to most previous MOF-derived metal catalyst-linked structures in powder form, which do not guarantee performance and stability at commercially demanding high currents,[37] free-standing a-Ru@GNL$_{500}$ displayed exceptional stability and performance at high current densities. Contact angle measurements show that the as-developed binder-free nano-leaves structure is super-aerophobic, and adhesive force measurements reveal that it is a highly preferable structure for bubble release, which is responsible for high performance and stability at high current densities.

4.2. Materials and methods

4.2.1.1. Materials:

Cobalt nitrate hexahydrate ($Co(NO_3)_2 \cdot 6H_2O$), 2-methylimidazole ($C_4H_6N_2$), ruthenium chloride hydrate ($RuCl_3 \cdot xH_2O$), iridium chloride hydrate ($IrCl_3 \cdot xH_2O$), palladium chloride ($PdCl_2$), absolute ethanol, commercial Pt/C (20 wt% Pt), Nafion (5 wt%) were purchased from Sigma-Aldrich. KOH (Emsure) and H_2SO_4 (95-97wt%, Emsure) were purchased from Merck. Commercial carbon cloth (CC) (Plain Carbon Cloth – 1071 HCB) was purchased from AvCarb Material Solutions. Millipore type III deionized water was used throughout all the experiments while needed.

4.2.1.2. Preparation of ZIF-67 nano leaves over CC:

Firstly, the commercial carbon cloth (CC) (3×4.5 cm^2) was washed with ethanol and DI water in a bath sonicator successively for 10 minutes each. Then, ZIF-67 nano leaves were grown vertically over each microfibre of cleaned CC using a facile method at room temperature.[1] Briefly, 1.314 g of 2-methyl imidazole and 0.582 g of $Co(NO_3)_2 . 6H_2O$ were dissolved in 40 mL of DI water each, respectively. Then, the two solutions were mixed in a 100 mL beaker, and the cleaned CC was placed vertically in the mixed solution. After 4 hours of reaction, the CC was collected, washed with DI water several times, and dried to obtain ZIF-67 nano leaves vertically grown over CC.

4.2.1.3. Preparation of GNLs:

The as-prepared ZIF-67 linked to CC was cut into pieces (3×1 cm^2), and n milliseconds voltage pulse of 30 V was applied through the length of the CC in an N_2-saturated airbag (Sigma-Aldrich) using a constant power supply capable of supplying voltage pulse. The transient current passing through CC produced ultrafast Joule heat, resulting in ZIF-67-derived graphitized nano leaves (GNL_n, where n could be any 200 ms, 500 ms, 1000 ms) vertically linked to CC. The quick graphitization by the said strategy was named transient electro-graphitization (TEG). The graphitization level can be precisely controlled by the voltage amplitude or pulse duration (as the higher voltage and pulse duration could result in higher Joule heating). The as-developed TEG-assisted ZIF-67-derived GNLs vertically linked to CC were used as support materials for HER catalyst growing.

4.2.1.4. Preparation of HER catalysts namely, Ru-SA@GNL$_{200}$, a-Ru@GNL$_{500}$, c-Ru@GNL$_{1000}$, Ir-NC@GNL$_{500}$, and Pd-NC@GNL$_{500}$:

The as-developed GNL_n (n = 200, 500, and 1000) linked to CC (3×1 cm^2) was immersed into an ethanolic solution (5 mL, 0.005 M) of $RuCl_3.xH_2O$ at room temperature. After 30 minutes, the CC decorated with GNL_n loaded with Ru salt was collected and then air-dried completely. Finally, for the synthesis of Ru-SA@GNL$_{200}$, a-Ru@GNL$_{500}$, and c-Ru@GNL$_{1000}$, a 50 ms voltage pulse of 30 V was applied through the length of the CC (decorated with GNL_n loaded with Ru salt) in the N_2-saturated airbag (Sigma-Aldrich) using the constant power supply capable of supplying voltage pulse. Ir-NC@GNL$_{500}$ and Pd-NC@GNL500 were prepared using a similar procedure but replacing $RuCl_3$. xH_2O with $IrCl_3$. xH_2O, and $PdCl_2$, respectively.

4.2.2. Materials characterization

The morphology and microscopic features of the as-developed samples were investigated by using field emission scanning electron microscopy (FESEM, Zeiss, Sigma-300), field emission transmission electron microscopy (FETEM, JEOL, 2100F), and high angle annular dark field scanning transmission electron microscopy (HAADF-STEM, Titan TM 80-300 (FEI) with probe Cs corrector). The crystalline structure of samples was analyzed using an X-ray diffractometer (Rigaku Technologies, Smartlab) with Cu Kα radiation. Raman spectroscopic measurements were performed on a Raman Spectrometer (Horiba Jobin Vyon, LabRam HR, laser wavelength 514 nm). The chemical compositions and oxidation states were detected by X-ray photoelectron spectroscopy (ESCALAB Xi+, Thermo Fisher). Mass loading of ruthenium in the best-performing sample was determined by inductively coupled plasma mass spectroscopy (ICP-MS) (Agilent, 7850 ICP-MS). The local structure study by X-ray absorption spectroscopy (XAS) of the Ru-based catalysts was conducted in Indus-2, a 2.5 GeV synchrotron radiation source facility in Raja Raman Centre for Advanced Technology. Athena software processed XAS data (background correction, normalization of XANES and EXAFS spectra).

4.2.3. Electrochemical measurements

HER performances were carried out in basic (1M KOH) and acidic (0.5M H_2SO_4) electrolytes, with saturated calomel electrode (CHI 150) as a reference, Pt wire as counter electrode in a basic electrolyte, and Ag/AgCl (KCl, 3M) electrode as a reference, graphite rod as counter electrode in an acidic electrolyte in a PARSTAT 3000A-DX potentiostat. A piece of 1×1 cm^2 of the catalysts developed over CC was directly used as the working electrode. All the HER polarization curves were recorded at 5 mV s^{-1} scan rate, and thereafter, iR was corrected. EIS spectra of the samples were collected in a frequency range of 10 kHz to 0.1 Hz. The double layer capacitance (C_{dl}) was determined from CV curves obtained in a non-faradaic region (1.1 V to 1.2 V versus RHE). Half the difference between anodic current (J_a) and cathodic current (J_c) was plotted against scan rates at a potential of 1.15 V versus RHE. The slope of the plot mentioned above gives the C_{dl} value, which is proportional to the ECSA of the samples.

4.3. DFT calculations

Based on density functional theory, this study's simulation work uses a well-known computational tool, the Vienna Ab-initio Simulation Package (VASP). Due to the periodic nature of the given system, the plane wave basis set[2] has been taken into account, with a kinetic energy cut-off of 450 eV, where all plane waves can be expanded. For the accuracy of total energy calculations, we have set 1E-5 eV as convergence criteria for ionic and electronic relaxations, i.e., when the energy difference between two successive electronic or ionic steps is 1E-5 eV, the calculation automatically stops. And -0.01 eV/Å is set for the ionic force convergence. A General Gradient Approximation of PBE functional[3] is incorporated to illustrate the effects of exchange and correlation forces among electrons. The Projected Augmented Wave method defines the Pseudo potential-based interaction between core and valence electrons. To consider the impact of weak Van der Waal forces among Ru, C, N, Co, and H atoms, the Grimme DFT-D2 dispersion scheme is employed. [4]

For the systems considered here, lattice parameters are 12.48 Å, 12.06 Å, and 25 Å along the a, b, and c axes, respectively. Along the c-direction, we have considered a total of 30 Å as the height of the DFT cell, and out of 30 Å, 15 Å is occupied by the system (for hybrid) considered, and 15 Å is the vacuum size to avoid the interaction with the repeating image. Two different Ru_{19} nanoclusters (NCs) have been chosen: amorphous and crystalline (octahedral phase). Next, nitrogen-doped graphene with 5 X 3 supercell is modeled with Ru19 NCs as a-Ru19@GN and c-Ru19@GN, respectively. In the last model, a-Ru19@GN is modeled with (001) planes of Co as a-Ru19@GN/Co (001). For crystalline Ru-NCs, we took the octahedral model of 19 Ru atom clusters as per the literature [5], and the calculation was done on atoms from both [111] and [100] planes. Regarding fixing the atoms, the whole system is relaxed without fixing any atom in the DFT calculation. But, for zero-point energy (ZPE) calculation for a particular atom, the entire system was fixed except for the specific atom. The reported structure is optimized by applying Monk-Horst pack sampling, with 5 X 5 X 1 k-points through integration in the Brillouin zone and 7 X 7 X 1 k-points considered for PDOS calculations.

Change of Gibb's free energy (G) is calculated using the given equation, $\Delta G = \Delta E + \Delta ZPE - T\Delta S - ne\Delta U$, where E is DFT energy, ZPE is zero–point energy, TS is an entropic part, n is the number of transferred electrons, and U is an applicable potential in the electrode. In this work, the values of entropy and ZPE for free molecules are taken from chemical databases (https://janaf.nist.gov) and think about a situation at U = 0 V in a free energy diagram.

4.4. Results and Discussion

4.4.1. Synthesis and characterization of crystallization tuneable Ru-NCs linked with graphitic nano-leaves

Graphitic nano-leaves (GNL) linked ruthenium nanoclusters (Ru-NCs) of tuneable crystallization level were synthesized through a two-stage pulsed current-induced fast Joule heating strategy schematically presented in **Figure 4.1a**. In the first stage, an array of a cobalt-based metal-organic framework (MOF, ZIF-67) on carbon cloth (CC) was pyrolyzed into cobalt nanoparticle-embedded GNL by passing a pulsed current (a few hundred milliseconds) through CC (details in Materials and methods). Nitrogen (N) doping in GNL concurrently occurred during this ultrafast current pulse-induced transient electro-graphitization (TEG), where nitrogen from the MOF structure served as the dopant source. In the second stage, uniform Ru nanoclusters (Ru-NCs) were linked by loading ruthenium salt ($RuCl_3$, xH_2O) over GNL and subsequent passing of a 50 ms current pulse. The magnitude and duration (in milliseconds) of the current pulse applied to CC determine the degree of graphitization of GNL. Notably, the degree of graphitization of GNL and the associated N-doping level assess the state of crystallization of Ru-NC, which can be either predominantly single-atom (Ru-SA), amorphous nanocluster (a-Ru-NC) or crystalline nanoparticle (c-Ru-NP), as will be discussed in the later sections.

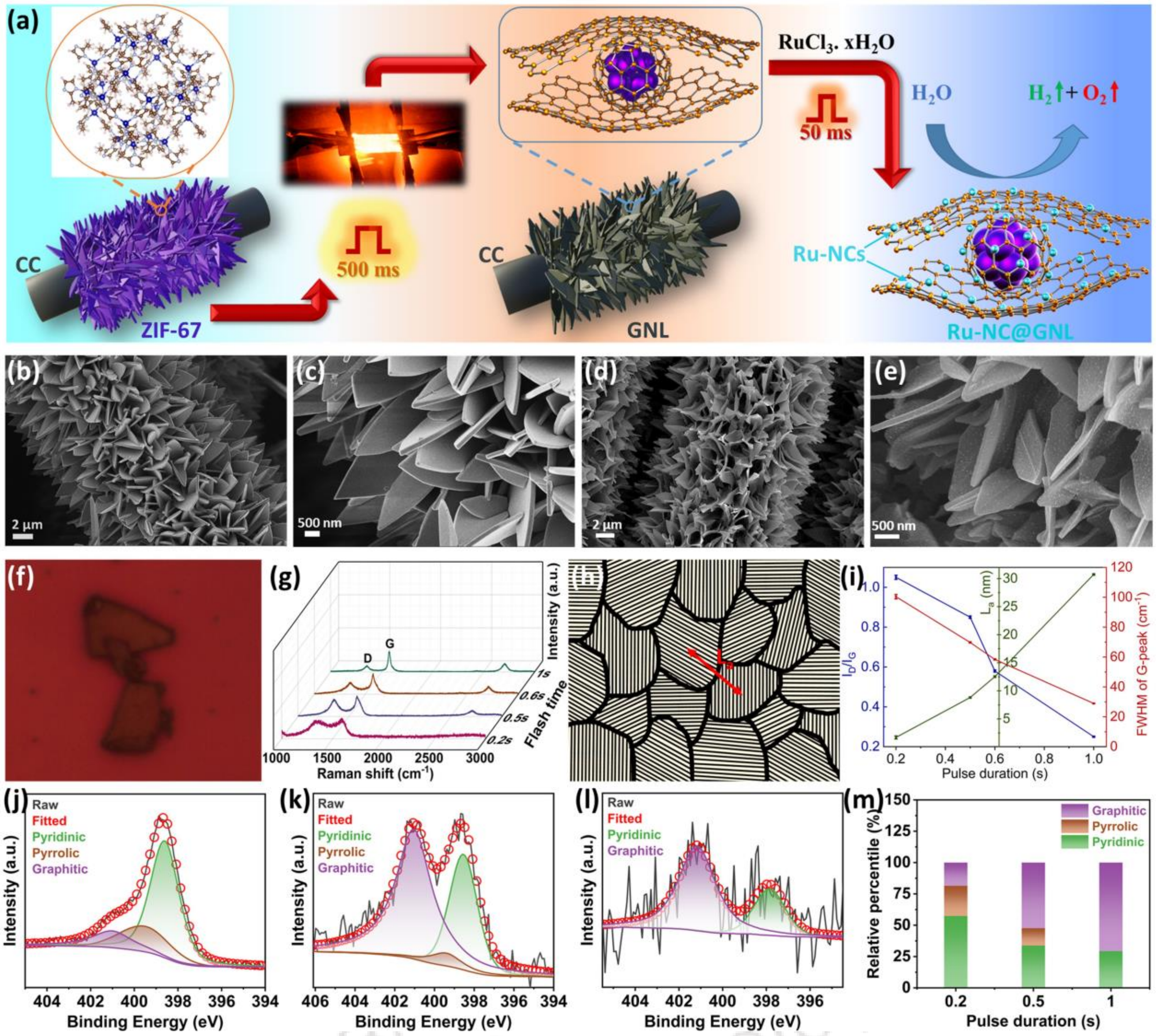

Figure 4.1: Synthesis and characterization of ZIF-67-derived GNL. (a) Schematic illustration of ZIF-67-derived GNL development and linking Ru-NCs, (b) and (c) low- and high-magnification FESEM images of ZIF-67 grown over CC, (d) and (e) low- and high-magnification FESEM images of the derivative GNL$_{500}$, (f) optical microscopic image of GNL$_{500}$ detached from CC for Raman analysis, (g) Raman spectra of GNL$_{200}$, GNL$_{500}$, GNL$_{600}$, and GNL$_{1000}$, (h) schematic diagram of graphitic domains, (i) variation of I_D/I_G, Γ_G, and L_a with current pulse duration, (j), (k), and (l) high-resolution N1s XPS spectra of GNL$_{200}$, GNL$_{500}$, and GNL$_{1000}$, respectively, and (m) bar diagram of relative content of different N-dopant configurations.

The field emission scanning electron microscope (FESEM) images in **Figure 4.1b, c** depict leaf-like MOF arrays that were hierarchically grown over CC. The TEG process transformed the MOFs into cobalt-embedded GNLs when the pulse duration was varied from 200 ms (GNL_{200}), 500 ms (GNL_{500}), to 1000 ms (GNL_{1000}); however, this process preserved the hierarchical nano-leaf morphology (**Figure 4.1d, e, Figure 4.2**, **Figure 4.3**). The morphology of GNL remains very similar after the loading of Ru-NCs (**Figure 4.4**) in the second stage, indicating no morphological evolution in the nanocluster-linking stage. The degree of graphitization of the GNLs was tuned by controlling the duration of the applied current pulse and was analyzed using Raman spectroscopy. Individual sheets of GNLs (**Figure 4.1f**) were analyzed to eliminate any effect of the CC substrate on the Raman signal. Raman spectra of the TEG-process-derived GNLs were recorded to study the evolution of the graphitization level with different pulse durations (**Figure 4.1g**). The Raman spectrum of graphitic materials possesses three prominent characteristic peaks: a D-peak at 1350 cm^{-1}, a G-peak at 1578 cm^{-1}, and a 2D-peak at 2700 cm^{-1}.[50] The G-peak corresponds to the in-plane C=C stretching vibration (E_{2g} modes) and is characteristic of the graphitic structures. The D-peak corresponds to the defects present in the carbonaceous materials, and the 2D peak is the overtone of the D peak. The degree of graphitization is measured by the intensity ratio of D and G-peak (I_D/I_G) or the FWHM of G-peak (Γ_G). The lower the value of I_D/I_G and Γ_G, the higher the degree of graphitization. It is evident from the Raman spectra in **Figure 4.1g** that I_D/I_G ratios and Γ_G follow the order: GNL_{200} > GNL_{500} > GNL_{600} >GNL_{1000}, suggesting a gradual increase in graphitization level with an increase in TEG duration. The Raman spectra were fitted with the three characteristic peaks for a detailed quantitative analysis (**Figure 4.5**). The estimated positions of the G-peak, I_D/I_G ratio, and FWHM of the G-peak (Γ_G) are tabulated in the insets of **Figure 4.5**. Further, the degree of graphitization can be directly estimated quantitatively from the average domain size (L_a) of the ordered graphitic region (sp^2 domain) (**Table 4.1)**, as represented schematically in **Figure 4.1h**.[50,51] In the schematic, a domain with parallelly oriented lines depicts the ordered graphitic region, and an increase in the domain size (L_a) signifies an increase in graphitic order. The value of sp^2 domain size L_a (nm) was estimated from the FWHM of G peak (Γ_G) by the formula,

$$\boldsymbol{\Gamma_G(L_a) = \Gamma_G(\infty) + Ce^{-L_a/(l_c/2)}} \tag{4.1}$$

where, $\Gamma_G(L_a)$ is the full-width half maxima (FWHM) of G-peak in the Raman spectra, $\Gamma_G(\infty) = 15\ cm^{-1}$, FWHM of G-peak in Raman spectra of pristine graphene, $C = 95\ cm^{-1}$,

$l_c = 32\ nm$, known as phonon coherence length.[6] Remarkably, the G-peak is redshifted from 1585.9 cm^{-1} to 1576.1 cm^{-1}, Γ_G decreases from 100.4 to 28.9, and I_D/I_G also decreases from 1.05 to 0.25 as pulse time increases from 200 milliseconds to one second.

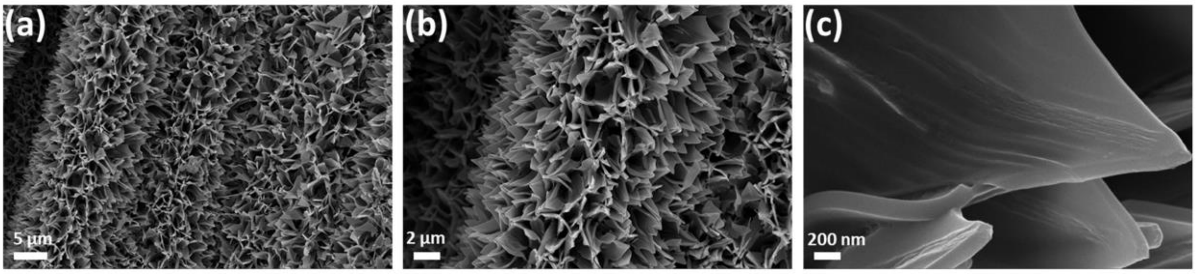

Figure 4.2: FESEM images of GNL$_{200}$.

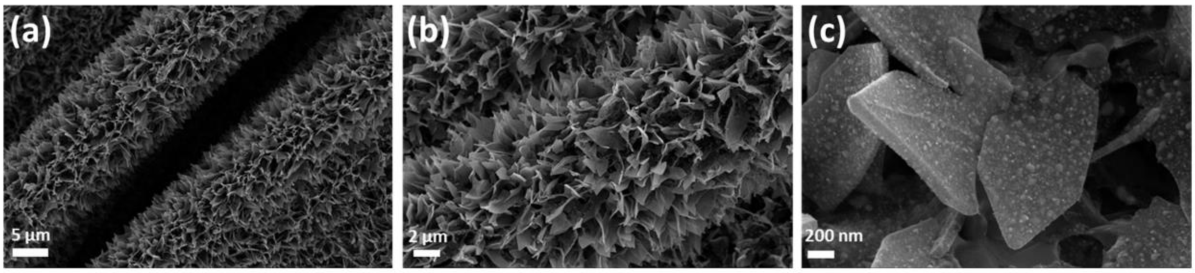

Figure 4.3: FESEM images of GNL$_{1000}$.

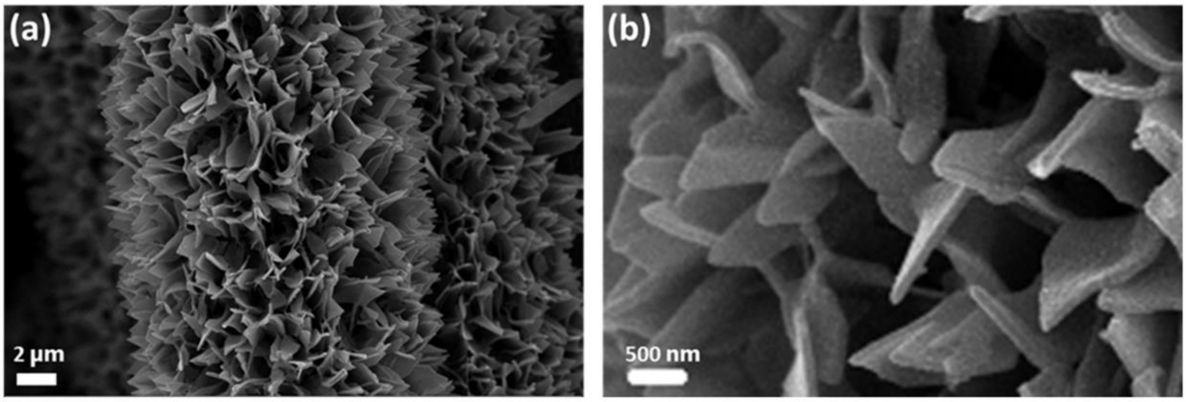

Figure 4.4: FESEM images of a-Ru@GNL$_{500}$.

The variations in I_D/I_G, FWHM of the G-peak, and L_a with pulse durations are also shown in **Figure 4.1i**. The gradual increase in L_a from 1.7 nm to 30.75 nm directly suggests a gradual increase in the degree of graphitization with increasing pulse duration. Thus, it is evident from Raman analysis that the graphitization level of the obtained GNL derived from MOF can be easily tuned by controlling the pulse width of the TEG. Graphitization of carbonaceous products is known to happen either through high-temperature annealing (> 3000 °C) or catalytic transition metal surface-induced activation, which is generally done through hours of processing (4-12 h) in a furnace. In our process, the observed tuneable graphitization can be attributed to both processes (high-temperature annealing (> 3000 °C) and catalytic transition metal surface-induced activation) within an ultrafast time scale. Current pulse-induced Joule heating can reach a few thousand degrees Celsius through a current-carrying filament within a millisecond time scale, and the temperature increases with increasing heating duration, following Joule's law.[47] In our case, this ultrafast process not only pyrolyzes the ZIF-67 MOF into a carbonaceous structure but also helps to graphitize it. Due to the current pulse-induced high temperature, in-situ generated cobalt nanoparticles also act as the catalysts to graphitize the MOF-pyrolyzed carbon.

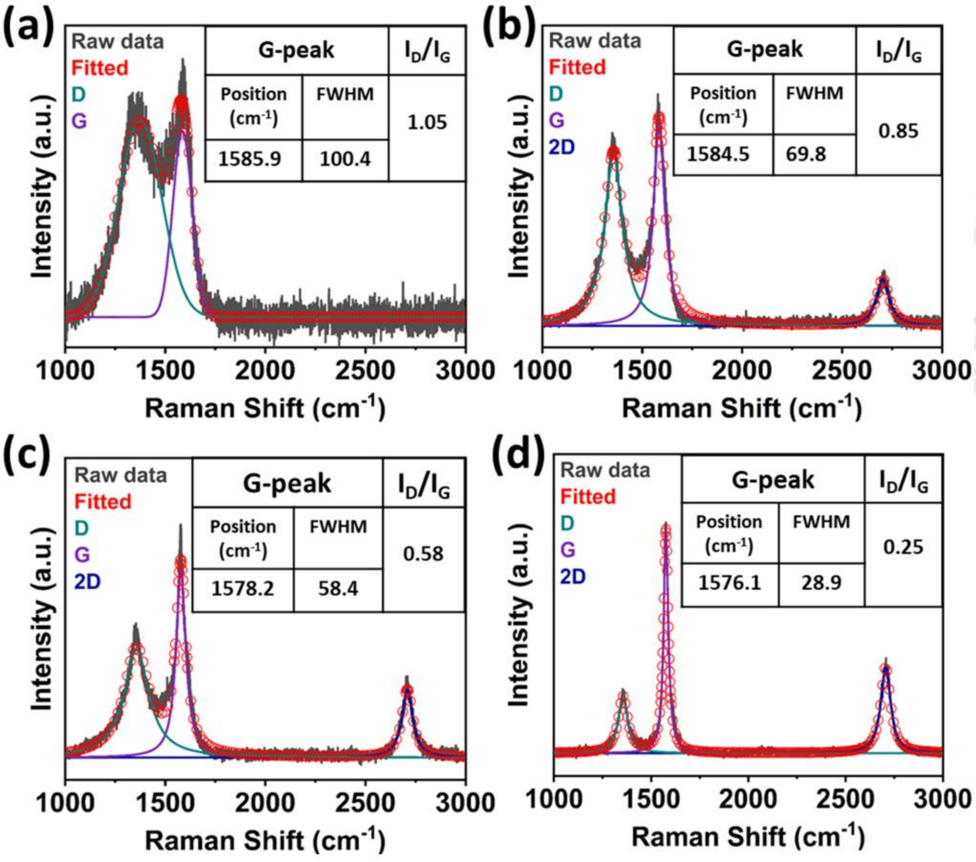

Figure 4.5: Fitted Raman spectra of (a) GNL$_{200}$, (b) GNL$_{500}$, (c) GNL$_{600}$, and (d) GNL$_{1000}$, inset: tables of position, FWHM of G-peak, and I_D/I_G ratio.

Table 4.1: Graphitic domain sizes of different GNLs.

Samples	L_a (nm)

GNL_{1000}	30.75
GNL_{600}	12.53
GNL_{500}	8.80
GNL_{200}	1.70

X-ray photoelectron spectroscopy (XPS) analysis was performed to determine the chemical compositions and state of the constituent elements. The N-doping concentration (at%), estimated from XPS survey scans (**Figure 4.6**), gradually decreased from 9.33 (GNL_{200}) to 4.67 (GNL_{500}) and 1.6 (GNL_{1000}) as the pulse duration was increased. The high-resolution N1s XPS spectra (**Figure 4.1j**, **k**, and **l**) consisted of three peaks corresponding to pyridinic (at 398.6 eV), pyrrolic (at 399.7 eV), and graphitic N (at 401.0 eV).[46,52,53] With the increase in pulse durations, the graphitic-N content gradually increased from 18.5% (200 ms) to 70.7% (1000 ms), with a decrease in the contribution of non-graphitic-N (pyridinic and pyrrolic), as depicted in **Figure 4.1m**. In the deconvoluted high-resolution C1s spectra (**Figure 4.7**), the relative intensity of the peak corresponding to C=C (sp^2 C) gradually increases with the gradual increase in TEG duration, suggesting progressive improvement of the graphitization level.

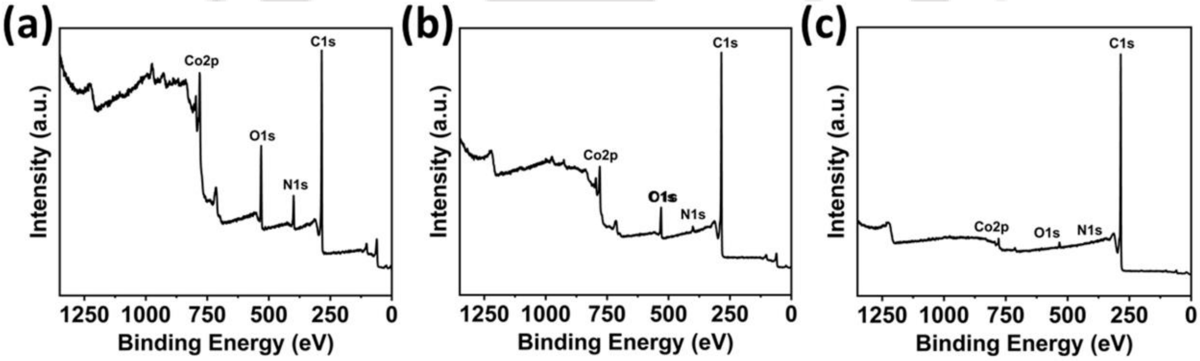

Figure 4.6: XPS survey scans of (a) GNL_{200}, (b) GNL_{500}, and (c) GNL_{1000}.

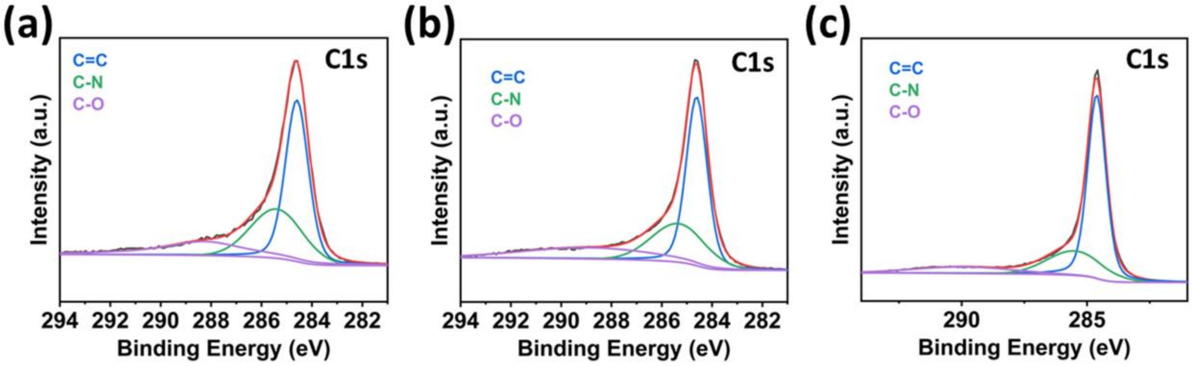

Figure 4.7: C1s XPS spectra of (a) GNL_{200}, (b) GNL_{500}, and (c) GNL_{1000}.

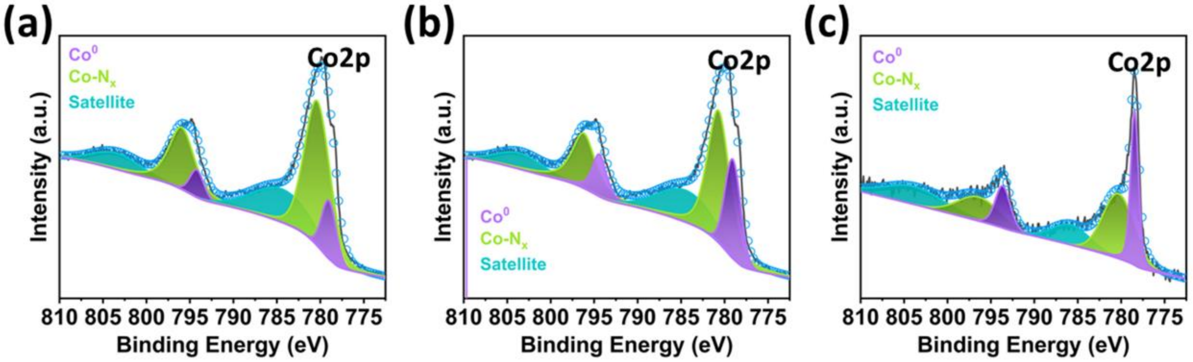

Figure 4.8: Co2p XPS spectra of (a) GNL_{200}, (b) GNL_{500}, and (c) GNL_{1000}

Two significant peaks in Co2p spectra (**Figure 4.8**) can be associated with metallic Co (Co^0) and Co linked to the N dopant site ($Co-N_x$ ($Co^{\delta+}$)).[43,46] The decreasing contribution of the latter with increasing TEG duration results from a gradual decrement in the N-content. Therefore, it is evident from the Raman and XPS spectroscopy that the TEG technique can precisely control the degree of graphitization and the content and configuration of the in-situ doped nitrogen. **Figure 4.9a** shows that the characteristic XRD peaks of ZIF-67 disappeared after the TEG, and new peaks of metallic cobalt appeared at 44.2° (111), 51.5° (200), and 75.8° (220), indicating the successful transformation of the MOFs into cobalt-embedded carbon structures. The resulting GNL peaks overlapped with those of the carbon cloth substrate at 26.2° (002) and 42.9° (100). Notably, even after Ru-linking, the peaks corresponding to Ru were missing in all the XRD patterns (**Figure 4.9b**), which could be either due to the poor crystallization of Ru or the formation of tiny Ru-clusters, which could produce a negligible signal for XRD.

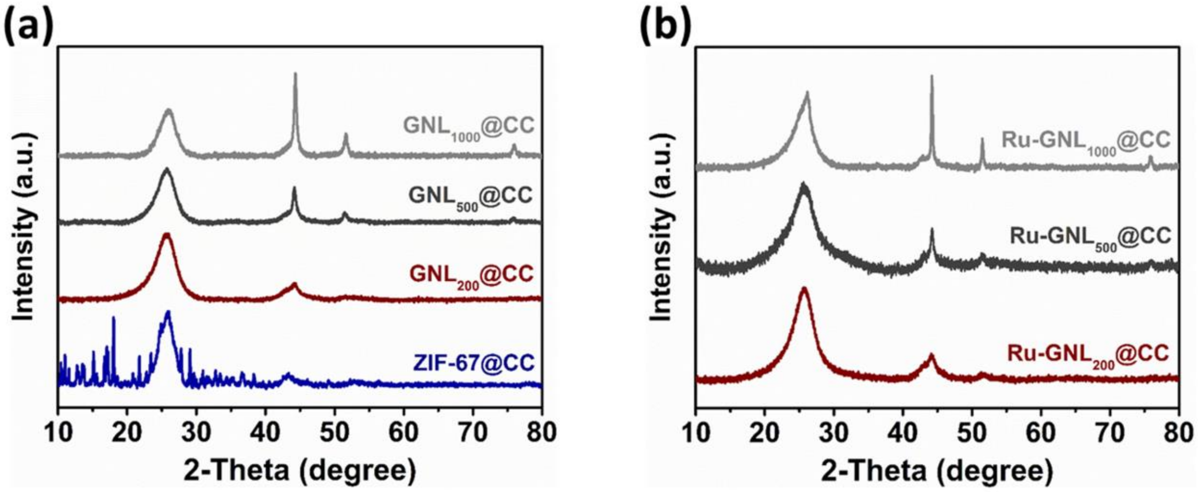

Figure 4.9: XRD patterns of (a) ZIF-67 and GNLs before Ru-loading, (b) GNLs after Ru-loading.

To inspect the variation in the crystalline status of the Ru-NCs developed over GNLs with different graphitization levels, transmission electron microscopy (TEM) and high-angle annular dark field scanning transmission electron microscopy (HAADF-STEM) analyses were conducted, and the results are presented in **Figure 4.10a-c**, **2e-g**, and **4.10i-k**. The XPS analysis of Ru is shown here (**Figure 4.10d**, **h,** and **k**) to inspect the variation in its chemical status in the respective samples. The TEM images of Ru-loaded GNL_{200} ($Ru@GNL_{200}$) (**Figure 4.10a** and **Figure 4.11a**) show nanoparticles (~10 nm) of Co, as identified from the HRTEM image, fast Fourier transform (FFT), and the corresponding inverse FFT (IFFT) with an inter-planar spacing of 0.205 nm (related to (111) plane) with a face-centered cubic (FCC) structure (**Figure 4.11b**). The absence of parallel graphitic layers in the HRTEM and IFFT images of GNL_{200} with dispersed broad bright regions in its FFT suggests a poor degree of graphitization (**Figure 4.11c**).

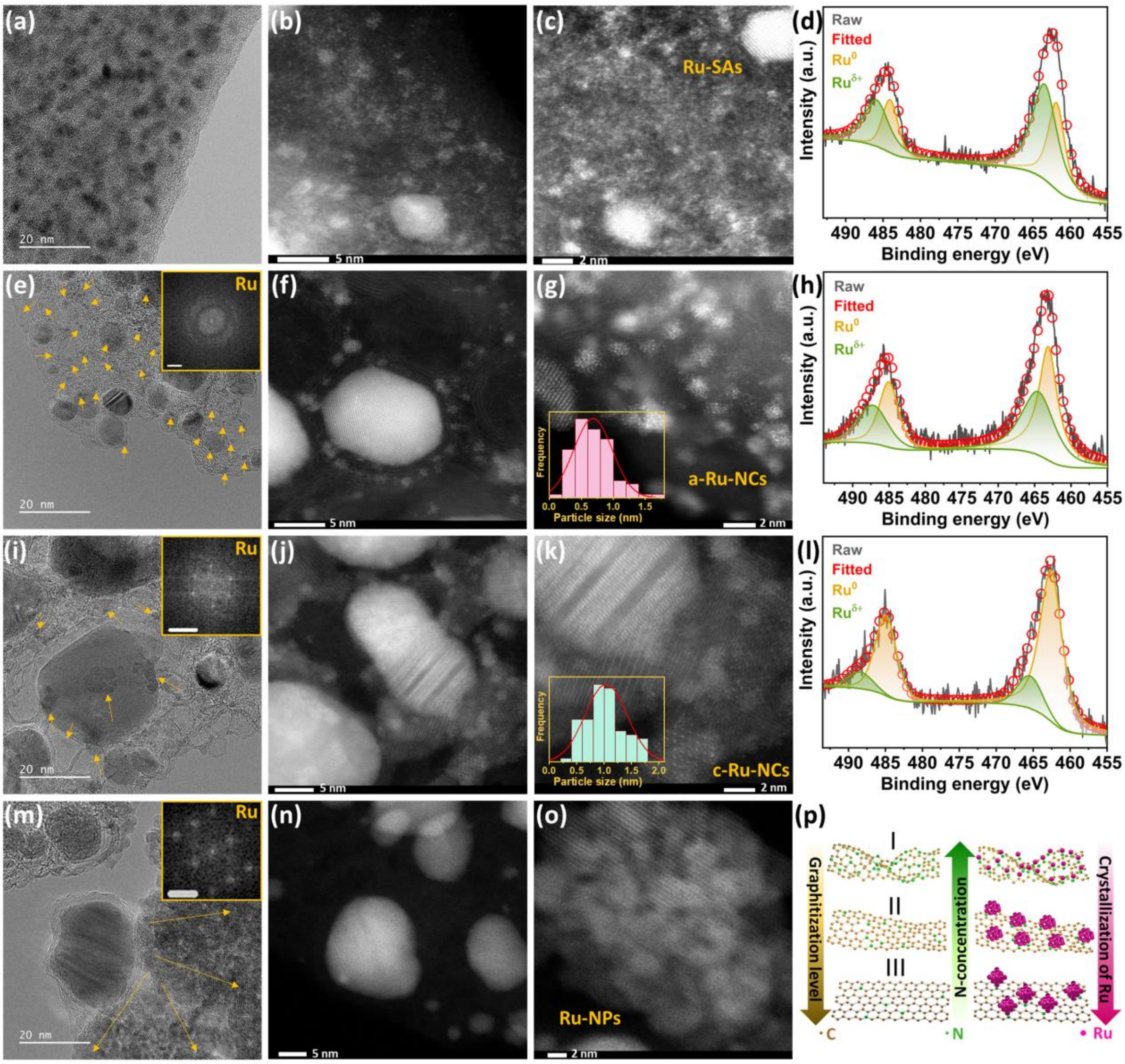

Figure 4.10: Crystallization control of Ru-NCs over graphitization tunable GNLs. (a) FETEM image, (b) low, (c) high-magnification HAADF-STEM images, and (d) Ru3p XPS spectra, of Ru-SA@GNL$_{200}$, (e) FETEM image, Ru-regions are indicated by the yellow arrows, inset: FFT pattern of Ru-region, (f) low, (g) high-magnification HAADF-STEM images, and (h) Ru3p XPS spectra, of a-Ru@GNL$_{500}$, (i)-(l) are the FETEM, low-, high-magnification HAADF-STEM images, and Ru3p XPS spectra of c-Ru@GNL$_{1000}$, respectively and (m)-(o) are the corresponding FETEM, and HAADF-STEM images of Ru@dGNL$_{500}$, respectively, (p) Scheme of Ru-NCs linking mechanism depending on the graphitization level and N-dopant concentration of GNLs.

Although XPS confirmed the presence of Ru in the Ru@GNL$_{200}$, its existence was not evident from the HRTEM image; however, they are visible in Cs-corrected HAADF-STEM images

(**Figure 4.10b**, **c**) and STEM EDS elemental mapping (**Figure 4.12**). In addition to the large Co nanoparticles, numerous Ru single atoms (Ru-SAs) and a few atomic clusters were dispersed throughout GNL$_{200}$ (Ru-SA@GNL), as shown in the HAADF-STEM images (**Figure 4.10b, c**). The high-resolution Ru3p XPS spectra (**Figure 4.10d**) were deconvoluted into two spin-orbit-split 3p$_{3/2}$ and 3p$_{1/2}$ peaks. The 3p$_{3/2}$ (3p$_{1/2}$) peak at around 461.8 eV (484.0 eV) corresponds to metallic Ru (Ru^0), and the peak at about 463.6 eV (485.9 eV) corresponds to Ru$^{\delta+}$, identified as Ru atoms linked to N-atoms of N-doped GNL$_{200}$.[43,53] The TEM image (**Figure 4.10e**), HRTEM image (**Figure 4.13a**), FFT pattern (**Figure 4.13b**), and IFFT image (**Figure 4.13c**) of Ru-linked GNL$_{500}$ (Ru@GNL$_{500}$) confirm the presence of crystalline Co nanoparticles similar to Ru-SA@GNL$_{200}$. Graphitic lattice fringes consisting of 3-7 layers are observed in the HRTEM image (**Figure 4.14a**), together with regions without fringes, suggesting a higher graphitization level in GNL$_{500}$ than in GNL$_{200}$. This is also consistent with the Raman analysis, as discussed earlier. The graphitic fringes, as depicted in the HRTEM image of the G-region, have a d-spacing of 0.350 nm, and the correlated FFT pattern contains two faint bright spots corresponding to the (002) planes of the graphitic structure (**Figure 4.14b**), again suggesting moderate graphitization. An IFFT image of the G-region is shown in **Figure 4.14c** for a better visualization of the crystal fringes.

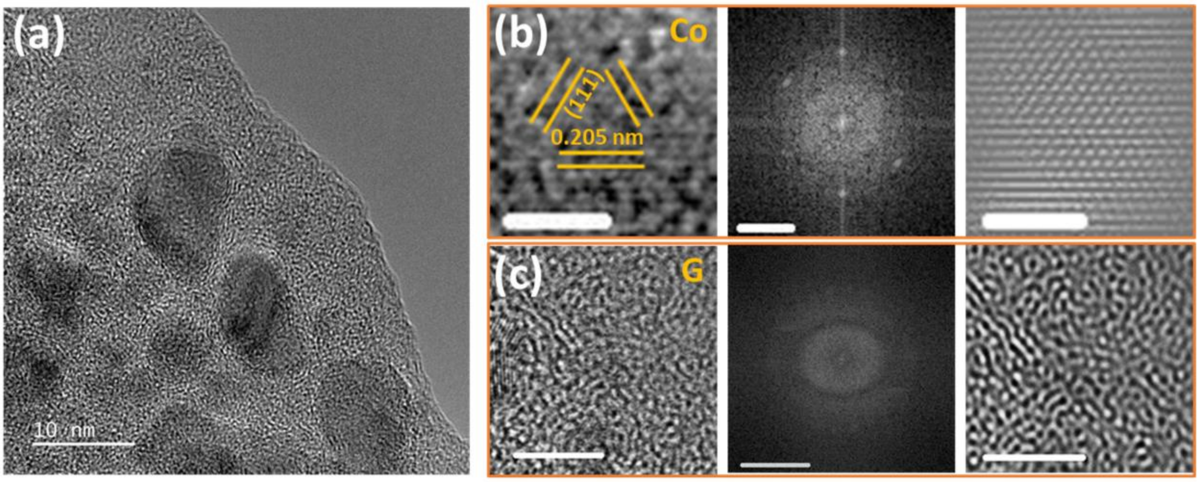

Figure 4.11: (a) Magnified TEM image of Ru-SA@GNL$_{200}$, (b) HRTEM image (scale bar: 2 nm), FFT pattern (scale bar: 2 1/nm), and IFFT image (scale bar: 2 nm) of Co-region, (c) corresponding HRTEM image, FFT pattern, and IFFT image of G-region (scale bar: 5 nm, 5 1/nm, 5 nm, respectively) of Ru-SA@GNL$_{200}$, respectively.

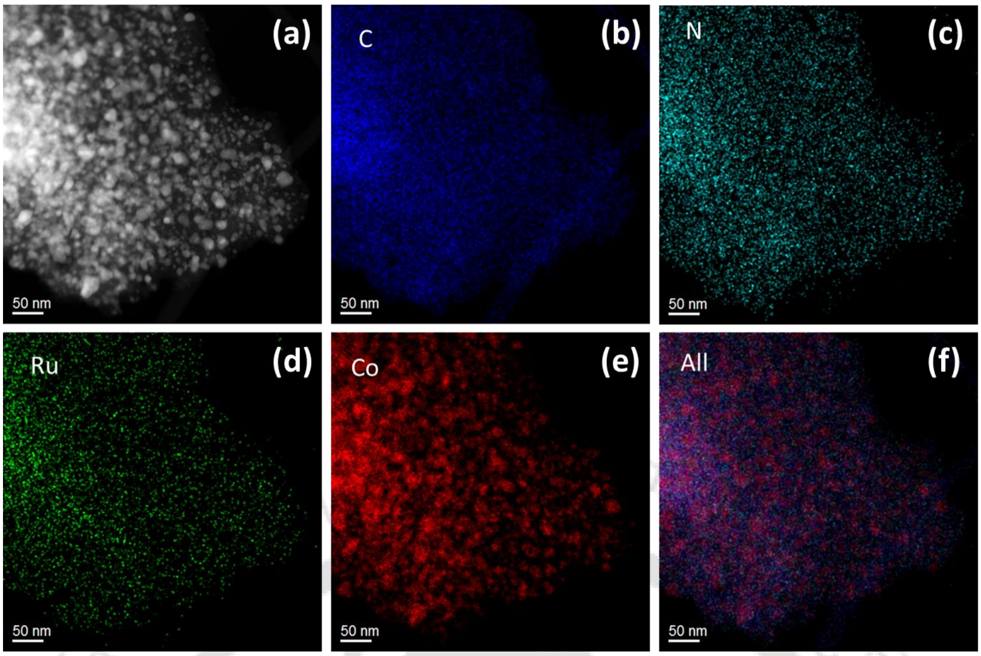

Figure 4.12: STEM EDS elemental mapping of a-Ru@GNL$_{200}$.

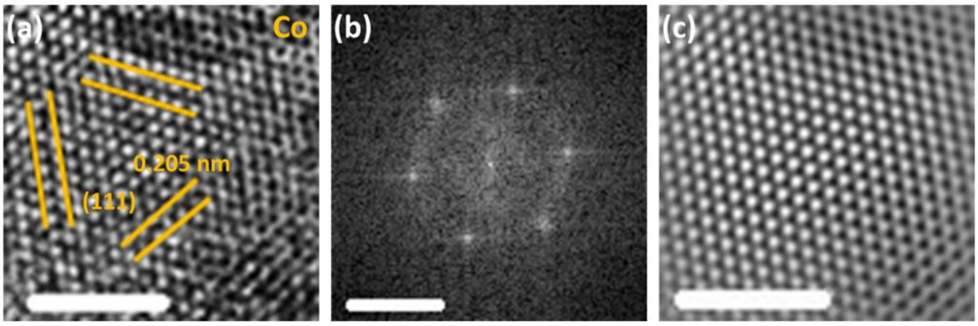

Figure 4.13: (a) HRTEM image, (b) FFT pattern, and (c) IFFT image of Co-region of a-Ru@GNL$_{500}$ (scale bar: 2 nm, 2 1/nm, 2 nm, respectively).

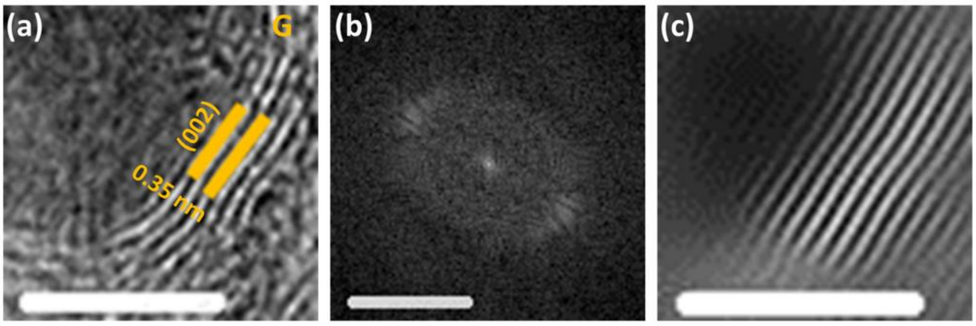

Figure 4.14: (a) HRTEM image, (b) FFT pattern, and (c) IFFT image of G-region of a-Ru@GNL$_{500}$ (scale bar: 5 nm, 5 1/nm, 5 nm, respectively).

Most importantly, uniformly distributed ultra-fine particles were observed in **Figure 4.10e,** as indicated by the yellow arrows. EDS mapping (**Figure 4.15**) clarified that the larger particles observed by TEM were cobalt, whereas the uniformly distributed tiny clusters were ruthenium. The HRTEM images (**Figure 4.16a**, **b**) and FFT pattern of one of the ultra-small Ru-NCs are depicted in the inset of **Figure 4.10e** (Ru-region), and the corresponding IFFT image is shown in **Figure 4.16c**. The absence of lattice fringes in the HRTEM and IFFT images of the Ru-NCs, with no well-defined bright spots in the corresponding FFT, suggests that Ru-NCs have disordered/amorphous (a-Ru) structures. Amorphous nanoclusters of an average size of ~0.7 nm, surrounding crystalline larger Co nanoparticles, are more clearly visible in HAADF-STEM images at different magnifications (**Figure 4.10f**, **g**, and **Figure 4.17)**.

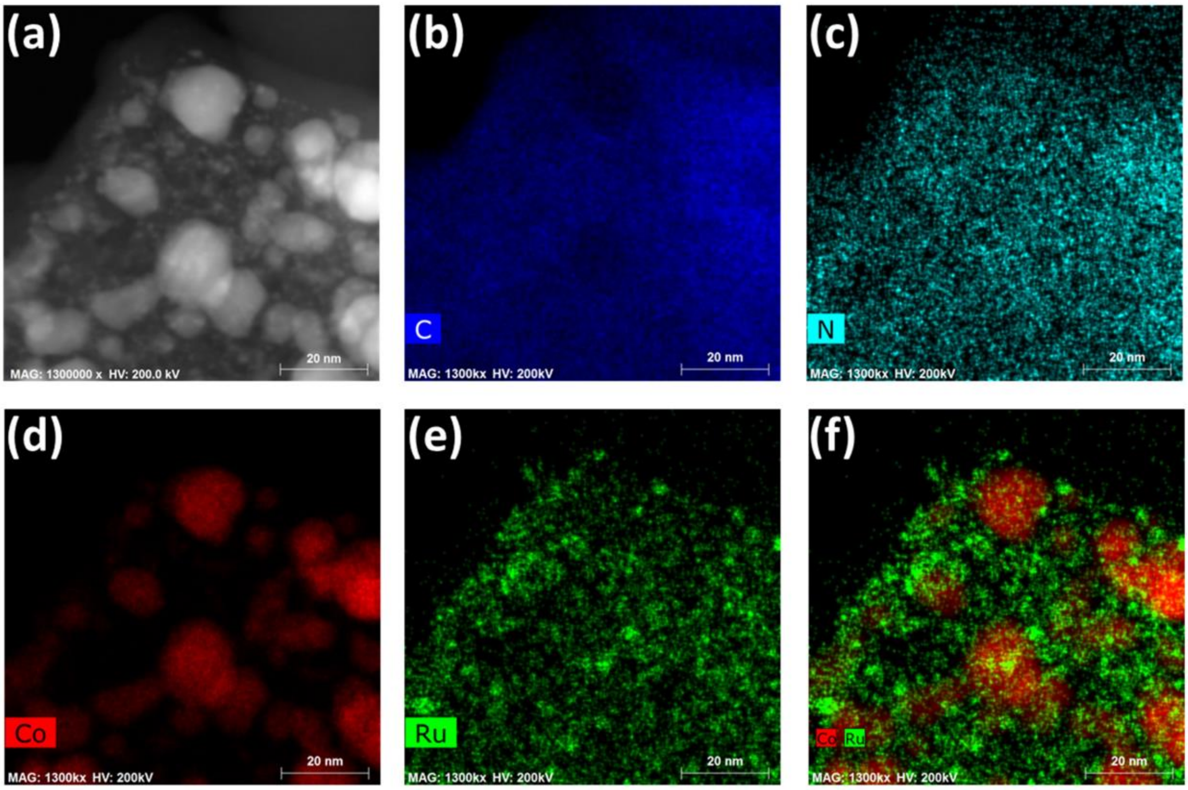

Figure 4.15: STEM EDS elemental mapping of a-Ru@GNL$_{500}$.

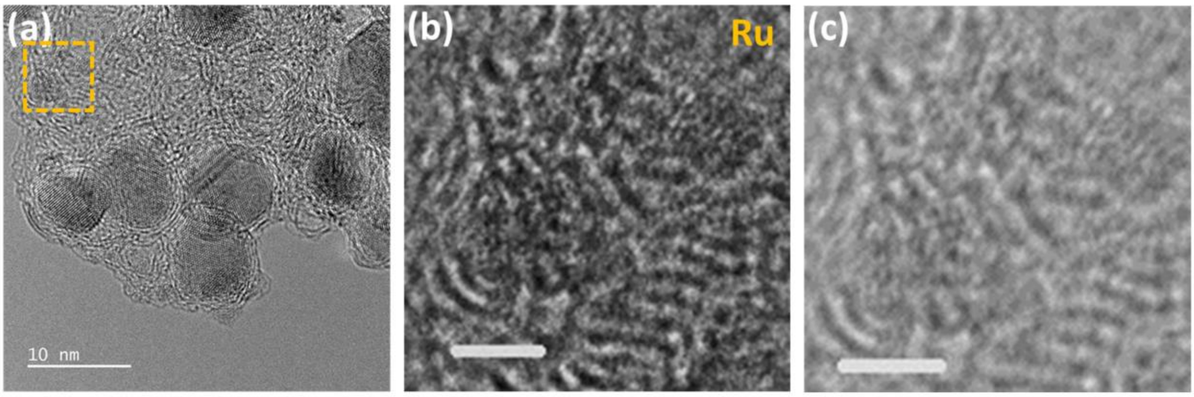

Figure 4.16: (a) Magnified TEM image of a-Ru@GNL$_{500}$, (b) HRTEM, and (c) IFFT images of selected Ru-region of a-Ru@GNL$_{500}$ (scale bars: 2 nm).

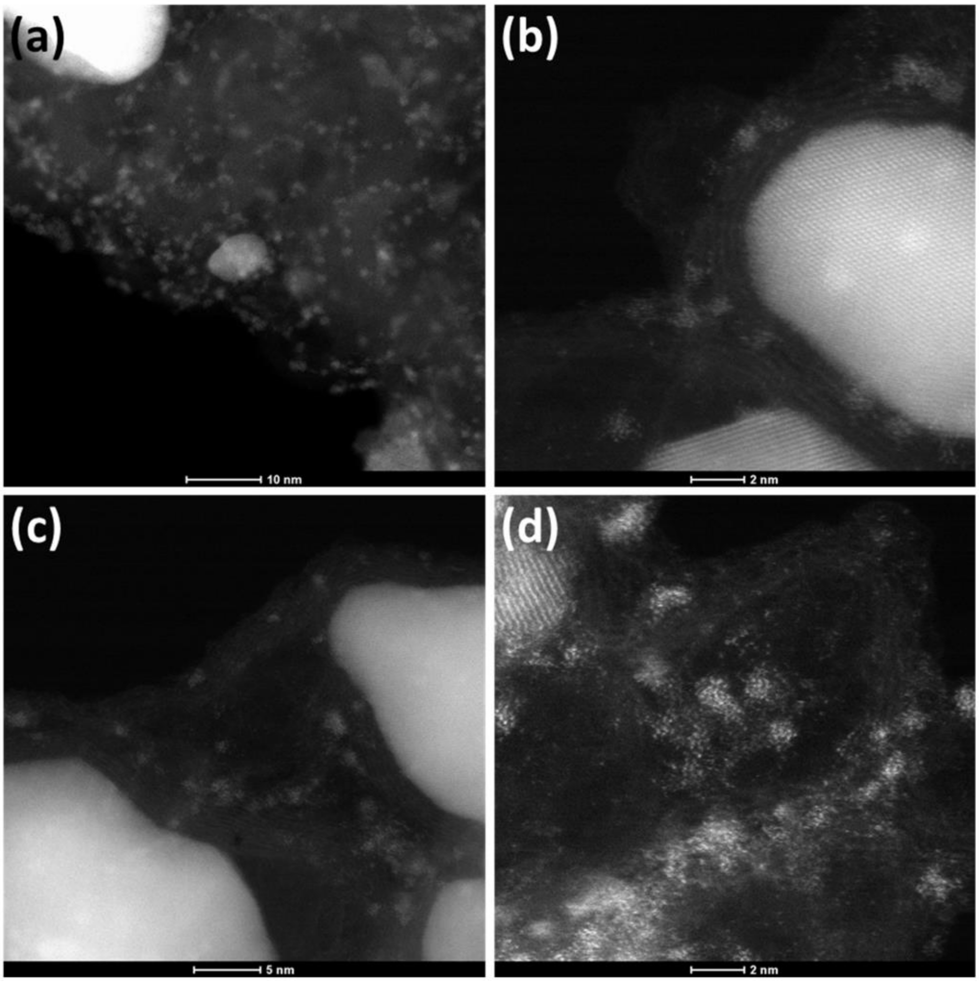

Figure 4.17: HAADF-STEM images of a-Ru@GNL$_{500}$.

High-resolution Ru3p XPS spectra of Ru-linked GNL$_{500}$ (a-Ru@GNL$_{500}$) (**Figure 4.10h**) show Ru^{0} and Ru$^{\delta+}$ related peaks with Ru^{0} dominating. The decreased contribution of Ru$^{\delta+}$ can be linked with a decrease in nitrogen dopant content in the base GNL$_{500}$ compared to GNL$_{200}$. The high-resolution XPS spectra of the other constituent elements (C1s, N1s, and Co2p) after Ru-linking (**Figure 4.18)** remained similar to those before Ru-linking. The only difference is observed in the high-resolution C1s spectra, where two extra peaks correspond to Ru3d$_{5/2}$ (281.7 eV) and Ru3d$_{3/2}$ (285.5 eV) appeared due to Ru-linking.

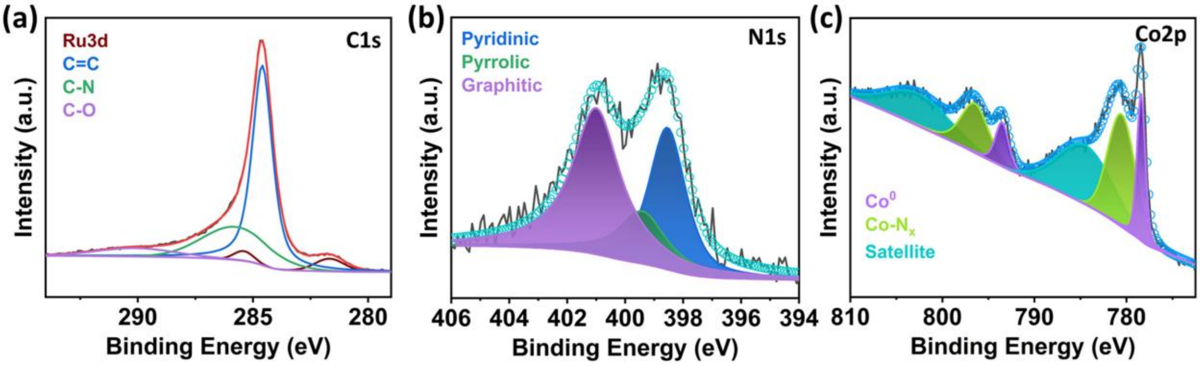

Figure 4.18: (a) C1s + Ru3d, (b) N1s, and (c) Co2p XPS spectra of a-Ru@GNL$_{500}$.

The linking of Ru to GNL$_{1000}$ (c-Ru@GNL$_{1000}$) led to the growth of crystalline Ru-NCs. TEM images (**Figure 4.10i, Figure 4.19**, **Figure 4.20**) revealed a highly graphitic, few-layered structure throughout the entire region, signifying a high degree of graphitization. The TEM images identified large particles as cobalt in the HRTEM image, FFT, and IFFT (**Figure 4.21**) and EDS elemental mapping (**Figure 4.22**). The uniformly distributed small particles, marked by yellow arrows, show the crystalline structure of Ru, as is evident from the lattice fringes in the HRTEM image (**Figure 4.23a**), with lattice spacings of 0.234 nm and 0.206 nm corresponding to (100) and (101) planes of hcp Ru, respectively. The bright spots in the FFT pattern (**Figure 4.10i)** and clear lattice fringes in the IFFT (**Figure 4.23b**) clarify the crystalline nature of Ru. The crystalline status of Co and Ru-NCs (average size of ~1.1 nm) is also evident from HAADF-STEM images shown in **Figure 4.10j, k,** and **Figure 4.24**. Notably, the Ru3p XPS spectra in **Figure 4.10l** indicate the further decrease in Ru$^{\delta+}$ states and, consequently, the rise of Ru^0 states resulting from the lowest nitrogen concentration in this sample.

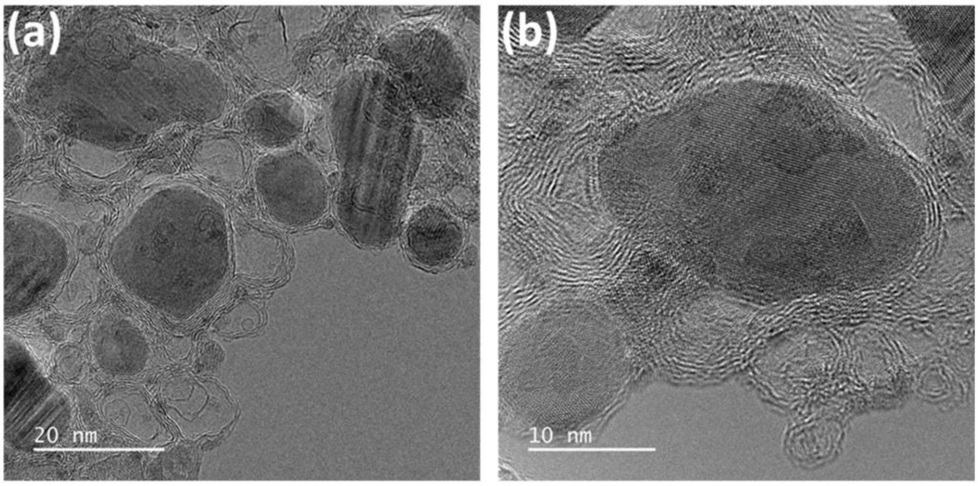

Figure 4.19: TEM images of c-Ru@GNL$_{1000}$.

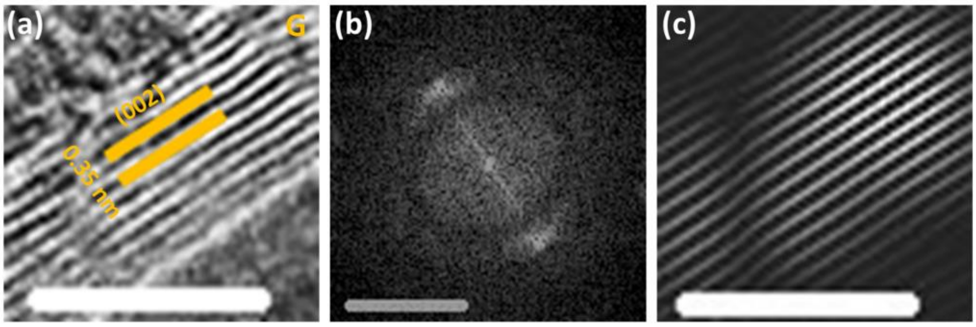

Figure 4.20: (a) HRTEM image, (b) FFT pattern, (c) IFFT image of G-region of c-Ru@GNL$_{1000}$ (scale bar: 5 nm, 5 1/nm, 5 nm, respectively).

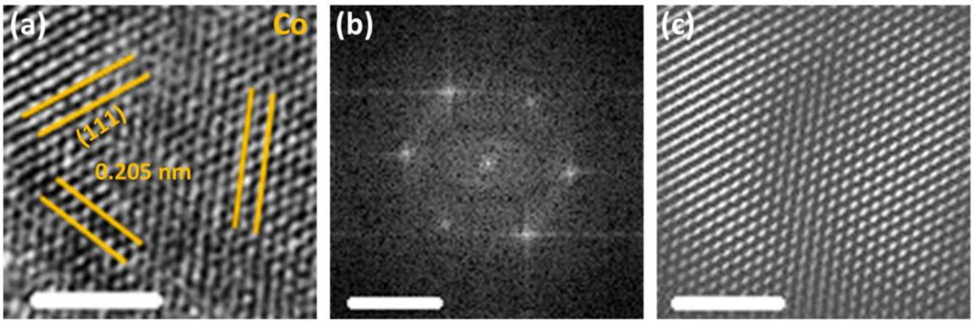

Figure 4.21: (a) HRTEM image, (b) FFT pattern, (c) IFFT image of Co-region of c-Ru@GNL$_{1000}$ (scale bar: 2 nm, 2 1/nm, 2 nm, respectively).

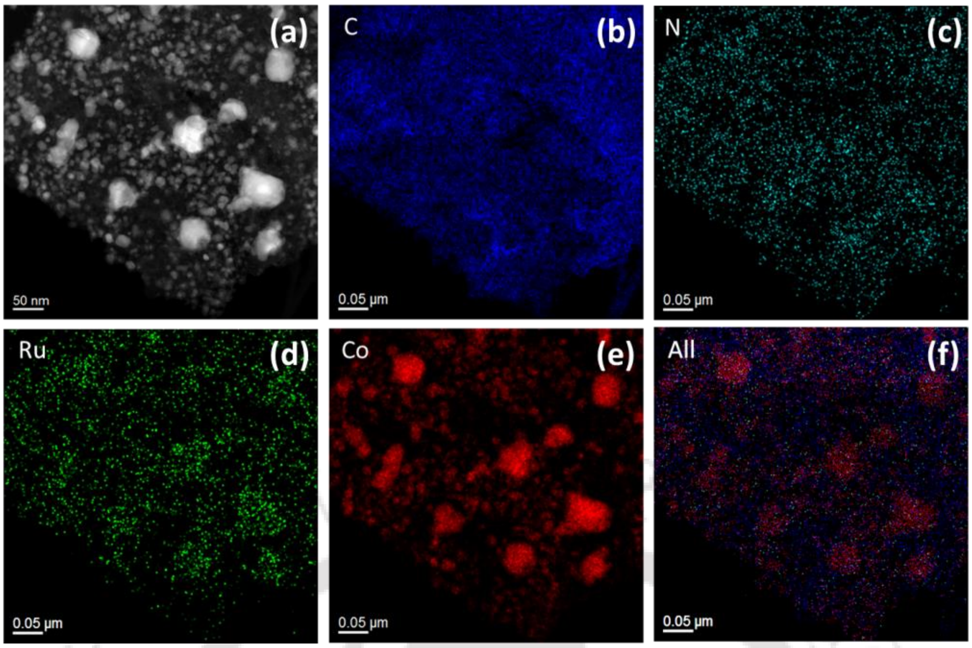

Figure 4.22: STEM EDS elemental mapping of c-Ru@GNL$_{1000}$.

The results discussed above establish that two-stage decoupled processing offers excellent control over the graphitization level of the MOF in the first stage and the size and crystalline status of the Ru-NCs linked in the second stage. To emphasize the importance of this two-stage processing, a comparison is made with a single-stage-processed sample in which graphitization and Ru-loading were done simultaneously by applying a single pulse (500 ms) to $RuCl_3$, xH_2O loaded MOF (Ru@dGNL$_{500}$) (details in Materials and methods). Unlike uniform dispersion of Ru-NCs in the two-stage processing, a massive aggregation of Ru-nanoparticles occurred (**Figure 4.10m** and **Figure 4.25a**, **b**) in Ru@dGNL$_{500}$, comparable to the size of the cobalt particles. The crystal fringes in the HRTEM and IFFT images, well-defined spots in FFT patterns, and HAADF-STEM images (**Figure 4.25c, d**, inset of **Figure 4.10m**, **Figure 4.26**, and **Figure 4.27**, **Figure 4.10o**, and **Figure 4.28**) confirm the crystalline status of the Ru, Co, and G-regions. This observation suggests that single-stage processing does not result in tunability over the crystalline status of Ru-NCs or uniform dispersion over the GNL. Rapid dynamic surface construction occurred during the current pulse-induced conversion of MOFs into GNL, which resulted in the aggregation of Ru over the surface of the GNL in Ru@dGNL$_{500}$.

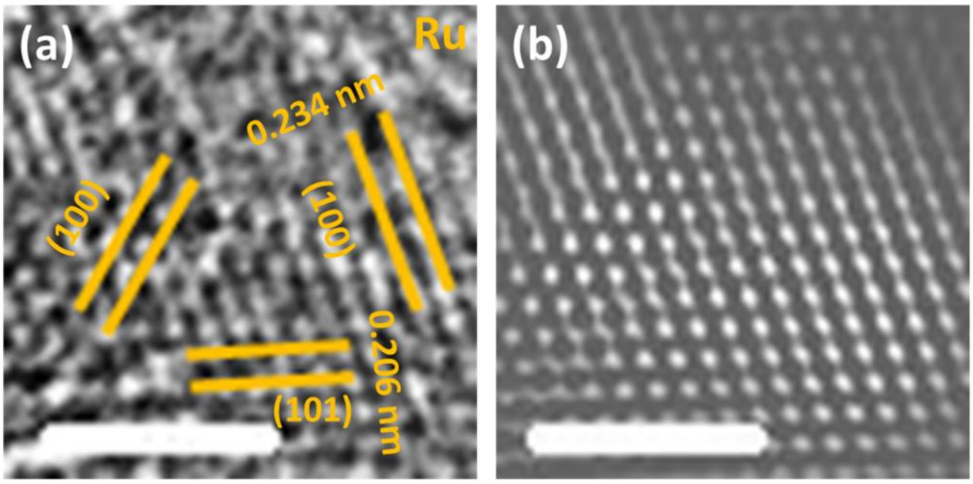

Figure 4.23: (a) HRTEM and (b) IFFT images of Ru-region of c-Ru@GNL$_{1000}$ (scale bars: 2 nm).

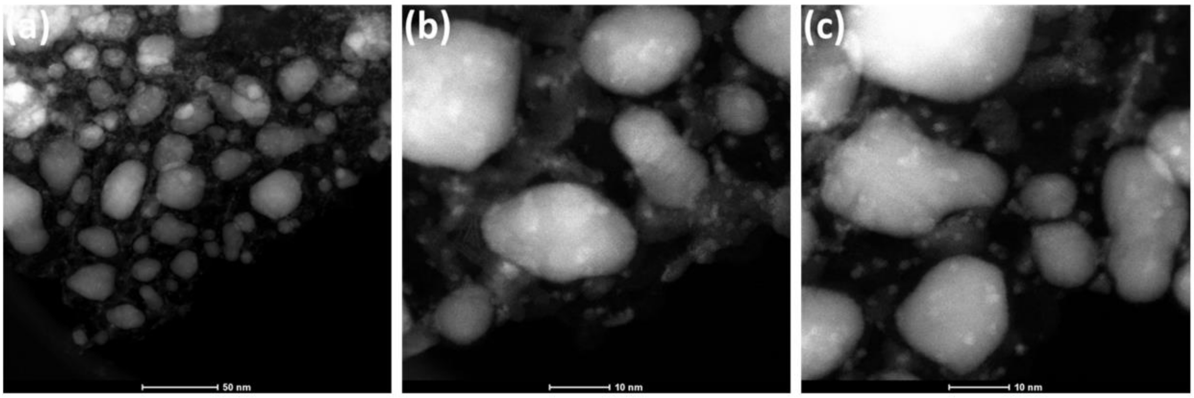

Figure 4.24: HAADF-STEM images of c-Ru@GNL$_{1000}$.

The results of Raman, XPS, TEM, and HAADF-STEM analyses suggested that Ru could be selectively crystallized in the form of predominantly Ru single-atoms (Ru-SAs), amorphous Ru nanoclusters (a-Ru-NCs), and crystalline Ru nanoclusters (c-Ru-NCs). Such selectivity in the Ru crystallization state can be linked to the variation in graphitization level and nitrogen doping concentration in GNL$_{200}$, GNL$_{500}$, and GNL$_{1000}$, as depicted in **Figure 4.10p**. Pyridinic N bound the supported catalysts in all the N-dopant configurations. Furthermore, defects are inevitable in low graphitic structures, which can trap single atoms and restrict the migration of metal atoms at high temperatures.[54] When ruthenium chloride over GNL$_{200}$ turns into ruthenium through thermal treatment, a significant number of available pyridinic nitrogen dopants, as well as defect sites of this non-graphitic carbon, anchor the ruthenium atoms and do not allow them to migrate to form clusters, thereby resulting in uniformly dispersed single-atom sites (**Figure 4.10p (I)**). A decrease of pyridinic nitrogen in GNL_{500} and a decrease in defect density (due to an increase in graphitization level) could not hold all the ruthenium atoms as single atom sites; thus, nearby atoms migrated to form a small cluster. However, ultrafast cooling of the system when a 50 ms pulse passes arrests the clustering of Ru atoms in a disordered/amorphous state (**Figure 4.10p (II)**). For the case of GNL_{1000}, the nitrogen content is low and highly graphitic, so nearby ruthenium atoms easily migrate to crystallize in the form of small crystalline nanoparticles, as presented in **Figure 4.10p (III)**.

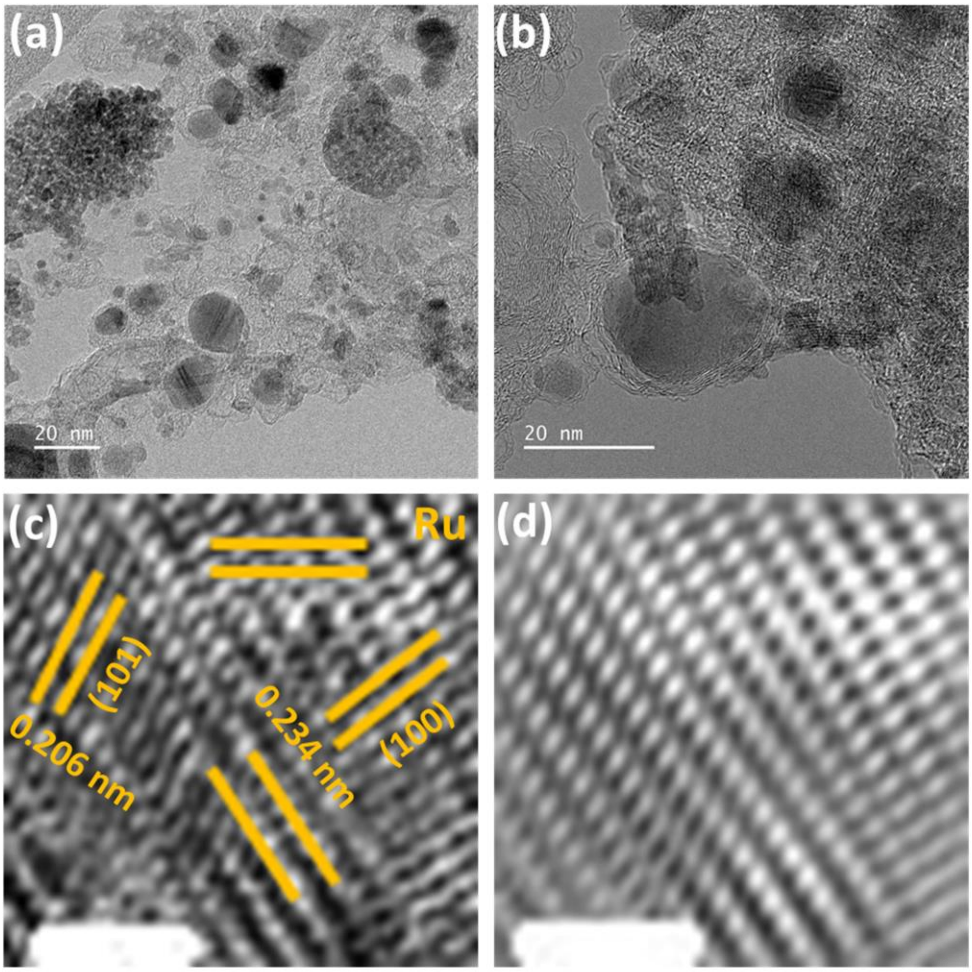

Figure 4.25: (a), (b) TEM images of Ru@$dGNL_{500}$, (c) HRTEM, and (d) IFFT images of Ru-region of Ru@$dGNL_{500}$ (scale bars: 2 nm).

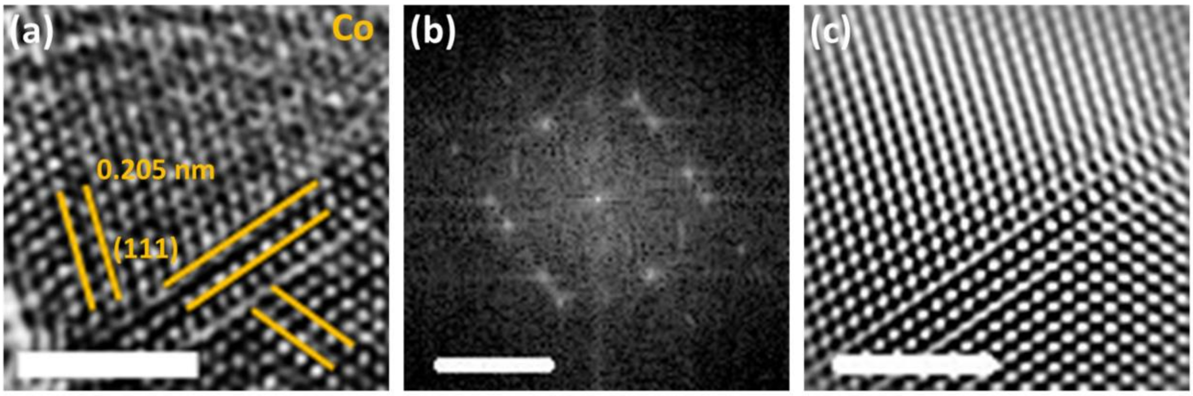

Figure 4.26: (a) HRTEM image, (b) FFT pattern, (c) IFFT image of Co-region of Ru@dGNL$_{500}$ (scale bar: 2 nm, 2 1/nm, 2 nm, respectively).

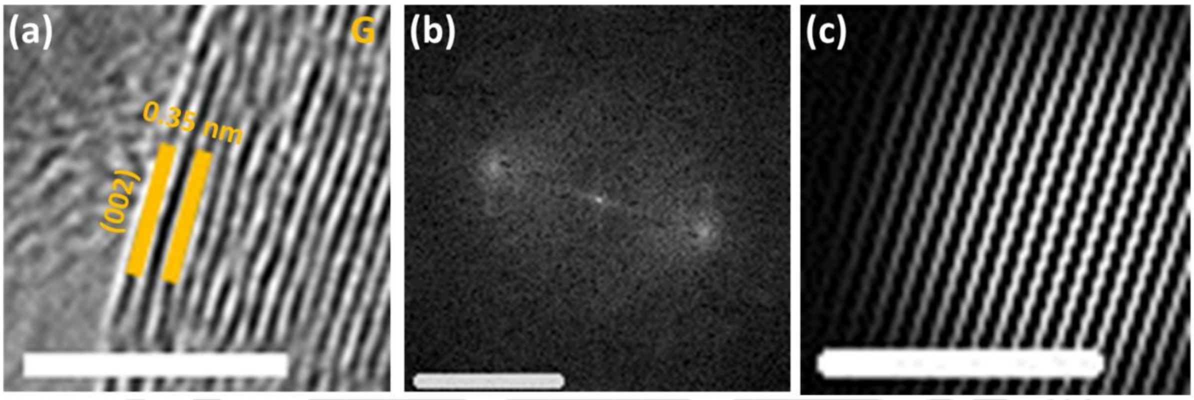

Figure 4.27: (a) HRTEM image, (b) FFT pattern, (c) IFFT image of G-region of Ru@dGNL$_{500}$ (scale bar: 5 nm, 5 1/nm, 5 nm, respectively).

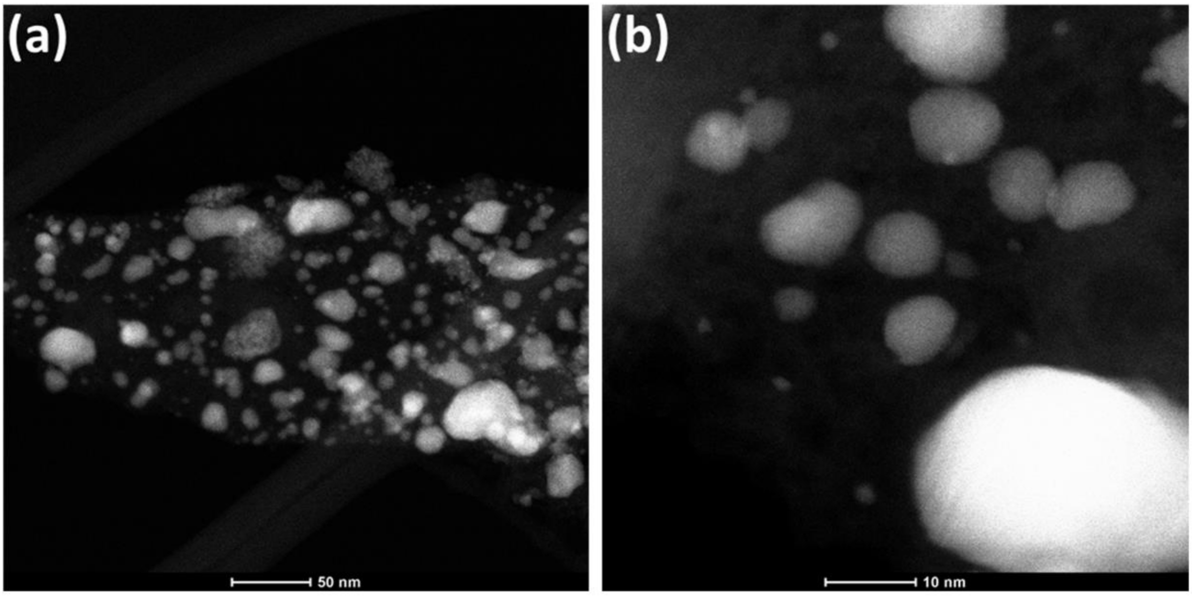

Figure 4.28: HAADF-STEM images of Ru@dGNL$_{500}$.

4.4.2. The universality of the pulsed current-induced two-stage process for uniformly dispersed metal nanocluster over GNL

To demonstrate the universality of our two-stage current pulse-induced processing, ultrafine nanoclusters of iridium and palladium were uniformly linked with GNL_{500}. The TEM images of Ir-linked GNL_{500} (**Figure 4.29a**, **b**, and **Figure 4.30)** again reveal the co-existence of larger cobalt particles, as evident from HRTEM, FFT, and IFFT images (**Figure 4.31**), accompanied by uniformly dispersed ultrafine Ir nanoparticles. These fine nanoparticles are crystalline, as is evident from HRTEM (**Figure 4.32a**), FFT (inset of **Figure 4.29a**), and IFFT (**Figure 4.32b**) images and the lattice spacings of 0.237 nm and 0.216 nm correspond to (111), and (200) planes of Ir, respectively. Atomic-resolution HAADF-STEM images at different magnifications (**Figures 4.29c**, **d**, and **4.33**) further clearly show the highly crystalline nature of the Ir nanoparticles (average size of ~ 1.3 nm).

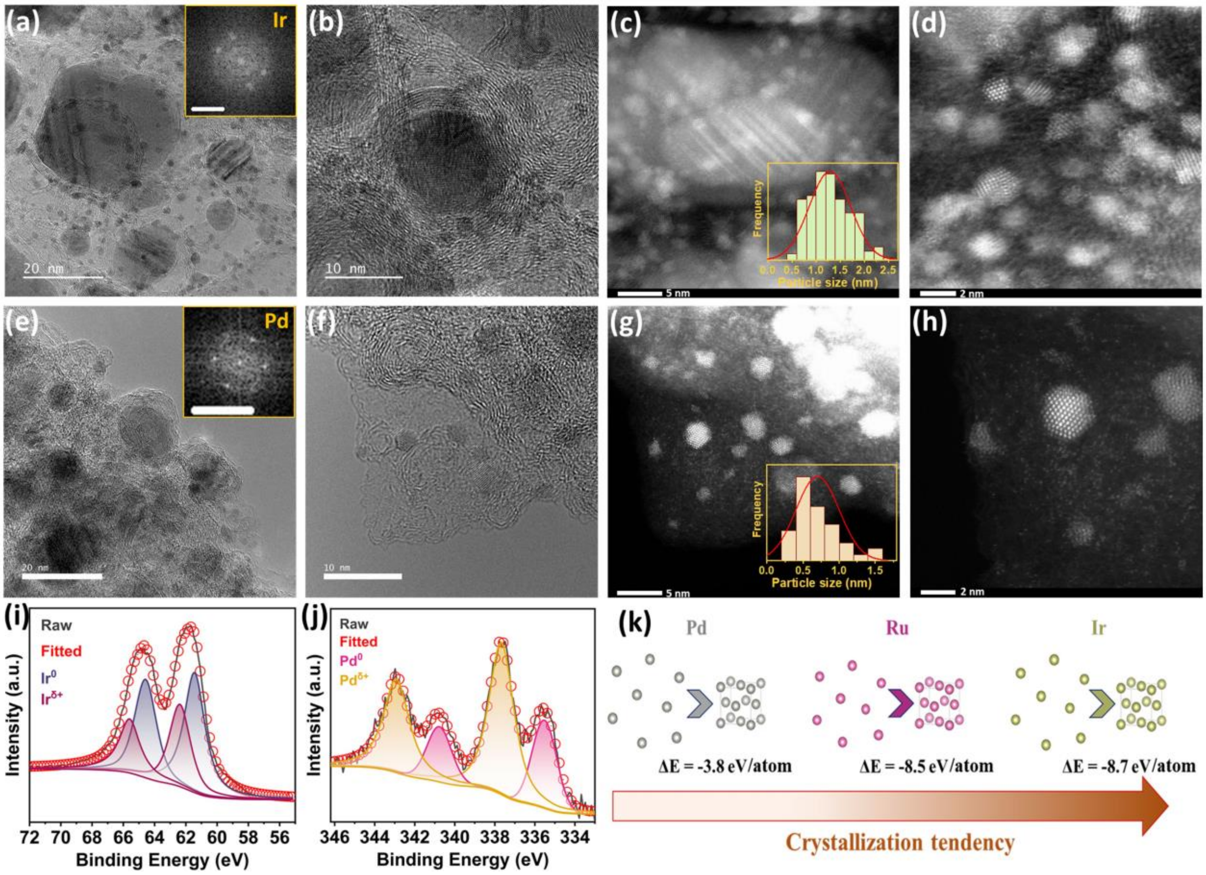

Figure 4.29: Universal linking of Ir-NCs and Pd-NCs over GNL_{500}. (a) FETEM image, inset: FFT pattern of Ir-region, and (b) magnified FETEM image, (c) low-, and (d) high-magnification HAADF-STEM images of Ir-NCs@GNL_{500}, (e)-(h) the corresponding FETEM,

FFT (inset), and HAADF-STEM images of Pd-NCs@GNL$_{500}$, (i) Ir4f, (j) Pd3d XPS spectra of Ir-NCs@GNL$_{500}$ and Pd-NCs@GNL$_{500}$, respectively, (k) crystallization tendencies of Ru, Ir, and Pd.

For palladium, the TEM images (**Figure 4.29e**, **f**, and **Figure 4.34**) reveal the presence of bigger cobalt particles together with small nanoparticles, both of which are crystalline, as is evident from HRTEM, FFT and IFFT images (**Figure 4.35**, inset of **Figure 4.29e**, **Figure 4.36**). The inter-planner spacings of 0.235 nm and 0.212 nm correspond to palladium's (111) and (200) planes, respectively. Importantly, atomic resolution HAAD-STEM images (**Figure 4.29g**, **h**, and **Figure 4.37**) reveal additional features with crystalline Pd nanoparticles (average size of ~ 0.7 nm). Uniformly dispersed numerous Pd single atoms were observed together with crystalline Pd nanoparticles. The deconvoluted Ir4f (**Figure 4.29i**) and Pd3d (**Figure 4.29j**) XPS spectra also show the existence of Ir^0(Pd^0) and Ir$^{\delta+}$ (Pd$^{\delta+}$), confirming their charge states similar to ruthenium as discussed earlier. Surprisingly, the same experimental conditions as those used for GNL$_{500}$ resulted in different crystallizations for Ru (amorphous nanoclusters), Ir (crystalline nanoparticles), and Pd (crystalline nanoparticles and single atoms). In the case of a-Ru@GNL$_{500}$, the highly dominant configuration is the amorphous cluster (**Figure 4.10f, g**), and the crystalline cluster is the main dominant feature in Ir-NCs@GNL$_{500}$ (**Figure 4.29c, d**). In contrast, the Pd-NCs@GNL$_{500}$ is dominated by single atoms (**Figure 4.29g, h**).

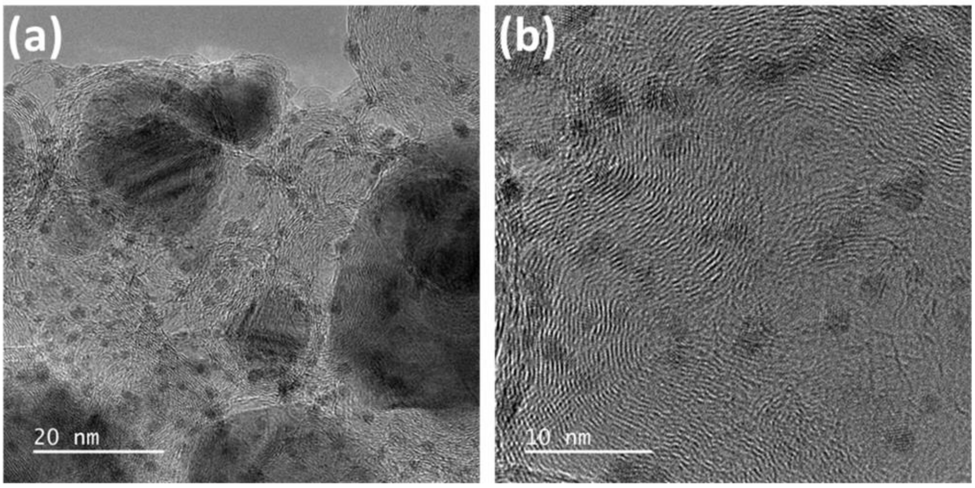

Figure 4.30: TEM images of Ir-NCs@GNL$_{500}$.

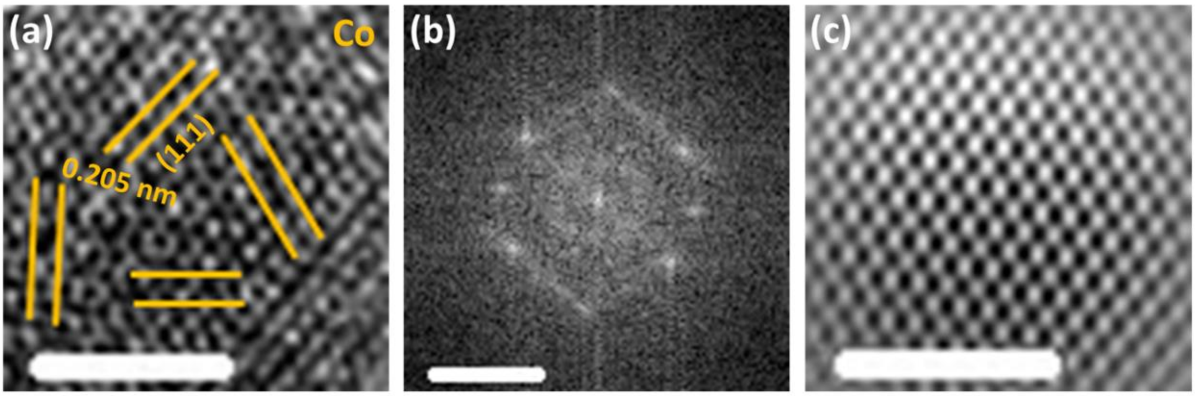

Figure 4.31: (a) HRTEM image, (b) FFT pattern, (c) IFFT image of Co-region of Ir-NCs@GNL$_{500}$ (scale bar: 2 nm, 2 1/nm, 2 nm, respectively).

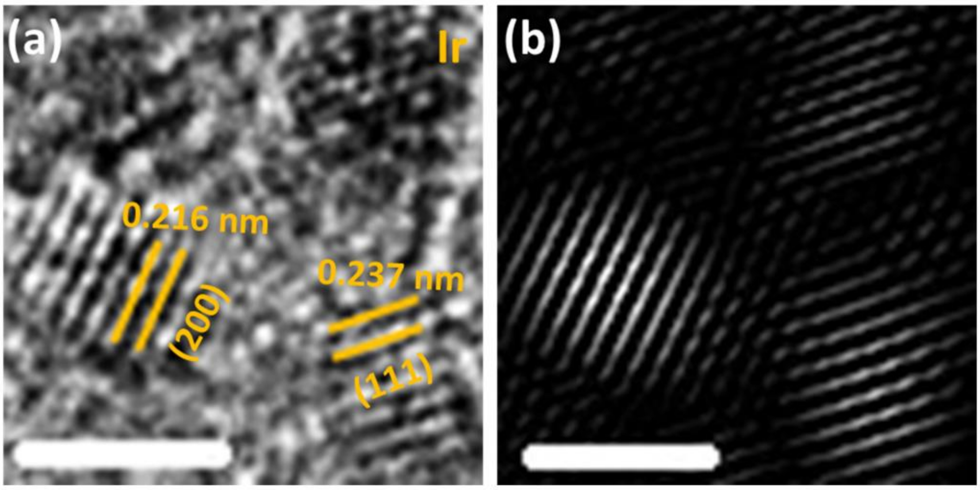

Figure 4.32: (a) HRTEM, and (b) IFFT images of Ir-region of Ir-NCs@GNL$_{500}$ (scale bars: 2 nm).

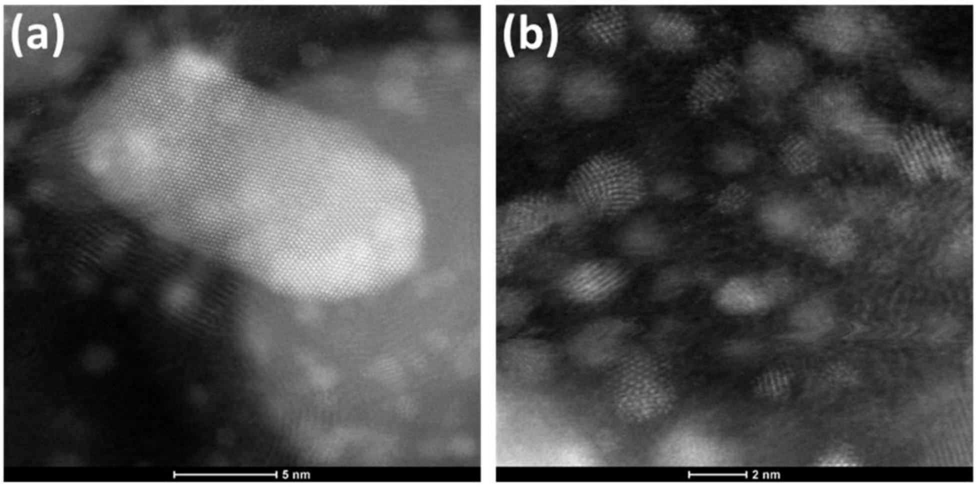

Figure 4.33: HAADF-STEM images of Ir-NCs@GNL$_{500}$.

Further, with significant features of amorphous (Ru) or crystalline (Ir) clusters, some single atoms are also visible in these two cases. The observed difference in the crystallization behavior of the significant feature (amorphous cluster for Ru, crystalline cluster for Ir, and single atomic case of Pd) can be explained by the difference in the crystallization tendency or the trend in the cohesive energy of nanocluster formation of the metals and the role of support.[55] The GNL_{500} support consists of nitrogen dopant sites/topological defects. They try to hold the atoms in their single-atomic configurations, but the crystallization tendency at high temperatures (due to 50 ms pulse) tends to make clustering of atoms. Although most Ru/Ir atoms participate in the clustering during this crystallization process, some may remain locked in the single atomic state, which can describe their presence with dominant amorphous (Ru) and crystalline (Ir) clusters. Since all the samples under consideration were developed under the same conditions on GNL500, the observed difference in crystallization trend can only be explained by the intrinsic crystallization tendency of the different metals. DFT calculation (**Figure 4.29k**) shows that Ir has the highest crystallization tendency; thus, despite the competitive role of the dopant/defect site, the atoms mostly crystallize into crystalline clusters even within a very short pulse duration of 50 ms. Meanwhile, defect or dopant sites of Pd keep the atoms mostly locked in the single atomic state, overcoming its atomic cohesion tendency due to its lowest crystallization tendency. On the other hand, Ru, having a crystallization tendency between Ir and Pd, the atomic cohesion could not fully crystallize within this short pulse duration, and it arrests in the amorphous state.

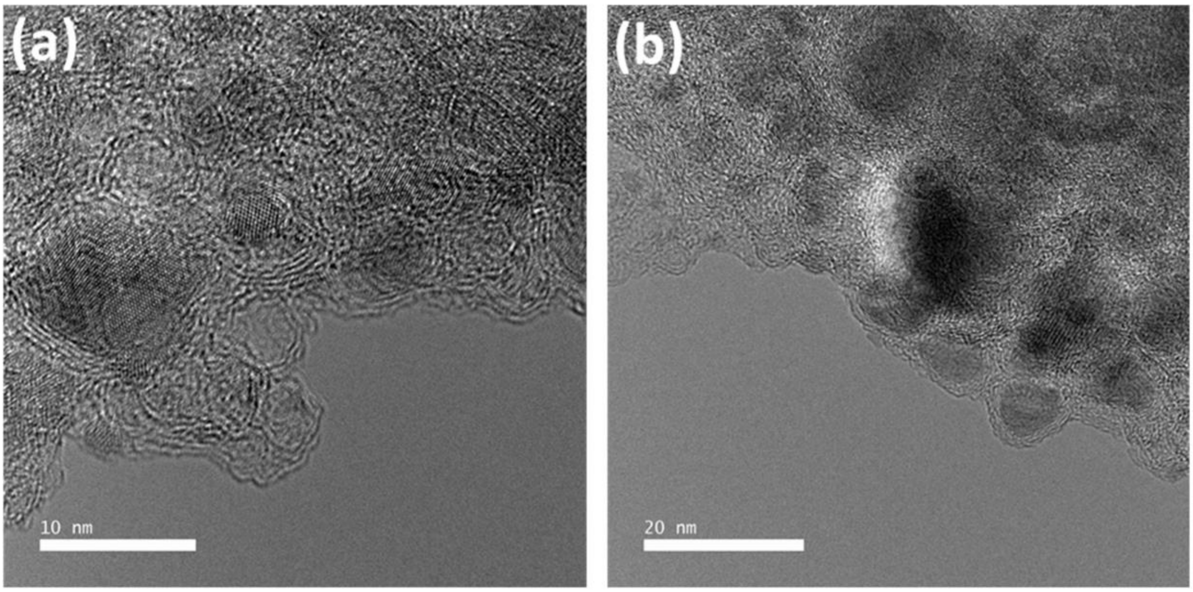

Figure 4.34: TEM images of Pd-NCs@GNL$_{500}$

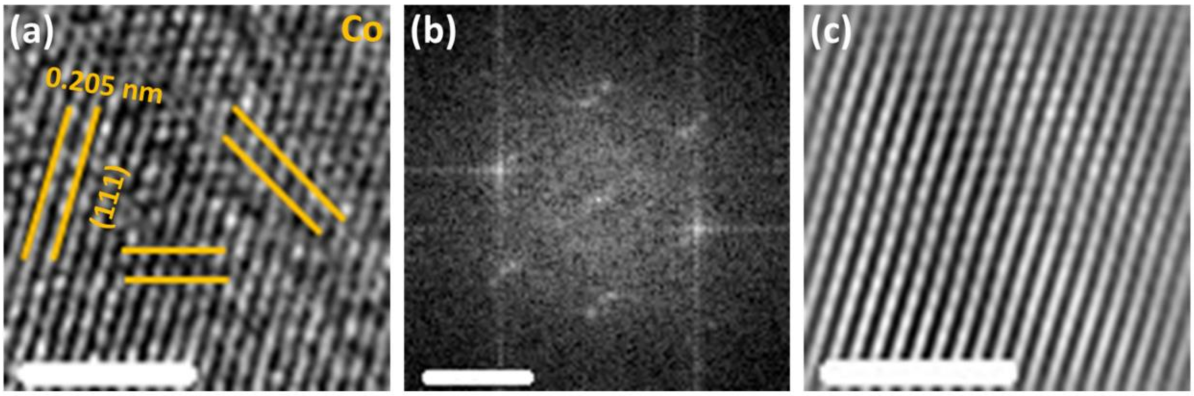

Figure 4.35: (a) HRTEM image, (b) FFT pattern, (c) IFFT image of Co-region of Pd-NCs@GNL$_{500}$ (scale bar: 2 nm, 2 1/nm, 2 nm, respectively).

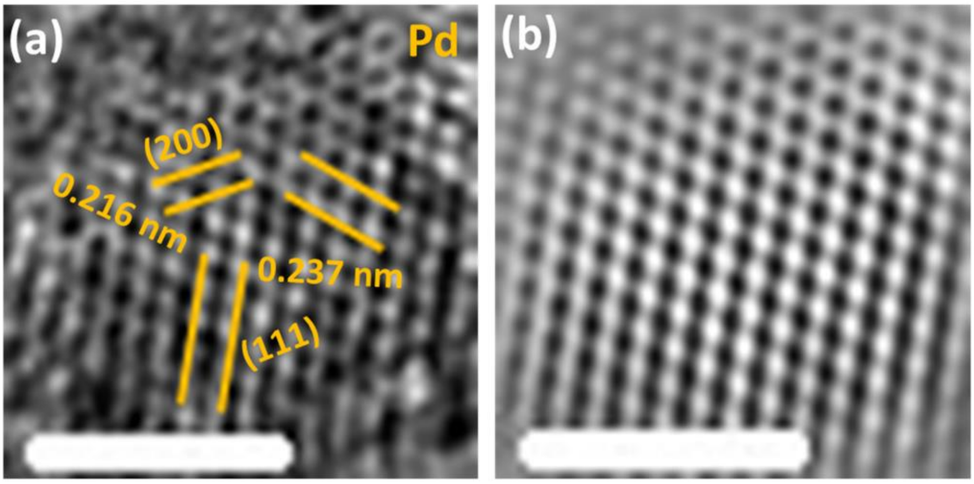

Figure 4.36: (a) HRTEM, and (b) IFFT images of Pd-region of Pd-NCs@GNL$_{500}$ (scale bars: 2 nm).

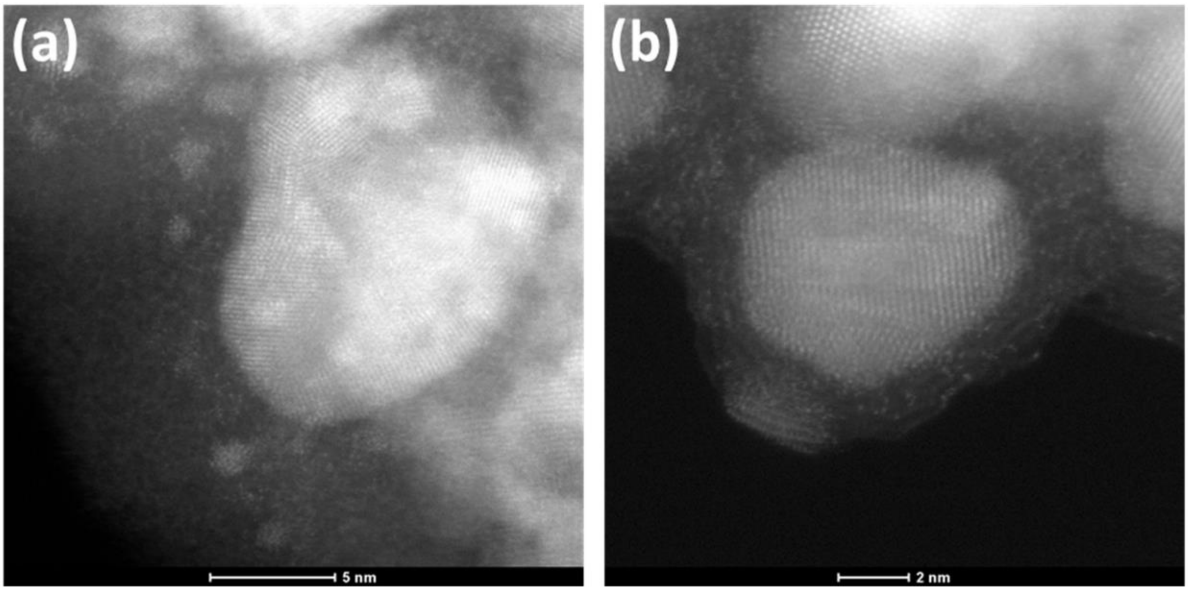

Figure 4.37: HAADF-STEM images of Pd-NCs@GNL$_{500}$.

4.4.3. Electrocatalytic performance towards HER

The ultra-small sizes of Ru-NCs, with their unique crystallization states, conducting GNL support with tunable graphitization and adequate N-doping, and the bubble-releasable open structure of GNL, all are expected to benefit their catalytic activity towards water splitting. The electrocatalytic hydrogen evolution reaction (HER) activity of Ru-NCs-linked GNLs was evaluated using linear sweep voltammetry (LSV) in a 1M KOH electrolyte with a saturated calomel as a reference electrode (**Figure 4.38a**). The LSV curves show that the activity of a-Ru@GNL$_{500}$ is the highest, and the required overpotentials (η) to deliver current densities of

10 mA cm^{-2} (η_{10}) and 100 mA cm^{-2} (η_{100}) are only 23.0 mV and 91.6 mV, respectively. These overpotential values are the lowest as compared to most of the HER catalysts reported to date (**Table 4.2**) and even lower than state-of-the-art Pt/C catalysts, which require η_{10} and η_{100} of 36.5 mV and 103.0 mV (**Figure 4.38a**), respectively. The Ru-SA@GNL$_{200}$ and c-Ru@GNL$_{1000}$ also show competitive HER performance with η_{10} of 37.4 mV and 64.1 mV, respectively, while η_{100} are 133.7 mV and 200.6 mV, respectively. The performance of GNL$_{500}$ alone showed much inferior performance (**Figure 4.38a**), requiring much higher overpotentials of 191.8 mV (η_{10}) and 309.8 mV (η_{100}), signifying the high HER activity of a-Ru@GNL$_{500}$ is associated with linked a-Ru-NCs. The Tafel slopes of the investigated catalysts were estimated from their LSV curves to evaluate their catalytic efficiency further. The a-Ru@GNL$_{500}$ catalyst exhibited impressively faster HER kinetics than the other catalysts (**Figure 4.38b**), which followed the Pt-like Volmer-Tafel mechanism for the HER, with a Tafel slope of 49 mV dec^{-1}, close to 42 mV dec^{-1} for the Pt/C catalyst.

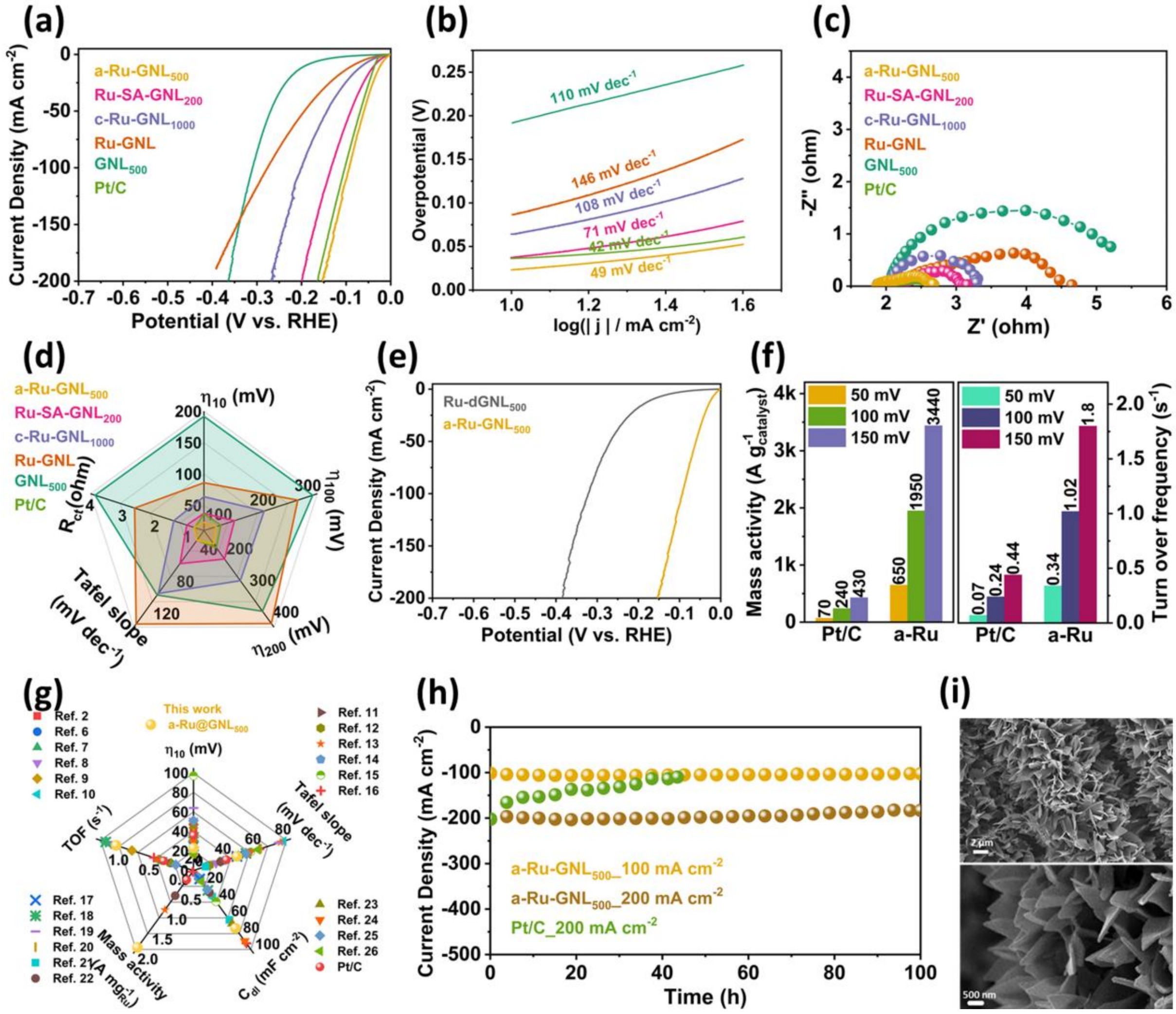

Figure 4.38: Electrochemical HER performance evaluation. (a) HER polarization curves (iR-corrected) of as-developed Ru-NCs catalysts and Pt/C in 1M KOH, (b) corresponding Tafel plots, and (c) Nyquist plots of the catalysts, (d) radar plot consisting of the performances of the developed catalysts in terms of the values of η_{10}, η_{100}, η_{200}, Tafel slopes, and R_{ct}, (e) LSV curves of Ru@dGNL$_{500}$ compared to a-Ru@GNL$_{500}$, (f) comparison of MA and TOF of a-Ru@GNL$_{500}$ and Pt/C, (g) comparison of HER performance of a-Ru@GNL$_{500}$ with other Ru-based reference catalysts, (h) chronoamperometry tests (stability) of a-Ru@GNL$_{500}$ for 100 hours compared to 50 hours test of Pt/C, (i) low- and high-magnification FESEM images of a-Ru@GNL$_{500}$ after 100 hours of stability test.

Table 4.2: Comparison table of HER performance of the developed catalyst and previously reported Ru-based HER catalysts.

Sl. No	**Sample Name**	**Ru Content (µg cm^{-2})**	**η_{10} (mV)**	**η_{100} (mV)**	**Tafel Slope (mV dec^{-1})**	**ECSA (C_{dl}) (mF cm^{-2})**	**Mass activity @100 mV (A g^{-1})**	**TOF (s^{-1})**		**Ref**
								@50 mV	**@100 mV**	
1	Ru/NC-400		39		49					[7]
2	Ru-ZrO2-x/C	18	35.6		29					[8]
3	RuNP-RuSA@CFN-800		33		37.16					[9]
4	Ni@Ni2P−Ru		51		35				1.10	[10]
5	Ru@C2N	285	17		38			0.76 @ η=25 mV		[11]
6	Ru-Mo2C/CN		34		80	32.7		1.2		[12]
7	RP-CPM		24		47.3	5.8				[13]
8	Au–Ru-2 NW	17	50		30.8			0.31		[14]
9	CoNiRu-NT		22	124	78	28.5	998		0.33	[15]
10	Ru3Sn7		27		40	7.7				[16]
11	Ru-NPs/SAs@N-TC		97		58	37.5				[17]
12	Ru-3/FNS		47		64	87.8	35.54	0.2	0.4	[18]
13	Ru-Cu@CM/CC		25	94	49	10.3				[19]
14	M-Co NPs@Ru SAs/NC		34	137	55	23.9		1.19 @ η=16 mV		[20]
15	Ru/NPC-2		64		76.8	14.16				[21]
16	RuCo/NCNF		41		64.8					[22]
17	Ru-POCA		22		28	59.6		0.24		[23]
18	Ru/D-NPC		23		38	26.4	639.9		0.130	[24]
19	Co@RuCo-3		46		50	64			0.115	[25]

20	RuCuOx/NC		29		57.7	85.1				[26]
21	Ru-Ni3N		51		55	23			0.04@ 150 mV	[27]
22	Ru MIs-doped MoS2		17		63	13.3				[28]
23	**Pt/C**	**400**	**36**	**104.0**	**42**		**240**	**0.07**	**0.24**	**This work**
24	**a-Ru@GNL$_{500}$**	**56.6**	**23**	**92.6**	**49**	**69.6**	**1950**	**0.34**	**1.02**	

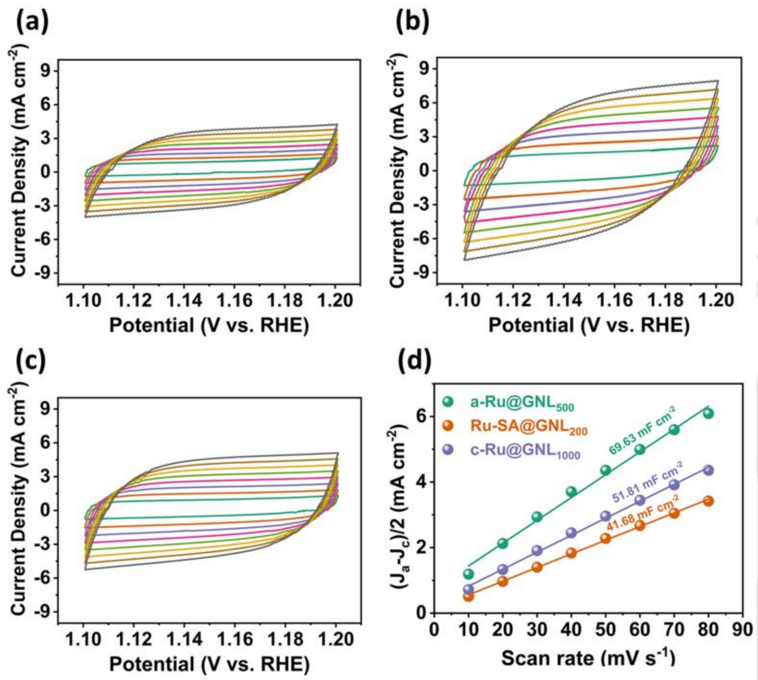

Figure 4.39: Cyclic voltammetry curves obtained in a non-faradaic region for (a) Ru-SA@GNL$_{200}$, (b) a-Ru@GNL$_{500}$, (c) c-Ru@GNL$_{1000}$, (d) current density difference versus scan rate plot to estimate C_{dl} for ECSA of different catalysts.

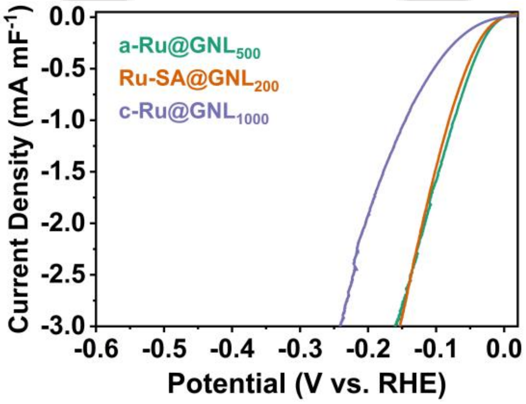

Figure 4.40: ECSA normalized HER LSV curves of the developed catalysts.

Nyquist plots were used to estimate the charge transfer resistance (R_{ct}) from the semicircle of the electrochemical impedance spectra (EIS) (**Figure 4.38c**) and to understand the origin of the catalytic activity. The R_{ct} values of the prepared catalysts follow the order as Pt/C (0.78 Ω) < a-Ru@GNL$_{500}$ (0.80 Ω) < Ru-SAs@GNL$_{200}$ (1.03 Ω) < c-Ru@GNL$_{1000}$ (1.43 Ω) < GNL$_{500}$ (3.86 Ω). The best-performing catalyst, a-Ru@GNL$_{500}$, had an optimal R_{ct} value close to the R_{ct} of the Pt/C catalyst, indicating a favorable charge transfer capability of a-Ru@GNL$_{500}$. The results of electrocatalytic activity ($\eta_{10}, \eta_{100}, \eta_{200}$, Tafel slope, R_{ct}) are summarized in the radar plot in **Figure 4.38d**, where the best performing HER catalyst a-Ru@GNL$_{500}$ possesses the smallest area covered in the radar plot, suggesting the smallest values of all the parameters and hence the super activity of this catalyst. To determine the origin of the variation in the HER activities of as-developed Ru-linked GNL catalysts, electrochemically active surface area (ECSA) was estimated by measuring electrical double-layer capacitance (C_{dl}) using cyclic voltammetry in the non-Faradic region (**Figure 4.39**). The estimated C_{dl} values are presented in **Figure 4.39d**, which shows that it follows the order a-Ru@GNL$_{500}$ > c-Ru@GNL$_{1000}$ > Ru-SA@GNL$_{200}$.The ECSA normalized LSV curves (**Figure 4.40**) showed that HER current at a particular overpotential is higher for a-Ru@GNL$_{500}$ than Ru-SA-GNL$_{200}$ and c-Ru@GNL$_{1000}$, which signifies better intrinsic catalytic activity of the former.

Generally, the overall overpotential (η) is contributed by three factors: $\eta = \eta_c + \eta_s + \eta_m$,[56] where, η_c is determined by the electronic activity of catalytic sites, η_s arises due to resistive potential drop at the catalytic support and catalyst body when an electron passes from the external circuit to the active material and η_m is determined by the mass transport limitations. Particularly η_m is high at high current densities due to blockage of the catalytic active sites by generated gas bubbles during HER, which limits the transport of reactive species to come in contact with the active sites. All the developed electrodes exhibited excellent mass transport efficiencies owing to their super-aerophobic structures, which will be discussed later. Considering the other two contributions, the observed variation in overpotentials can be attributed to their variation in intrinsic activity (η_c) and the difference in graphitization level, which can control η_s. The graphitic structure is known to provide high conductivity owing to delocalized pi-electrons.[57,58] Thus, an increase in graphitization level with the pulse duration can lower the resistive loss (low η_s). Thus, lower overpotentials of a-Ru@GNL$_{500}$ as compared to Ru-SAs@GNL$_{200}$ can be attributed to the higher graphitization level of the former (low η_s)

as well as its higher intrinsic activity (low η_c) due to better reaction kinetics, as is evident from EIS analysis. Despite having the highest graphitization level (lowest η_s), the c-Ru@GNL$_{1000}$ shows lower performance as compared to other counterparts due to low intrinsic activity (higher η_c). To emphasize the importance of our two-stage current pulse-induced processing, catalytic activities of Ru@dGNL$_{500}$ and a-Ru@GNL$_{500}$ were compared, in which the former showed much inferior performance with high η_{10} (166 mV) value (**Figure 4.38e**). Heavy agglomeration of Ru occurred in the single-stage process, resulting in an inferior performance of Ru@dGNL$_{500}$.

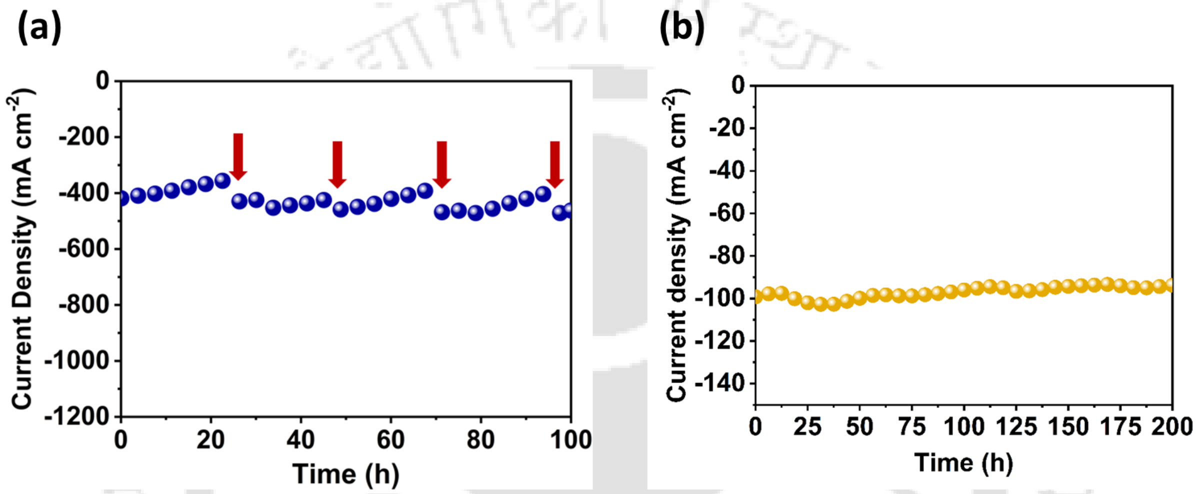

Figure 4.41: Chronoamperometry test of a-Ru@GNL$_{500}$ at (a) 400 mA cm^{-2} for 100 h, (b) 100 mA cm^{-2} for 200 h.

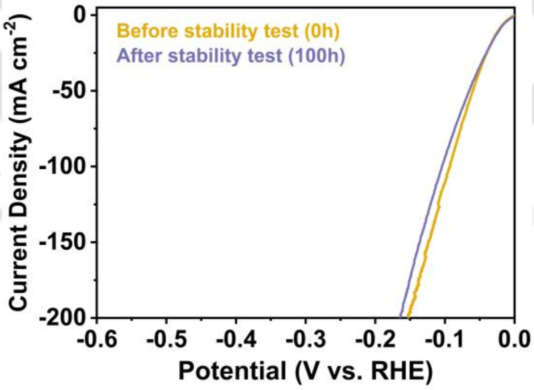

Figure 4.42: LSV curves before and after the stability test for 100 h.

The ultimate goal of designing ruthenium-based catalysts is to achieve high performance with minimal use of noble metal ruthenium. Mass-specific activity (MA) and turnover frequency (TOF) are vital parameters for evaluating the intrinsic activity of the catalysts. The MA and

TOF of the best-performing a-Ru@GNL$_{500}$ and commercial Pt/C catalysts are shown in **Figure 4.38f**. a-Ru@GNL$_{500}$ exhibited an MA of 1950 A g_{Ru}^{-1}, and a TOF of 1.02 s^{-1} at 100 mV, which were considerably higher than those of the commercial Pt/C catalyst. A comprehensive comparison of overpotentials (η_{10}), Tafel slopes, TOFs, MA, and ruthenium loading for our best-performing catalysts, and recently reported top-performing ruthenium-based HER catalysts are presented in **Figure 4.38g** and **Table 4.2**. **Figure 4.38g** and **Table 4.2** display that a-Ru@GNL$_{500}$ is one of the best-performing catalysts reported to date from all the figures of merits. In addition to a low onset potential, long-term operational stability is a crucial metric for HER catalysts, particularly at demanding high operating currents. The operational stability of the best-performing catalyst (a-Ru@GNL$_{500}$) was evaluated by continuously running the HER process for 100 h in chronoamperometry mode, maintaining the initial current density at high values of 100 mA cm^{-2}, 200 mA $cm^{-2,}$ and 400 mA cm^{-2}. a-Ru@GNL$_{500}$ showed very stable HER performance at all the current densities, as is evident from **Figure 4.38h** and **Figure 4.41a**. a-Ru@GNL$_{500}$ exhibited a very stable performance after 200 hours of HER operation (**Figure 4.41b**). In comparison, current density falls by ~50% for the Pt/C catalyst after only 40 hours while operating at 200 mA cm^{-2}. Notably, a decrease in water content due to fast dissociation at a high current (400 mA cm^{-2}) increases the concentration of KOH in the electrolyte, which leads to an increase in HER current with time. However, with a change of electrolyte every 25 hours, the current reached a value similar to the initial value, demonstrating excellent stability when operated at a very high current of 400 mA cm^{-2}. After 100 hours of stability operation at 100 mA cm^{-2}, the LSV curve of the a-Ru@GNL$_{500}$ catalyst did not show any significant change, which also suggests the high stability of the catalyst (**Figure 4.42**).

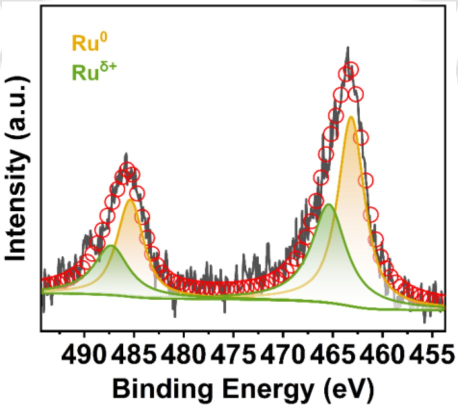

Figure 4.43: Ru3p XPS spectra of a-Ru@GNL$_{500}$ after HER.

Rupturing forces due to bubble detachment and electrolyte convection are common causes of catalyst detachment and collapse of the electrode structure, which degrade the stability of the catalysts during long-term water splitting. The gas-releasing open structure of the electrode, which consists of a robust graphitic GNL, can withstand the rupturing forces and provide excellent operational durability. The robustness of the structure is evident from the FESEM images after the stability test at the high current of 100 mA cm^{-2}, which shows no noticeable change compared to the structure before the stability test (**Figure 4.38i**). The XPS result (**Figure 4.10h** and **Figure 4.43**) suggests that the oxidation states (Ru^0, $Ru^{\delta+}$) of Ru are almost unaltered after HER. However, there is only a slight increase in the metallic Ru^0 state, possibly due to the agglomeration of some Ru atoms that were initially connected with nitrogen dopant sites. The agglomeration of Ru nanoclusters during HER is also confirmed by STEM images (**Figure 4.44**) of the sample captured after HER. However, the Co 2p XPS spectrum after HER suggests that a new deconvoluted peak appears at around 782 eV, corresponding to the Co^{2+} state, which resulted in a significant decrease in the contribution of metallic Co (Co^0 state) and Co connected to N-atoms (designated by Co-N_x, $Co^{\delta+}$ state) (**Figure 4.45a**). Thus, a considerable change in Co's chemical state to Co^{2+} was observed after the HER process. Considering that the HER is a cathodic process, cobalt oxidation is not expected during this process. To know the exact origin of the oxidation of cobalt, we did the XPS measurement of the sample after immersing it in the KOH electrolyte for a couple of minutes without applying any bias. The XPS spectrum (**Figure 4.45b**) reveals that Co gets oxidized to Co^{2+} spontaneously in the alkaline solution. Thus, the observed oxidation in Co to Co^{2+} after HER may not be related to this cathodic process. Still, it is just the self-oxidation of Cobalt in the electrolyte's alkaline condition. However, local pH change, as happens during HER, may promote such oxidization.[59]

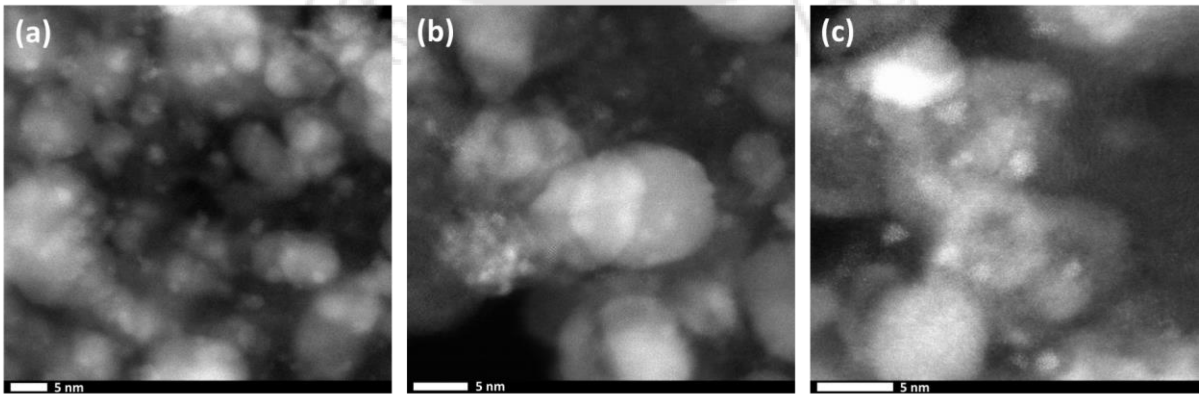

Figure 4.44: STEM images of a-Ru@GNL_{500} after HER.

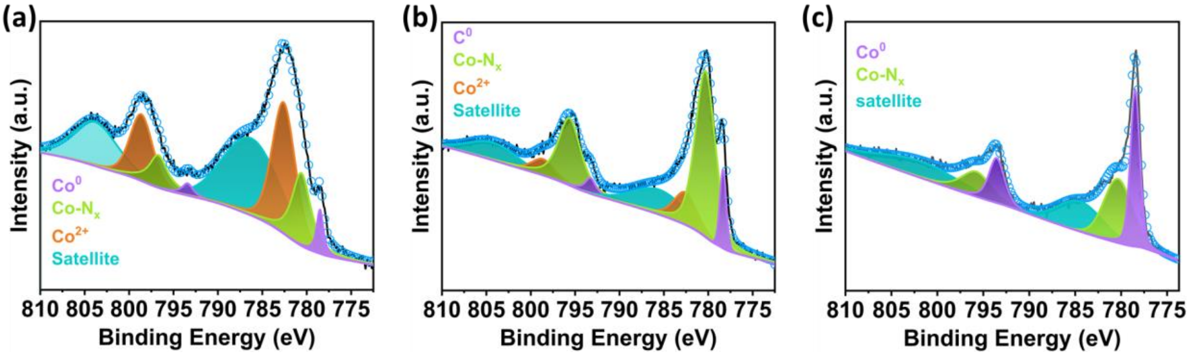

Figure 4.45: Co2p XPS spectra of (a) a-Ru@GNL$_{500}$ after HER, (b) a-Ru@GNL$_{500}$ just after immersing in 1 M KOH, (c) acid-etched (in 6 M HCl) a-Ru@GNL$_{500}$.

To understand the role of surface cobalt, which gets oxidized in the alkaline electrolyte during HER, we purposefully did an acid etching of the as-developed sample in strong acid (6M HCl) for 24 hours. The XPS survey scan after this acid etching shows a significant decrease of cobalt content in the samples (from 2.81 at% to 1.04 at%), which signifies the removal of cobalt accessible by the acid. The high-resolution XPS spectrum of Co2p (**Figure 4.45c**) shows that acid etching significantly decreases the Co-N$_x$ content compared to Co^0. From this observation, we can conclude that cobalt Co-N$_x$ represents the surface cobalt, which is more accessible to acid and thus gets etched out. In contrast, the cobalt remains in the system, fully encapsulated with a graphitic layer. Significantly, the HER measurement after this acid etching only slightly decreases the HER activity compared to the samples without acid washing (**Figure 4.46**). This observation signifies that the surface cobalt in the sample has only a minimal effect on HER activity; the main activity arises from the Ru-NC. The cobalt particles covered with graphitic shells have a promotional effect on HER activity, which will be discussed through DFT calculation later.

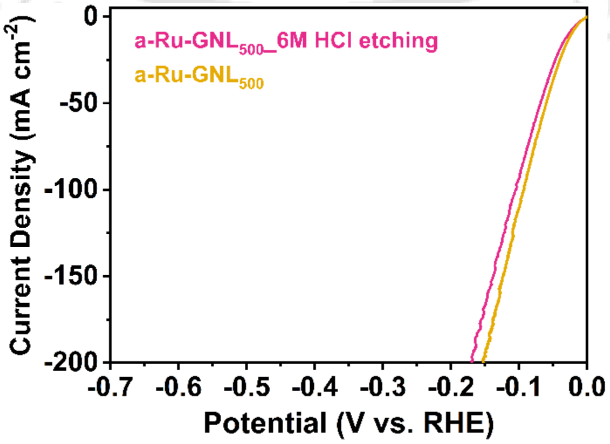

Figure 4.46: LSVs of a-Ru@GNL$_{500}$ before and after acid etching.

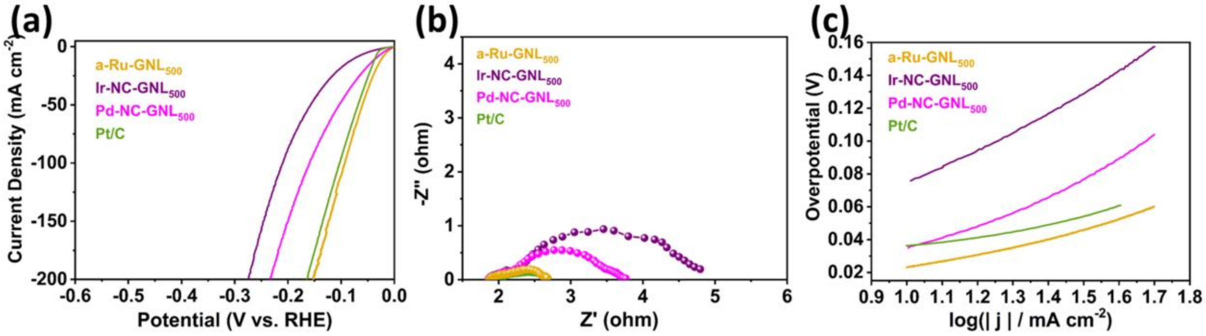

Figure 4.47: Electrochemical HER performance of the developed catalysts.

Interestingly, the Ir@GNL$_{500}$ and Pd@GNL$_{500}$ also exhibited excellent catalytic activities, as is evident from their LSV curves (**Figure 4.47**). The η_{10} for Pd@GNL$_{500}$ and Ir@GNL$_{500}$ are only 35 and 75 mV, respectively. The intrinsic activity of iridium is known to be higher than that of palladium;[60] However, the lower overpotential of Pd@GNL$_{500}$ compared to that of Ir@GNL$_{500}$ can be attributed to the higher atomic utilization in the former because of the presence of a significant number of single atom sites (**Figure 4.29g, h**). Out of the developed catalysts, a-Ru@GNL$_{500}$ and Ir@GNL$_{500}$ also exhibited excellent performance in acidic (0.5 M H_2SO_4) and neutral (1M phosphate buffer solution) electrolytes (**Figure 4.48** and **Figure 4.49)**, thus establishing the importance of the developed catalysts for universal pH use. The required η_{10} for Ir@GNL$_{500}$ and a-Ru@GNL$_{500}$ are 28 mV and 62 mV in acidic and 79 mV and 75 mV in neutral electrolytes, respectively.

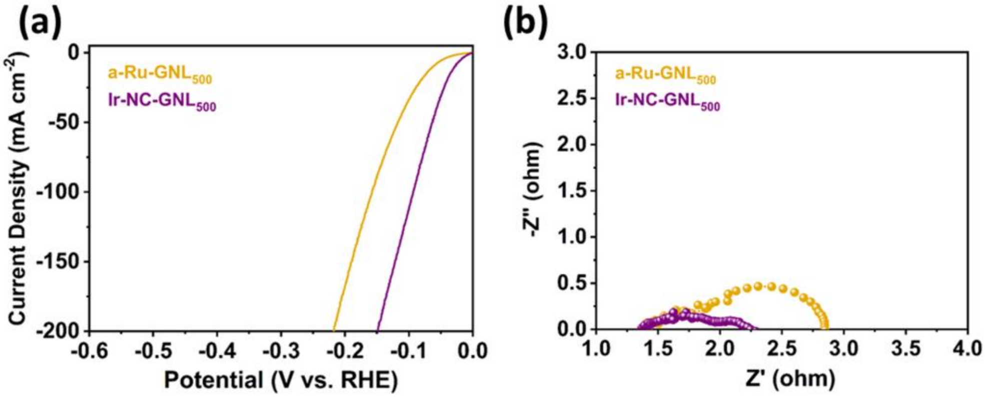

Figure 4.48: HER performance in 0.5M H_2SO_4.

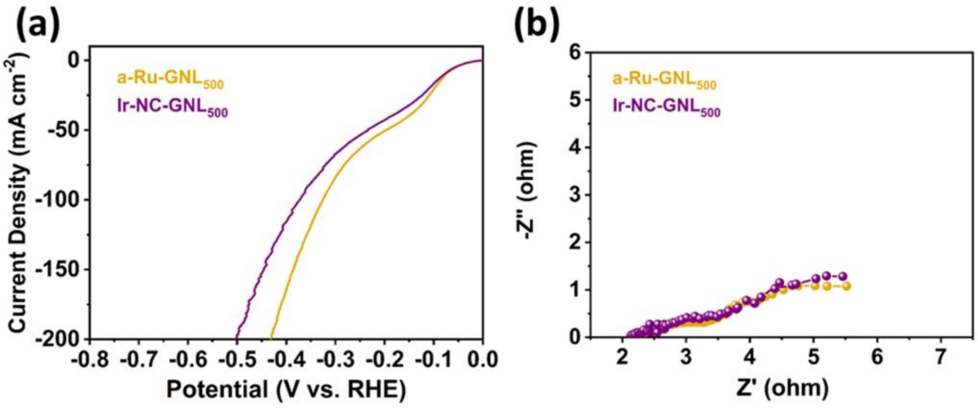

Figure 4.49: HER performance in 1M PBS.

4.4.4. Contact angle and study of bubble dynamics at the HER electrodes

The contact angles and dynamics of the gas bubbles generated in situ at the HER electrode were analyzed to understand the origin of the high catalytic activity and exceptional stability. The aerophobic nature of electrodes can give lower η_m due to minimal blockage of the active sites by HER-generated bubbles, the easy release of bubbles puts less rupturing force on the electrode to give high operational stability.[38–40,61]

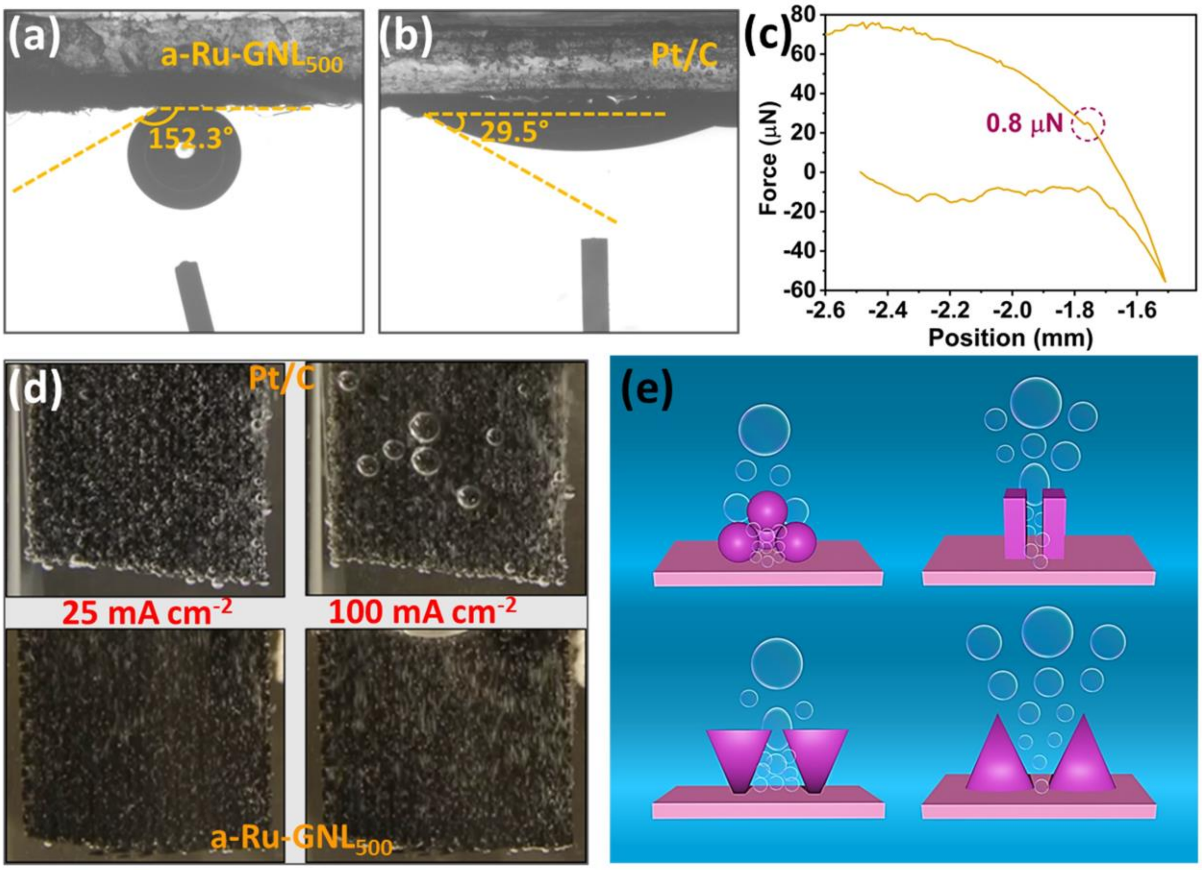

Figure 4.50: Study of bubble release dynamics. Contact angle of air bubble with (a) a-Ru@GNL$_{500}$, and (b) Pt/C, (c) bubble adhesive force measurements for a-Ru@GNL$_{500}$, (d) snapshot of a-Ru@GNL$_{500}$ and Pt/C electrodes operating at lower (25 mA cm^{-2}) and higher (100 mA cm^{-2}) HER currents, (e) scheme of bubble release mechanism for different type of nanostructures.

The bubble contact angle of a-Ru@GNL$_{500}$ was very high (152.3°) compared with that of the Pt/C-based electrode (29.5°), suggesting the super-aerophobic nature of a-Ru@GNL$_{500}$, which means that the bubble easily detached from the former electrode and tended to adhere to the latter (**Figure 4.50a, b**). The super-aerophobic behavior of a-Ru@GNL$_{500}$ was also confirmed by the bubble adhesion analysis, which showed a significantly smaller bubble adhesive force of only 0.8 µN (**Figure 4.50c**). The snapshots of the bubble dynamics during the HER of a-Ru@GNL$_{500}$ and Pt/C electrodes at a current density of 25 mA cm^{-2} and a comparatively higher current density of 100 mA cm^{-2} are depicted in **Figure 4.50d**. The Pt/C electrode exhibits smaller bubble formation at lower currents and considerable bubble formation at higher currents. Conversely, no significant bubble formation was observed even at higher currents for the champion catalyst, a-Ru@GNL$_{500}$. In contrast, the a-Ru@GNL$_{500}$ electrode shows faster bubble release, and no such giant bubble formation occurs. The release phenomenon of the bubbles could be understood from **Figure 4.50e**, which shows that a binder-free oriented structure, similar to the a-Ru@GNL$_{500}$, is beneficial for bubble release. This super-aerophobic nature of a-Ru@GNL$_{500}$ not only helps to give excellent operational stability under dynamic HER conditions but also benefits the reduction of η_m at high current density.

4.4.5. Local structure studies of the catalysts by XANES and EXAFS and evaluation of electrocatalytic properties by in-situ Raman spectroscopy

X-ray absorption near-edge spectroscopy (XANES) of the developed samples, along with the reference samples (Ru-foil and RuO_2) (**Figure 4.51a**), was utilized to understand the different valence states suggested by XPS spectra (**Figure 4.10d, h, l**). The XANES spectra indicate that the near-edge spectrum of c-Ru@GNL$_{1000}$ is closest to the near-edge spectrum of the metallic Ru-foil, suggesting a dominant metallic Ru^0 state compared to the $Ru^{\delta+}$ state. The near-edge spectrum of Ru-SA@GNL$_{200}$ is situated at the farthest position from the Ru-foil and closest to the spectrum of RuO_2, meaning the dominant $Ru^{\delta+}$ state compared to the metallic Ru^0 state. On the other hand, the near-edge spectrum of a-Ru@GNL$_{500}$ is situated at an intermediate position, suggesting an intermediate valence state. The XPS spectra also depicted these observations of the proportion of Ru in different valence states in different samples.

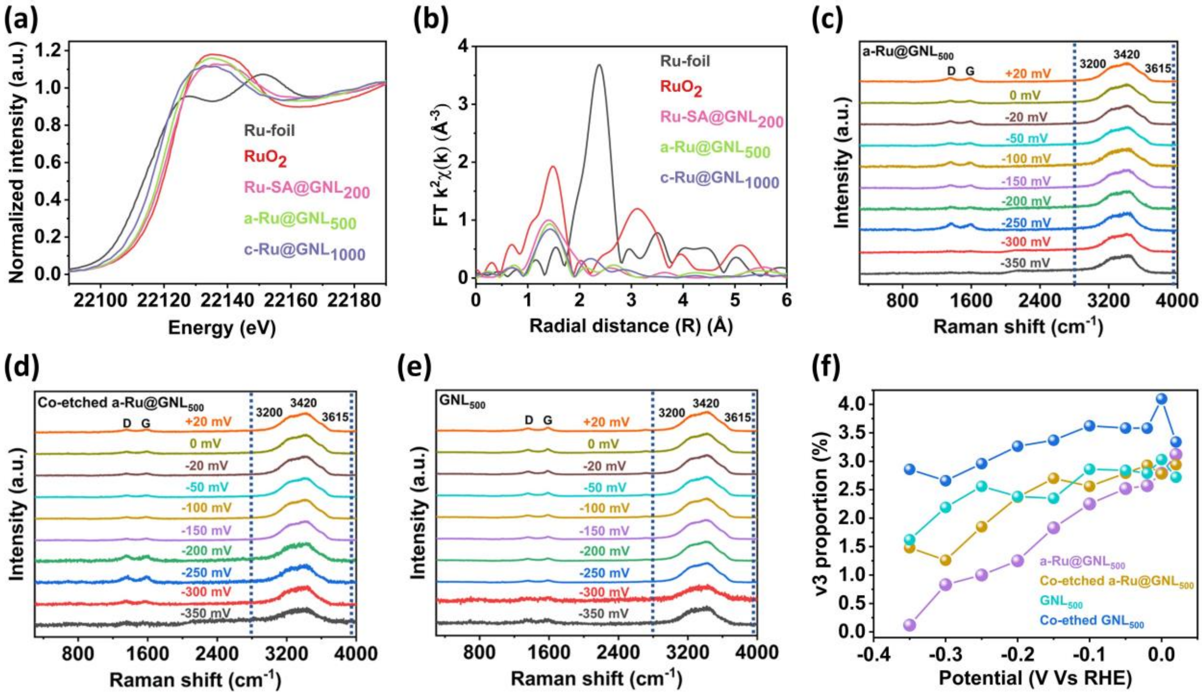

Figure 4.51: Understanding the Local structure and catalytic properties. (a) XANES, and (b) EXAFS of the as-developed Ru-based catalysts and reference samples (Ru-foil, RuO_2), in-situ Raman spectra (recorded at gradually increased negative potentials) of (c) the best-performing catalyst, a-Ru@GNL_{500}, (d) Co-etched (removal of Co by 6M HCl) a-Ru@GNL_{500}, and (e) the catalyst support, GNL_{500}, (f) variation of the proportion of 3rd deconvoluted peak (v3) with potential vs RHE.

Fourier-transformed (FT) k3-weighted extended X-ray absorption fine structure (EXAFS) (**Figure 4.51b**) curves for Ru-foil and RuO_2 show firm peaks of Ru-Ru and Ru-O at 2.38 Å and 1.49 Å, respectively. For all the as-developed samples, there is a dominant peak of Ru-N at around 1.41 Å, signifying the coordination of ruthenium with the N-dopant site of carbon. For the case of c-Ru@GNL_{500}, there is a peak at 2.30 Å, which is very similar to the position of the Ru-Ru of metal foil, which is expected due to the crystalline nature of the Ru-nanoclusters. On the other hand, the Ru-Ru peak for a-Ru@GNL_{500} appears at a more significant separation of 2.64 Å, which can be correlated to the more significant interatomic separation in the amorphous/disordered cluster.[62] The Ru-SA@GNL_{200} shows very similar features to a-Ru@GNL_{500}, having a small Ru-Ru peak at 2.61 Å. The appearance of this Ru-

Ru peak in Ru-SA@GNL$_{200}$ can be associated with some disordered clusters that coexisted with the single atom-dominated sample, as seen from its HAADF-STEM images (**Figure 4.10b**, **c**). Further, the XANES spectra (**Figure 4.52a**) indicated that the near-edge spectrum is only slightly shifted towards that of the near-edge spectrum of the metallic Ru-foil after HER, suggesting a slight increase in Ru^0 contribution and a slight decrease in Ru$^{\delta+}$ contribution. In EXAFS spectra (**Figure 4.52b**) of a-Ru@GNL$_{500}$ after HER, the Ru-Ru peak shifted towards a lower value (2.45 Å) compared to the sample before HER (2.64 Å), signifying the agglomeration of the atoms, consistent with the conclusion of XPS data.

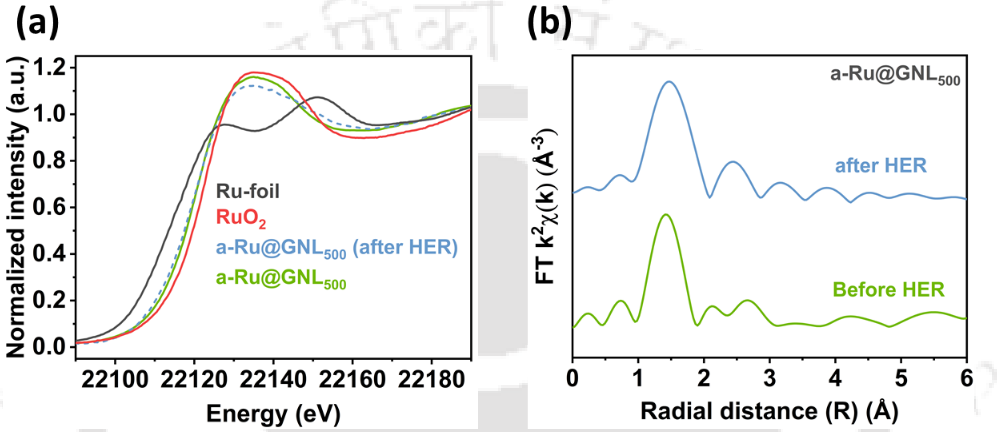

Figure 4.52: (a) XANES spectra (b) EXAFS spectra of a-Ru@GNL$_{500}$ before and after HER.

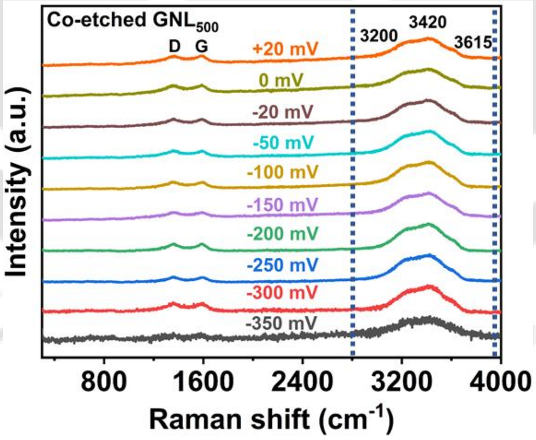

Figure 4.53: In-situ Raman spectra of acid etched (removal of Co) catalyst support, Co-etched GNL$_{500}$.

An in-situ Raman spectroscopy experiment was utilized to gain insight into the catalytic properties of the best-performing catalyst, a-Ru@GNL$_{500}$. To understand the origin of high catalytic properties of a-Ru@GNL$_{500}$, an in-situ Raman experiment was also performed for the support, GNL$_{500}$ (sample without cobalt loading) together with their surface cobalt etched counterparts (Co-etched- a-Ru@GNL$_{500}$ and Co-etched-GNL$_{500}$), in 1 M KOH electrolyte. The Raman spectra of all the samples consist of three major peaks: a D-peak at 1350 cm^{-1}, a G-peak at 1578 cm^{-1}, and a peak at around 3450 cm^{-1} corresponding to interfacial water (catalyst surface and water interface) during the HER reaction. As the Raman spectra did not exhibit any Raman signal corresponding to metal (Ru, Co), any intrinsic change in the catalyst during in-situ measurement was not detectable from the in-situ Raman spectroscopy (**Figure 4.51c-e**, **Figure 4.53**). However, for all samples, the peak corresponding to the interfacial water at around 3450 cm^{-1} constantly changed its shape with increasing applied negative potentials during the in-situ measurement, which can be linked with water dissociation at the catalyst surface, which is a critical step for alkaline HER.

For an insightful understanding of the reason for this evolution leading to the change in the shape of the interfacial water peak, the peak was deconvoluted by fitting with three peaks (**Figure 4.54**, **4.55**, **4.56**, **4.57**): peak1(ν_1) at 3200 cm^{-1}, peak2 (ν_2) at 3420 cm^{-1} corresponding to the tetrahedral and trihedral coordinated water molecules that participate in the HER, respectively, and peak3 (ν_3) at 3615 cm^{-1} corresponds to the dangling O-H bond of the interfacial water molecules that are inactive toward HER.[63] So, ν_1 and ν_2 peaks are related to water dissociation, and ν_3 peak is associated with the inactive water molecules during HER. Thus, the decline rate of the ν_3 peak proportion (area of ν_3 / area of (ν_1 + ν_2)) with increased HER potential is the determining factor of the water dissociation capability of an HER catalyst. Compared to the GNL500 sample, Co-etched-GNL500 shows a slower downward fall of ν3 peak proportion with increased HER potential, indicating that surface cobalt of the former plays a significant role in the water splitting process (**Figure 4.51f**). It is evident from **Figure 4.51f** that the a-Ru@GNL$_{500}$ exhibits the fastest downward trend of ν_3 proportion with increased HER potential, signifying the highest water-cleaving capability of our best-performing catalyst. Interestingly, the decline rate of ν_3 peak proportion in Co-etched a-Ru@GNL$_{500}$ does not differ much from that of a-Ru@GNL$_{500}$. This observation indicates that although surface cobalt has a role in water splitting process, as is evident from the comparison of the decline rate of the ν_3 peak of GNL$_{500}$ and Co-etched-GNL$_{500}$, the role of surface cobalt is much smaller in a-Ru@GNL$_{500}$ as the activity of a-Ru (together with underlying graphitic wrapped cobalt) is itself is much higher as comparison. This in situ Raman investigation perfectly matches our electrocatalytic data, where the etching of surface cobalt shows a minimal change in the LSV curve, as shown in **Figure 4.46**.

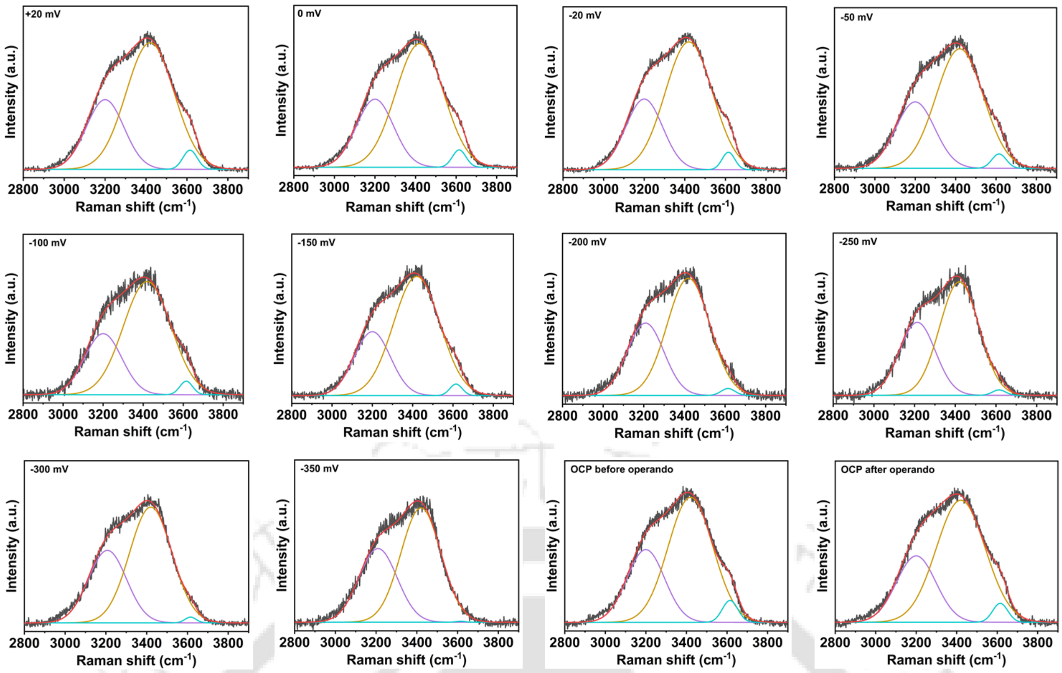

Figure 4.54: The fitted peaks of in-situ Raman spectra of a-Ru@GNL$_{500}$ corresponding to three types of interfacial water at different operating potentials.

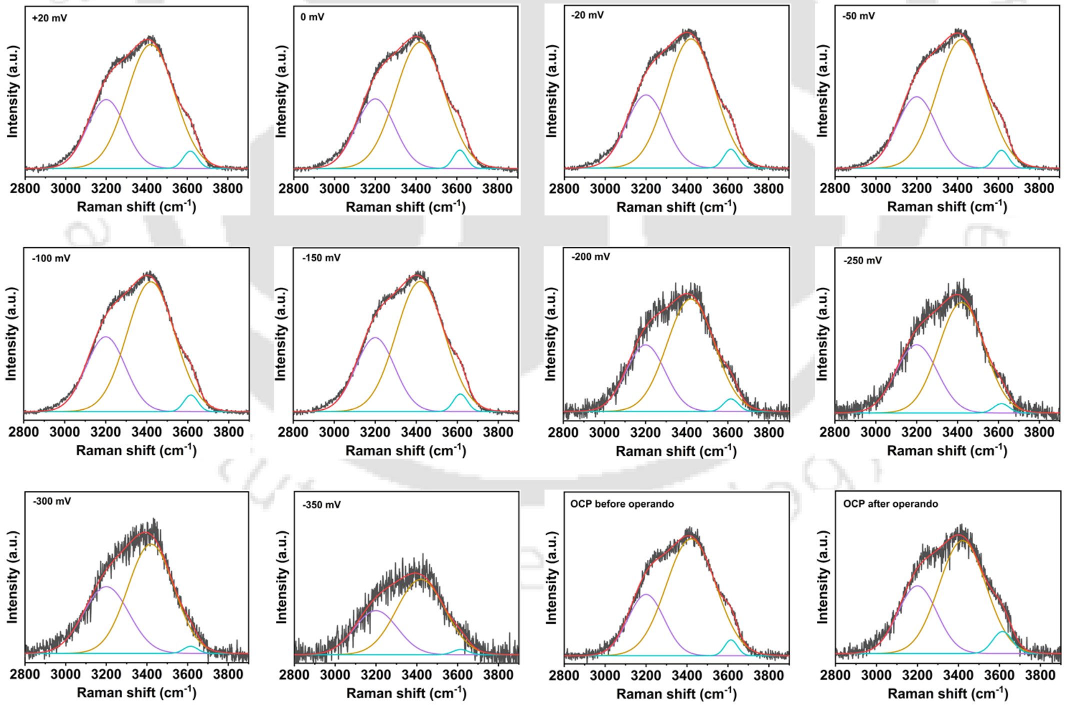

Figure 4.55: The fitted peaks of Raman spectra of Co-etched a-Ru@GNL$_{500}$ corresponding to three types of interfacial water at different operating potentials.

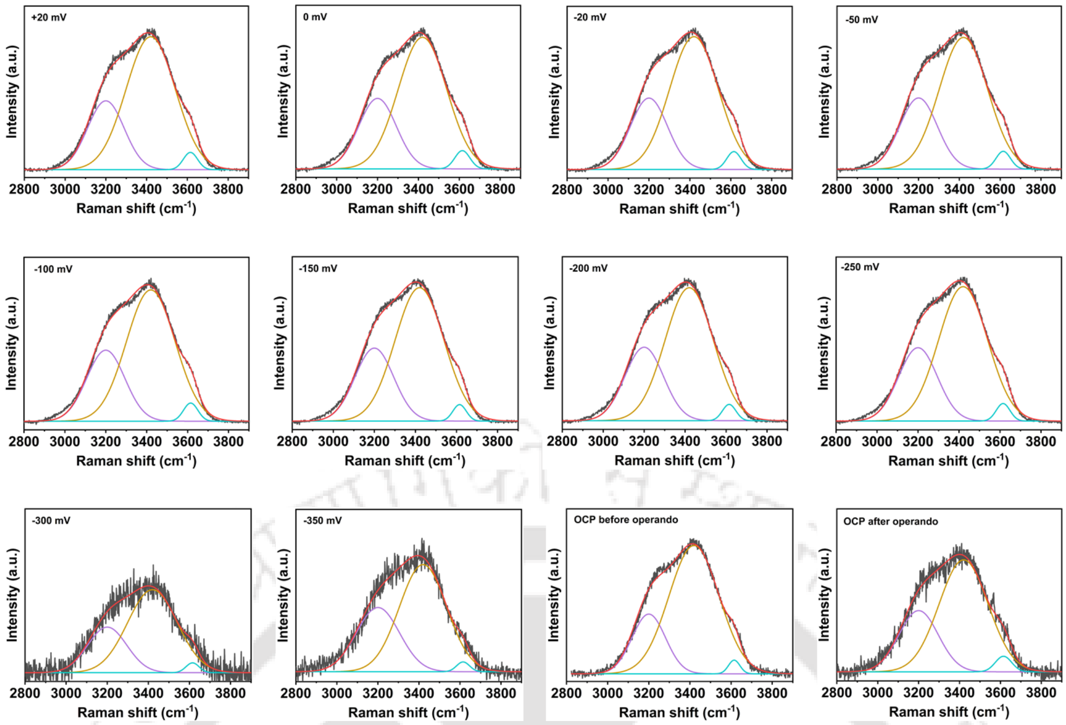

Figure 4.56: The fitted peaks of Raman spectra of GNL$_{500}$ corresponding to three types of interfacial water at different operating potentials.

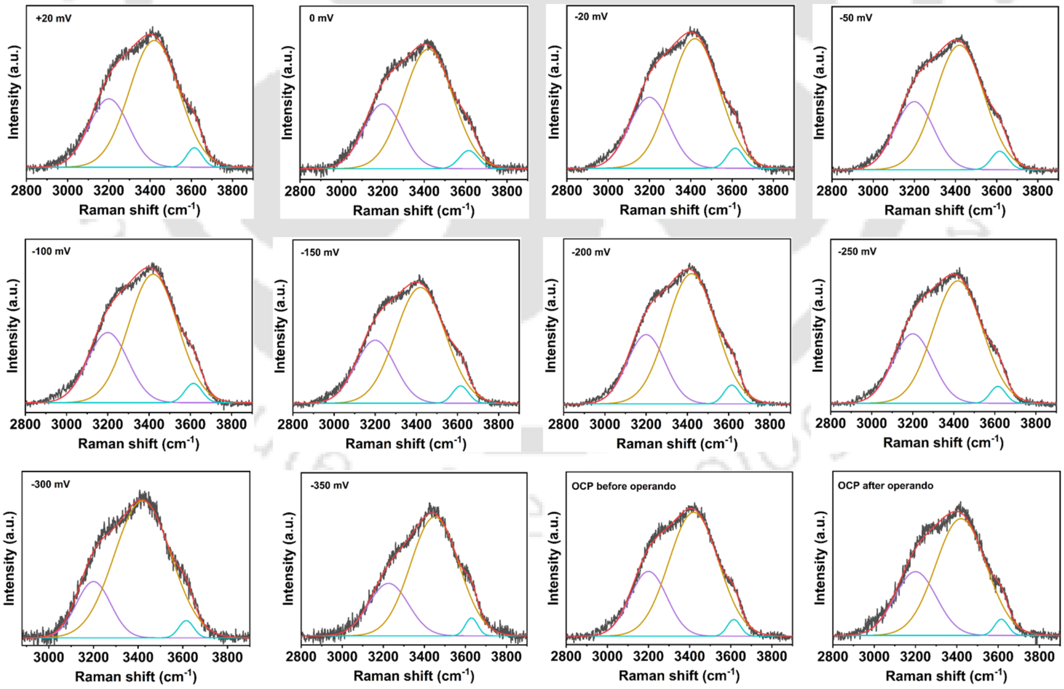

Figure 4.57: The fitted peaks of Raman spectra of Co-etched GNL$_{500}$ corresponding to three types of interfacial water at different operating potentials.

4.4.6. Origin of catalytic activity from density functional theory (DFT)

DFT calculations were performed to gain insight into the electronic origin of the catalytic activity of a-Ru@GNL$_{500}$. First, to show the difference in the intrinsic activity of amorphous Ru (a-Ru) compared to its crystalline counterpart (c-Ru), atomistic models were constructed consisting of a-Ru and c-Ru linked with N dopant sites over the graphene layer (**Figure 4.58**). The role of Co was then elucidated by considering the Co underlying the graphene in the a-Ru system (**Figure 4.59**). Hereafter, these models are referred to as a-Ru@NG, c-Ru@NG, and a-Ru@NG(Co). The a-Ru@NG(Co) model structure mimicked the best-performing sample, a-Ru@GNL$_{500}$. The hydrogen evolution reaction consists of two elementary steps: chemical adsorption of a proton: $H^+ + e \rightarrow H^*$ and chemical desorption: $H^* + H^+ + e \rightarrow H_2$. Out of these elementary processes, the change in Gibb's free energy (ΔG_H) in the first step is widely used as a descriptor to estimate the catalytic activity of an HER catalyst, and its value closer to zero is desirable for better HER catalytic activity.

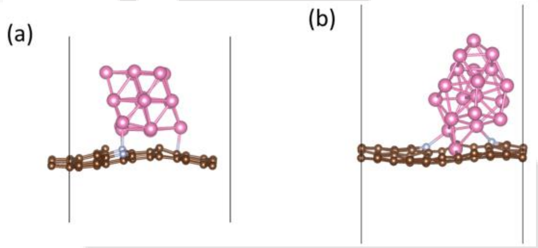

Figure 4.58: Model structures of (a) c-Ru@NG, (b) a-Ru@NG for DFT calculations.

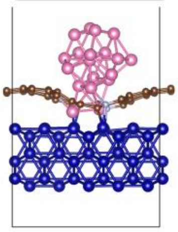

Figure 4.59: Model structure of a-Ru@NG (Co) for DFT calculations.

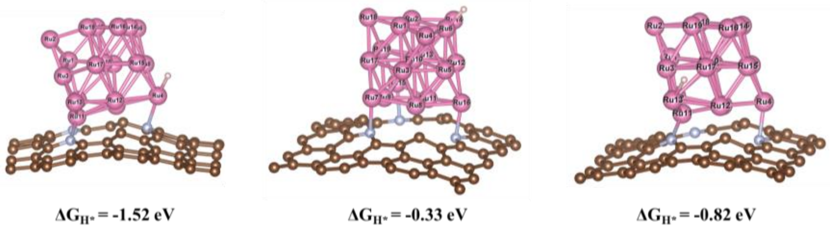

Figure 4.60: Gibb's free energy changes of H-adsorption for c-Ru19@GN.

Table 4.3: HER activity trend of Ru sites in c-Ru19@GN.

Ru sites	**ΔG_{H^*} (eV)**
Ru4	-1.52
Ru6	-0.33
Ru13	-0.82

For the case of c-Ru@GN, Gibb's free energy change (ΔG_{H^*}) for all the three non-equivalent sites, Ru4, Ru6, and Ru13 (**Figure 4.60**), is given in **Table 4.3**. This shows that Ru6 is the most active site for c-Ru@GN. On the other hand, all the sites of a-Ru@GN are non-equivalent, and the H adsorption configuration at all the different exposed sites is given in **Figure 4.61**. Calculated values of ΔG_{H^*} for all these sites are presented in **Table 4.4**. These results indicate multiple active sites (Ru1, Ru11, Ru16, Ru16-Ru18), which give low ΔG_{H^*} values, of which Ru1 shows the highest activity. The H adsorption configurations and calculated ΔG_{H^*} for selected sites are provided in **Figure 4.62** and **Table 4.5**, respectively. Among the Ru sites, Ru11 is the most active HER site at a-Ru19@GN (Co). Interestingly, the underlying cobalt present in the system alters the activity of the existing active sites in a-Ru19@GN and plays a significant role in altering the activity at the sites close to the interface due to the interfacial charge transfer, as is evident from the plot (**Figure 4.63**). The optimized structures of hydrogen-adsorbed catalysts are presented in **Figure 4.64a-c**. The calculated ΔG_{H} values are depicted in **Figure 4.64d**, which shows the following trend: a-Ru@NG(Co) < a-Ru@NG < c-Ru@NG.

The lower value of $|\Delta G_{H}|$ in a-Ru@NG compared to c-Ru@NG signifies better HER activity of the former. Furthermore, the cobalt promotes HER by lowering the ΔG_{H} value further in a-Ru@NG(Co) compared to a-Ru@NG. It is well known that the adsorption of reactive species over transition metals (TM) occurs because of the overlap of the d-band of TM and the reactive species. Thus, the d-band profile and its center position determine the adsorption/desorption process in catalytic reactions. The partial density of states (PDOS) of the d-bands of the structural models were compared to gain insights into the electronic origin of this trend. From **Figure 4.64e-g**, it is evident that there is a significant variation in their PDOS; the d-band center of a-Ru@GN is lower than its crystalline counterpart (c-Ru19@GN). With the addition of underlying cobalt in the case of a-Ru19@GN/(Co), the d-band center further shifts away from Fermi energy. As suggested by Bumuller et al., there is a linear correlation of H-adsorption energies with d-band centers; the higher the negative d-band center, the lower the H-adsorption energy.[64] This difference in the d-band profile gives rise to a variation in the bonding strength of the absorbed H.

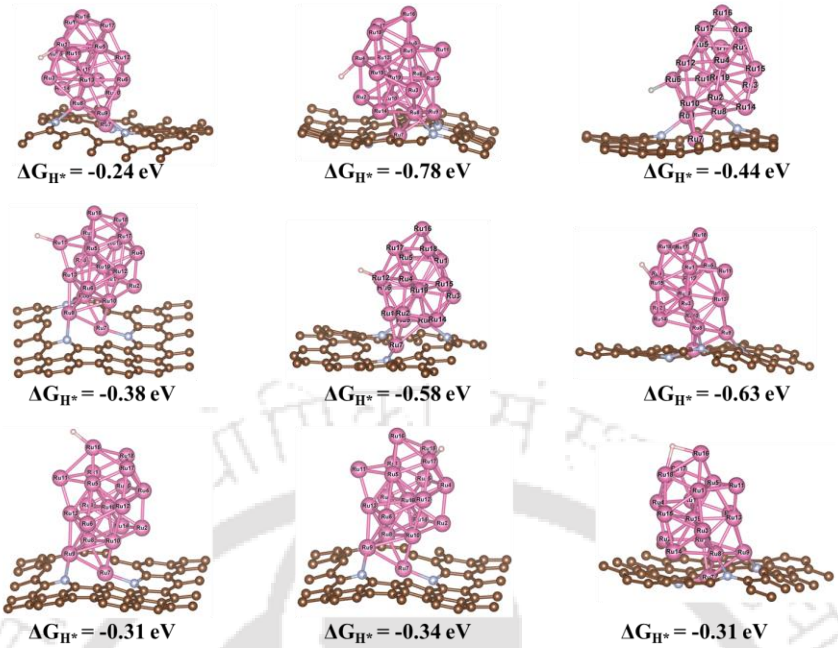

Figure 4.61: Gibb's free energy changes of H-adsorption for a-Ru19@GN.

Table 4.4: HER activity trend of Ru sites in a-Ru19@GN.

Ru sites	**ΔG_{H*} (eV)**
Ru1	-0.24
Ru4	-0.78
Ru5	-0.42
Ru6	-0.44
Ru10	-0.46
Ru11	-0.38
Ru12	-0.58
Ru13	-0.45
Ru14	-0.58
Ru15	-0.63
Ru16	-0.31
Ru17	-0.34
Ru16-Ru18	-0.31
Ru18	-0.60

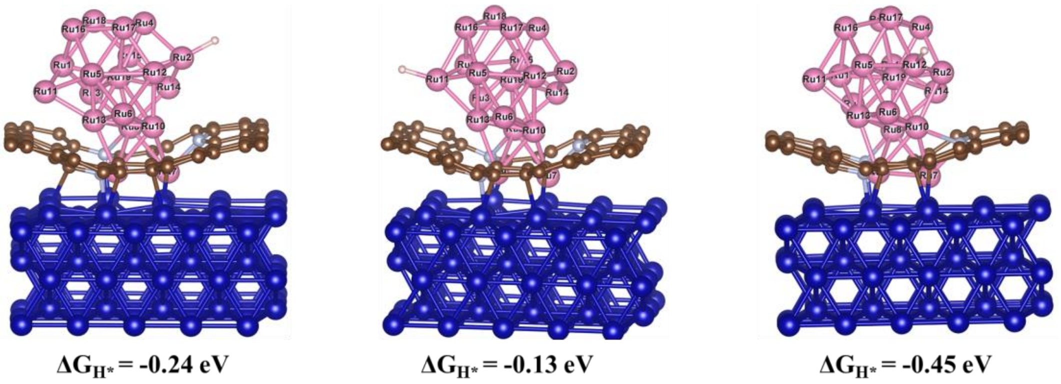

$\Delta G_{H^*} = -0.24$ eV $\Delta G_{H^*} = -0.13$ eV $\Delta G_{H^*} = -0.45$ eV

Figure 4.62: Gibb's free energy changes of H-adsorption for a-Ru19@GN (Co).

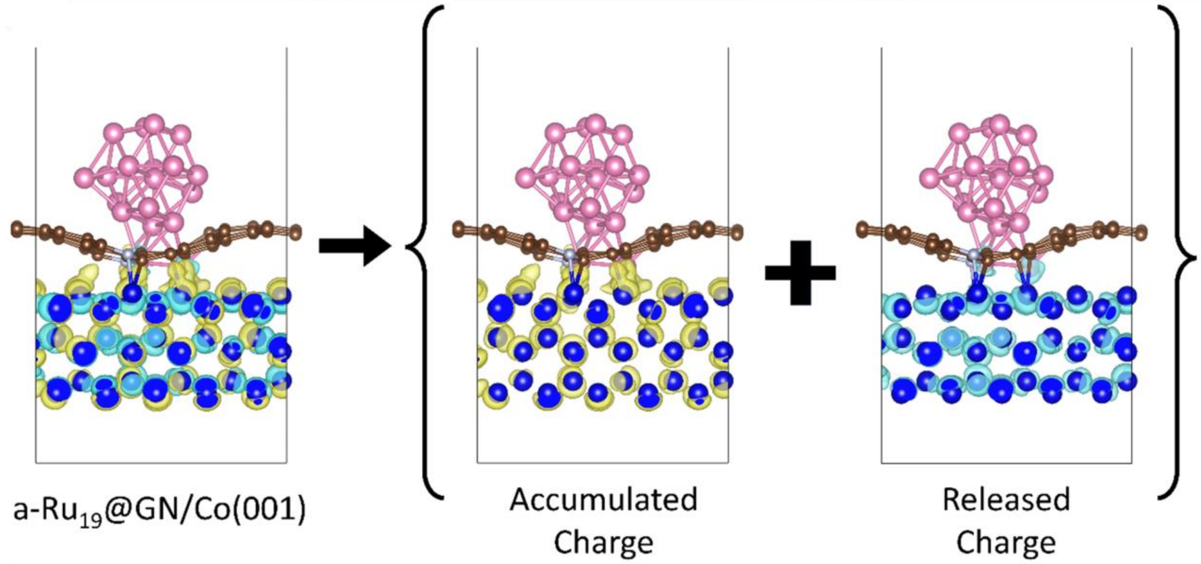

Figure 4.63: Charge density difference after adding Co (001) layer with a-Ru19@GN.

Table 4.5: HER activity trend of Ru sites in a-Ru19@GN (Co).

Ru sites	**ΔG_{H^*} (eV)**
Ru1	-0.58
Ru2	-0.24
Ru11	-0.13
Ru12	-0.45

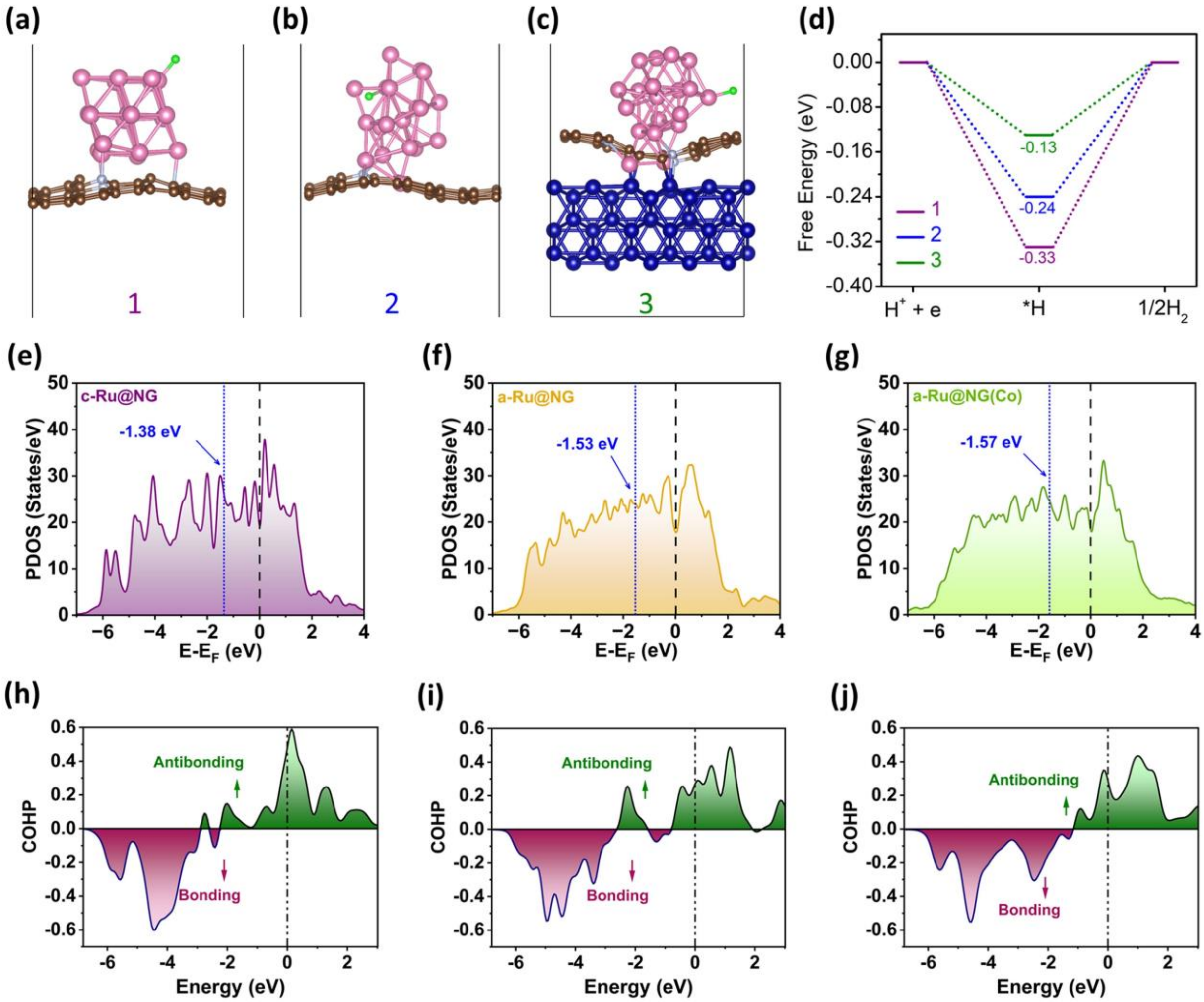

Figure 4.64: DFT calculations for disordered/amorphous and ordered/crystalline Ru-NCs linked with N-doped graphene. Relaxed structure of H-adsorbed (a) c-Ru@NG, (b) a-Ru@NG, and (c) a-Ru@NG (Co), (d) H-adsorption free energy diagram of the model structures, (e)-(g) PDOSs highlighted with d-band center (indicated by dashed line), and (h)-(j) COHP diagram of the single nearest neighbor of Ru (active site)-Ru contact for the corresponding model structures.

This bonding strength variation can be directly reflected from the crystal orbital Hamiltonian population (COHP) calculations (**Figure 4.64h-j**) of the bonding strength of the single nearest neighbor of Ru (Active Site)-Ru contact. The figures demonstrate that although the occupancy of antibonding states below the Fermi level for a-Ru@NG and c-Ru@NG is the same (0.26e), the smaller $|\Delta G_H|$ value for a-Ru@NG compared to c-Ru@NG originated from different ΔZPE-TΔS value, which gives a moderate binding of H^+ in the former and higher HER activity. The underlying cobalt in a-Ru@NG(Co) further lowers the antibonding occupancy to 0.17e, providing efficient binding of H^+ and making the HER phenomena the finest.

4.5. Conclusion

This study proposed an ultrafast strategy to fabricate highly efficient and exceptionally stable hydrogen evolution reaction (HER) electrodes using amorphous ruthenium nanoclusters (~ 0.7 nm) linked to oriented graphitic nano-leaves (GNLs) with a highly adjustable graphitization level. Hierarchically oriented metal-organic frameworks (MOFs), specifically ZIF-67, transformed into GNLs with progressively higher graphitization levels and I_D/I_G ratios of 1.05, 0.85, and 0.25 when subjected to current pulses of 200, 500, and 1000 ms, respectively. The addition of ruthenium with another ultrashort pulse (50 ms) resulted in the uniform dispersion of either predominantly single atoms (Ru-SAs), amorphous nanoclusters (a-Ru-NCs), or crystalline nanoparticles (c-Ru-NPs), depending on the degree of graphitization and intrinsic nitrogen doping content of the GNL support. The developed a-Ru@GNL_{500} exhibited state-of-the-art HER activity, requiring overpotentials of 23.0 mV and 91.4 mV to achieve current densities of 10 mA cm^{-2} and 100 mA cm^{-2}, respectively, surpassing benchmark Pt/C catalysts under the same experimental conditions. The catalyst demonstrated exceptional stability over 100 hours under high HER current densities of 200 mA cm^{-2} and 400 mA cm^{-2}, owing to its robust and super-aerophobic nature (bubble contact angle of 152.3°), enabling bubble release with an adhesion force as low as 0.8 μN to withstand destructive tensile and shaking forces resulting from bubble rupture. The higher graphitic level of GNL contributed to reduced overpotential (η_s) due to resistive loss, while its aerophobic structure ensured excellent mass transport, thereby decreasing mass transport-limited overpotential (η_m). DFT analysis revealed a low filling of the antibonding orbital (0.26e) in the amorphous nanocluster, further reduced to 0.17e by the synergistic effect of cobalt in the system. Graphitization and crystallization are versatile strategies that can be extended to the development of high-performance catalysts for various applications, including the oxygen evolution reaction (OER), urea oxidation reaction (UOR), nitrogen reduction reaction (NRR), oxygen reduction reaction (ORR), carbon dioxide reduction reaction (CO_2RR), and nitrate reduction reaction (NitRR). These strategies offer high surface area, high conductivity, easy mass transfer, and controlled catalyst growth.

References

[1] C. Zhang, J. Sha, H. Fei, M. Liu, S. Yazdi, J. Zhang, Q. Zhong, X. Zou, N. Zhao, H.

Yu, Z. Jiang, E. Ringe, B. I. Yakobson, J. Dong, D. Chen, J. M. Tour, *ACS Nano* **2017**, *11*, 6930.

[2] M. Lao, G. Zhao, P. Li, T. Ma, Y. Jiang, H. Pan, S. X. Dou, W. Sun, *Adv. Funct. Mater.* **2021**, *31*, DOI 10.1002/adfm.202100698.

[3] S. Ye, F. Luo, T. Xu, P. Zhang, H. Shi, S. Qin, J. Wu, C. He, X. Ouyang, Q. Zhang, J. Liu, X. Sun, *Nano Energy* **2020**, *68*, 104301.

[4] X. Shao, M. Liang, A. Kumar, X. Liu, H. Jin, S. Ajmal, V. Q. Bui, H. T. D. Bui, J. Lee, N. Q. Tran, J. Yu, Y. Cho, M. G. Kim, H. Lee, *Adv. Energy Mater.* **2022**, *12*, 1.

[5] Y. Li, T. Xu, Q. Huang, L. Zhu, Y. Yan, P. Peng, F. F. Li, *ACS Catal.* **2023**, *13*, 7597.

[6] M. Kim, S. hoon Kim, J. Park, S. Lee, I. Jang, S. Kim, C. Y. Lee, O. J. Kwon, H. C. Ham, J. T. Hupp, N. Jung, S. J. Yoo, D. Whang, *Adv. Funct. Mater.* **2023**, DOI 10.1002/adfm.202300673.

[7] T. Luo, J. Huang, Y. Hu, C. Yuan, J. Chen, L. Cao, K. Kajiyoshi, Y. Liu, Y. Zhao, Z. Li, Y. Feng, *Adv. Funct. Mater.* **2023**, *33*, 1.

[8] Y. Liu, S. Liu, Y. Wang, Q. Zhang, L. Gu, S. Zhao, D. Xu, Y. Li, J. Bao, Z. Dai, *J. Am. Chem. Soc.* **2018**, *140*, 2731.

[9] J. Mahmood, F. Li, S. M. Jung, M. S. Okyay, I. Ahmad, S. J. Kim, N. Park, H. Y. Jeong, J. B. Baek, *Nat. Nanotechnol.* **2017**, *12*, 441.

[10] J. Chen, C. Chen, Y. Chen, H. Wang, S. Mao, Y. Wang, *J. Catal.* **2020**, *392*, 313.

[11] Y. Li, J. Zhang, Y. Liu, Q. Qian, Z. Li, Y. Zhu, G. Zhang, *Sci. Adv.* **2020**, *6*, DOI 10.1126/sciadv.abb4197.

[12] Q. Lu, A. L. Wang, Y. Gong, W. Hao, H. Cheng, J. Chen, B. Li, N. Yang, W. Niu, J. Wang, Y. Yu, X. Zhang, Y. Chen, Z. Fan, X. J. Wu, J. Chen, J. Luo, S. Li, L. Gu, H. Zhang, *Nat. Chem.* **2018**, *10*, 456.

[13] Y. Wang, S. Wang, Z. L. Ma, L. T. Yan, X. B. Zhao, Y. Y. Xue, J. M. Huo, X. Yuan, S. N. Li, Q. G. Zhai, *Adv. Mater.* **2022**, *34*, 1.

[14] Z. Wang, Z. Lin, Y. Wang, S. Shen, Q. Zhang, J. Wang, W. Zhong, *Adv. Mater.* **2023**, *35*, 1.

[15] B. Yan, D. Liu, X. Feng, M. Shao, Y. Zhang, *Adv. Funct. Mater.* **2020**, *30*, 1.

[16] C. Zhang, Y. Cui, C. Jiang, Y. Li, Z. Meng, C. Wang, Z. Du, S. Yu, H. Tian, W. Zheng, *Small* **2023**, *19*, DOI 10.1002/smll.202301721.

[17] P. Li, W. Wei, J. Li, Y. Liu, K. Fan, L. Zong, L. Wang, *J. Alloys Compd.* **2023**, *947*, 169630.

[18] H. Zhang, H. Su, M. A. Soldatov, Y. Li, X. Zhao, M. Liu, W. Zhou, X. Zhang, X. Sun,

Y. Xu, P. Yao, S. Wei, Q. Liu, *Small* **2021**, *17*, DOI 10.1002/smll.202105231.

[19] H. Lan, Y. Yang, Y. Wu, M. Liu, F. Li, F. Wang, X. Cui, T. Gao, *Fuel* **2023**, *341*, DOI 10.1016/j.fuel.2022.126996.

[20] J. Guan, W. Chen, Y. Zhu, L. Wang, Y. Fu, B. Guo, M. Zhang, *J. Alloys Compd.* **2023**, *942*, 168941.

[21] L. Lin, C. Pei, R. Ding, Y. Li, H. S. Park, X. Yu, *Int. J. Hydrogen Energy* **2023**, *48*, 20350.

[22] W. Li, H. Zhang, K. Zhang, W. Hu, Z. Cheng, H. Chen, X. Feng, T. Peng, Z. Kou, *Appl. Catal. B Environ.* **2022**, *306*, 121095.

[23] H. Huang, H. Jung, C. Y. Park, S. Kim, A. Lee, H. Jun, J. Choi, J. W. Han, J. Lee, *Appl. Catal. B Environ.* **2022**, *315*, 121554.

[24] J. Wang, B. Guo, J. Sun, Y. Zhou, C. Zhao, Z. Wei, J. Guo, *Appl. Catal. B Environ.* **2023**, *324*, 122169.

[25] X. Gao, W. Zang, X. Li, Z. Wang, L. Zheng, Z. Kou, *Chem. Eng. J.* **2022**, *451*, 138698.

[26] X. Li, S. Han, Z. Qiao, X. Zeng, D. Cao, J. Chen, *Chem. Eng. J.* **2023**, *453*, 139803.

[27] C. Zhao, J. Wang, Y. Gao, J. Zhang, C. Huang, Q. Shi, S. Mu, Q. Xiao, S. Huo, Z. Xia, J. Zhang, X. Lu, Y. Zhao, *Adv. Funct. Mater.* **2024**, *34*, 1.

[28] S. Wu, D. Chen, S. Li, Y. Zeng, T. Wang, J. Zhang, J. Yu, S. Mu, H. Tang, *Adv. Sci.* **2023**, *10*, 1.

[29] J. Zhu, R. Lu, W. Shi, L. Gong, D. Chen, P. Wang, L. Chen, J. Wu, S. Mu, Y. Zhao, *Energy Environ. Mater.* **2023**, *6*, 1.

[30] X. Gu, M. Yu, S. Chen, X. Mu, Z. Xu, W. Shao, J. Zhu, C. Chen, S. Liu, S. Mu, *Nano Energy* **2022**, *102*, 107656.

[31] Y. Pan, J. Gao, E. Lv, T. Li, H. Xu, L. Sun, A. Nairan, Q. Zhang, *Adv. Funct. Mater.* **2023**, *33*, 1.

[32] Y. Wu, Y. Li, J. Gao, Q. Zhang, *SusMat* **2021**, *1*, 66.

[33] Q. Wu, X. Yang, J. Yang, P. Liu, G. Ding, Z. Chen, G. Liao, *J. Colloid Interface Sci.* **2023**, *644*, 238.

[34] G. Wu, X. Zheng, P. Cui, H. Jiang, X. Wang, Y. Qu, W. Chen, Y. Lin, H. Li, X. Han, Y. Hu, P. Liu, Q. Zhang, J. Ge, Y. Yao, R. Sun, Y. Wu, L. Gu, X. Hong, Y. Li, *Nat. Commun.* **2019**, *10*, 1.

[35] S. Liu, L. Dai, Y. Qu, Y. Qiu, J. Fan, X. Li, Q. Zhang, X. Guo, *Mater. Chem. Front.* **2021**, *5*, 6648.

[36] H. S. Oh, H. N. Nong, T. Reier, A. Bergmann, M. Gliech, J. Ferreira De Araújo, E. Willinger, R. Schlögl, D. Teschner, P. Strasser, *J. Am. Chem. Soc.* **2016**, *138*, 12552.

[37] Q. Wen, Y. Zhao, Y. Liu, H. Li, T. Zhai, *Small* **2022**, *18*, 1.

[38] C. Zhang, Z. Xu, N. Han, Y. Tian, T. Kallio, C. Yu, L. Jiang, *Sci. Adv.* **2023**, *9*, DOI 10.1126/sciadv.add6978.

[39] G. B. Darband, M. Aliofkhazraei, S. Shanmugam, *Renew. Sustain. Energy Rev.* **2019**, *114*, 109300.

[40] X. Bu, Z. Mao, Y. Bu, Q. Quan, Y. Meng, Z. Lai, D. Chen, P. Xie, H. Li, C. Liu, X. Wang, S. P. Yip, J. Lu, J. C. Ho, *Appl. Catal. B Environ.* **2023**, *320*, DOI 10.1016/j.apcatb.2022.121995.

[41] T. Li, Q. Dong, Z. Huang, L. Wu, Y. Yao, J. Gao, X. Wang, H. Zhang, D. Wang, T. Li, R. Shahbazian-Yassar, L. Hu, *Adv. Mater.* **2022**, *34*, 1.

[42] J. Yang, D. He, W. Chen, W. Zhu, H. Zhang, S. Ren, X. Wang, Q. Yang, Y. Wu, Y. Li, *ACS Appl. Mater. Interfaces* **2017**, *9*, 39450.

[43] Y. Tong, J. Liu, L. Wang, B. J. Su, K. H. Wu, J. Y. Juang, F. Hou, L. Yin, S. X. Dou, J. Liu, J. Liang, *Adv. Funct. Mater.* **2022**, *32*, DOI 10.1002/adfm.202205654.

[44] S. Ji, Y. Chen, Q. Fu, Y. Chen, J. Dong, W. Chen, Z. Li, Y. Wang, L. Gu, W. He, C. Chen, Q. Peng, Y. Huang, X. Duan, D. Wang, C. Draxl, Y. Li, *J. Am. Chem. Soc.* **2017**, *139*, 9795.

[45] J. Ying, G. Jiang, Z. Paul Cano, L. Han, X. Y. Yang, Z. Chen, *Nano Energy* **2017**, *40*, 88.

[46] H. Huang, S. Zhou, C. Yu, H. Huang, J. Zhao, L. Dai, J. Qiu, *Energy Environ. Sci.* **2020**, *13*, 545.

[47] Y. C. Han, M. L. Liu, L. Sun, X. C. Li, Y. Yao, C. Zhang, S. Y. Ding, H. G. Liao, L. Zhang, F. R. Fan, M. Moskovits, Z. Q. Tian, *Nano Energy* **2022**, *97*, 107125.

[48] G. M. Karim, P. Dutta, A. Majumdar, A. Patra, S. K. Deb, S. Das, N. V. Dambhare, A. K. Rath, U. N. Maiti, *Carbon N. Y.* **2023**, *203*, 191.

[49] Y. Yao, Z. Huang, P. Xie, L. Wu, L. Ma, T. Li, Z. Pang, M. Jiao, Z. Liang, J. Gao, Y. He, D. J. Kline, M. R. Zachariah, C. Wang, J. Lu, T. Wu, T. Li, C. Wang, R. Shahbazian-Yassar, L. Hu, *Nat. Nanotechnol.* **2019**, *14*, 851.

[50] J. Bin Wu, M. L. Lin, X. Cong, H. N. Liu, P. H. Tan, *Chem. Soc. Rev.* **2018**, *47*, 1822.

[51] J. Ribeiro-Soares, M. E. Oliveros, C. Garin, M. V. David, L. G. P. Martins, C. A. Almeida, E. H. Martins-Ferreira, K. Takai, T. Enoki, R. Magalhães-Paniago, A. Malachias, A. Jorio, B. S. Archanjo, C. A. Achete, L. G. Cançado, *Carbon N. Y.* **2015**,

95, 646.

[52] X. Shao, M. Liang, M. G. Kim, S. Ajmal, A. Kumar, X. Liu, H. S. Jung, H. Jin, F. Cao, J. Yu, K. M. Tran, H. Ko, J. Lee, J. W. Bae, H. Lee, *Adv. Funct. Mater.* **2023**, *33*, DOI 10.1002/adfm.202211192.

[53] Q. He, Y. Zhou, H. Shou, X. Wang, P. Zhang, W. Xu, S. Qiao, C. Wu, H. Liu, D. Liu, S. Chen, R. Long, Z. Qi, X. Wu, L. Song, *Adv. Mater.* **2022**, *34*, 1.

[54] L. Wu, S. Hu, W. Yu, S. Shen, T. Li, *npj Comput. Mater.* **2020**, *6*, 1.

[55] A. Vig, E. Doan, K. Yang, *Nanomaterials* **2023**, *13*, DOI 10.3390/nano13162356.

[56] T. Kou, S. Wang, Y. Li, *ACS Mater. Lett.* **2021**, *3*, 224.

[57] S. Latil, L. Henrard, *Phys. Rev. Lett.* **2006**, *97*, 1.

[58] S. V. Morozov, K. S. Novoselov, M. I. Katsnelson, F. Schedin, D. C. Elias, J. A. Jaszczak, A. K. Geim, *Phys. Rev. Lett.* **2008**, *100*, 11.

[59] H. Tan, B. Tang, Y. Lu, Q. Ji, L. Lv, H. Duan, N. Li, Y. Wang, S. Feng, Z. Li, C. Wang, F. Hu, Z. Sun, W. Yan, *Nat. Commun.* **2022**, *13*, 1.

[60] J. Durst, C. Simon, F. Hasché, H. A. Gasteiger, *J. Electrochem. Soc.* **2015**, *162*, F190.

[61] L. Shang, Y. Zhao, X. Y. Kong, R. Shi, G. I. N. Waterhouse, L. Wen, T. Zhang, *Nano Energy* **2020**, *78*, 105375.

[62] J. Lin, J. Ding, H. Wang, X. Yang, X. Zheng, Z. Huang, W. Song, J. Ding, X. Han, W. Hu, *Adv. Mater.* **2022**, *34*, 1.

[63] Y. Zhu, M. Klingenhof, C. Gao, T. Koketsu, G. Weiser, Y. Pi, S. Liu, L. Sui, J. Hou, J. Li, H. Jiang, L. Xu, W. H. Huang, C. W. Pao, M. Yang, Z. Hu, P. Strasser, J. Ma, *Nat. Commun.* **2024**, *15*, DOI 10.1038/s41467-024-45654-9.

[64] D. Bumüller, A. S. Hehn, E. Waldt, R. Ahlrichs, M. M. Kappes, D. Schooss, *J. Phys. Chem. C* **2017**, *121*, 10645.

Chapter 5

Pulsed-thermal-shock tuned Cu/Cu_2O/Ni hetero-phase towards optimized reaction kinetics during highly boosted hydrogen evolution reaction

Pulsed-thermal-shock tuned $Cu/Cu_2O/Ni$ hetero-phase towards optimized reaction kinetics during highly boosted hydrogen evolution reaction

This study presents a facile and ultrafast pulsed-thermal-shock (PTS) strategy for developing a $Cu/Cu_2O/Ni$ hetero-phase catalyst linked to MOF-derived carbon nanostructures (CNs) optimized for the hydrogen evolution reaction (HER). The unique PTS protocol, requiring only milliseconds, transforms bimetallic MOFs into ready-to-use electrodes while preserving nanosheet morphology. Notably, the catalyst undergoes a rare and favorable in-situ cathodic phase evolution and morphological transformation during HER, converting Cu_2O into metallic Cu and enhancing active site accessibility. The optimized $Cu/Cu_2O/Ni$-C hetero-phase catalyst demonstrates exceptional catalytic activity with an overpotential of just 46 mV to achieve 10 mA cm^{-2}, comparable to state-of-the-art Pt/C catalyst. Advanced characterizations, including XRD, in-situ Raman, FESEM, TEM, XPS, and synchrotron-based XANES and EXAFS, confirm the dynamic reconstruction of the catalyst during HER. The results underscore hetero-phase catalysts' synergistic electronic properties and self-reconstruction capabilities, paving the way for cost-effective and high-performance alternatives to noble metal catalysts.

5.1. Introduction

Developing Transition metal (TM)-based nanocatalysts has become a primary choice for hydrogen and oxygen evolution reaction (HER and OER) in alkaline electrolytes due to their tremendous success as earth abundance, low-cost, and highly active HER catalysts.[1–5] However, the activity and durability of TM-based catalysts are far behind those of noble metal-based (Pt, Ru, Ir, Pd, etc.) catalysts.[6–14] However, the scarcity and sky-high cost limit the application of noble metals as HER catalysts. Therefore, extensive research has been devoted to designing TM-based hetero-phase catalysts with synergistic electronic properties favorable to HER catalysis. For instance, transition metal alloys, oxides, carbides, chalcogenides, and their heterostructures have excellent activity towards HER, comparable to the activity of the noble metal-based HER catalysts.[15–18]

Nevertheless, the phase evolution of the catalysts during catalysis often positively impacts the catalytic activity and the stability of the catalysts. Sometimes, the phase/morphology evolution is beneficial in improving the activity and stability of the catalysts.[19,20] Therefore, a significant amount of research has been carried out to design TM-based hetero-phase catalysts, which can self-improve their catalytic activity/stability by phase/morphology evolution during catalysis. TM hetero-phase catalysts' phase/morphology transformation is typical at the anode where the

OER occurs.[21–24] For instance, the transition metal sulfides and phosphides are often transformed into transition metal hydroxides or oxyhydroxides at the anode during OER.[21,25] Consequently, the OER activity/stability has been significantly improved. On the other hand, the cathodic phase evolution during HER is rare. Therefore, special attention is needed to develop transition metal-based hetero-phase catalysts with synergistic electronic properties, which have the ability of HER-favourable in-situ cathodic phase evolution and morphology transformation.

Herein, we are reporting a facile, unique, ultrafast cost and energy-efficient pulsed-thermal-shock (PTS) strategy of transforming Ni, Cu, and Co-based bimetallic metal-organic frameworks (MOF) into complex hetero-phase ($Cu/Cu_2O/Ni-C$) catalyst for HER. In particular, bimetallic (Ni-Cu and Co-Cu) MOF nanosheets decorated with uniformly dispersed metallic Cu and Cu_2O nanoclusters were facilely synthesized by hydrothermal methods. The unique Cu/Cu_2O decorated MOF complexes were then transformed into $Cu/Cu_2O/Ni-C$ hetero-phase nanocatalysts by several ultrashort current pulses of only 50 ms duration. In contrast to the conventional MOF pyrolysis, which requires several hours of high-temperature (≥1000°C) heating in a furnace, the unique PTS protocol transforms the MOFs momentarily and reduces the thermal budget. Moreover, the MOF-derived $Cu/Cu_2O/Ni-C$ hetero-phase obtained by the PTS technique was utilized as a ready-to-use catalyst electrode for HER. Most importantly, the as-developed hetero-phase catalyst underwent a unique and rare cathodic phase evolution and surface morphology transformation during HER catalysis. Advantageously, the self-reconstruction of the hetero-phase catalyst due to the in-situ phase/morphology evolution during catalysis resulted in improved catalytic activity and stability towards HER. The optimized resultant $Cu/Cu_2O/Ni-C$ hetero-phase catalyst exhibited a high activity comparable to the state-of-the-art Pt/C catalyst towards HER. It requires an overpotential of only 46 mV to achieve a current density of 10 mA cm^{-2}, which is closer to the value of the Pt/C catalyst. The high HER performance is attributed to the synergistic electronic properties of the different phases in the complex hetero-phase catalyst and the catalyst's unique HER-favourable cathodic phase/morphology evolution. Witnessing the positive impact of the phase/morphology evolution, the in-situ reconstruction of the catalyst was monitored by XRD, in-situ Raman, FESEM, TEM, XPS and synchrotron-based X-ray absorption spectroscopy (XANES, FT-EXAFS, and WT-EXAFS). All the characterization techniques suggested the in-situ reconstruction of the best-performing $Cu/Cu_2O/Ni-C$ hetero-phase catalyst due to phase and morphology evolution during HER.

5.2. Materials and methods

5.2.1. Materials

$Ni(NO_3)_2.6H_2O$, $Co(NO_3)_2.6H_2O$, $Cu(NO_3)_2.2.5H_2O$, benzene dicarboxylic acid (BDC), salicylic acid, dimethyl-formamide (DMF), ethanol, and KOH were purchased from Sigma-Aldrich. Commercial carbon cloth (CC) (Plain Carbon Cloth – 1071 HCB) was purchased from AvCarb Material Solutions. Millipore DI water was used for the experiments when needed.

5.2.2. Synthesis of mono- and bimetallic MOFs

DMF, ethanol, and water were mixed in a 1:1:1 volume ratio to make a solution of 72 ml. Then, salicylic acid (0.863 mmol) and BDC (1 mmol) were added to the solution and stirred for 10 minutes. After that, $Ni(NO_3)_2.6H_2O$ (3 mmol) and $Cu(NO_3)_2.2.5H_2O$ (3 mmol) were added to the solution and stirred for 15 minutes to make a homogeneous solution. The final solution was poured into a Teflon-lined autoclave, and then a carbon cloth of (4.5×3 cm2) was vertically immersed. Then, the autoclave containing the mixed solution and vertical carbon cloth was put in an oven and left for 16 hours at 150°C. After that, the carbon cloth coated with NiCu-MOF was collected and washed in DMF and ethanol several times and then dried in a vacuum oven. Hence, the NiCu-MOF linked to carbon cloth (NiCu-MOF@CC) was prepared. Similarly, the CoCu-MOF was prepared by replacing $Ni(NO_3)_2.6H_2O$ (3 mmol) with $Co(NO_3)_2.6H_2O$ (3 mmol) into the solution at the starting following a similar protocol.

5.2.3. Development of MOF-derived mono- and hetero-phase catalysts

Forty successive (30 V) electric pulses of 50 ms duration and a one-second gap in between them are applied through the length of the carbon cloth (3×1 cm^2) in which the MOFs are grown. The electric pulses produce ultrafast thermal shock due to Joule heating; as a result, the ready-to-use catalyst electrodes were developed.

5.2.4. Material characterization

The as-developed samples' morphology and microscopic features were investigated using field emission scanning electron microscopy (FESEM, Zeiss, Sigma-300) and field emission transmission electron microscopy (FETEM, JEOL, 2100F). The crystalline structure of samples was analyzed using an X-ray diffractometer (Rigaku Technologies, Smartlab) with Cu Kα radiation. Raman spectroscopic measurements were performed on a Raman Spectrometer (Horiba Jobin Vyon, LabRam HR, laser wavelength 514 nm). The chemical compositions and oxidation states were detected by X-ray photoelectron spectroscopy (ESCALAB Xi+, Thermo

Fisher). The catalysts' local structure study by X-ray absorption spectroscopy (XAS) was conducted in Indus-2, a 2.5 GeV synchrotron radiation source facility at Raja Raman Centre for Advanced Technology. Athena software processed XAS data (background correction, normalization of XANES and EXAFS spectra).

5.2.5. Electrochemical characterization of the HER catalysts

HER performances were performed in 1M KOH electrolyte, with a saturated calomel electrode (CHI 150) as a reference and Pt wire as a counter electrode in a PARSTAT 3000A-DX potentiostat. A piece of 1×1 cm^2 of the catalysts developed over CC was used as the working electrode. All the HER polarization curves were recorded at 5 mV s^{-1} scan rate, and thereafter, iR was corrected. EIS spectra of the samples were collected in a frequency range of 10 kHz to 0.1 Hz.

5.3. Results and discussion

5.3.1. Synthesis and characterization of earth-abundant hetero-phase nanocatalysts

A unique ultrafast pulsed-thermal-shock (PTS) strategy (**Figure 5.1a**) was employed to obtain the earth-abundant bimetallic Co-Cu and Ni-Cu-based catalysts for hydrogen evolution reaction (HER). The synthesis of the catalysts is a simple two-stage process. In the first stage, bimetallic MOFs (metal-organic frameworks) were uniformly grown over carbon cloth (CC) using the hydrothermal method.[2,26,27] Next, the MOFs were converted into metal-embedded carbon with the help of 40 ultrashort (50 ms) successive electric pulses (30 V). The electric pulses applied through CC led to a substantial current flow within that ultrashort duration, producing thermal shock due to Joule heating. The ultrafast Joule heating/cooling resulted in bimetallic, $Cu/Cu_2O/Co-C@CC$, and $Cu/Cu_2O/Ni-C@CC$ hetero-phase catalysts, in which metal nanoparticles are embedded into carbon nanosheets. These PTS-derived catalysts linked to carbon cloth were utilized as ready-to-use electrodes for HER.

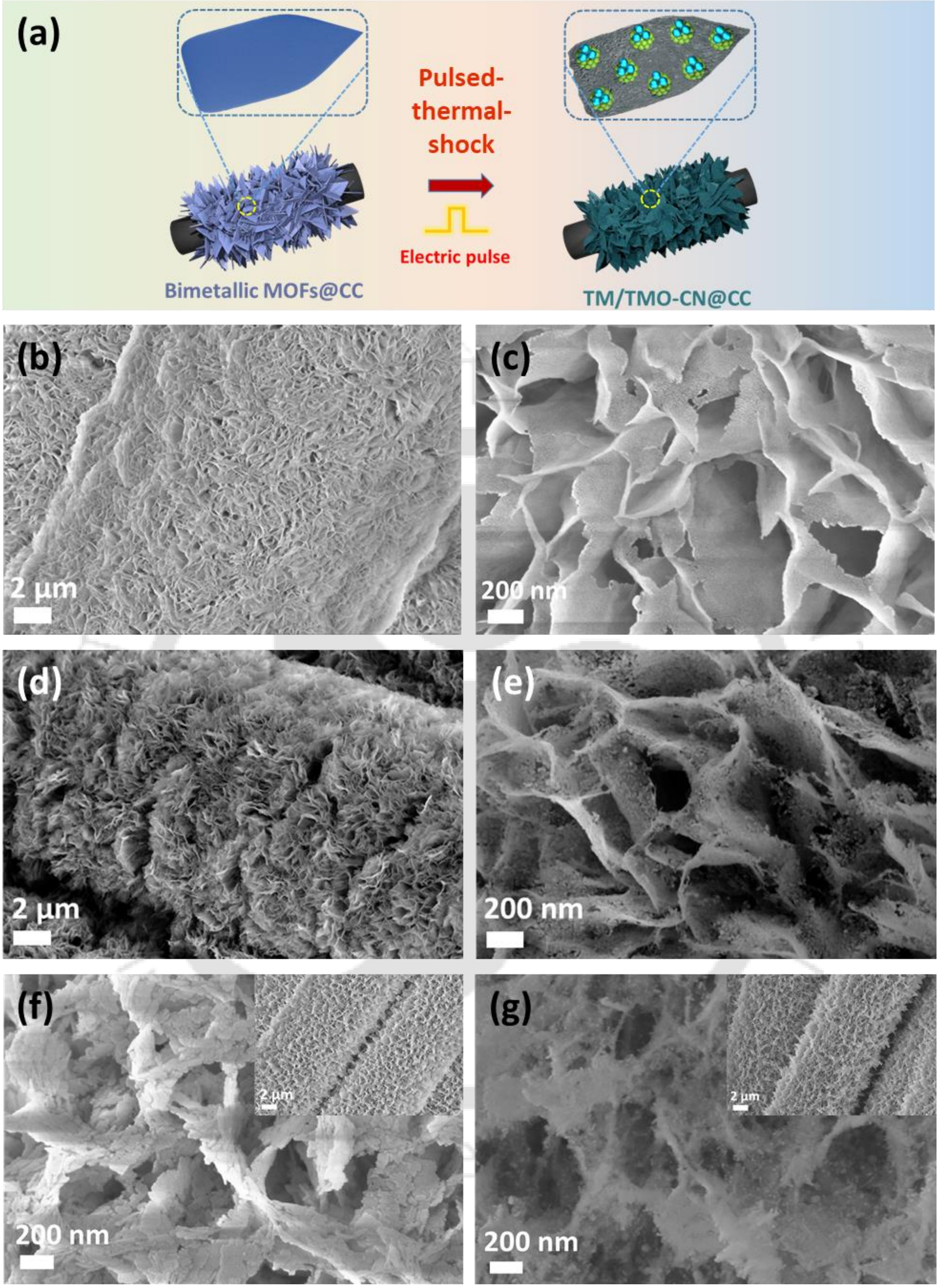

Figure 5.1: Synthesis and morphological characterization of NiCu-MOF-derived heterostructure catalysts. (a) Schematic illustration of pulsed-thermal-shock (PTS) strategy for the ultrafast development of Ni/Cu-based heterostructures catalysts ($Cu/Cu_2O/Ni-C$) over carbon cloth (CC), (b) low and (c) high-magnified FESEM images of NiCu-MOF@CC, (d) low and € high-magnified FESEM images of $Cu/Cu_2O/Ni-C$@CC, FESEM images of (f) CoCu-MOF@CC and (g) its derivative $Cu/Cu_2O/Co-C$@CC after PTS.

The morphology analysis was carried out by field emission scanning electron microscopy (FESEM). The FESEM image of NiCu-MOF reveals a sheet-like morphology, where the array of densely packed MOF nanosheets with smooth surfaces are linked to CC (**Figure 5.1b**, **c**). After PTS, the sheet-like structure was preserved in the bimetallic Cu/Cu_2O/Ni-C@CC catalyst (**Figure 5.1d**). However, the nanosheets exhibited significant morphological changes. They became rougher and more porous, with the appearance of tiny particulates interconnected to form the nanosheets (**Figure 5.1e**). This transformation indicates the formation of a rough, porous nanosheet architecture, likely enhancing surface area and active site accessibility. Likewise, the FESEM image of CoCu-MOF also reveals the sheet-like morphology, although the nanosheets are made of some grains of MOF, making the surface bumpy (**Figure 5.1f**). After PTS, the morphology remains unaltered, although the grains became almost indistinguishable, making the surface uniform. On the other hand, numerous tiny particulates are dispersed all over the surface of the nanosheets, making the surface significantly rough (**Figure 5.1g**).

The change in crystalline phases of the MOFs after thermal shock was monitored by X-ray diffraction (XRD) analysis. The X-ray patterns of NiCu-MOF@CC and CoCu-MOF@CC (**Figure 5.2a** and **b**) consist of familiar peaks at around 8-10°, 14-20°, and 28-45° corresponding to the MOF phase. The most prominent MOF phase peak is 9.12° for NiCu-MOF@CC and 8.96° for CoCu-MOF@CC. MCu-MOF@CC (M=Ni and Co) consists of extra XRD peaks corresponding to Cu and Cu_2O. Notably, in NiCu-MOF@CC, the peaks related to metallic Cu (43.50°, 50.64°, and 74.26°) have relatively higher intensity compared to Cu_2O-related peaks (36.70°, 42.62°, 61.60°, 73.66°), suggesting presence of dominant metallic Cu along with significant Cu_2O phase coexisted with MOF phase (**Figure 5.2a**). Conversely, in CoCu-MOF@CC, the Cu_2O phase is dominant, along with the metallic Cu and MOF phases (**Figure 5.2b**). After the pulsed thermal shock, the peaks corresponding to the MOF phase disappeared after the shock pyrolysis, as is evident from the XRD pattern of Cu/Cu_2O/Ni-C@CC (**Figure 5.2a**) and Cu/Cu_2O/Co-C@CC (**Figure 5.2b**), inferring complete pyrolysis of the thin MOFs nanosheets. Three new peaks (44.58°, 51.98°, and 76.42°) correspond to metallic Ni that appeared in the XRD pattern of Cu/Cu_2O/Ni-C@CC after the PTS pyrolysis of NiCu-MOF. Similarly, Co-peaks appeared in the Cu/Cu_2O/Co-C@CC's XRD pattern. The appearance of the Ni-related peaks and disappearance of MOF-related peaks in the XRD patterns proved the transformation of NiCu-MOF into carbon with embedded Ni and Cu after PTS. Interestingly, the relative intensity of Cu_2O peaks in both Ni- and Co-based bimetallic catalysts decreases significantly after the thermal shock. The decrease in intensity is related to the thermal (partial) reduction of Cu_2O and partial conversion of it into metallic Cu.

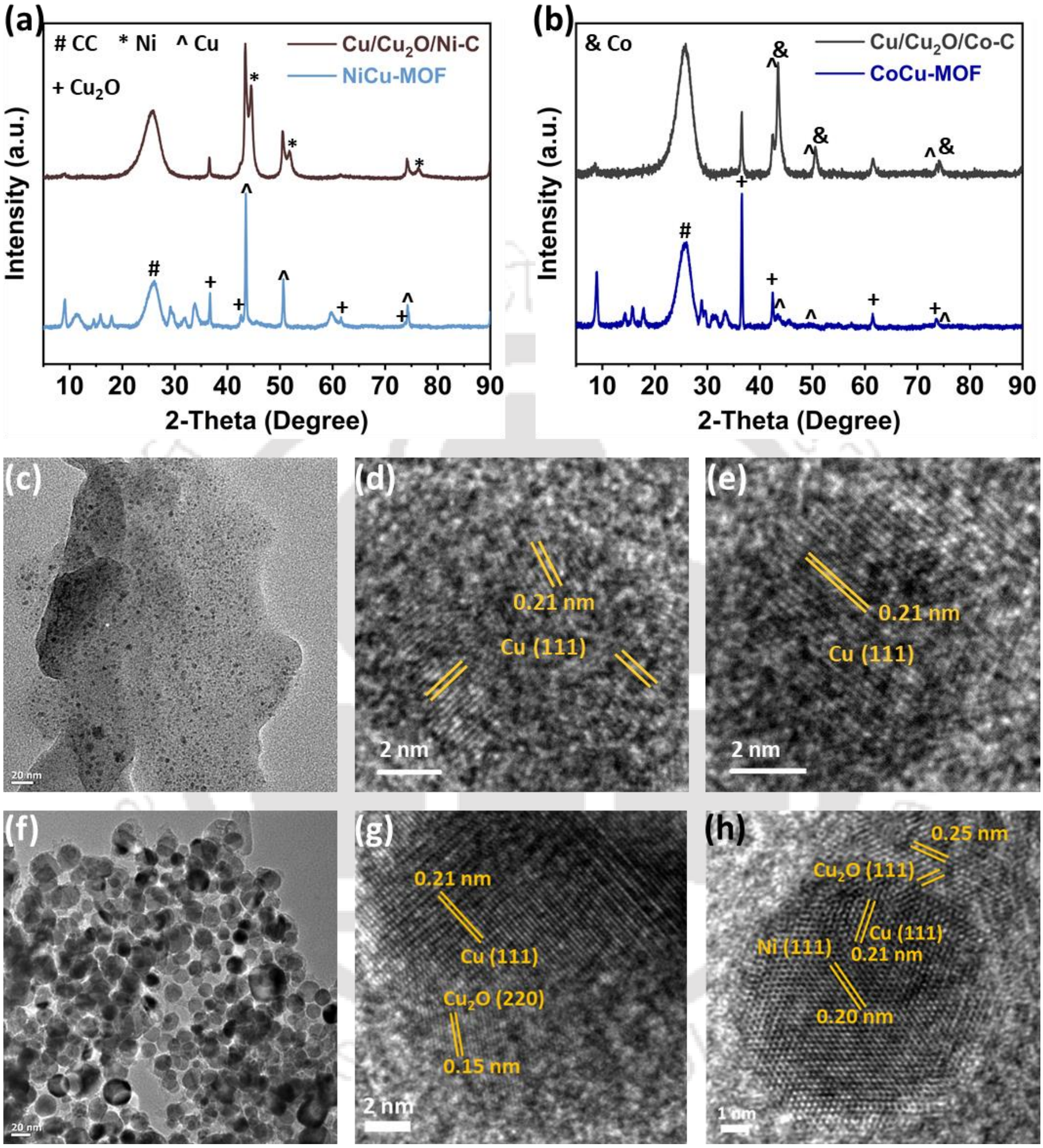

Figure 5.210: Characterization of PTS-assisted bimetallic MOF-derived nanocatalysts. XRD pattern of (a) NiCu-MOF@CC and its PTS-derived catalyst ($Cu/Cu_2O/Ni-C@CC$), (b) CoCu-MOF and its PTS-derived counterpart ($Cu/Cu_2O/Ni-C@CC$), (c) TEM image and (d), € HRTEM images of NiCu-MOF, (f) TEM image and (g), (h) HRTEM images of $Cu/Cu_2O/Ni-C@CC$ catalyst.

Transmission electron microscopy (TEM) was employed to visualize and understand the structural change in $Cu/Cu_2O/Ni$-C from NiCu-MOF after pulsed thermal shock. **Figure 5.2c** is the TEM image of a NiCu-MOF nanosheet, where several tiny nanoparticles are uniformly dispersed. As discussed earlier in XRD analysis, in NiCu-MOF, metallic Cu and Cu_2O phases co-existed with the MOF phase. The tiny nanoparticles observed in the TEM image are the nanoclusters of Cu/Cu_2O phases, which are uniformly dispersed all over the surface of the MOF nanosheet. The presence of a metallic Cu phase on the surface of NiCu-MOF was further confirmed by the HRTEM images (**Figure 5.2d** and **e**), where the lattice fringes of metallic Cu (d_{111} = 0.208 nm) are clearly visible. **Figure 5.2f** is the TEM image of the PTS-assisted NiCu-MOF-derived $Cu/Cu_2O/Ni$-C nanosheet. The TEM image of $Cu/Cu_2O/Ni$-C reveals that uniformly dispersed nanoparticles (uniform size) of Cu, Cu_2O, and Ni, as suggested by the XRD pattern also, are embedded into the MOF-derived carbon. The nanoparticles revealed by the TEM image are nothing but the particulates observed in the FESEM image of $Cu/Cu_2O/Ni$-C nanosheets (**Figure 5.1e**) earlier. Like the FESEM images, the TEM image also indicated the presence of pores within the $Cu/Cu_2O/Ni$-C nanosheet. For further insight into the structure of the nanoparticles, HRTEM images are captured as depicted in **Figure 5.2g** and **h**. The HRTEM images proposed that the metallic Cu (d_{111} = 0.208 nm), Cu_2O (d_{111} = 0.245 nm), and metallic Ni phases (d_{111} = 0.202 nm) coincide within the carbon nanosheet, forming hetero-phase nanocatalysts like Cu/Cu_2O (**Figure 5.2g**), $Ni/Cu/Cu_2O$ (**Figure 5.2h**). Due to their electronic synergy between different phases, these hetero-phase nanocatalysts have high catalytic activity towards hydrogen evolution reaction (HER).[17,18,28]

5.3.2. Electrocatalytic HER performance of the as-developed hetero-phase catalysts

The simple ultrafast PTS-assisted MOF-derived transition metal-based complex hetero-phase nanocatalysts were used as electrodes for electrocatalytic HER. Electrochemical measurements like linear sweep voltammetry (LSV) and electrochemical impedance spectroscopy (EIS) (Nyquist plot) were employed to evaluate the HER activity of the unique PTS-assisted MOF-derived catalysts. The basic HER activity-determining parameters are the overpotential (η_a), the Tafel slope, and the charge transfer resistance (R_{ct}) during HER. η_a is the potential vs. RHE required to achieve an HER current density of ‘a’ mA cm^{-2}, determined from the HER LSV curves. Tafel slope is the slope of overpotential vs logarithmic current density. R_{ct} is the resistance of electron transfer from catalyst to H^+ ions during HER, which is the diameter of the EIS spectra in the Nyquist plot. The HER performance of a catalyst is optimized by minimizing η_a, Tafel slope, and R_{ct}; the lesser the value of these parameters, the higher the

HER activity of the catalyst. The HER performance of the catalyst was optimized by taking the feedback from the LSV curves. The successive LSV cycles of NiCu-MOF-derived Cu/Cu_2O/Ni-C catalyst (**Figure 5.3a**) were recorded to monitor if any change in the catalyst's activity occurred. Notably, the first LSV cycles exhibited a significant hump ranging from +0.1 V to -0.1 V vs. RHE, the peak of which is situated at around 0.0 V vs RHE. Surprisingly, on the next cycle onwards, the hump disappeared, and the performance was progressively improved, as the overpotential was decreasing on increasing LSV cycles until the 5th cycle. After the 5th cycle, no significant change was observed in LSV cycles, and the optimized performance of the Cu/Cu_2O/Ni-C hetero-phase catalyst was achieved. These dynamic changes in the LSV curves and the self-improvement of the catalytic activity during operation indicate an HER-favourable reconstruction of the Cu/Cu_2O/Ni-C hetero-phase catalyst. This unique dynamic evolution on the cathode is rare, although typical on the anode for transition metal-based catalysts. Similar phenomena were observed for the CoCu-MOF-derived Cu/Cu_2O/Co-C catalyst, although the monometallic Ni-MOF-derived Ni-C is the exception. The origin of the dynamic evolution on the cathode and the HER-favourable self-reconstruction of the bimetallic MCu-MOF-derived catalysts will be discussed in detail in the later sections.

The unique pulsed-thermal-shock (PTS) strategy for synthesizing MOF-derived catalysts was also optimized by observing the LSV curves for different conditions (**Figure 5.3b**). For instance, NiCu-MOF was pyrolyzed by three PTS conditions like 30 pulses, 40 pulses, and 50 pulses to obtain Cu/Cu_2O/Ni-C_30p, Cu/Cu_2O/Ni-C, and Cu/Cu_2O/Ni-C_50p. The overpotentials (η_{10}) to achieve a current density of 10 mA cm^{-2} of the Ni-Cu-based catalysts follow: Cu/Cu_2O/Ni-C (46 mV) < Cu/Cu_2O/Ni-C_30p (65 mv) < Cu/Cu_2O/Ni-C_50p (176 mV), suggesting minimum overpotential for Cu/Cu_2O/Ni-C, obtained by 40 current pulses for thermal shock. Thus, the 40 current pulses condition was considered the optimized PTS condition to get the MOF-derived catalysts. The LSV curves (**Figure 5.3b**) of the PTS-assisted MOF-derived catalysts suggested that the Ni-based Cu/Cu_2O/Ni-C hetero-phase catalyst has the superior activity towards HER compared to Co-based hetero-phase Cu/Cu_2O/Co-C, and Ni-based monometallic Ni-C catalysts. The HER activity of the best-performing catalyst (Cu/Cu_2O/Ni-C) is quite comparable to the state-of-the-art Pt/C catalyst. The best-performing Cu/Cu_2O/Ni-C needed an overpotential (η_{10}) of only 46 mV, closer to the Pt/C catalyst (32 mV). The overpotentials (η_{10}) of the as-developed catalysts followed the trend: Cu/Cu_2O/Ni-C (46 mV) < Cu/Cu_2O/Co-C (128 mV) < Ni-C (154 mV). Therefore, the Co-based hetero-phase has significantly lower activity than the Ni-based hetero-phase, and the activity of the monometallic Ni-based catalyst was even worse than the Co-based hetero-phase catalyst.

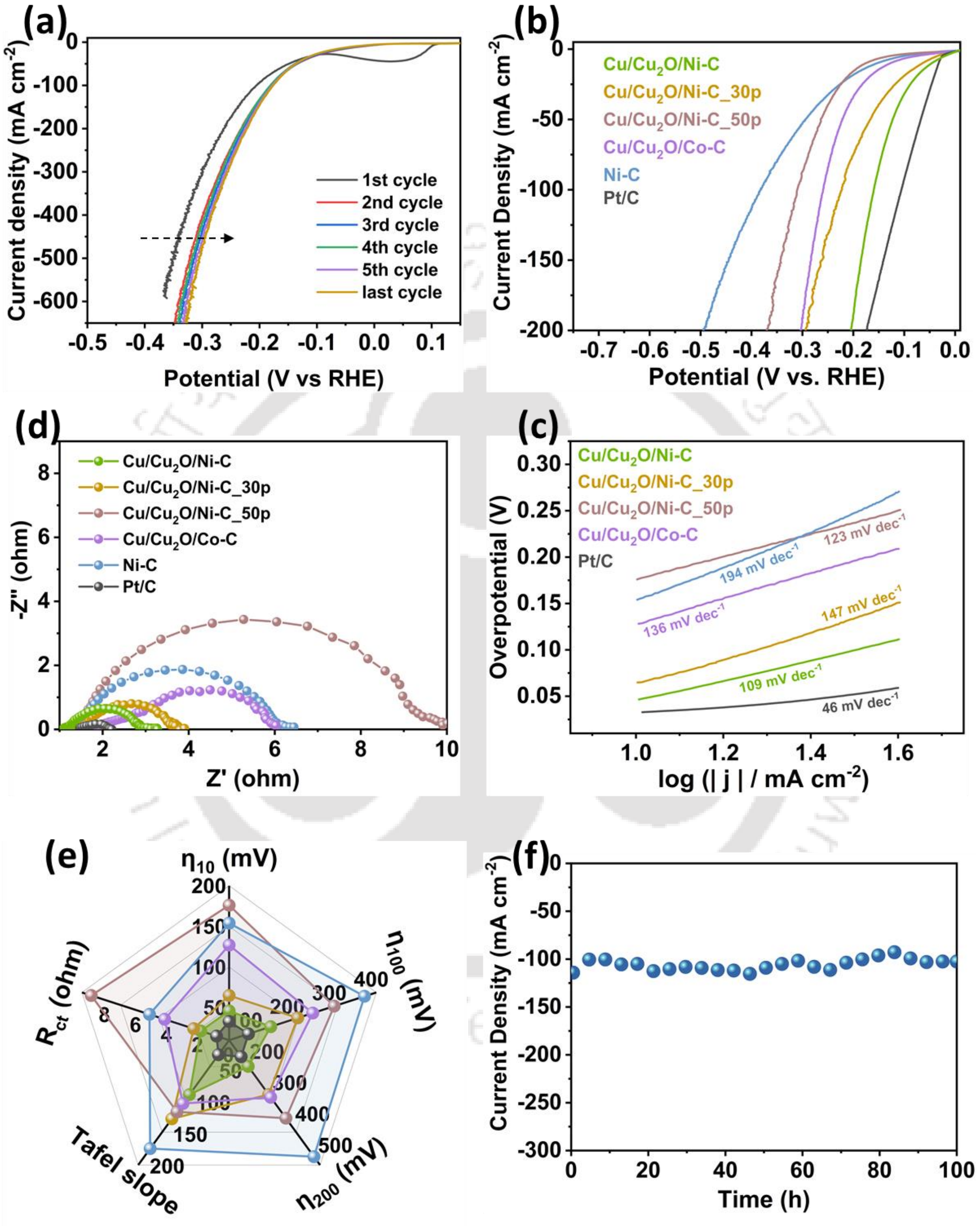

Figure 5.3: Electrocatalytic HER performance of the as-developed catalysts in 1M KOH. (a) consecutive HER LSV cycles of Cu/Cu$_2$O/Ni-C@CC, (b) HER LSV curves of the as-developed catalysts, corresponding (c) Tafel slopes, (d) Nyquist plot, (e) radar plot of HER performance determining parameters for the developed catalysts, (f) stability test of the best

performing $Cu/Cu_2O/Ni-C@CC$ as HER catalyst, operating at a high current density as 100 mA cm^{-2}.

Among the developed catalysts, $Cu/Cu_2O/Ni-C$ has the smallest Tafel slope (109 mV dec^{-1}), suggesting faster HER kinetics of $Cu/Cu_2O/Ni-C$ compared to $Cu/Cu_2O/Co-C$ (136 mV dec^{-1}) and Ni-C (194 mV dec^{-1}) (**Figure 5.3c**). The EIS spectra in the Nyquist plot (**Figure 5.3d**) suggest that the best-performing $Cu/Cu_2O/Ni-C$ catalyst has the smallest semicircle among MOF-derived catalysts. The charge transfer resistance (R_{ct}) estimated from the EIS spectra follows the following trend: $Cu/Cu_2O/Ni-C$ (2.19 Ω) < $Cu/Cu_2O/Co-C$ (4.17 Ω) < Ni-C (5.14 Ω), indicating faster charge transfer during HER in Ni-based hetero-phase catalysts compared to Co-based hetero-phase and monometallic Ni-based catalyst. The quick charge transfers eventually resulted in faster HER kinetics and better activity of the best-performing hetero-phase catalyst, as suggested by the Tafel plot and LSV curves. The HER performance evaluation parameters are plotted in the radar plot (**Figure 5.3e**). The $Cu/Cu_2O/Ni-C$ catalyst occupies the smallest area in the radar plot among the MOF-derived catalyst, which is again closer to the state-of-the-art Pt/C catalyst, signifying excellent activity of the unique PTS-assisted MOF-derived Ni-based hetero-phase catalyst in all aspect of the performance evaluation parameters. Notably, the best-performing catalyst exhibited almost no activity loss after continuous operation at a high current density of -100 mA cm^{-2} for 100 hours, witnessing its high stability. The high HER activity and the stability of the $Cu/Cu_2O/Ni-C$ hetero-phase catalyst are attributed to the straightforward, unique ultrafast PTS technique, which is responsible for developing favorable hetero-phase. As discussed earlier, the electronic synergy among different phases of the Cu/Cu2O/Ni-C hetero-phase catalyst, dynamic evolution, and HER-favourable self-reconstruction of the catalyst at the cathode during operation led to the exceptional catalytic activity and stability towards HER. Further insight is inevitable to understand the self-improvement of the HER performance due to the reconstruction of the catalysts during catalysis.

5.3.3. Characterization of the hetero-phase catalysts post HER electrocatalysis and in-situ investigation

Further insight is inevitable to understand the self-improvement of the HER performance due to the reconstruction of the catalysts during catalysis. Advanced characterization tools investigate the dynamic change in the catalysts' morphology, phase, structure, and chemical state during/after catalysis. The best-performing catalyst (Cu/Cu_2O/Ni-C@CC) preserved its sheet-like morphology after HER (**Figure 5.4a** and **b**). However, the surface became a more particulate type, rough, and porous (**Figure 5.4b**) than the catalyst before HER (**Figure 5.1e**), likely further enhancing the surface area and active site accessibility, resulting in enhanced HER performance, as discussed in the previous section. XRD analysis revealed if any phase change in the catalysts occurred after the HER. As mentioned, the NiCu-MOF-derived bimetallic catalyst (Cu/Cu2O/Ni-C) consists of three phases. The XRD pattern of Cu/Cu_2O/Ni-C after HER suggested that the peaks related to the Cu_2O phase disappeared, and the relative intensities of the peaks associated with metallic Cu increased considerably (**Figure 5.4c**). The observations from the XRD pattern of Cu/Cu_2O/Ni-C after HER signified the transformation of the Cu_2O phase to metallic Cu ($Cu_2O \rightarrow Cu$) after HER. This observation was also apparent from the first HER LSV cycle (**Figure 5.3a**), where a hump was observed. That hump was related to the electrochemical reduction of Cu_2O into metallic Cu ($Cu^+ \rightarrow Cu^0$) at potential ranging from +0.1 V to -0.1 V vs RHE during HER LSV. Similar phenomena were observed for Co-based catalysts (Cu/Cu_2O/Co-C) after HER (**Figure 5.4d**). However, some new XRD peaks (19.18°, 32.62°, 38.06°, 51.48°, 58.00°) appeared in Cu/Cu_2O/Co-C after HER, which were related to β-$Co(OH)_2$ layers (d_{001} = 3.29 Å), signifying partial conversion of metallic Co to layered β-$Co(OH)_2$. Interestingly, $Ni(OH)_2$ peaks are absent in the XRD pattern of Cu/Cu_2O/Ni-C after HER (**Figure 5.4c**), suggesting either no conversion of metallic Ni to $Ni(OH)_2$ after HER or conversion of Ni to few layers of amorphous/disordered $Ni(OH)_2$. TEM analysis was carried out after HER to further clarify the Cu_2O and metallic Ni phase conversion in Cu/Cu_2O/Ni-C (**Figure 5.4e**, **f**, and **g**).

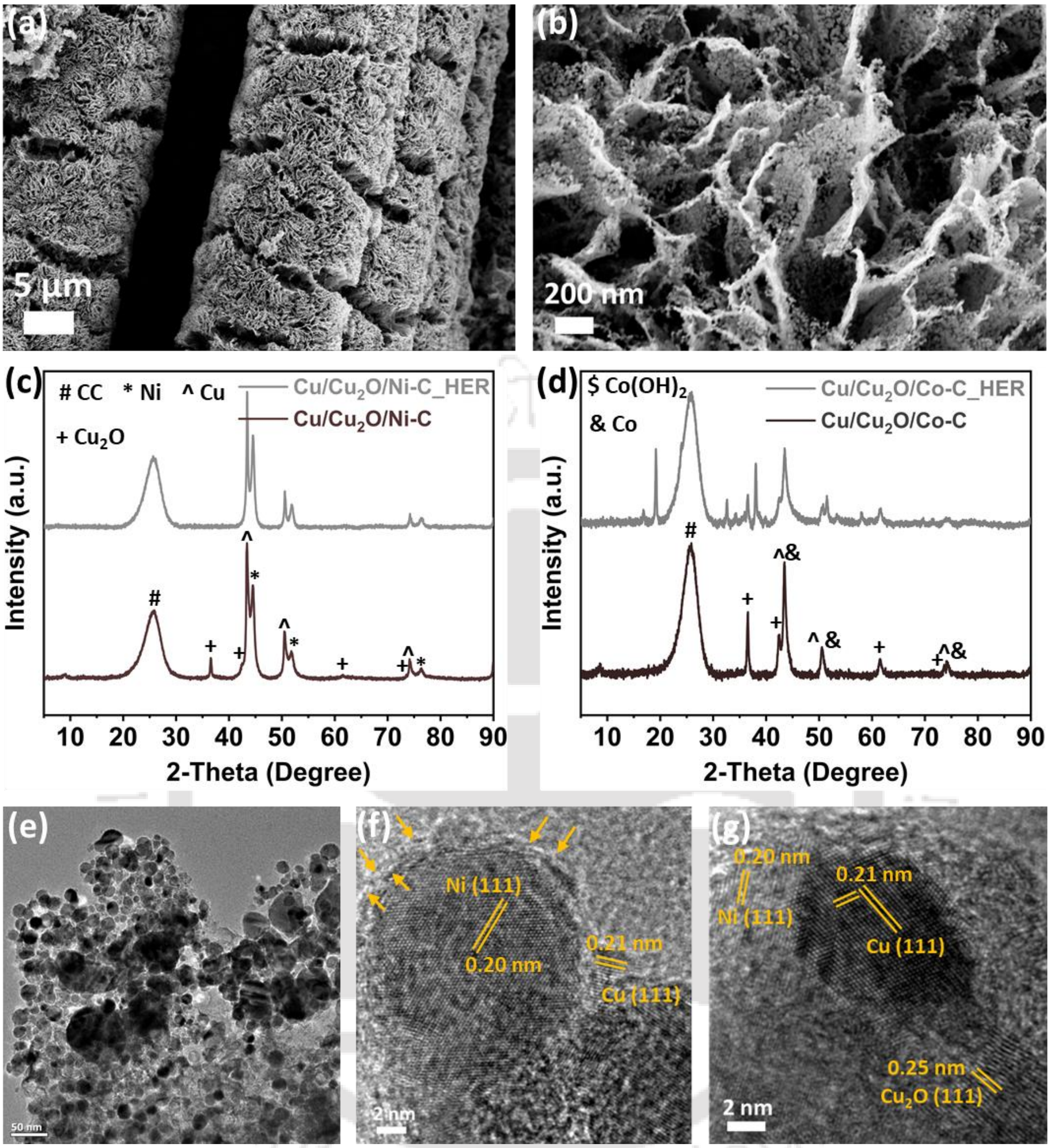

Figure 5.4: Characterization of the catalysts after HER (20 LSV cycles, EIS). (a) low and (b) high-magnified FESEM images of $Cu/Cu_2O/Ni\text{-}C@CC$ after HER, XRD pattern of (c) $Cu/Cu_2O/Ni\text{-}C@CC$ and (d) $Cu/Cu_2O/Co\text{-}C@CC$ before and after HER, (e) TEM image and (f), (g) HRTEM images of $Cu/Cu_2O/Ni\text{-}C$ catalyst.

Figure 5.4e is the TEM image of a porous $Cu/Cu_2O/Ni\text{-}C$ nanosheet after HER, where the hetero-phase catalyst nanoparticles are dispersed throughout the nanosheet, similar to the catalyst before HER. However, the nanoparticles are more densely packed than the catalyst before HER. Like the catalyst before HER, metallic Ni and Cu phases are coinciding to form a hetero-phase, as the HRTEM image signified (**Figure 5.4f**). A few layers surrounding the Ni nanoparticle are visible in the HRTEM image (**Figure 5.4f**). Similar to the $Co(OH)_2$ generated after HER in the Co-based hetero-phase catalyst, as evident from the XRD pattern of $Cu/Cu_2O/Co\text{-}C$ after HER (**Figure 5.4d**), the layers visible in the HRTEM image (**Figure 5.4f**) are possibly the $Ni(OH)_2$ layers (indicated by yellow arrows), formed after HER. However, the layers are almost disordered/amorphous, and a few layers surround the Ni nanoparticle, so the $Ni(OH)_2$ phase was not detectable in the XRD pattern (**Figure 5.4c**) of $Cu/Cu_2O/Ni\text{-}C$ after HER. Notably, the HRTEM image after HER (**Figure 5.4g**) suggested that the Cu_2O phase did not wholly transform into Cu but partially. The observations from FESEM, XRD, and TEM analysis indicated that the bimetallic hetero-phase catalyst underwent a surface morphology transformation and a transformation in the phases after electrocatalytic HER.

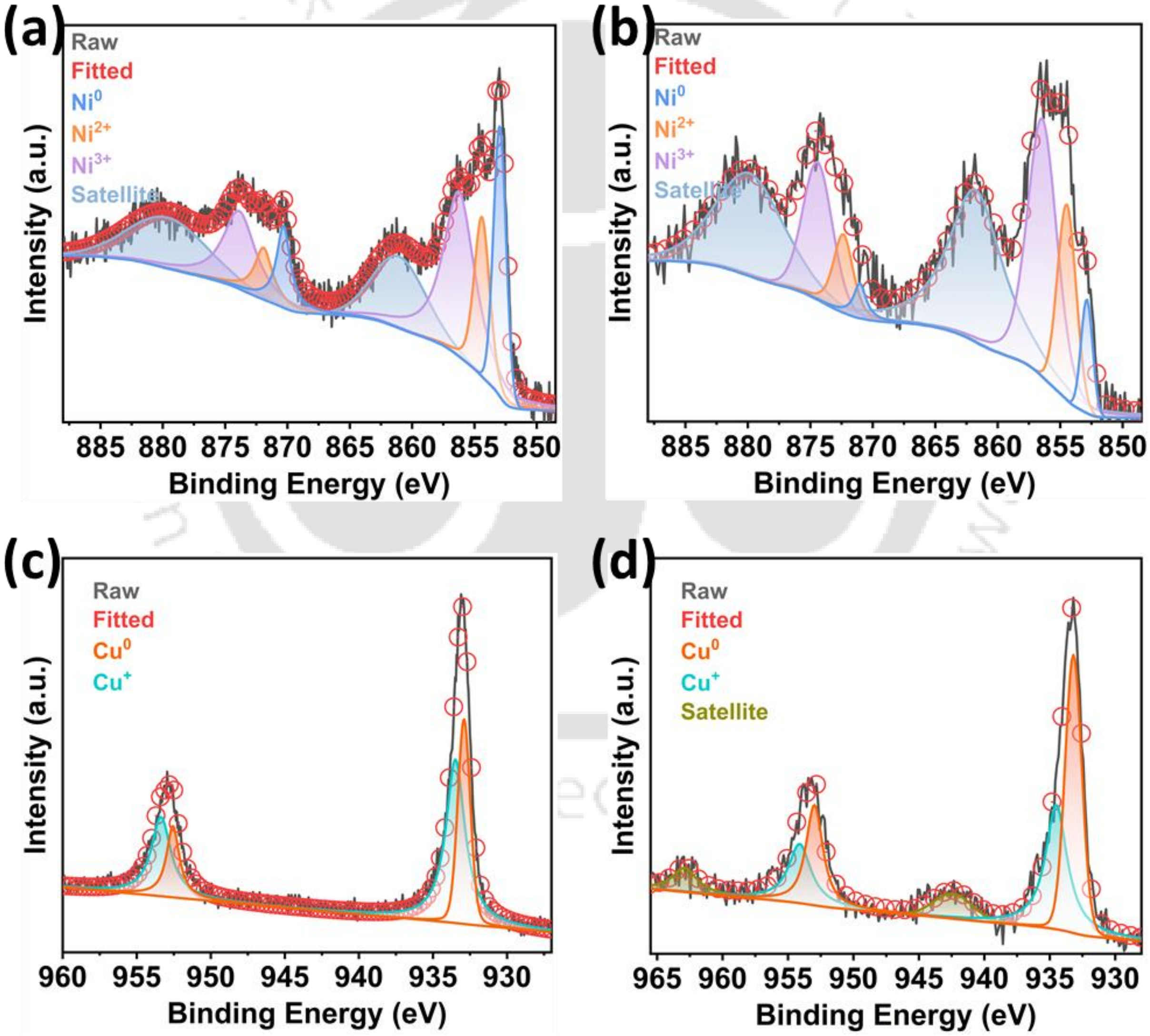

Figure 5.5: High-resolution Ni2p XPS spectra of $Cu/Cu_2O/Ni\text{-}C$ (a) before and (b) after HER, high-resolution Cu2p XPS spectra of $Cu/Cu_2O/Ni\text{-}C$ (c) before and (d) after HER.

X-ray photoelectron spectroscopy (XPS) analysis was carried out to further investigate the catalyst's transformations after HER. High-resolution Ni2p XPS spectra (**Figure 5.5a**, **b**) consist of three deconvoluted peaks corresponding to metallic Ni^0 (2p3/2: 853.0 eV, 2p1/2: 870.3 eV), Ni^{2+} (2p3/2: 854.5 eV, 2p1/2: 871.9 eV), and Ni^{3+} (2p3/2: 856.3 eV, 2p1/2: 873.9 eV). Before HER, the metallic Ni^0 state was dominant over higher oxidation states. However, after HER, the metallic Ni^0 peak was significantly suppressed, and the higher oxidation states of Ni became dominant, indicating the transformation of the surface of metallic Ni^0 to higher oxidation states. This observation strongly supports the result of HRTEM analysis, where the surface of the Ni nanoparticle was surrounded by the $Ni(OH)_2$ layers. Cu2p XPS spectra (**Figure 5.5c**, **d**) consist of two deconvoluted peaks related to metallic Cu^0 state (2p3/2: 932.9 eV, 2p1/2: 952.5 eV) and Cu^+ state (2p3/2: 933.5 eV, 2p1/2: 953.4 eV). As XRD and TEM analysis suggested, the XPS spectra also indicated the transformation of Cu_2O to metallic Cu ($Cu^+ \rightarrow Cu^0$), as the relative area of Cu^+ related peak was significantly decreased and the metallic Cu^0 peak was increased.

Till now, the FESEM, XRD, TEM, XPS, and electrochemical analyses suggested that the phase and surface morphology of the bimetallic hetero-phase catalysts (namely $Cu/Cu_2O/Ni-C$ and $Cu/ Cu_2O/Co-C$) were transformed after catalysis and these transformations are in favorable to HER. Still, it is unclear exactly when and at what HER LSV potential or after how many LSV cycles those HER-favourable transformations occurred. Therefore, the critical task is to reveal the real-time understanding of the best-performing catalyst's phase and surface morphology transformations. XRD analysis of the best-performing catalyst was conducted (**Figure 5.6a**) for different LSV potentials around the hump (+0.2 to -0.2 V vs RHE) observed in the first LSV cycle (**Figure 5.3a**) and also for one and two successive complete LSV cycles. The XRD patterns in **Figure 5.6a** unveiled that the intensity of the peaks (prominent peak is at around 36.70°) correspond to the Cu_2O phase continuously and significantly decreased when the LSV potential was varied from +0.2 V via +0.1 V to 0.0 V vs RHE. The Cu_2O peaks completely disappeared at -0.1 V vs RHE, signifying the transformation of the Cu_2O phase. The in-situ Raman spectroscopy again confirmed this observation to understand the real-time evolution of the catalyst during the HER. The Raman spectra of Cu_2O consist of three significant peaks at around 144.8 cm^{-1}, 214.3 cm^{-1}, and 642.0 $cm^{-1,}$ corresponding to Cu-O vibrations. As the pure metals are Raman inactive, the in-situ Raman spectra of the best-performing catalyst only consist of the peaks related to Cu_2O, confirming the presence of the same in the catalyst (**Figure 5.6b**). The in-situ Raman analysis revealed that the Raman peaks associated with Cu-O vibrations were significantly reduced at +0.1 V and vanished after 0.0 V vs. RHE, again confirming the transformation of the surface of Cu_2O to metallic Cu. However, XRD analysis suggested that the complete transformation occurred after -0.1 V vs RHE. It is not contradictory to the in-situ Raman analysis because Raman provides the information on the surface, whereas the XRD pattern provides the average information of the whole catalyst. As Cu_2O started transforming at +0.1 V vs. RHE, the surface was reduced to metallic Cu after 0.0 V vs. RHE, and after -0.1 V vs RHE, the bulk of the Cu_2O phase was almost entirely reduced to metallic Cu.

The FESEM analysis monitored the dynamic transformation of the surface morphology. The FESEM images at different potentials ranging from +0.2 V to -0.1 V vs. RHE were captured to visualize the dynamic changes of the surface of the best-performing catalyst (**Figure 5.6c-f**). The FESEM images unveiled that the surface of the nanosheets gradually became a more particulate structure, making it rougher and more porous as the potential varied from +0.2 V to -0.1 V vs RHE. This dynamic change in the surface morphology during LSV resulted in high surface area and increased active site accessibility of the catalyst, hence the increased activity of the catalyst towards HER.

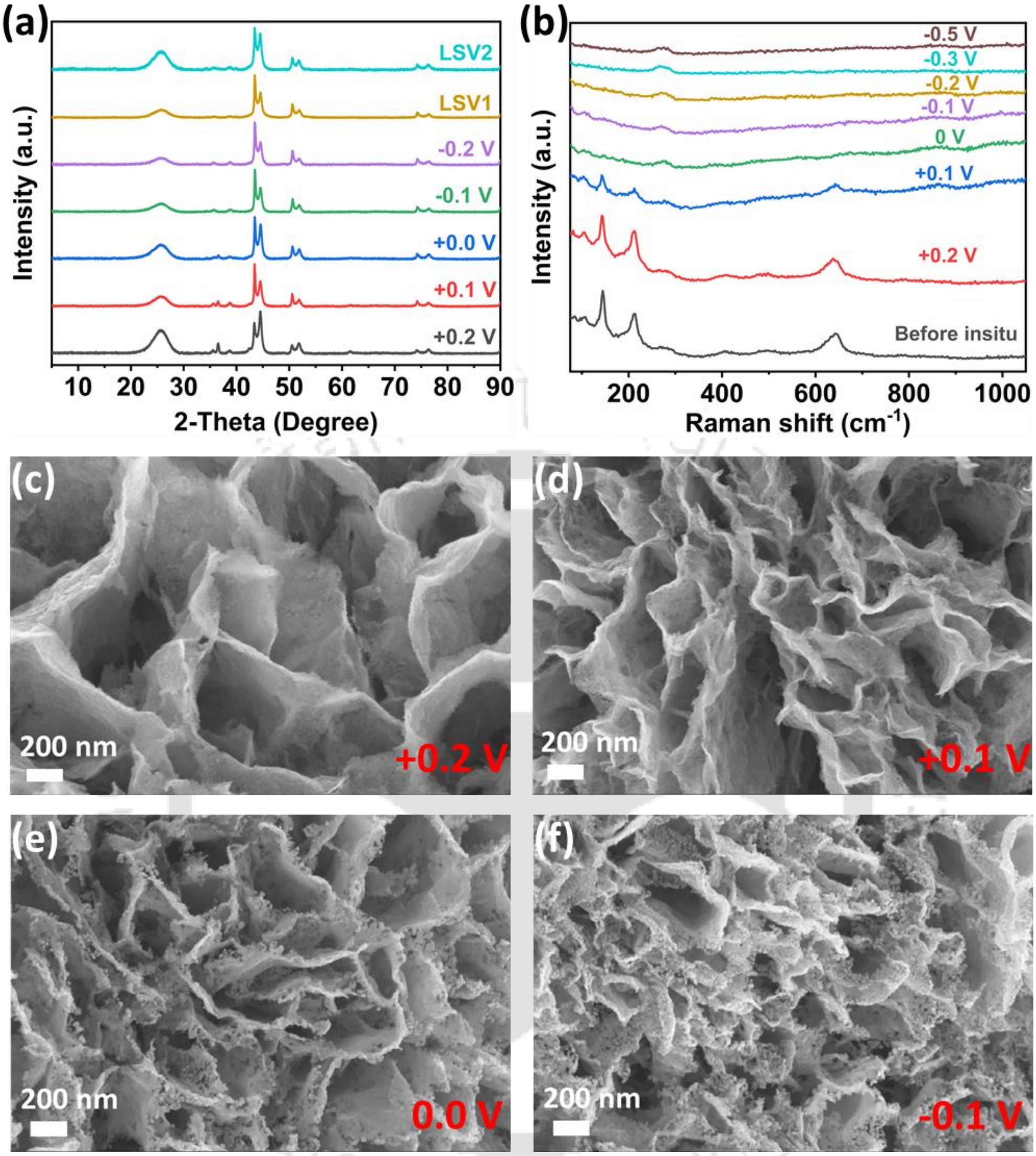

Figure 5.6: (a) XRD patterns of Cu/Cu_2O/Ni-C@CC at increasing HER LSV potentials Vs RHE, (b) in-situ Raman spectra of Cu/Cu_2O/Ni-C@CC, (c)-(f) FESEM images of Cu/Cu_2O/Ni-C@CC at increasing HER LSV potentials, respectively.

5.3.4. Local structure investigation of the catalyst by synchrotron-based X-ray absorption spectroscopy

Characterizing a catalyst and understanding its catalytic behavior is incomplete without knowing the local atomistic structure and coordination environment of the catalyst atoms of interest. Synchrotron-based X-ray absorption spectroscopy was employed to unveil the oxidation state of the elements and, most importantly, to understand the atomic coordination of the catalysts. The X-ray absorption near edge spectra (XANES) were utilized to reveal the oxidation state of the catalyst's elements. The extended X-ray absorption fine structure spectra (EXAFS) were used to understand the catalyst's local atomistic structure and the catalyst atoms' coordination environment. The Ni K-edge XANES spectra in **Figure 5.7a** indicated that the near-edge spectrum of the best-performing catalyst (Cu/Cu_2O/Ni-C) before HER is closer to the near-edge spectrum of the metallic Ni-foil, suggesting the metallic nature of Ni (Ni^0).

On the other hand, after HER, the near-edge spectrum of the catalyst (Cu/Cu_2O/Ni-C_HER) slightly shifted towards the near-edge spectrum of NiO, suggesting a marginal oxidation of the metallic Ni phase. The observation from the Ni K-edge XANES spectra confirmed the observation of the earlier XPS analysis. The corresponding Fourier transformed EXAFS (FT-EXAFS) in **Figure 5.7b** consists of some peaks related to the first coordination cell, second coordination cell, and so on from lower radial distance to higher. The dominant peak in the FT-EXAFS of Ni-foil is related to the Ni-Ni first coordination cell. The FT-EXAFS of NiO consists of two prominent peaks; the first peak is related to Ni-O's first coordination cell, and the second peak is associated with Ni-Ni's first coordination cell of NiO. The FT-EXAFS of the best-performing catalyst before HER has one prominent peak corresponding to the Ni-Ni first coordination cell at the same position as Ni-foil. On the other hand, after HER, the Ni-Ni first coordination cell slightly shifted to the higher R-value towards the Ni-Ni first coordination cell of Ni-O, suggesting a bit of oxidation of the metallic Ni phase.

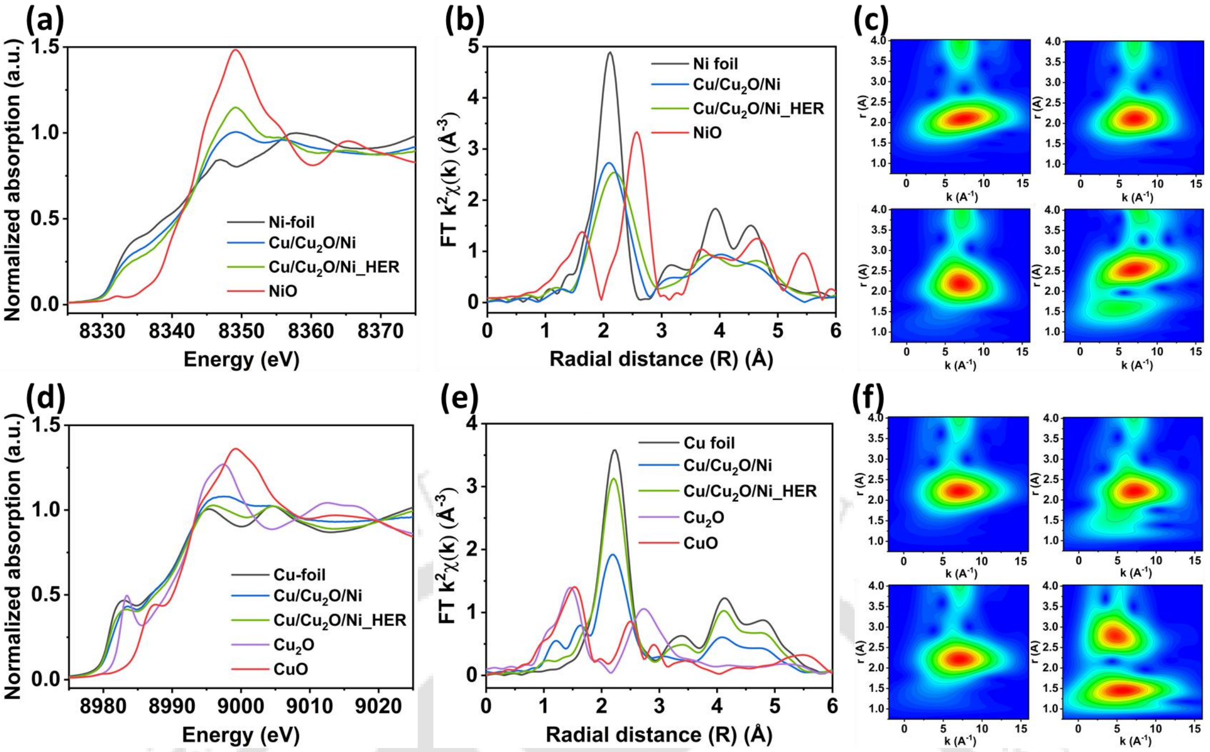

Figure 5.7: Local structure investigation of Cu/Cu$_2$O/Ni-C@CC before and after HER. Ni K-edge (a) XANES spectra, (b) EXAFS spectra, and (c) wavelet transformed EXAFS (WT-EXAFS) spectra, Cu K-edge (d) XANES spectra, (e) EXAFS spectra, and (f) WT-EXAFS spectra.

However, it seems that the Ni-O coordination cell-related peak is not present in the FT-EXAFS of the best-performing catalyst after HER, although the XANES suggested slight oxidation of the Ni phase after HER. The wavelet-transformed EXAFS (WT-EXAFS) presented in **Figure 5.7c** resolved the ambiguity. The WT-EXAFS of Ni-foil (top-left) has one significant color spot centered at around 2.0 Å related to Ni-Ni coordination. On the other hand, NiO has two significant color spots centered at around 1.4, Å corresponds to Ni-O coordination, and at around 2.5, Å corresponds to Ni-Ni coordination (bottom-right WT-EXAFS). Like Ni-foil, the best-performing catalyst before HER exhibited only Ni-Ni coordination (top-right WT-EXAFS). On the contrary, as expected, the catalyst after HER exhibited a faded color spot at around 1.4 Å, signifying the faint presence of Ni-O coordination (bottom-left WT-EXAFS) associated with a few layers of amorphous Ni(OH)$_2$. Likewise, the Cu K-edge XANES (**Figure 5.7d**) suggested that the near-edge spectrum of the best-performing catalyst shifted towards the metallic Cu-foil spectrum after HER, indicating the reduction of Cu$_2$O to Cu after HER. The FT-EXAFS (**Figure 5.7e**) and the corresponding WT-EXAFS (**Figure 5.7f**) suggested that the Cu-O coordination (1.35 Å) significantly decreased and Cu-Cu coordination (2.2 Å) significantly increased, confirming the previous observation of reduction of Cu_2O phase and transformation into metallic Cu phase.

5.3.5. Possible mechanism for the HER activity:

From the XRD, TEM, XPS, Raman, and XANES/EXAFS studies, the high HER activity of Cu/Cu2O/Ni-C can be explained and correlated. During the catalytic process, in-situ activation of the catalysts happened in which multi-modal porosity was introduced, partial oxidation of Ni into amorphous phase (possibly hydroxide), and Cu_2O converted to Cu. The highly porous activated sheet-like structure with in-plane porosity can greatly help mass transfer during the catalytic process, which is key to getting high performance, particularly at high currents. Partial oxidation of Ni is apparent from XPS and XANES investigations. The absence of any XRD peak after catalysis indicates the amorphous phase of the in-situ Ni-based hydroxide phase. Xue et al. also observed the conversion of Ni into a hydroxide phase during HER.[29]. However, unlike Xu et al.'s work, Ni's conversion into surface hydroxide is minimal because Ni is protected with a MOF-derived graphitic layer in our case. A thin amorphous coating of $Ni(OH)_2$ has been shown to significantly benefit the HER activity of catalysts in alkaline conditions.[30] An additional water dissociation step is needed in alkaline conditions to get protons for the HER process. The overcoating of $Ni(OH)_2$ acts as a water dissociation catalyst to produce protons, which can be transferred to the underlying catalytic sites for their conversion into H_2. Nickel underlying the in-situ formed $Ni(OH)_2$ can act as the leading HER catalytic active site, and the fragile nature of the hydroxide layer benefits the proton transfer to Ni sites.[30] The Ni also forms an interface with Cu, as is evident from TEM observation. Copper (Cu) is not a suitable HER catalyst due to its filled d-orbital (d^{10}). Thus, $Ni(OH)_2$ sheathed Ni can act as the main HER catalyst in the system, where its interface with Cu can benefit the activity of Ni due to interfacial charge transfer from Cu to Ni due to their slightly different electronegativity ($\chi_{Ni} = 1.91, \chi_{Cu=}1.9$). This electron transfer can change and increase the d-band filling of Ni, thus reducing the adsorption strength of hydrogen (*H), which benefits the HER process. The role of Cu_2O in the catalysts can be ignored because it is majorly converted to Cu during HER, and this process did not decrease HER performance; instead, it increases considerably.

5.4. Conclusion

The in-situ phase and morphology-driven reconstruction of the catalyst during HER demonstrates the transformative potential of PTS-derived $Cu/Cu_2O/Ni$-C hetero-phase catalyst.

The rare cathodic phase evolution, involving partial transformation of Cu_2O to metallic Cu and dynamic surface restructuring, significantly enhances the catalyst's activity and stability. Advanced characterization techniques reveal that these transformations optimize the electronic interactions among phases, promoting efficient charge transfer and active site accessibility. The Cu/Cu_2O/Ni-C achieves a remarkable HER performance with an overpotential of 46 mV for 10 mA cm^{-2}, rivaling the Pt/C catalyst. Furthermore, its operational stability over prolonged periods highlights its potential for practical alkaline electrolyzer applications. This work establishes the viability of PTS as a rapid, scalable method for designing next-generation electrocatalysts with tailored properties, offering a robust platform for extending this approach to other electrocatalytic reactions.

References

[1] Y. C. Han, M. L. Liu, L. Sun, X. C. Li, Y. Yao, C. Zhang, S. Y. Ding, H. G. Liao, L. Zhang, F. R. Fan, M. Moskovits, Z. Q. Tian, *Nano Energy* **2022**, *97*, 107125.

[2] W. Jiang, L. Xia, B. Ferreira Gomes, M. Haumann, H. Dau, C. Roth, W. Lehnert, M. Shviro, *Small* **2024**, *20*, 1.

[3] A. Majumdar, P. Dutta, A. Sikdar, H. Lee, D. Ghosh, S. N. Jha, S. Tripathi, Y. Oh, U. N. Maiti, *Small* **2022**, *18*, 1.

[4] Q. Liang, H. Jin, Z. Wang, Y. Xiong, S. Yuan, X. Zeng, D. He, S. Mu, *Nano Energy* **2019**, *57*, 746.

[5] A. Naderi, M. Jourshabani, M. Razi Asrami, B. K. Lee, *Chem. Eng. J.* **2024**, *484*, 149111.

[6] Q. He, Y. Zhou, H. Shou, X. Wang, P. Zhang, W. Xu, S. Qiao, C. Wu, H. Liu, D. Liu, S. Chen, R. Long, Z. Qi, X. Wu, L. Song, *Adv. Mater.* **2022**, *34*, 1.

[7] J. Mahmood, F. Li, S. M. Jung, M. S. Okyay, I. Ahmad, S. J. Kim, N. Park, H. Y. Jeong, J. B. Baek, *Nat. Nanotechnol.* **2017**, *12*, 441.

[8] Z. Zhao, Z. Liu, A. Zhang, X. Yan, W. Xue, B. Peng, H. L. Xin, X. Pan, X. Duan, Y. Huang, *Nat. Nanotechnol.* **2022**, *17*, 968.

[9] Z. Li, J. Zou, X. Xi, P. Fan, Y. Zhang, Y. Peng, D. Banham, D. Yang, A. Dong, *Adv. Mater.* **2022**, *34*, 1.

[10] Q. Wang, C. Q. Xu, W. Liu, S. F. Hung, H. Bin Yang, J. Gao, W. Cai, H. M. Chen, J. Li, B. Liu, *Nat. Commun.* **2020**, *11*, 1.

[11] Y. Weng, K. Wang, S. Li, Y. Wang, L. Lei, L. Zhuang, Z. Xu, *Adv. Sci.* **2023**, *10*, 1.

[12] Y. Li, T. Xu, Q. Huang, L. Zhu, Y. Yan, P. Peng, F. F. Li, *ACS Catal.* **2023**, *13*, 7597.

[13] T. Jiang, Y. Yuan, S. Liu, A. J. Hunt, G. Tan, *ACS Omega* **2020**, *5*, 16021.

[14] H. Liu, C. Liu, X. Zong, Y. Wang, Z. Hu, Z. Zhang, *Int. J. Hydrogen Energy* **2023**, DOI 10.1016/j.ijhydene.2023.04.150.

[15] Z. Zhang, Y. Tan, T. Zeng, L. Yu, R. Chen, N. Cheng, S. Mu, X. Sun, *Nano Res.* **2021**, *14*,

2353.

[16] J. Ren, Q. Wang, Q. Xiang, C. Yang, Y. Liang, J. Li, J. Liu, D. Qian, *Chem. Eng. Sci.* **2023**, *280*, 119026.

[17] W. Liu, P. Bai, S. Wei, X. Kong, C. Yang, L. Xu, *Appl. Catal. B Environ.* **2024**, *348*, 123831.

[18] Y. Wang, S. Wang, Z. L. Ma, L. T. Yan, X. B. Zhao, Y. Y. Xue, J. M. Huo, X. Yuan, S. N. Li, Q. G. Zhai, *Adv. Mater.* **2022**, *34*, 1.

[19] J. Feng, X. Wang, H. Pan, *Adv. Mater.* **2024**, *2411688*, 1.

[20] L. Shao, X. Han, L. Shi, T. Wang, Y. Zhang, Z. Jiang, Z. Yin, X. Zheng, J. Li, X. Han, Y. Deng, *Adv. Energy Mater.* **2024**, *14*, 1.

[21] B. Wang, X. Wang, Z. Wang, K. Srinivas, X. Zhang, B. Yu, D. Yang, W. Zhang, T. C. Lau, Y. Chen, *Chem. Eng. J.* **2021**, *420*, 1.

[22] H. Huang, S. Zhou, C. Yu, H. Huang, J. Zhao, L. Dai, J. Qiu, *Energy Environ. Sci.* **2020**, *13*, 545.

[23] C. Andronescu, S. Barwe, E. Ventosa, J. Masa, E. Vasile, B. Konkena, S. Möller, W. Schuhmann, *Angew. Chemie - Int. Ed.* **2017**, *56*, 11258.

[24] K. Huang, J. Xia, Y. Lu, B. Zhang, W. Shi, X. Cao, X. Zhang, L. M. Woods, C. Han, C. Chen, T. Wang, J. Wu, Y. Huang, *Adv. Sci.* **2023**, *10*, 1.

[25] S. Wu, D. Chen, S. Li, Y. Zeng, T. Wang, J. Zhang, J. Yu, S. Mu, H. Tang, *Adv. Sci.* **2023**, *10*, 1.

[26] X. Liang, H. He, X. Yang, W. Lü, L. Wang, X. Li, *J. Energy Storage* **2021**, *42*, 103105.

[27] C. Zhao, Y. Chen, S. Gong, W. Tan, H. Pan, X. Liu, Q. Shi, *J. Saudi Chem. Soc.* **2024**, *28*, 101856.

[28] X. Zhou, W. Xu, Y. Liang, H. Jiang, Z. Li, S. Wu, Z. Gao, Z. Cui, S. Zhu, *ACS Catal.* **2024**, *14*, 12251.

[29] S. Xue, Y. Liang, S. Hou, Y. Zhang, H. Jiang, *ChemSusChem* **2022**, *15*, DOI 10.1002/cssc.202201072.

[30] C. Wan, Z. Zhang, J. Dong, M. Xu, H. Pu, D. Baumann, Z. Lin, S. Wang, J. Huang, A. H. Shah, X. Pan, T. Hu, A. N. Alexandrova, Y. Huang, X. Duan, *Nat. Mater.* **2023**, *22*, 1022.

Chapter 6

Summary and Outlook

Summary and Outlook

6.1. Summary of the thesis

This thesis focuses on the development of innovative ultrafast synthesis techniques and their application in designing graphitic carbon nanostructures and nanohybrids for energy storage and electrocatalysis. Addressing key challenges in conventional material synthesis provides scalable, efficient, and tunable approaches for creating high-performance supercapacitors and hydrogen evolution reaction (HER) catalysts. It also offers advanced characterizations and atomistic modeling to address energy storage and electrocatalysis challenges. By emphasizing precise control over porosity, graphitization, and nanocatalyst crystallization, it demonstrates the potential of graphitic carbon nanostructures and their hybrids for high-performance supercapacitors and hydrogen evolution reaction (HER) catalysts. Below are the key findings of this thesis in detail:

6.1.1. Development of ultrafast synthesis techniques

The transient Joule heating (TJH) and transient electro-graphitization (TEG) methods introduced in this thesis represent a paradigm shift in material synthesis. These techniques achieve ultrafast heating (to over 1000 K) and cooling within milliseconds, enabling the precise fabrication of porous graphene frameworks and MOF-derived graphitic nano-leaves (GNLs).

These methods allowed the direct transformation of carbon precursors and MOFs into functional nanostructures, significantly reducing the thermal budget and processing time compared to conventional methods. They also enabled independent control over critical parameters such as graphitization, porosity, and metal nanocatalyst crystallization, making them highly versatile for large-scale material production.

6.1.2. Control of Porosity for Enhanced Surface Area

Achieving hierarchical porosity was critical to this work, as it directly influences ion accessibility and charge transport. The TJH and TEG techniques facilitated the creation of porous graphene and perforated GNLs with nano-to-microscale porosity, resulting in materials with high surface area and ion transport efficiency.

These materials demonstrated exceptional performance in supercapacitors. Symmetric supercapacitors fabricated with porous graphene achieved an areal capacitance of 380.2 mF cm^{-2}, while wearable asymmetric supercapacitors incorporating GNLs exhibited an energy density of 107.8 μWh cm^{-2}. The hierarchical porosity also contributed to long-term stability and mechanical durability, making these devices suitable for flexible and wearable applications.

6.1.3. Graphitization Control for Enhanced Conductivity

The ability to tune graphitization levels of carbon nanostructures was a significant achievement of this work. The TJH and TEG methods enabled precise control over graphitic order, resulting in highly conductive materials optimized for energy storage and catalytic applications.

For instance, GNLs derived from MOFs were graphitized at varying levels by adjusting the TJH pulse duration. This flexibility allowed for tailored conductivity and surface functionalities, essential for charge storage and catalytic activity. Moreover, restoring graphitic order after anodic oxidation ensured that porosity enhancement did not compromise electrical conductivity, maintaining high performance in supercapacitors and HER catalysts.

6.1.4. Tunability of Crystallization of Metal Nanoclusters for Catalysis

A unique aspect of this work was the tunability of metal nanocluster crystallization depending on the graphitization level of the carbon support. The TEG method enabled independent control over both processes by decoupling the pyrolysis of MOFs from nanocatalyst growth.

The degree of graphitization influenced the crystallization states of supported ruthenium (Ru) nanoclusters, producing single atoms, amorphous nanoclusters, and crystalline nanoparticles. For example, amorphous Ru nanoclusters on GNLs with intermediate graphitization (a-Ru@GNL$_{500}$) demonstrated exceptional HER activity. These catalysts required an overpotential of only 23 mV to achieve a current density of 10 mA cm^{-2}, outperforming state-of-the-art Pt/C catalysts.

This tunability is critical for optimizing catalytic performance, as the electronic interaction between the nanocatalyst and the carbon support depends on the crystallization state. Density functional theory (DFT) calculations revealed that amorphous Ru nanoclusters exhibited favorable hydrogen adsorption free energy (ΔG_{H*}), accelerating reaction kinetics. The synergistic interaction between cobalt embedded in the graphitic layers and the amorphous Ru clusters further enhanced performance.

6.1.5. Creation of Hetero-Phase Interfaces

Developing hetero-phase interfaces, such as $Cu/Cu_2O/Ni-C$ and Ru/Co-NP/GNL systems, introduced synergistic effects that significantly boosted catalytic activity. These interfaces facilitated efficient charge transfer and dynamic phase transformations during catalytic reactions, enhancing HER performance.

For instance, the $Cu/Cu_2O/Ni-C$ catalyst exhibited an overpotential of 46 mV at 10 mA cm^{-2}, comparable to noble metal catalysts. Such hetero-phase systems provide a promising pathway for developing cost-effective and high-performance electrocatalysts.

6.1.6. Advanced Characterizations for Deeper Insights

Cutting-edge characterization techniques, including XANES, EXAFS, and TEM, provided valuable insights into the structure-property relationships of the developed materials. These techniques revealed dynamic morphological transformations and electronic interactions during HER, validating the efficacy of the ultrafast synthesis methods.

The Insights gained from these advanced characterizations were instrumental in optimizing material properties and understanding the mechanisms underlying their superior performance.

6.1.7. Atomistic Understanding Through DFT

Density functional theory (DFT) calculations provided atomistic insights into the catalytic mechanisms of HER. They revealed how the electronic structure of Ru nanoclusters interacted with graphitic supports, reducing antibonding orbital occupancy and enhancing catalytic activity.

These simulations highlighted the importance of controlling hydrogen adsorption energetics (ΔG_{H*}) and the cooperative effects at hetero-interfaces, offering a rational design strategy for next-generation catalysts.

6.2. Outlook

The methodologies and insights developed in this thesis pave the way for exciting future research directions, emphasizing broader applications, improved performance, and sustainability.

Advancing material tunability

The ability to tune material properties such as conductivity, surface area, porosity, and electronic structure by adjusting the carbon support's graphitization level and the size, crystallinity, and heterostructure of the supported nanocatalysts is a major strength of this work. Future research can leverage this tunability to design materials for specific applications, such as hybrid supercapacitor-battery systems or multifunctional catalysts for electrosynthesis.

Scaling Up for Industrial Applications

The TJH and TEG methods demonstrated scalability, but industrial-scale production needs further optimization. Collaborations with industry could facilitate the development of large-scale setups for manufacturing advanced materials. Integrating these materials into commercial energy devices, such as electrolyzers and supercapacitors, would validate their performance under real-world conditions.

Expanding Applications Beyond HER

The tunability of graphitization and crystallization demonstrated in this work can be extended to other catalytic processes, including oxygen evolution reaction (OER), carbon dioxide reduction reaction (CO_2RR), nitrogen reduction reaction (NRR), and nitrate reduction reaction (NitRR). These processes are essential for sustainable chemical production and environmental remediation.

The developed materials could also find applications in pollutant degradation, water splitting under sunlight, and CO_2 capture, leveraging their tailored surface and electronic properties.

Enhancing Catalyst Stability and Performance

Improving the long-term stability of the catalysts under harsh industrial conditions is critical. Alloying strategies, such as combining multiple transition metals, could enhance catalytic activity and durability while minimizing noble metal content. Further research should also focus on optimizing hetero-interfaces to balance stability and activity.

Promoting Sustainability and Green Chemistry

Future research should explore renewable or waste-derived precursors for synthesizing carbon nanostructures, ensuring environmentally friendly production. Additionally, integrating these materials into renewable energy systems, such as solar-powered electrolyzers, could further reduce the carbon footprint of the energy cycle.

Advancing Wearable Energy Storage Devices

The results of this thesis demonstrate the potential for integrating high-performance materials into flexible and wearable electronics. Future work could focus on developing multifunctional devices that combine energy storage with sensors or photovoltaics. Conducting durability tests under practical conditions will ensure reliability in real-world applications.

By addressing these directions, the methodologies and insights developed in this thesis can drive significant advancements in sustainable energy technologies. Integrating ultrafast synthesis techniques, advanced characterizations, and computational modeling will accelerate progress toward scalable, efficient, and environmentally friendly solutions for energy storage and catalysis. I hope this thesis work will contribute to bridging the gap between laboratory-scale research and industrial-scale applications.

Permission and attributions

- The content of Chapter 2 is based on the following published work:

Carbon 203 (2023) 191-201, in collaboration with Pronoy Dutta, Abhisek Majumdar, Amalika Patra, Sujit Kumar Deb, Snehasish Das, Neha V. Dambhare, Arup K. Rath, and Uday Narayan Maiti.

- The content of Chapter 3 is based on an unpublished work in collaboration with Amalika Patra, Sujit Kumar Deb, Snehasish Das, Priyam Mukherjee, Pranab Bera, Hemanta Upadhya, Arup K. Rath, and Uday Narayan Maiti.

- The content of Chapter 4 is based on the following published work:

Adv. Funct. Mater. 2024, 34, 2315460, in collaboration with Amalika Patra, Sujit Kumar Deb, Hemanta Upadhya, Snehasish Das, Priyam Mukherjee, Waleed Ahmad, Narad Barman, Ranjit Thapa, Neha V Dambhare, Arup Kumar Rath, Jaysri Das, Uttam Manna, Rajashri R. Urkude, Youngtak Oh, and Uday Narayan Maiti.

- The content of Chapter 5 is based on unpublished work in collaboration with Snehasish Das, Priyam Mukherjee, Pranab Bera, Hemanta Upadhya, and Uday Narayan Maiti.